



<https://theses.gla.ac.uk/>

Theses Digitisation:

<https://www.gla.ac.uk/myglasgow/research/enlighten/theses/digitisation/>

This is a digitised version of the original print thesis.

Copyright and moral rights for this work are retained by the author

A copy can be downloaded for personal non-commercial research or study, without prior permission or charge

This work cannot be reproduced or quoted extensively from without first obtaining permission in writing from the author

The content must not be changed in any way or sold commercially in any format or medium without the formal permission of the author

When referring to this work, full bibliographic details including the author, title, awarding institution and date of the thesis must be given

Enlighten: Theses

<https://theses.gla.ac.uk/>
research-enlighten@glasgow.ac.uk

**DETECTION OF STABLE ISOTOPES USING
RESONANCE IONISATION SPECTROSCOPY**

**Shauna Lynn Taylor Drysdale, B.Sc.
Department of Physics and Astronomy
University of Glasgow**

**Presented as a thesis for the degree of Doctor of Philosophy
in the University of Glasgow
September 1989**

© Shauna Lynn Taylor Drysdale , 1989

ProQuest Number: 10999284

All rights reserved

INFORMATION TO ALL USERS

The quality of this reproduction is dependent upon the quality of the copy submitted.

In the unlikely event that the author did not send a complete manuscript and there are missing pages, these will be noted. Also, if material had to be removed, a note will indicate the deletion.



ProQuest 10999284

Published by ProQuest LLC (2018). Copyright of the Dissertation is held by the Author.

All rights reserved.

This work is protected against unauthorized copying under Title 17, United States Code
Microform Edition © ProQuest LLC.

ProQuest LLC.
789 East Eisenhower Parkway
P.O. Box 1346
Ann Arbor, MI 48106 – 1346

ACKNOWLEDGEMENTS

I would like to thank the following people who have provided assistance in the course of this work :-

--- my supervisor Dr. Kenneth W.D. Ledingham for constant advice and encouragement during the period of this research,

--- my fellow research students, Dr. Michael Towrie, Dr. Michael H.C. Smyth, Dr. Christine M. Houston and Mr. Paul T. McCombes for their considerable assistance during experimental work,

--- Drs. Ravi P. Singhal, Derek T. Stewart and Robert Jennings for helpful discussions and suggestions,

---Drs. Colin Raine and Russell J. Jenkins for assistance with computing for data acquisition and analysis,

--- Mr. Robert Maxwell, Mr. Thomas McCanny and Mr. D. Alan Seath for technical support and advice.

I would also like to give my special thanks to my family, Mr. Charles H.F. Sturrock and Mr. Alan K. Dykes for invaluable support and encouragement. Finally, I would like to acknowledge the Science and Engineering Research Council for their financial support.

PUBLICATIONS

Detection of toluene in proportional counter gas by resonant two photon ionisation spectroscopy

S.L.T. Drysdale, K.W.D. Ledingham, C. Raine, K.M. Smith, M.H.C. Smyth, D.T. Stewart, M. Towrie and C.M. Houston

Nucl. Inst. and Meth. A252 (1986) 521

Investigation of the effect of gas purification on the background laser ionisation in proportional counters

S.L.T. Drysdale, A.P. Land, K.W.D. Ledingham, C. Raine, K.M. Smith, M.H.C. Smyth, D.T. Stewart, M. Towrie and C.M. Houston

ALEPH 86-30 (distr. TPCC-AL) (1986)

Applications of resonant ionisation spectroscopy to accelerator based high energy physics

K.W.D. Ledingham, J.W. Cahill, S.L.T. Drysdale, C. Raine, K.M. Smith, M.H.C. Smyth, D.T. Stewart, M. Towrie and C.M. Houston

"Resonance Ionisation Spectroscopy 1986" Inst. Phys. Conf. Ser. No. 84

Multiphoton transitions in caesium vapour

C.M. Houston, S.L.T. Drysdale, K.W.D. Ledingham, C. Raine, K.M. Smith, M.H.C. Smyth, D T. Stewart and M. Towrie

"Resonance Ionisation Spectroscopy 1986" Inst. Phys. Conf. Ser. No. 84

Detection of toluene in proportional counter gas by resonant ionisation two photon spectroscopy

S.L.T. Drysdale, K.W.D. Ledingham, C. Raine, K.M. Smith, M.H.C. Smyth, D.T. Stewart, M. Towrie and C.M. Houston
CERN - EP / 86-28 (February 1986)

Potential of resonant ionisation mass spectroscopy for detecting environmentally important radioactive nuclides

M.H.C. Smyth, S.L.T. Drysdale, R. Jennings, K.W.D. Ledingham, D.T. Stewart, M. Towrie, C.M. Houston, M.S. Baxter and R.D. Scott
"Resonance Ionisation Spectroscopy 1986" Inst. Phys. Conf. Ser. No. 84

The Glasgow resonant mass spectrometer

M. Towrie, S.L.T. Drysdale, R. Jennings, A.P. Land, K.W.D. Ledingham, P.T. McCombes, R.P. Singhal, M.H.C. Smyth, D.T. Stewart, C.M. Houston and C.J. McLean

"Resonance Ionisation Spectroscopy 1988" Inst. Phys. Conf. Ser. No. 94

Molecular and collisional processes during three photon ionisation transitions in caesium and rubidium vapours

M.H.C. Smith, S.L.T. Drysdale, R. Jennings, A.P. Land, K.W.D. Ledingham, R.P. Singhal, D.T. Stewart, M. Towrie and C.M. Houston

"Resonance Ionisation Spectroscopy 1988" Inst. Phys. Conf. Ser. No. 94

Application of resonant ionisation spectroscopy to depth profiling in III - V semiconductor devices

C.J. McLean, J.H. Marsh, J.W. Cahill, S.L.T. Drysdale, R. Jennings, A.P. Land, K.W.D. Ledingham, P.T. McCombes, R.P. Singhal, M.H.C. Smyth, D.T. Stewart and M. Towrie

"Resonance Ionisation Spectroscopy 1988" Inst. Phys. Conf. Ser. No. 94

Two and three photon ionisation transitions in caesium vapour

C.M. Houston, S.L.T. Drysdale, R. Jennings, A.P. Land, K.W.D. Ledingham, R.P. Singhal, M.H.C. Smyth, D.T. Stewart and M. Towrie

J. Phys. D. : Appl. Phys. 21 (1988) S 59

Trace analysis using a commercial resonant ionisation mass spectrometer

M. Towrie, S.L.T. Drysdale, R. Jennings, A.P. Land, K.W.D. Ledingham, P.T. McCombes, R.P. Singhal, M.H.C. Smyth and C.J. McLean

(To be submitted to the Int. Jour. Mass Spec. and Ion Phys.)

CONTENTS

	Page
SUMMARY	1
Chapter 1 INTRODUCTION AND THEORY	4
1.1 INTRODUCTION	4
1.11 Resonance Ionisation Spectroscopy	4
1.12 Historical Background of RIS	7
1.13 Historical Background of RIMS	9
1.14 Laser Ionisation Studies at Glasgow University	12
1.2 THEORY	14
1.21 Two Photon Ionisation	14
1.22 Population Rate Equations	20
1.23 Effect of Linewidth on the Reaction Rate	24
1.24 Selection Rules	27
1.25 Rydberg States	28
1.26 Theory of Molecular Dimers	30
Chapter 2 INSTRUMENTATION	34
2.1 Introduction	34
2.2 Laser Systems	35
2.3 Excimer Laser	35
2.4 Excimer Pumped Dye Laser	37
2.5 Nd:YAG Laser	40
2.6 Second Harmonic Generation	42
2.7 Measurement and Attenuation of Laser Power	45
2.8 Proportional Counter	45
2.9 Counter Gas	47
2.10 Proportional Counter Housing	48
2.11 Quadrupole Mass Spectrometer	49
2.12 Time of Flight Mass Spectrometer	51
2.13 The Reflectron	53
2.14 LSI 11 Data Acquisition System	55
2.15 Data Acquisition for the Time of Flight Mass Spectrometer	56

Chapter 3	RIS OF CAESIUM VAPOUR	58
3.1	Introduction	58
3.2	Two Photon Transitions	60
3.3	6s - Rydberg Transitions	63
3.4	6s - ns and 6s - nd Transitions	65
Chapter 4	RIS OF RUBIDIUM VAPOUR	70
4.1	Introduction	70
4.2	Two Photon Ionisation of Rubidium	71
4.3	Three Photon Ionisation of Rubidium	73
4.4	Pressure Dependence of Three Photon Ionisation of Rubidium	76
4.5	Atomic Mass Spectra	78
4.6	Molecular Mass Spectra	79
Chapter 5	LASER TIME OF FLIGHT MASS SPECTROMETER	82
5.1	Introduction	82
5.2	Vaporisation of Sample	82
5.3	Use of SIMS as an Analytical Technique	84
5.4	Sputtering Mechanism	86
5.5	Matrix Effects	87
5.6	Minibeam Ion Gun	89
5.7	Laser Desorption	90
5.8	Resonant Ionisation	92
5.9	Detection Using Time of Flight Mass Spectrometers	93
5.10	Resolution of the Time of Flight Mass Spectrometer	94
5.11	Laser Mass Spectrometer for Ultra - Trace Analysis	97
5.12	Preliminary Results	98
5.13	Sensitivity of Laser TOF Mass Spectrometry	101

Chapter 6	RESULTS OF LASER INDUCED IONISATION IN A TIME OF FLIGHT MASS SPECTROMETER	104
6.1	Introduction	104
6.2	Laser Ionisation of Ambient Organic Vapour	105
6.3	Laser Ionisation of NBS Coal Samples	107
6.4	RIMS of NBS Coal Samples	112
6.5	Carbon Clustering Effects - Background	115
6.6	Carbon Clustering Results from TOF Mass Spectrometer	120
Chapter 7	CONCLUSIONS AND FUTURE PROGRAMMES	124
7.1	RIS of Caesium Vapour	124
7.2	RIS of Rubidium Vapour	124
7.3	Time of Flight Mass Spectrometer	125
7.4	Autoionisation	126
7.5	Further Experiments using the TOF Mass Spectrometer	127
7.6	Molecular Spectroscopy	129
7.7	Supersonic Cooling	130
7.8	Detection of Radioactive Caesium	131
	APPENDICES	132
Appendix1	Applications of Resonant Ionisation Spectroscopy to Accelerator Based High Energy Physics	132
Appendix2	Laser Mass Spectrometer for Depth Profiling	141
References		144

SUMMARY

The laser ionisation studies group was formed in 1983 with the initial task of using the resonance ionisation technique to detect impurities in counter gases used in multiwire drift chambers at CERN. After completion of this high energy physics application, the technique was then directed towards the development of a combination of resonance ionisation with mass spectrometry (RIMS) for the purpose of ultra sensitive trace analysis. To this end, two resonance ionisation time of flight mass spectrometers have been designed and constructed, one designed primarily for ultra trace element analysis and the other for depth profiling in semiconductors.

In order to maximise the sensitivity of the RIMS technique, the physics behind the resonance ionisation process must be clearly understood. Therefore, the ionisation spectroscopy of the alkali metals caesium and rubidium was investigated using a proportional counter and also a quadrupole mass spectrometer to distinguish between the two isotopes of rubidium.

Chapter 1 gives a brief history of resonance ionisation spectroscopy, and explains the basic ideas behind the technique. Theoretical rate equations relating to the two photon ionisation case are given, and the appropriate saturation conditions are derived.

The experimental apparatus is described in detail in Chapter 2. All types of lasers used are described, and the operation of the three detectors used (proportional counters, quadrupole mass spectrometers and time of flight mass spectrometers) is explained.

Chapters 3 and 4 document the results obtained from the proportional counter

and the quadrupole mass spectrometer. The spectroscopy of caesium metal using a proportional counter is described in Chapter 3. Two and three photon ionisation spectra are shown, and investigations made into the requirements for saturation of these transitions is discussed. Rubidium ionisation spectra using both the proportional counter and the quadrupole mass spectrometer are presented in Chapter 4. The author was largely responsible for molecular mass spectra obtained using the quadrupole mass spectrometer.

Chapter 5 explains the choice of time of flight mass spectrometers, and describes the construction and operation of the two laser ionisation mass spectrometers at Glasgow. The technique of laser desorption is also explained. In the later sections of the chapter, methods for optimising the resolution of the laser mass spectrometers are discussed.

The initial results taken from the trace analysis instrument at Glasgow are presented in Chapter 6. This chapter can be divided into three distinct sections. Firstly, spectra of the background ionisation within the spectrometer are shown and discussed, and experiments to discover the source of the ionisation are described. As carbon was found to be a major contaminant in the spectra obtained, further spectra of pure graphite were recorded. This progressed to a study of carbon clustering effects, documented in the final section of this chapter. In the second section, laser desorbed spectra of standard reference material (NBS coal samples) were obtained in order to investigate the qualitative and quantitative accuracy of this non resonant technique. Results of resonant ionisation detection of rubidium at sub parts per million levels are then given, and are compared with the non resonant detection technique to establish the sensitivity and suitability of RIMS in trace element detection. The author was largely responsible for the experimental results and solely responsible for the data analysis in this chapter.

The concluding chapter suggests improvements which could enhance the detection sensitivity, and describes future experiments on both spectrometers at Glasgow.

Research work relating to high energy physics is described in Appendix 1. The first section deals with the identification of two sources of background ionisation, phenol and toluene. Section 2 describes research carried out on a gas purification system for the ALEPH Time Projection Chamber at CERN, and establishes its effectiveness at removing oxygen and water contaminants from the counter gas. The author was responsible for the study of the gas purification system. Appendix 2 describes the second laser resonant ionisation mass spectrometer constructed at Glasgow for the main purpose of depth profiling in semiconductors.

CHAPTER 1 INTRODUCTION AND THEORY

1.1 INTRODUCTION

1.11 Resonance Ionisation Spectroscopy

The last decade has seen much development in research in the laser induced ionisation field, mainly due to the advent of high powered pulsed lasers. The main application of this research is the possible detection of very small numbers of atoms or molecules. This analytical technique, known as Resonance Ionisation Spectroscopy, was initially developed by G.S. Hurst and co-workers at Oak Ridge National Laboratory in the USA and also by a group headed by V.S. Letokhov in the USSR.

Figure 1.1 shows the basic idea behind resonance ionisation. Every element has an individual set of bound atomic energy levels and a continuum of unbound energy levels. If laser photons are wavelength tuned to precisely match the energy difference between the ground state and a higher bound energy state, an electronic transition may occur between the two levels. Further laser photons of the correct wavelength may then induce further transitions in the atom, which reach the continuum and result in ionisation. This stepwise process is known as resonant ionisation. A typical cross section for resonant excitation is around $10^{-11} - 10^{-12} \text{ cm}^2$, and the corresponding cross section for ionisation is approximately $10^{-17} - 10^{-18} \text{ cm}^2$. The total cross section is then given by $\sigma_E \sigma_I \tau = 10^{-36} - 10^{-38} \text{ cm}^4 \text{ sec}$, where τ is the lifetime of the intermediate state (10^{-8} sec).

Non resonant ionisation can occur when the energies of the incident photons do not correspond to particular transitions (Figure 1.2). The atom is then said to be

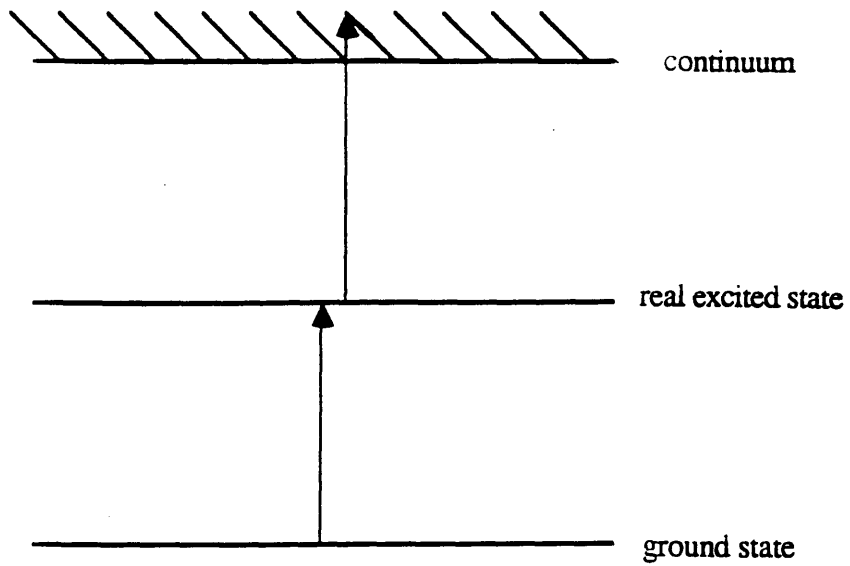


Figure 1.1 Two photon resonant ionisation via a real state ($\tau \sim 10^{-8}$ sec)

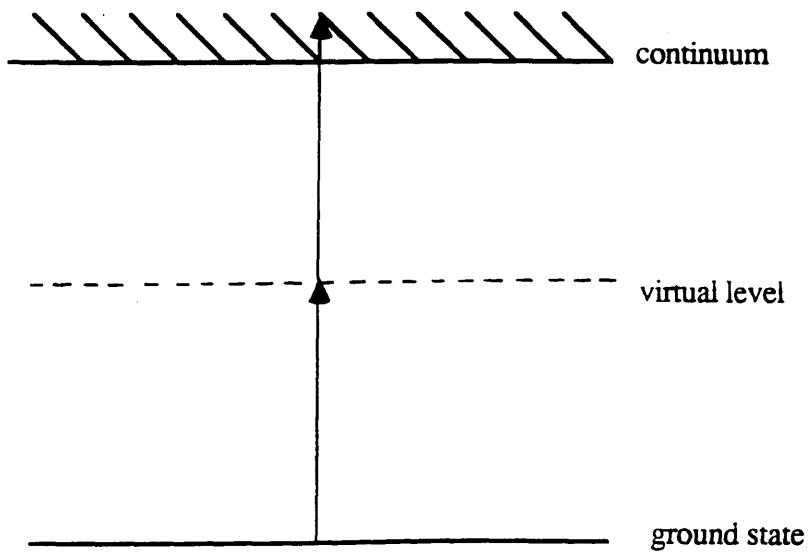


Figure 1.2 Two photon non resonant ionisation via a virtual state ($\tau \sim 10^{-15}$ sec)

ionised through virtual states. This non resonant process has a greatly reduced probability of resulting in ionisation. A typical cross section for a two photon non resonant process is $10^{-48} - 10^{-57} \text{ cm}^4\text{sec}$ (Chin and Lambropoulos 1984). Therefore, as each element has a unique set of energy levels, the photon energy required to resonantly ionise one type of atom will only succeed in non-resonantly ionising all other species. Thus high element selectivity is achieved through the large difference between resonant and non resonant probabilities.

A major advantage of the resonance ionisation process is its ability to be 100% efficient, i.e. every atom in the ground state can be resonantly ionised. Theoretical rate equations (see Section 1.22) show that a photon flux density of around $10^{23} \text{ photons/cm}^2\text{/sec}$ is required to saturate a typical two photon resonant ionisation process. This level of flux is impossible to achieve through conventional monochromatic light sources having flux densities of around $10^{16} \text{ photons/cm}^2\text{/sec}$. Pulsed dye lasers, however, can output flux densities of $10^{28} \text{ photons / cm}^2 / \text{sec}$ which would easily saturate a two photon process. As detectors which are 100% efficient are available, the highest analytical sensitivity and even single atom detection has been observed (Hurst et al 1979).

G. S. Hurst et al (1979) have developed five basic ionisation schemes which enable almost all elements to be ionised using only two lasers (see Figure 1.3). The only elements excluded are helium and neon, which have extremely high ionisation potentials, and are therefore very difficult to ionise.

Scheme 1, two photon resonant ionisation, is the simplest scheme requiring only one laser. The first photon from the laser beam excites an electron in the atom from the ground state to a real intermediate level lying more than halfway to the continuum. A

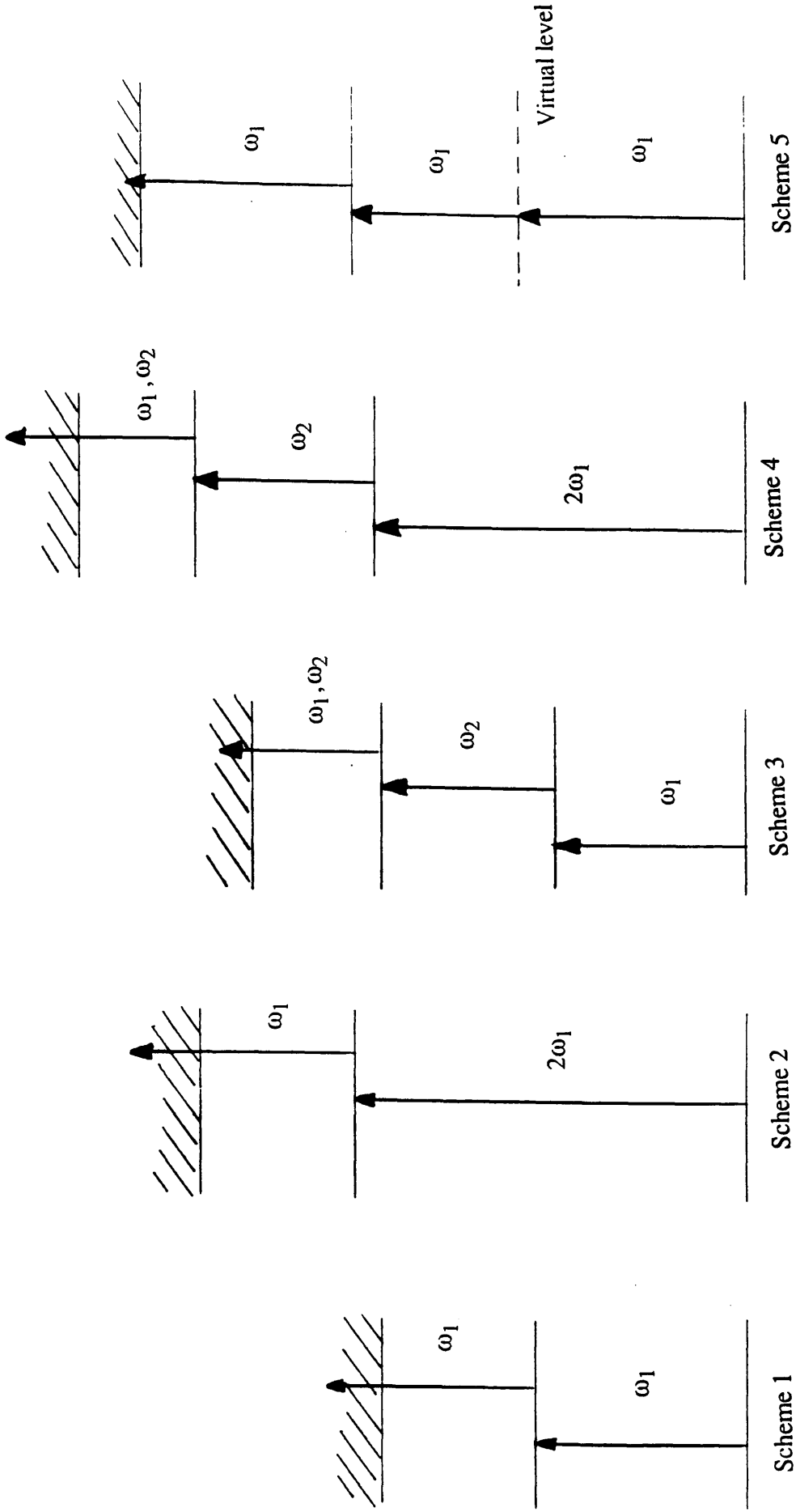


Figure 1.3 Resonant ionisation schemes (Hurst 1979)

second photon from the same laser pulse causes ionisation by promoting the excited electron to the continuum. This process is most suitable for atoms having ionisation potentials of less than about 8 eV, as the maximum energy of a photon from a commercially available dye laser is around 4 eV.

Scheme 2 utilises frequency doubling of the laser to reach the excitation stage. Ionisation is brought about by photons in the fundamental beam, ω_1 .

Two lasers are required for ionisation in Scheme 3. The first laser excites an electron to a real intermediate level from which it is raised to a higher lying real state by absorption of a second photon, ω_2 , from a laser of different wavelength. Ionisation can then result from absorption of a photon from either laser.

The first transition in Scheme 4 requires frequency doubling of the first laser output, ω_1 . The final ionisation step may be induced by a photon from either the second laser or the fundamental beam of the first. This scheme is more suited to atoms with high ionisation potentials.

It is also possible to ionise via virtual states, as in Scheme 5. The main disadvantage of this method is that saturation is more difficult to achieve due to the short lifetime of the virtual state, ($\tau \sim 10^{-15}$ sec compared to the lifetime of a real state $\sim 10^{-8}$ sec). It is useful, however, for reaching a real state which would normally be forbidden for one photon transitions.

Figure 1.4 shows the optimum ionisation schemes for almost all elements as proposed by Hurst. A question mark is used to denote possible schemes which have uncertainties in the positions of the atomic levels. A number of factors were taken into

account in arriving at the suggested schemes, e.g. the spacing of the energy level to the first excited state, the ionisation potential of the atom, the allowed or forbidden transitions and specifications of available pulsed lasers.

In any of the above schemes, alternative methods to photoionisation in the final step to the continuum may be used. This is often favourable as the bound - continuum transition requires a high level of laser flux for saturation, which would result in a substantial increase in the background signal, and would limit sensitivity. It would therefore be preferable to replace the laser in the ionisation step with a process which does not involve photons. Excitation of the atom could still be induced by laser, but the background signal would be minimised, as the saturation of a bound - bound transition can be achieved at much lower fluence.

The ionisation step can be brought about by a number of different processes, provided the excitation stages are sufficiently close to the continuum (usually within around 1/40 eV). Examples of these processes are ionisation by an electric field of magnitude 10 KV / cm or by different collisional processes such as associative or Penning ionisation. Table 1.1 compares the sensitivity of RIS with other existing analytical techniques, and shows RIS to be the most sensitive technique with lowest detection limits by up to three orders of magnitude, (Bekov and Letokhov 1983a).

1.12 Historical Background of RIS

Laser ionisation studies began around 1979 with the introduction of tunable dye lasers. Ambartsumyan et al (1971) were the first to report resonant ionisation of the $5s_{1/2} - 5p_{3/2}$ transition in rubidium.

TABLE 1.1

Comparison of Various Analytical Techniques (Bekov and Letokhov 1983)

Method	Detection Limit (Calibrated solutions- near ideal conditions)	Detection Limit (Real Solutions)	Selectivity for Elements
Atomic Absorption Spectroscopy	$10^{-4} - 10^{-9}$	$10^{-4} - 10^{-7}$	moderate
Neutron Activation Analysis	$10^{-5} - 10^{-9}$	$10^{-5} - 10^{-9}$	moderate
Spark Mass Spectrometry	$10^{-6} - 10^{-8}$	$10^{-5} - 10^{-7}$	high
Laser Fluorescence Spectrometry	$10^{-6} - 10^{-11}$	$10^{-5} - 10^{-8}$	high
Laser Resonant Ionisation Spectrometry (RIS)	$10^{-11} - 10^{-14}$	$10^{-8} - 10^{-11}$	ultrahigh

The process of resonance ionisation spectroscopy was first developed by G. S. Hurst in 1975 in an experiment in measuring the population of the He (2^1S) metastable state resulting from proton excitation. A two photon resonance ionisation scheme was used, and this experiment proved that the RIS technique could be used to convert quantum-selected excited states to ionisation with near unit efficiency.

In 1977, single atom detection of caesium was demonstrated by Hurst and co-workers at Oak Ridge, using a proportional counter for detection. In the next year, Bekov et al (1978) used photo - excitation combined with electric field ionisation for the detection of single atoms of ytterbium. Around the same time, the group at Oak Ridge demonstrated the saturated dissociation and detection of molecular CsI, thus proving the feasibility of detecting single molecules. Bekov et al (1978b) also demonstrated the single atom detection of sodium using electric field ionisation. Hurst (1979, 1988) and Letokhov (1987) have outlined the experimental techniques required in single atom detection and have reviewed the wide ranging applications of this high analytical sensitivity.

Bekov and Letokhov developed techniques to enable trace elements to be detected in natural substances, for example the aluminium content of river and seawater was determined at parts per billion level (Bekov et al 1983), aluminium in human blood (Bekov and Letokhov 1983), and amounts of ruthenium in salt water and fish bones was measured (Bekov et al 1985).

Following initial caesium experiments, other alkali metals such as rubidium have been studied (Bushaw and Whitaker 1981) for the purpose of more detailed study of Rydberg levels and collisional processes.

The process of resonance ionisation spectroscopy is not restricted to atomic species. Brophy and Rettner (1979) monitored atmospheric pollutants such as aniline by laser two photon ionisation spectroscopy. Siomos et al (1981) recorded two photon ionisation spectra of organic solutes, showing that the RIS process is not restricted to solids or gases. Further work on liquids was carried out by Yamada et al (1983) who studied aromatic molecules in solution using non-resonant laser two photon ionisation.

1.13 Historical Background of RIMS

The advantages of combining the selectivity of resonance ionisation with a mass spectrometer became apparent as early as 1978. Initial work involved molecules (Antonov et al 1978, Boesl et al 1980).

The RIMS acronym was first applied by a number of research groups who combined resonant ionisation with modified thermal ionisation mass spectrometry. This usage has been expanded to include any instrument which combines resonant ionisation with mass spectrometry for analytical purposes. RIMS was first demonstrated with isotopic separation of potassium by Beekman et al (1980) using a quadrupole mass spectrometer. Young and Donahue (1983) recorded separate ionisation spectra of neodymium and samarium from a mixture of the two using a magnetic sector mass spectrometer. The analytical application and demonstration of RIMS followed (Donahue et al 1982, Miller et al 1982, Fassett et al 1983). The development of RIMS has proceeded in several different directions, using CW or pulsed laser, different types of sample generation, and different methods of mass separation.

Although quadrupole mass spectrometers have been used successfully, for example in the detection of noble gas atoms (Chen et al 1983), Time of Flight mass

spectrometers have become popular due to their ability to display complete mass spectra for each laser pulse, thus avoiding measurement problems due to laser power variations.

Boesl et al (1980) used Time of Flight techniques in the ionisation of polyatomic molecules which were improved in 1982 by the inclusion of an electrostatic ion mirror. Donahue et al (1984, 1985) have conducted a series of experiments using a magnetic sector spectrometer to detect various nuclides, for example plutonium and uranium.

Studies of molecules by RIMS has also gained momentum in recent years. Lubman et al (1980) have studied multiphoton ionisation in naphthalene and azulene and in substituted aromatic molecules (1985), and supersonic cooling has been used in the discrimination of Cresol isomers (Tembruell and Lubman 1984) and substituted benzenes (Sin et al 1984).

There has been a considerable amount of research conducted on trace element analysis using RIMS. A detailed review on analytical applications of RIMS has recently been published (Fassett and Travis 1988). In trace analysis, a mass spectrometer with a high transmission efficiency is desirable. The first stage of trace analysis is the vaporisation of the sample into neutral atoms. This has been achieved by a number of methods. The use of a high energy argon ion beam has been demonstrated (Winograd et al 1982, Kimock et al 1983, Parks et al 1983). The technique of SIRIS (Sputter Initiated RIS) was developed by Parks et al (1984) for commercial analysis by Atom Sciences, Inc. and was shown to have a sensitivity limit of two parts per billion. The development of surface analysis by resonant ionisation of sputtered atoms (SARISA) at Argonne National Laboratory combines time of flight mass filtering with a background suppressing velocity analyser (Young et al 1987).

Thermal atomisation from a high temperature filament has also been incorporated into the RIMS technique (Donohue et al 1982, Moore et al 1984,1985, Fassett et al 1983). It was found that pulsing of the thermal source resulted in an improvement in the temporal efficiency by an order of magnitude (Donohue et al 1984, Fassett et al 1984a). A glow discharge method was adopted by Harrison et al (1984), whilst Bekov and Letokhov (1983) utilised an atomic oven with a time of flight mass spectrometer for trace analysis.

RIMS techniques have involved the use of both pulsed lasers (Donohue et al 1982, Miller et al 1982, Fassett et al 1983) and CW lasers (Miller and Nogar 1983). To date, there have been insufficient individual element comparisons to reach definite conclusions about the preferred laser mode. Young et al (1984) suggest that the most sensitive RIMS analysis may involve a pulsed laser system coupled with a pulsed sample system. An alternative CW laser system, however, particularly with narrow band lasing, offers a different approach to isotopic analysis which will also eliminate isobaric interference, but which may require a relatively large sample. This would be especially useful in determination of abundance sensitivity, ie. separation of isotopes. It is also possible to use high repetition copper vapour lasers (Kronert et al 1985, Bekov et al 1986) to increase the temporal efficiency.

Work has also been carried out on the use of laser ablation as an evaporation technique. LARIS (laser ablation resonance ionisation spectroscopy) has been used by Mayo et al (1982) for the detection of sodium impurities in silicon at one part in 10^{11} level using a proportional counter. Laser ablation has also been used in combination with TOF mass spectrometry for the detection of chromium in stainless steel (Williams et al 1984).

A method developed at SRI, California by Becker and Gillen (1984) called SALI (surface analysis by laser ionisation) uses non-resonant ionisation of neutral atoms and molecules using a focussed UV laser beam, followed by reflecting TOF mass spectrometry. In this arrangement, it is the mass spectrometer, rather than the laser, which discriminates against background and provides element analysis. This process is particularly useful where many species need to be investigated simultaneously, where the types of species are unknown or where molecules being studied have a complex or unknown spectroscopy. A comparison of resonant and non-resonant ionisation of ion sputtered neutrals has been made by Young et al (1987).

1.14 Laser Ionisation Studies at Glasgow University

In experimental high energy physics, the use of pulsed lasers to simulate particle tracks for the calibration of large, multiwire chambers has been under investigation. Initial research at Glasgow centred around the determination of suitable seeding agents for laser calibration of multiwire chambers at CERN, and on the identification of impurities responsible for the laser induced ionisation using proportional counters (Towrie 1987, Drysdale et al 1986). After completion of this research, work began on the construction and testing of a laser ionisation mass spectrometer designed primarily for ultra-trace analysis.

Before trace analysis could be carried out, it was necessary to study the basic spectroscopy involved, in order to determine the optimum resonant transitions, laser power levels and linewidths, and to investigate the use of Rydberg levels, autoionisation states and electric field ionisation. These techniques are inherent in the sensitivity of trace analysis.

Laser ionisation spectroscopy of caesium was carried out initially using a proportional counter. Work consequently progressed to the study of rubidium metal. Rubidium has two naturally occurring isotopes, and hence detection by mass spectrometer is desirable. A quadrupole mass spectrometer was employed, and could be used as an alternative to the proportional counter. After spectroscopy work was completed, the resonance ionisation of rubidium was investigated in a TOF mass spectrometer designed at Glasgow. The RIMS instrument at Glasgow has facilities for sample evaporation by either laser desorption or ion beam sputtering, two pulsed dye laser systems for resonance ionisation, and analysis by TOF mass spectrometer (Towrie 1988). Results obtained using this instrument are documented in Chapter 6.

1.2 THEORY

1.21 Two Photon Ionisation

Two photon ionisation is the simplest form of multiphoton ionisation and involves only one intermediate state between the ground state and the continuum (see Figure 1.1). In general, the cross section for excitation to the intermediate state is a few orders of magnitude larger than the ionisation cross section, ie. $\sigma_{\text{excitation}} = 10^{-11} - 10^{-12} \text{ cm}^2$ whereas $\sigma_{\text{ionisation}} = 10^{-17} - 10^{-18} \text{ cm}^2$ (Bekov and Letokhov 1983). If during the laser pulse, all atoms initially in the ground state become converted to ion pairs, the transition has been saturated. The larger cross section for excitation allows the excitation stage to become saturated at much lower power levels than the ionisation stage. Commercially available pulsed lasers, however, are capable of producing sufficient power to allow saturation of both stages. The following theory establishes the two main conditions necessary to achieve complete saturation of this ionisation.

The fluence condition must be satisfied

$$\phi \sigma_{\text{ionisation}} \gg 1 \quad (1)$$

where ϕ is the laser fluence, ie. the number of photons per unit area of beam. The fluence can be expressed in terms of the flux, Φ , the number of photons per unit area per unit time, ie. $\phi = \Phi T$.

In addition, the flux condition

$$\sigma_{\text{excitation}} \Phi \gg 1/\tau \quad (2)$$

must also be satisfied, where Φ is the laser flux and τ is the lifetime of the intermediate state. Clearly, the lifetime of the intermediate state determines the required flux. As a

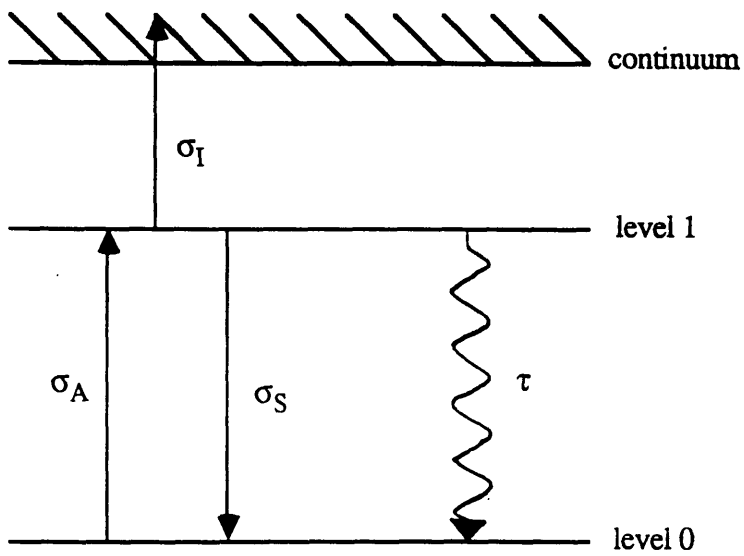


Figure 1.21 Two photon resonance ionisation

result, ionisation via a real intermediate state with lifetime of around 10^{-8} seconds will require a much lower flux for saturation than through a virtual state of lifetime 10^{-15} seconds approximately (see Figure 1.2).

From Figure 1.21, the rate of change of population of the ground, intermediate and continuum levels are, respectively :-

$$\frac{dN_0}{dt} = -N_0\sigma_A\Phi + \frac{N_1}{\tau} + N_1\sigma_S\Phi \quad (3)$$

$$\frac{dN_1}{dt} = N_0\sigma_A\Phi - \frac{N_1}{\tau} - N_1\sigma_S\Phi - N_1\sigma_I\Phi \quad (4)$$

$$\frac{dN_I}{dt} = N_1\sigma_I\Phi \quad (5)$$

where N_0 , N_1 and N_I are the populations of atoms in states 0, 1 and the continuum respectively,

Φ is the laser flux,

τ is the mean lifetime for spontaneous emission from state 1,

σ_A is the cross section for stimulated absorption from states 0 \rightarrow 1

σ_I is the cross section for ionisation from state 1 \rightarrow continuum

σ_S is the cross section for stimulated emission

In equilibrium, the stimulated emission cross section σ_S is equal to the stimulated absorption cross section σ_A .

Now adding equations 3 and 4 gives,

$$\frac{dN_0}{dt} = -\frac{dN_1}{dt} - N_1\sigma_I\Phi \quad (6)$$

Differentiating equation 4 with respect to time, and using equation 6, gives

$$\frac{d^2 N_1}{dt^2} = \sigma_A \Phi \frac{dN_0}{dt} - \frac{1}{\tau} \frac{dN_1}{dt} - \sigma_A \Phi \frac{dN_1}{dt} - \sigma_I \Phi \frac{dN_1}{dt}$$

Rearranging gives

$$\begin{aligned} \frac{d^2 N_1}{dt^2} &= -\sigma_A \Phi \frac{dN_1}{dt} - \sigma_A \sigma_I \Phi^2 N_1 - \frac{1}{\tau} \frac{dN_1}{dt} - \sigma_A \Phi \frac{dN_1}{dt} - \sigma_I \Phi \frac{dN_1}{dt} \\ &= \frac{dN_1}{dt} \left[-\sigma_A \Phi - \frac{1}{\tau} - \sigma_A \Phi - \sigma_I \Phi \right] - \sigma_A \sigma_I \Phi^2 N_1 \end{aligned}$$

Therefore

$$\frac{d^2 N_1}{dt^2} + \left[(2\sigma_A + \sigma_I) \Phi + \frac{1}{\tau} \right] \frac{dN_1}{dt} + \sigma_A \sigma_I \Phi^2 N_1 = 0 \quad (7)$$

Let

$$(2\sigma_A + \sigma_I) \Phi + \frac{1}{\tau} = 2b \quad (8)$$

and also

$$\sigma_A \sigma_I \Phi^2 = w^2 \quad (9)$$

Then

$$\frac{d^2 N_1}{dt^2} + 2b \frac{dN_1}{dt} + w^2 N_1 = 0 \quad (10)$$

If N_1 is of the form $e^{-\lambda t}$ then

$$\frac{dN_1}{dt} = -\lambda e^{-\lambda t} \quad \text{and} \quad \frac{d^2 N_1}{dt^2} = \lambda^2 e^{-\lambda t}$$

and equation 10 becomes

$$\lambda^2 - 2b\lambda + w^2 = 0 \quad (11)$$

This equation is quadratic in λ . Its roots are given by

$$\lambda = \frac{2b \pm \sqrt{(4b^2 - 4w^2)}}{2} \quad (12)$$

Therefore the two roots are

$$\lambda_1 = b - \sqrt{b^2 - w^2} \quad \text{and} \quad \lambda_2 = b + \sqrt{b^2 - w^2} \quad (13)$$

Thus a solution is

$$N_1 = Ae^{-(b+\sqrt{b^2-w^2})t} + Be^{-(b-\sqrt{b^2-w^2})t}$$

where A and B are constants. By using the condition that $A = -B$ since $N_1 = 0$ at $t = 0$,

$$N_1 = A[e^{-\lambda_1 t} - e^{-\lambda_2 t}] \quad (14)$$

In order to evaluate A, equation 14 is substituted into equation 4 to give

$$A[-\lambda_1 e^{-\lambda_1 t} + \lambda_2 e^{-\lambda_2 t}] = N_0 \sigma_A \Phi + N_1 \left[-\frac{1}{\tau} - \sigma_A \Phi - \sigma_I \Phi \right] \quad (15)$$

If $N_0(0)$ is the population of state 0 at time $t = 0$ then

$$N_0(0) = \frac{A[\lambda_2 - \lambda_1]}{\sigma_A \Phi}$$

Rearranging gives

$$A = \frac{N_0(0)\sigma_A\Phi}{[\lambda_2 - \lambda_1]}$$

and equation 14 becomes

$$N_1 = \frac{N_0(0)\sigma_A\Phi}{[\lambda_2 - \lambda_1]} [e^{-\lambda_1 t} - e^{-\lambda_2 t}] \quad (16)$$

Now, if the intermediate state is real and if the laser is tuned to near the line centre, it can be assumed that

$$\sigma_A = \sigma_S \gg \sigma_I$$

Equation 8 therefore can be simplified to

$$2b = 2\sigma_A\Phi + \frac{1}{\tau}$$

which implies $b^2 \gg w^2$ and $\lambda_2 \gg \lambda_1$

Thus equation 16 simplifies to

$$N_1 = \frac{N_0(0)\sigma_A\Phi}{\lambda_2} [e^{-\lambda_1 t}] \quad (17)$$

$$\text{Also, as } \lambda_2 \approx 2b \approx 2\sigma_A\Phi + \frac{1}{\tau}$$

$$N_1 = \frac{N_0(0)\sigma_A\Phi}{2\sigma_A\Phi + \frac{1}{\tau}} [e^{-\lambda_1 t}] \quad (18)$$

In order to test the validity of the flux and fluence conditions for saturation, they will be used to calculate $N_I(T)$, the number of atoms ionised during the laser pulse length, T.

Assuming the flux condition, equation 18 becomes

$$N_1 = \frac{N_0(0)}{2} [e^{-\lambda_1 t}] \quad (19)$$

In order to evaluate N_1 , a value for λ_1 must be calculated.

$$\begin{aligned} \lambda_1 &= b - b \left[1 - \frac{w^2}{b^2} \right]^{1/2} \\ &= b - b \left[1 - \frac{1}{2} \frac{w^2}{b^2} \right] = \frac{1}{2} \frac{w^2}{b} \end{aligned}$$

using a first order binomial approximation, and assuming $b^2 \gg w^2$. Therefore

$$\lambda_1 = \frac{\sigma_A \sigma_I \Phi^2}{2\sigma_A \Phi + \frac{1}{\tau}} = \frac{\sigma_I \Phi}{2}$$

Now from equation 5,

$$\begin{aligned} N_I &= \sigma_I \Phi \int_0^T N_1 \\ &= \sigma_I \Phi \int_0^T \frac{N_0(0)}{2} [e^{-\lambda_1 t}] \\ &= \sigma_I \Phi \frac{N_0(0)}{2} \left[-\frac{1}{\lambda_1} e^{-\lambda_1 t} \right]_0^T \\ &= \sigma_I \Phi \frac{N_0(0)}{2} \left[-\frac{1}{\lambda_1} e^{-\lambda_1 T} + \frac{1}{\lambda_1} \right] \end{aligned}$$

Assuming the fluence condition, this becomes

$$N_I = \frac{\sigma_I \Phi N_0(0)}{2\lambda_1}$$

$$= \frac{2\sigma_I \Phi N_0(0)}{2\sigma_I \Phi}$$

$$= N_0(0)$$

Therefore, if the flux and fluence conditions hold, all the atoms initially in the ground state will become ionised during the laser pulse. This is the definition of saturation.

Typical values for the terms are :- $T = 10^{-8}$ sec, $\tau = 10^{-8}$ sec, $\sigma_I = 10^{-18}$ cm², and $\sigma_A = 10^{-11} - 10^{-12}$ cm². Therefore, in order to satisfy the flux condition for saturation,

$$\phi \gg 10^{11} - 10^{12} \text{ photons / cm}^2.$$

Since the number of photons in $1J = 5 \times 10^{15} \times \lambda$ (nm), saturation occurs when

$$\phi \gg 4.4 - 0.44 \text{ nJ / mm}^2.$$

The fluence condition,

$$\phi \sigma_I \gg 1$$

requires that the fluence for saturation is

$$\phi \gg 10^{17} - 10^{18} \text{ photons / cm}^2$$

$$\text{ie. when } \phi \gg 4.4 - 0.44 \text{ mJ / mm}^2.$$

1.22 Population Rate Equation Model

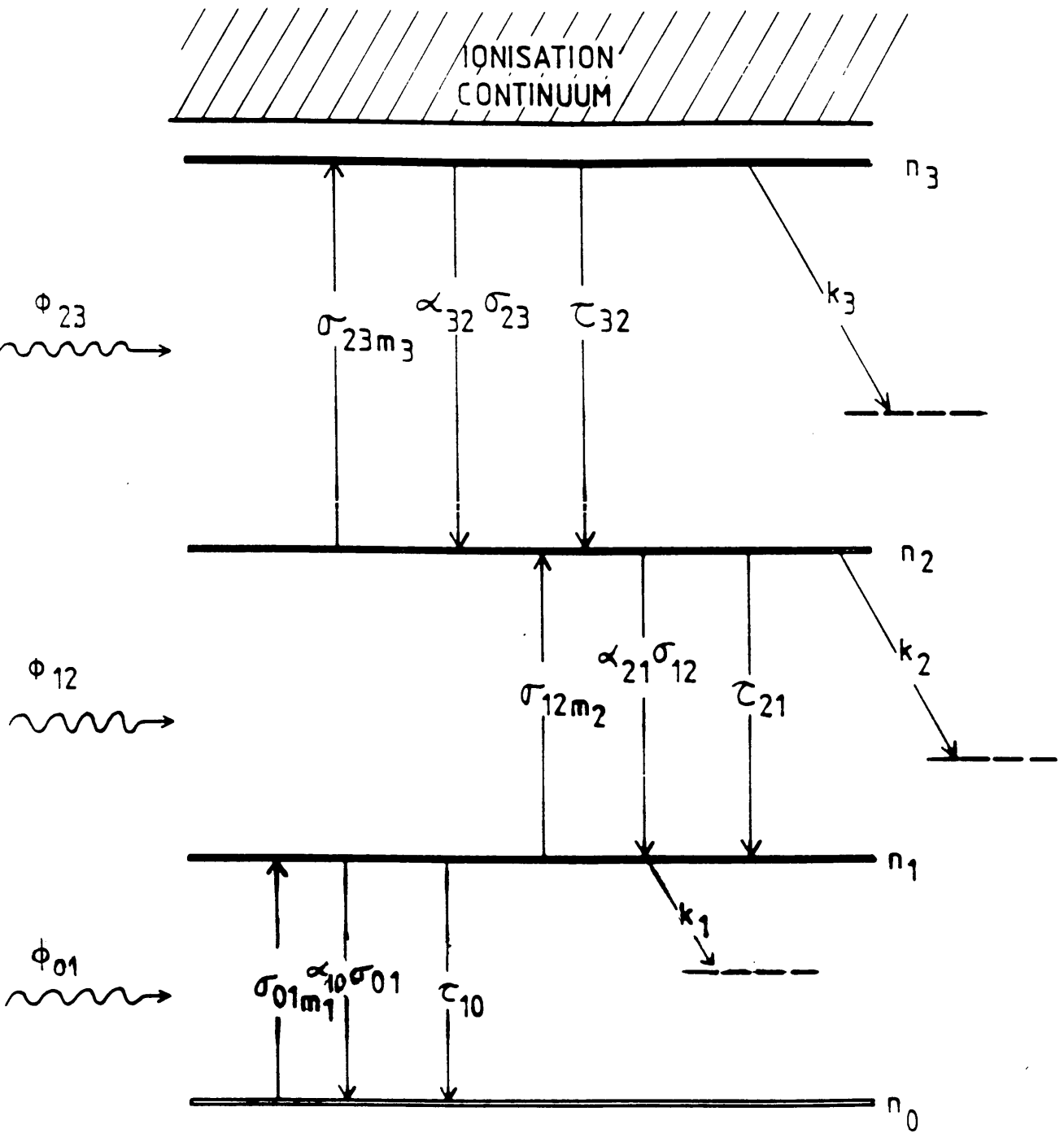
The theoretical explanation of the Resonance Ionisation Spectroscopy technique requires a general comprehensive model which can be applied to a variety of situations. A quantum mechanical approach starting with Schrodinger's time dependent equation,

$$h \frac{d}{dt} | \Psi(t) \rangle = H | \Psi(t) \rangle \quad (20)$$

where H , the Hamiltonian, is an operator defining the energy of the particle, can be used to derive transition rates via perturbation theory. This is the only existing fully valid theory describing the action of electromagnetic radiation with atoms (see Dermtroder 1982 for full derivation). This approach, while useful for simple systems containing two or three atomic levels, becomes too mathematically complex for systems with four or more levels. The rate equation model explained below, however, uses atomic cross sections and lifetimes of states in a non quantum mechanical method to derive transition rates, and can be applied to more complicated systems involving extra excited states or irreversible decay modes. In certain circumstances, in particular if the coherence length of the laser is short, both quantum mechanics and rate equations yield identical solutions. In addition, rate equations can be used to study effects such as the influence of laser temporal and spatial profiles, and spectral features of the lasers used. The validity of this model has been studied by Ackerhalt and Shore (1977) and is, in general, applicable to RIS if the coherence properties of the laser play an insignificant role in the dynamics. For moderate laser powers of less than a few mJ/cm^2 with a pulse duration of 10 nanoseconds and a bandwidth of 0.05nm, coherence effects are expected to be negligible (Ackerhalt and Shore 1977).

The following rate equation model is based on a four level system where the ground state and three other excited states participate in the process of stepwise resonant excitation of the atom (see Figure 1.22). The excited states decay by spontaneous or stimulated emission of photons or can undergo collisions with gas phase atoms, thereby changing the relative populations of the states. Simpler RIS schemes can be obtained from this general scheme of Figure 1.22 by setting the appropriate cross sections to zero. Multiphoton processes involving more than two photons can be incorporated into any step by choosing the appropriate value for the exponent of the corresponding laser flux. The cross section would then have the units $\text{cm}^{2m}\text{sec}^{m-1}$, where m is the number

Figure 1.22 Population rate equation model for a four level system



of photons absorbed.

From Figure 1.22, the rate equations for the scheme may be written

$$n_0 = -An_0 + Bn_1$$

$$n_1 = An_0 - (B + C + CP)n_1 + Dn_2$$

$$n_2 = Cn_1 - (D + E + EP)n_2 + Fn_3$$

$$n_3 = En_2 - (F + G)n_3$$

where

$$A = \sigma_{01m_1} \phi_{01}^{m_1}$$

$$C = \sigma_{12m_2} \phi_{12}^{m_2}$$

$$D = \alpha_{21} C + \tau_{21}^{-1}$$

$$EP = k_2$$

$$G = k_3$$

$$B = \alpha_{10} A + \tau_{10}^{-1}$$

$$CP = k_1$$

$$E = \sigma_{23m_3} \phi_{23}^{m_3}$$

$$F = \alpha_{32} E + \tau_{32}^{-1}$$

In the above notation, σ_{ijm} refers to the cross section for an m -photon process for the excitation state j from state i , α_{ji} is the ratio of statistical weights g_j and g_i of the two states and τ_{ji} is the mean lifetime for spontaneous decay from level j to level i .

The equations simplify to give a fourth order differential equation in n_3 ,

$$\begin{aligned} n_3'''' + (A + B + C + CP + D + E + EP + F + G) n_3''' \\ + [(A + B + C + CP + D + E + EP)(F + G) + (A + B + C + CP)(D + E + EP) \\ + A(C + CP) - EF - CD] n_3'' \\ + \{[(A + B + C + CP)(D + E + EP) + A(C + CP) - CD](F + G) \\ + A(C + CP)(D + E + EP) - ACD - (A + B + C + CP)EF\} n_3' \\ + \{[A(C + CP)(D + E + EP) - ACD](F + G) - (C + CP)AEF\} n_3 = 0 \end{aligned}$$

This equation has four real positive roots p_i leading to a general solution $n_3(t)$ of the form,

$$n_3(t) = \sum \beta_i \exp(-p_i t)$$

Putting in the initial condition that at time $t = 0$, the number of ground state atoms is N_0 and the other states are unpopulated, leads to the equations,

$$n_2(t) = \frac{1}{E} \sum_i \beta_i (-p_i + F + G) \exp(-p_i t)$$

$$n_1(t) = \frac{1}{CE} \sum_i \beta_i [-EF + (-p_i + F + G)(-p_i + D + E + EP)] \exp(-p_i t)$$

$$n_0(t) = \frac{1}{ACE} \sum_i \beta_i \{ -EF + (-p_i + F + G)(-p_i + D + E + EP) \} \\ (-p_i + B + C + CP) - DC(p_i + F + G) \} \exp(-p_i t)$$

These equations then provide a complete solution to the dynamics of the RIS process, and the population yield of any state can be calculated as a function of any combination of the variable parameters.

In a recent paper by Singhal et al (1988), this rate equation model was used to interpret resonance ionisation data acquired by Bekov et al (1978) for the ytterbium atom. Calculated ion yield curves were compared with the experimental data, and values for the absorption cross section for the third excitation stage to Rydberg levels was calculated, assuming a flat top temporal profile. Further analysis into the effect of a Gaussian or spiked laser profile showed that the ion yield curves produced for these laser temporal profiles were indistinguishable from those for a flat top pulse profile, the maximum difference being 0.5%. The ion yield was also shown to be insensitive to differences in pulse length between 2 and 15 nanoseconds. It can therefore be deduced that for the RIS technique, the details of the laser time profile are not significant, and the

ion yield depends mainly on laser fluence. The temporal profile was important, however, for multiphoton transitions, and in particular when the laser flux was much smaller than the level required for saturation. It was also found that the lifetime of the intermediate state affected the ion yield only when its value was considerably smaller than the laser pulse length.

1.23 Effect of Linewidth on the Reaction Rate

The Einstein coefficients for spontaneous and stimulated emission are related to each other according to

$$B_{ab} = \frac{g_b}{g_a} B_{ba} \quad \text{and} \quad B_{ba} = \frac{c^3}{8\pi\nu^3 h} A_{ba}$$

for a transition from level a to level b with central frequency ν_0 , where g_a and g_b are the statistical weights of levels a and b (Eastham 1986). The atomic transition line and the laser radiation at frequency ν_0 have spectral distributions $f(\nu)$ and $g(\nu)$ which can be normalised as follows,

$$\int f(\nu) d\nu = 1 \quad \text{and} \quad \int g(\nu) d\nu = 1$$

The interaction rate $R(\nu)d\nu$ for the transition from state a to state b is

$$R(\nu)d\nu = \frac{n_a g_b}{g_a} B_{ba} f(\nu) W(\nu) d\nu$$

where n_a is the density of atoms per unit volume in state a, and $W(\nu)d\nu$ is the laser energy density in the frequency interval from ν to $\nu+d\nu$. The spectral function of the laser $g(\nu)$ is related to the laser energy per unit volume $W(\nu)$ by

$$W(\nu)d\nu = \phi \frac{h\nu}{c} g(\nu)d\nu$$

where ϕ is the laser flux. Therefore, the interaction rate can be written

$$R(\nu)d\nu = n_a \frac{g_b}{g_a} \frac{c^3}{8\pi\nu^3 h} A_{ba} f(\nu) \phi \frac{h\nu}{c} g(\nu) d\nu \quad (21)$$

or more simply,

$$R(\nu)d\nu = n_a \phi g(\nu) \sigma(\nu) d\nu$$

where

$$\sigma(\nu) = \frac{g_b}{g_a} \frac{\lambda^2 A_{ba}}{8\pi} f(\nu)$$

The reaction rate for the full frequency range is therefore,

$$R = \int R(\nu)d\nu = n_a \phi \int g(\nu) \sigma(\nu) d\nu \quad (22)$$

This reaction rate is dependent on the spectral profiles of the transition line $f(\nu)$ and on the laser profile $g(\nu)$. A Lorentzian profile is a good approximation to an atomic lineshape, although a Doppler broadened lineshape can be more accurately described by a Voigt profile, which is a convolution of the Gaussian and Lorentzian forms. The spectral profile of the laser is dependent on the particular broadening mechanisms within the laser. A homogeneously broadened laser has a Lorentzian lineshape whereas an inhomogeneously broadened laser line has a Gaussian shape. The lineshapes can be expressed as follows,

$$\text{Lorentzian} : \quad y(\nu) = \frac{\Delta\nu_H}{\pi} \left[(\nu - \nu_0)^2 + \Delta\nu_H^2 \right]^{-1}$$

Gaussian :
$$y(\nu) = \frac{1}{\Delta\nu_H} \left(\frac{\ln 2}{\pi} \right)^{\frac{1}{2}} \exp \left[- \ln 2 \left(\frac{\nu - \nu_0}{\Delta\nu_H} \right)^2 \right]$$

where $\Delta\nu_H$ is the half width at half maximum (HWHM). The pulsed lasers used in RIMS experiments generally have a linewidth which is very much larger than the atomic linewidth, ie. $\Delta\nu_{(\text{laser})} \gg \Delta\nu_{(\text{transition})}$. As a result, the variation of the laser flux about ν_0 can be neglected as the integrand in equation 22 obtains contributions from only those frequencies where the atomic profile is significant. The reaction rate can therefore be written,

$$R = n_a \phi \frac{1}{\Delta\nu_{HL}} \left(\frac{\ln 2}{\pi} \right)^{\frac{1}{2}} \frac{g_b}{g_a} \frac{\lambda^2 A_{ba}}{8\pi} \int f(\nu) d\nu \quad (23)$$

Here we have assumed a Gaussian laser profile of half width $\Delta\nu_{HL}$ to be very much greater than the atomic linewidth $\Delta\nu_{HA}$. The variation of λ^2 over the atomic line profile is negligible. From the normalisation of $f(\nu)$,

$$R = n_a \phi \frac{\Delta\nu_{HA}}{\Delta\nu_{HL}} \left(\frac{\ln 2}{\pi} \right)^{\frac{1}{2}} \frac{g_b}{g_a} \frac{\lambda^2 A_{ba}}{8\pi \Delta\nu_{HA}} \quad (24)$$

If the full widths are written as $\Delta\nu$, then it follows that

$$R = n_a \phi \frac{\Delta\nu_A}{\Delta\nu_L} 2 \left(\frac{\ln 2}{\pi} \right)^{\frac{1}{2}} \frac{g_b}{g_a} \frac{\lambda^2}{8\pi} \frac{A_{ba}}{\Delta\nu_A} \quad (25)$$

Evaluating the numerical parts gives

$$R \cong n_a \sigma_{ab} \frac{\Delta\nu_A}{\Delta\nu_L} \phi \quad (26)$$

where

$$\sigma_{ab} = \frac{g_b}{g_a} \frac{\lambda^2 A_{ba}}{8\pi\Delta\nu_A}$$

The factor $\Delta\nu_A / \Delta\nu_L$ accounts for the unused photons in the laser beam.

1.24 Selection Rules

A transition rate is the probability per second that an atom in a certain energy level will make a transition to another energy level. Selection rules specify which transitions have rates so small that they are not normally observed. All selection rules can be obtained from transition rate calculations (Eisberg and Resnick 1974). When a photon interacts with an electron, the energy of the electron will change and its orbital angular momentum, L or its spin, S will also change. A photon of light has intrinsic angular momentum (spin) of 1. According to the laws of momentum conservation, the angular momentum of the electron must change by 1 with each successively absorbed photon. The selection rules for single photon electric dipole transitions are given below (Eastham 1986), and are valid if the spin orbit interaction is small.

$$\Delta L = +/- 1$$

$$\Delta S = 0$$

$$\Delta J = 0, +/- 1$$

where J is the total angular momentum for the system ($\underline{J} = \underline{L} + \underline{S}$). The parity, determined by $(-1)^l$, must therefore change in an electric dipole transition. The polarisation of the laser light results in the further rules (Sobelman 1979) :-

For linearly polarised light , $\Delta m_j = 0$

For circularly polarised light , $\Delta m_j = \pm 1$

where m_j is the z component of the total angular momentum and is equal to the sum of the z components of the orbital angular momentum m_l and the spin m_s .

The use of multiphoton transitions, however, has the advantage of reaching excited atomic states which are normally forbidden by electric dipole selection rules, eg. a normally forbidden transition between an s and a d state can proceed via a virtual state by using two photon excitation. The selection rules for two photon transitions are given:-

$$\Delta L = 0, \pm 2$$

$$\Delta J = 0, \pm 1, \pm 2$$

For linearly polarised light $\Delta m_j = 0$

For circularly polarised light $\Delta m_j = \pm 2$

The parity, $(-1)^l$, will therefore not change during a two photon transition. In general, the selection rules for an n photon transition are derived by applying the single photon rules n times (Letokhov and Chebotayev 1977).

1.25 Rydberg States

An effective method of resonant ionisation is the multistep photoionisation to high lying states still below the ionisation limit followed by ionisation by electric field, IR radiation or collisional effects. These Rydberg states are highly excited states of atoms near the ionisation limit (generally within 1/40 th of an electron volt of the continuum). For atoms with one optically active electron, the position of the energy levels in the vicinity of the ionisation limit E_i is given by

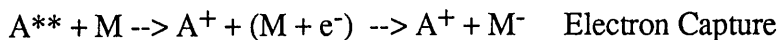
$$E_n = E_i - \frac{R_y}{(n^*)^2}$$

where $R_y = 13.6\text{eV}$ is the Rydberg constant and n^* is the effective principal quantum number, ie.

$$n^* = n - \Delta$$

where Δ is the quantum defect.

The cross section for photoionisation of Rydberg atoms is very small, and decreases as n^{*5} (Sobelman 1979). Rydberg atoms will, however, be highly susceptible to collisional effects because of their large geometric size, large polarisability, small binding energy and long lifetimes. With increasing n^* , the atomic collisional cross section is increased, since the atomic radius increases with n^{*2} . Taking into account the weak bonding of an excited electron, large values for the collisional ionisation of Rydberg atoms can be expected (Letokhov 1987). This method has been successfully applied by Niemax (1983), to efficiently ionise highly excited Rydberg atoms of rubidium, with the collisional ionisation probability being close to unity for $n > 25$. Collisional ionisation may occur through any of the following mechanisms,



where A^{**} is used to denote a highly excited state of atom A, and M is the buffer gas atom or molecule.

1.26 Theory of Molecular Dimers

As two atoms approach each other, the valence electrons on each begin to experience the attractive potential of the other nucleus, and a rearrangement of the electron distribution takes place so as to minimise the total energy of the system. The effect is that of an attractive force between the two atoms, increasing as the separation distance is decreased until ultimately repulsive forces between the nuclei become important. Eventually, an equilibrium position is reached, where R_0 is the equilibrium separation of the nuclei and D is the molecule's dissociation energy. This electronic energy curve is the potential curve governing the nuclear motion.

A molecule composed of two ground state atoms will give rise to a ground state potential curve. If one atom is in an excited state, this gives rise to another electronic potential curve differing from the ground state curve. Molecules in general exhibit a number of different electronic states, in analogy with atomic electronic structures. When a molecule experiences an electronic transition, jumping from one electronic configuration to another, the radiation involved falls in the visible or the ultraviolet regions of the spectrum.

In general, each electronic state has an individual set of vibrational energy levels, each of which has associated with it a set of rotational states, as shown in Figure 1.23. Both the vibrational and rotational energies are quantised, and the wavefunctions describing the system are functions of the vibrational and rotational as well as electronic quantum numbers.

Schrodinger's equation for a molecule involves functions of the nuclear co-ordinates as well as the electronic, and the wavefunction can be separated into the nuclear and electronic parts, ie.

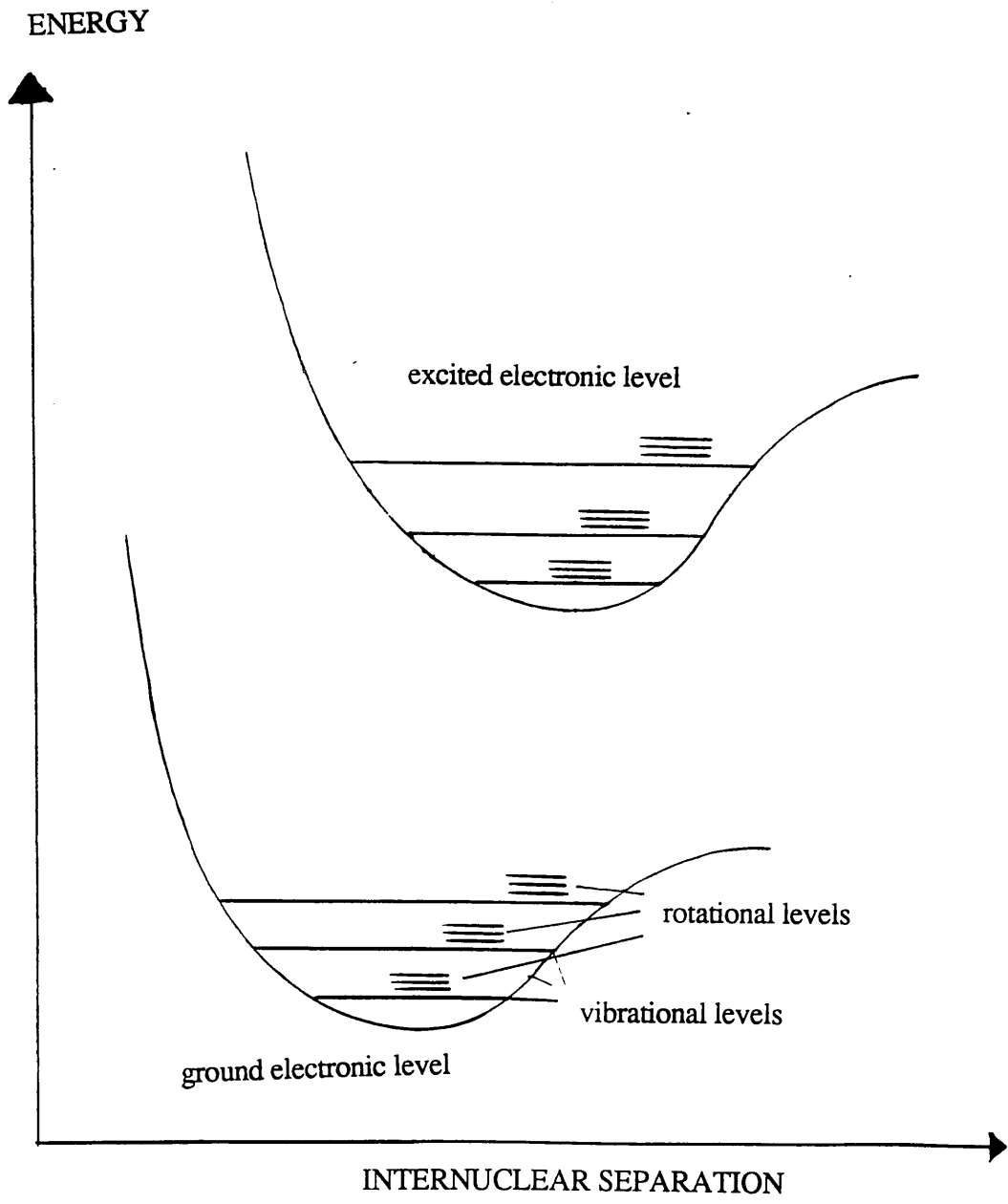


Figure 1.23 Vibrational and rotational energy levels associated with two electronic states of a molecule

$$\Psi = \Psi_e (r_i, R_n) \chi_n (R_n)$$

where R_n are the co-ordinates of the nucleus and r_i are the electronic co-ordinates. By the Born-Oppenheimer approximation (Thorne 1988), χ_n can be written as the product of two functions, $\Psi_v(R)$ representing vibration of the nucleus and $\Psi_r(\theta, \phi)$ representing molecular rotation. Thus the total wavefunction can be written

$$\Psi = \Psi_e \Psi_v \Psi_r$$

ie. the total wavefunction of the molecule is the product of the electronic, vibrational and rotational wavefunctions which are assumed independent of each other. The total energy can be written

$$E = E_e + E_v + E_r$$

E_e is essentially the dominant term, as vibrational energies amount to a few tenths of an electron volt, while rotations have energies some two orders of magnitude smaller.

If one or both atoms are in an excited state, several stable molecular states may form from each pair of atomic states, as a result of the different ways in which their angular momentum may be coupled. The coupling of angular momenta in a molecule is similar to the situation in an atom, with one important difference due to the presence of an electric field along the internuclear axis. The individual angular momentum components, l , are quantised along this axis with components m_l , and it is the sum $\sum m_l$ that is significant rather than L . This resultant is called the orbital angular momentum, and is given the symbol Λ and the states with $\Lambda = 0, 1, 2, 3, \dots$ are designated the letters $\Sigma, \Pi, \Delta, \Phi, \dots$ in analogy with the atomic S, P, D, F... configurations. The

axial component of the total momentum, Ω , is the magnitude of the orbital momentum and the axial component of the spin momentum, Σ , ie.

$$\Omega = |\Lambda + \Sigma|$$

The electron density, $|\Psi|^2$, in a homonuclear molecule must always be symmetric with respect to the midpoint between the two nuclei, but the wavefunction itself can either be symmetric ($\Psi \rightarrow \Psi$) known as gerade, or anti-symmetric ($\Psi \rightarrow -\Psi$) known as ungerade. This parity is shown by a subscript g or u, and depends on the parity of the individual atoms and their l values.

Another important consideration is the symmetry of the electron cloud with respect to reflection in any plane drawn through both nuclei. The electron density will be symmetric with respect to any plane, but the wavefunction can be either positive or negative. In a Σ state, only one of these options is possible, and a superscript of either + or - is used in the notation. All closed shells are Σ^+ states. Both + and - symmetry occur in states for which Λ is not equal to zero.

As in the atomic case, there are restrictions on the allowed transitions. The total angular momentum must change, therefore

$$\Delta J = 0, \pm 1 \quad \text{but} \quad \Delta J = 0 \not\leftrightarrow \Delta J = 0$$

Selection rules exist for the parity and symmetry conditions, ie.

$$+ \leftrightarrow +, \quad - \leftrightarrow -, \quad \text{but} \quad + \not\leftrightarrow -$$

$$u \leftrightarrow g \quad \text{but} \quad u \not\leftrightarrow u, \quad g \not\leftrightarrow g$$

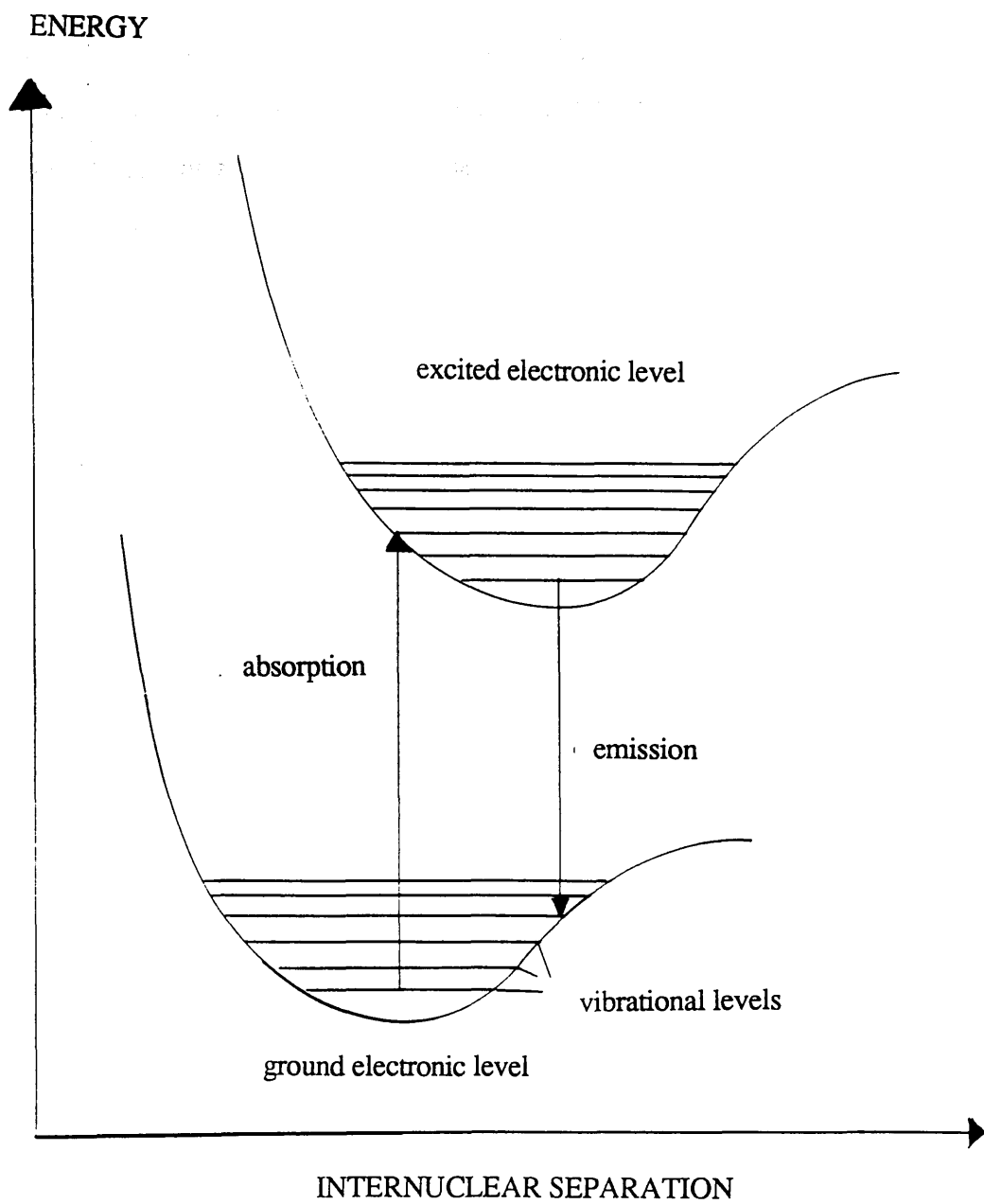


Figure 1.24 Franck - Condon principle for single photon transitions in molecules

The number of strong bands seen in a spectrum is determined by the transition probabilities of the various levels, which are governed by the Frank - Condon principle, which is illustrated in Figure 1.24. The shape of the wavefunctions of the vibrational levels is such that the most probable value of R, the internuclear separation, is near the "turning points" at the ends of the horizontal lines, ie. where the velocity is zero. The exception is $v = 0$ which has a central maximum. By the Born - Oppenheimer approximation, the internuclear separation remains fixed during a transition, and hence transitions can only be represented by vertical lines. Thus the most probable vibrational transitions are between levels whose probability maxima occur at around the same internuclear separation.

The molecular notation usually takes the following general form,

$$^{2S+1} \Lambda_{g \text{ or } u}$$

where S is the resultant spin of the electrons in the molecule. For heteronuclear molecules, the electronic levels have the same designation, but are not classified as g or u, since the molecule no longer has a centre of symmetry. The ground state is usually denoted by an X and the excited states by A, B, C, ..etc.

CHAPTER 2 INSTRUMENTATION

2.1 Introduction

The following chapter describes the optical and electronic arrangements used throughout this research. The complete systems are described in this introduction, followed by a more detailed discussion of each individual component. Firstly, all laser systems and relevant optics are described, followed by explanations of the various ion detection systems and their corresponding data acquisition methods.

The experimental arrangement for the study of caesium and rubidium vapours using a proportional counter is shown in Figure 2.1. An excimer laser of wavelength 308nm was used to optically pump a dye laser. A variety of organic dyes can be used to produce lasing action over the 400nm-700nm range. The dye laser output can be frequency doubled using Inrad doubling crystals. If doubled light alone is required, the fundamental beam can be removed by filters or by dispersion through a quartz prism. The laser beam is generally collimated through a 1x1 mm² aperture and an attenuator before passing through the ionisation region of the proportional counter. A joulemeter positioned after the proportional counter was used to monitor laser fluence. The level of laser fluence could also be adjusted by use of a variable attenuator. During the study of the spectroscopy of rubidium, the proportional counter was at one stage replaced by a quadrupole mass spectrometer in order to distinguish between the two isotopes of rubidium.

Ionisation signals from the proportional counter and laser intensity signals were amplified and delayed to ensure that the peak positions were coincident before being fed into a peak sensing ADC. The resultant digitised signals were then stored on floppy disk, and an IBM mainframe computer could also be used for detailed analysis of the

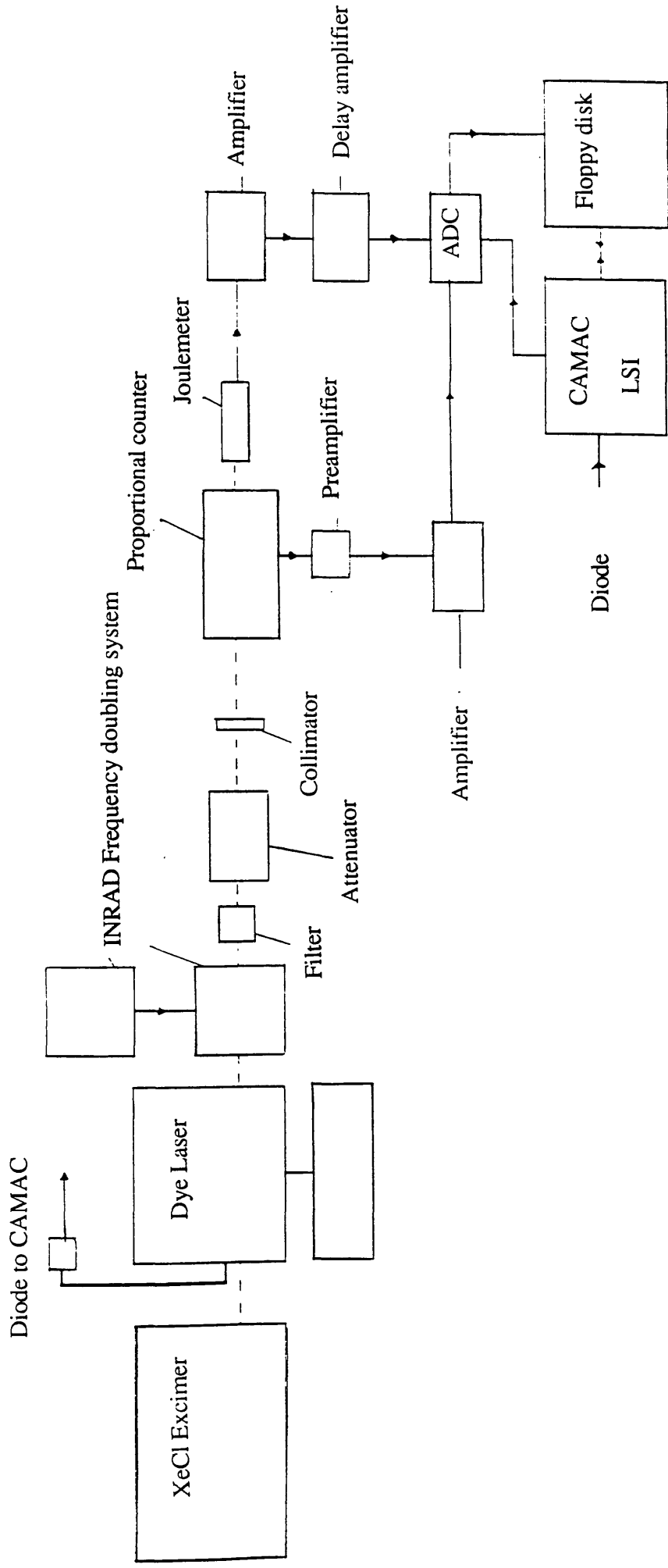


Figure 2.1 Experimental arrangement for spectroscopy using the proportional counter

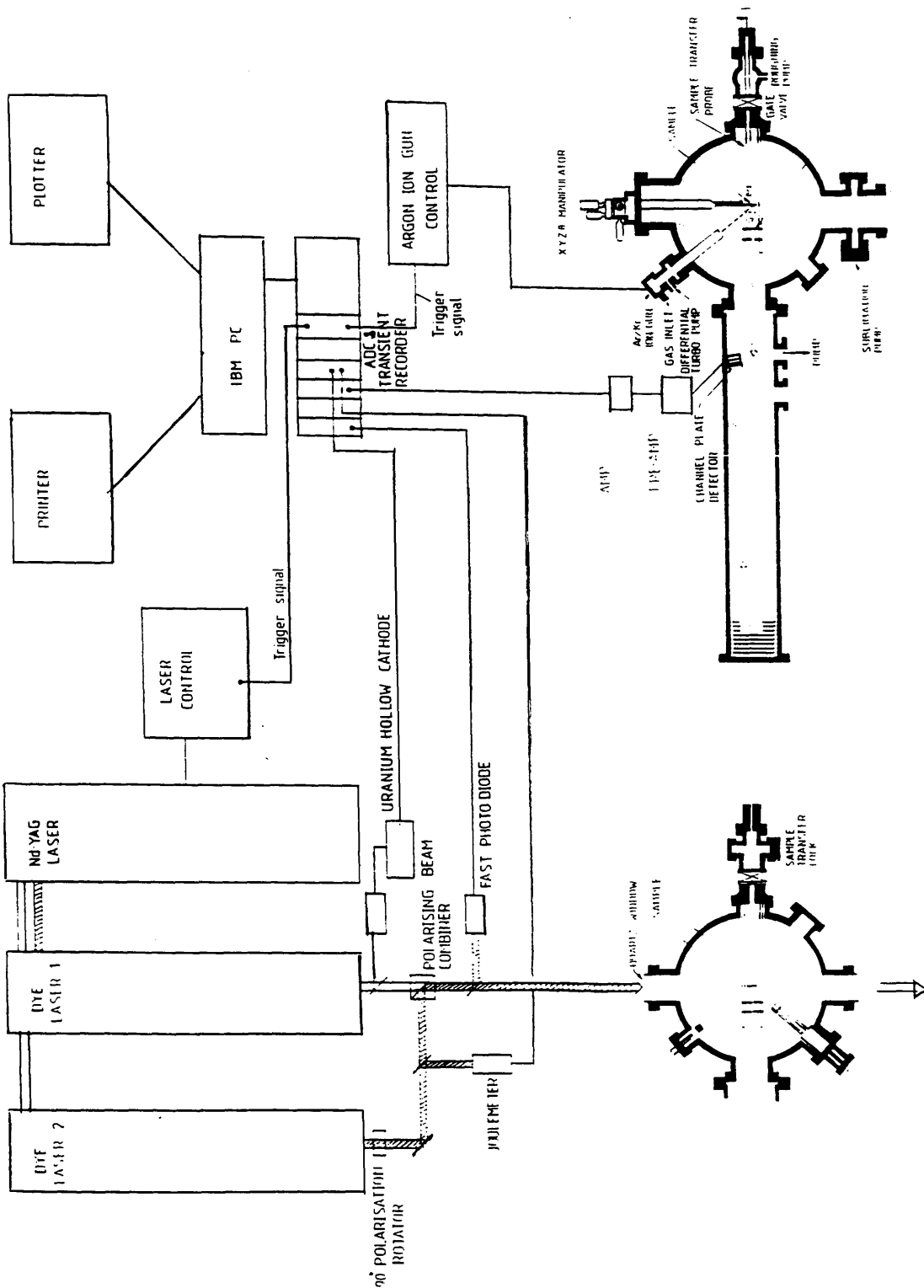


Figure 2.2 Experimental arrangement for resonant ionisation mass spectrometry (RIMS)

data.

After completion of the spectroscopy of caesium and rubidium, work began on the development and testing of the laser time of flight mass spectrometer. When the system became fully operational, it was used to study a number of aspects of laser desorption, and also for an initial demonstration of the sensitivity of the resonant ionisation mass spectrometry process using samples containing rubidium. A diagram of the experimental arrangement is shown in Figure 2.2. A detailed explanation of the individual components making up the system is given in later sections of this chapter.

2.2 Laser Systems

Two separate laser systems have been used in this research. Firstly, a Lumonics excimer laser pumping a single Lumonics dye laser was used in the study of caesium and rubidium spectroscopy, and in the detection of impurities in proportional counter gas. A frequency doubled Spectron Nd:YAG laser was used in the gas purification studies, and also in conjunction with a dual Spectron dye laser system for the development of a Laser Time of Flight Mass Spectrometer.

2.3 Excimer Laser

Excimer lasers are very high powered molecular lasers capable of producing very short, very intense pulses of light. They operate by producing an electrical discharge through the gas medium containing a mixture of rare gases and halogens. Excimer lasers are different in concept to normal molecular lasers because the ground state of the molecules is not bound and the constituents of the gas mixture repel each other at interatomic distances characteristic of most diatomic molecules. This is, in effect, a bound free system. Excitation of this active medium via an electrical discharge

sufficiently modifies the state of the atom, so that there is an attractive force with the other atoms in the gas.

Bound states occur from the formation of one ground state atom and one electronically excited atom. The two atoms are then paired together at a small separation distance, creating an excited state dimer, or excimer. Lasing action arises as the excimer molecule returns to the ground state and dissociates. If one or both of the excited state atoms are rare gas atoms, the amount of excitation energy is extremely large. Thus the metastable excimer state is an important system for storing high energies. An unusual feature of excimer systems is that as long as the excimer state is populated, a population inversion automatically exists, and lasing action can occur. Thus every excited molecule contributes a photon to the laser beam, instead of only sufficient photons being emitted to equalise the populations of the upper and lower states. A schematic diagram showing the energy levels for an excimer laser is shown in Figure 2.3.

Some excimer systems are not suitable for lasing because they have bound states at a higher energy than the excimer state, and if these are accessible from the excimer state via the absorption of a photon, they will reduce the effective population inversion and may halt lasing action. Intermolecular collisions may also dissociate the excimer before stimulated emission can occur, resulting in a loss of efficiency.

Suitable active media for excimer lasers include excited rare gas dimers (eg. Ar_2^* , Xe_2^*), rare gas oxides (eg. XeO^*) or rare gas atoms in combination with halide atoms. The laser used in this research was a Lumonics TE 860-3 filled with XeCl gas. Lasing action arises from XeCl^* excimers produced by an electrical discharge of about 32kV. This gives a wavelength output of 308nm with an energy of around 80mJ per pulse. It was necessary to replace the gas mixture after a few days' operation due to a reduction in power. The output beam was a rectangular shape of dimensions 8mm x

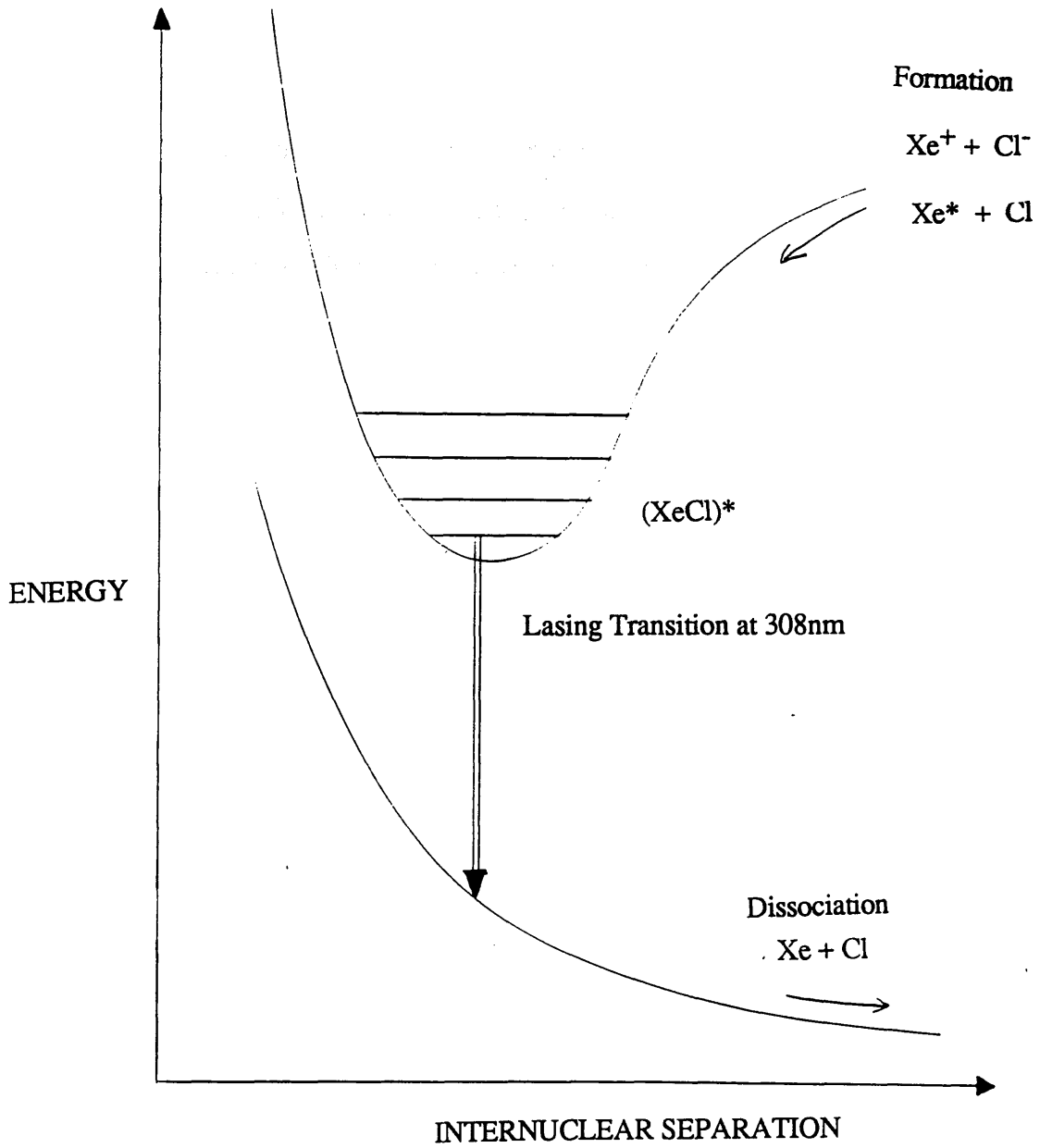


Figure 2.3 Excimer laser energy levels

12mm and was used to optically pump the dye laser. The pulse width of the laser is 8ns-12ns with a beam divergence of 2.4mR x 6mR. This UV output is particularly useful in pumping dye laser systems.

The excimer laser may be operated using either stable or unstable resonator optics. Stable optics allow the light to pass a large number of times through the lasing medium before emerging out of the optical cavity. This, however, results in a larger beam divergence than is produced using unstable resonator optics. When pumping the dye laser, a slightly divergent beam is preferable, and hence stable optics were installed.

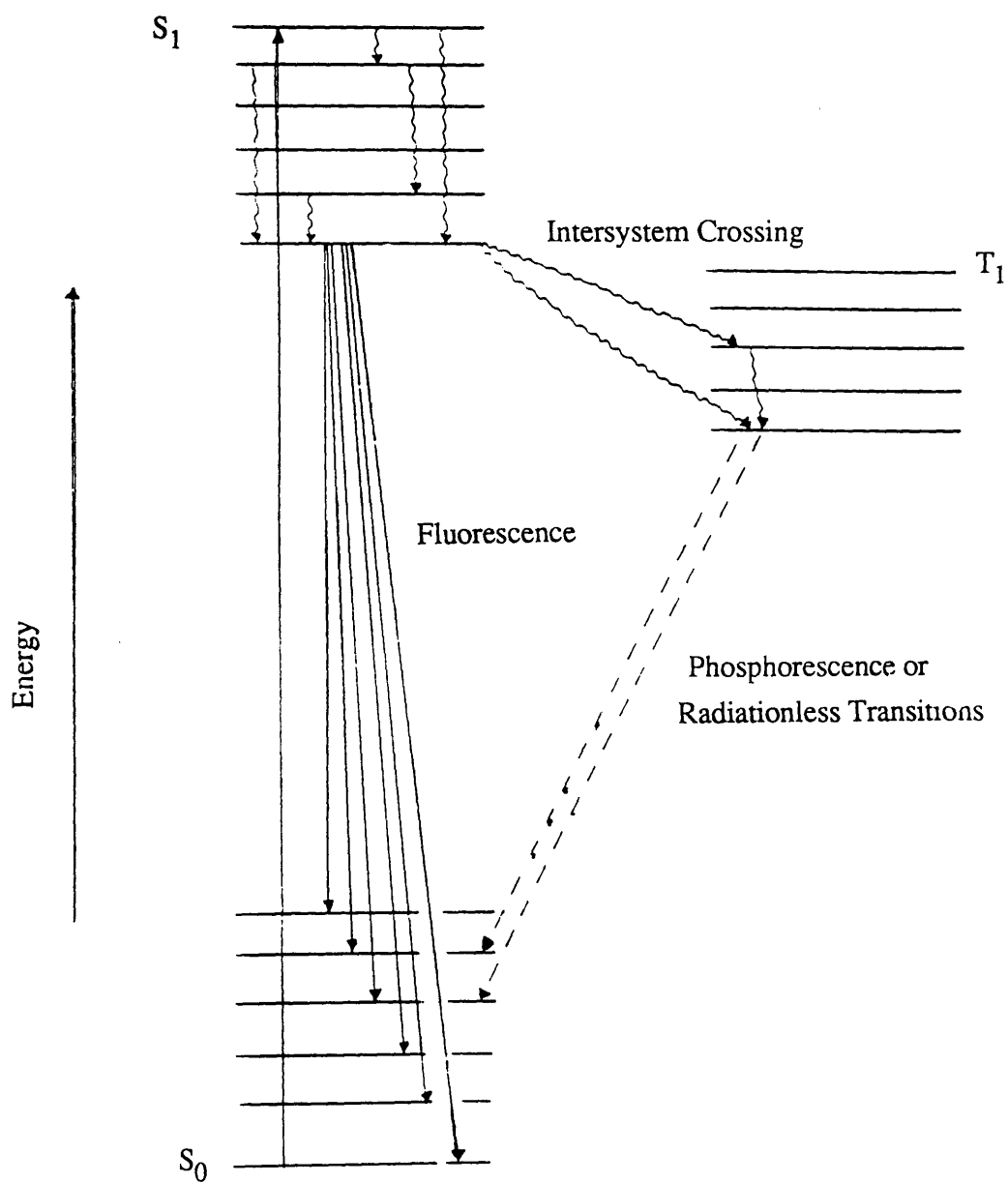
2.4 Excimer Pumped Dye Laser

Dye lasers are broadly tunable systems where the output wavelength for a particular dye can extend over 50nm or more in the visible region. Practically, about ten different dyes are sufficient to obtain laser output of any wavelength in the visible region.

Dye lasers operate on the principle of fluorescence properties of organic dyes. The electronic structure of the organic dye molecules is responsible for the fluorescent characteristics. When the dye is excited by an external source of short wavelength light, it fluoresces by absorbing a photon at the excitation wavelength and subsequently emitting a photon at the fluorescence wavelength. The energy difference between the absorbed and emitted photon is accounted for by a non - radiative transition in the dye.

A typical energy level diagram for a dye molecule is shown in Figure 2.4. It consists of a ground state S_0 , a series of excited singlet states S_1, \dots, S_n , and a series of triplet states T_1, \dots, T_n . The singlet states occur when the total spin of the excited electrons in each molecule equals zero. The triplet states occur when the total spin is unity. According to selection rules, transitions between singlet and triplet states are far

Figure 2.4 Dye molecule energy levels



less likely than transitions between two singlet or two triplet states. Each electronic state of the dye molecule contains a set of vibrational and rotational levels. Because of the interaction of dye molecules with the solvent, the closely spaced rovibronic levels are collisionally broadened to such an extent that the different fluorescence lines overlap, resulting in a continuous band. An organic solvent such as methanol or toluene is usually used to dissolve the dye in its powder form.

The maximum power output of a dye laser depends on the solvent used and on the wavelength of the pump source as well as the type of dye and the alignment of the optical cavity. Dye lasers are always optically pumped. The essential requirement of the pump source is that it has an output near the peak of the dye absorption band. The dye molecule is excited from low lying rovibronic levels in the ground state S_0 to higher lying rovibronic levels in the electronically excited state S_1 . The molecule can spontaneously decay to lower lying S_1 levels or may return via non-radiative transitions. Lasing action occurs between the lower lying ro-vib levels in S_1 and the higher levels in S_0 . Collisional de-excitation quickly transfers the molecules back to their ground state. The path via radiationless transitions to and from triplet states is a loss mechanism which can be inhibited by appropriate solvents and additives. The laser output occurs at longer wavelengths than the pump source.

Most laser dyes have extremely high small signal gains, and hence only a small amount of active medium is required. However, the intense absorption and subsequent heating of this small volume necessitates a continuous circulation of the dye. Failure to keep the dye circulating results in decomposition of the heated dye.

A range of fluorescent frequencies are produced as a result of the broad band structure of the dye's energy levels, and therefore a wavelength selecting element is required in the optical cavity. The Lumonics dye laser uses a diffraction grating as a

combined end mirror and dispersive element. The required wavelength can be selected by rotating the grating to change the angle to the optic axis of the laser cavity, allowing only a very narrow band of wavelengths satisfying the equation,

$$m \lambda = 2 d \sin \theta$$

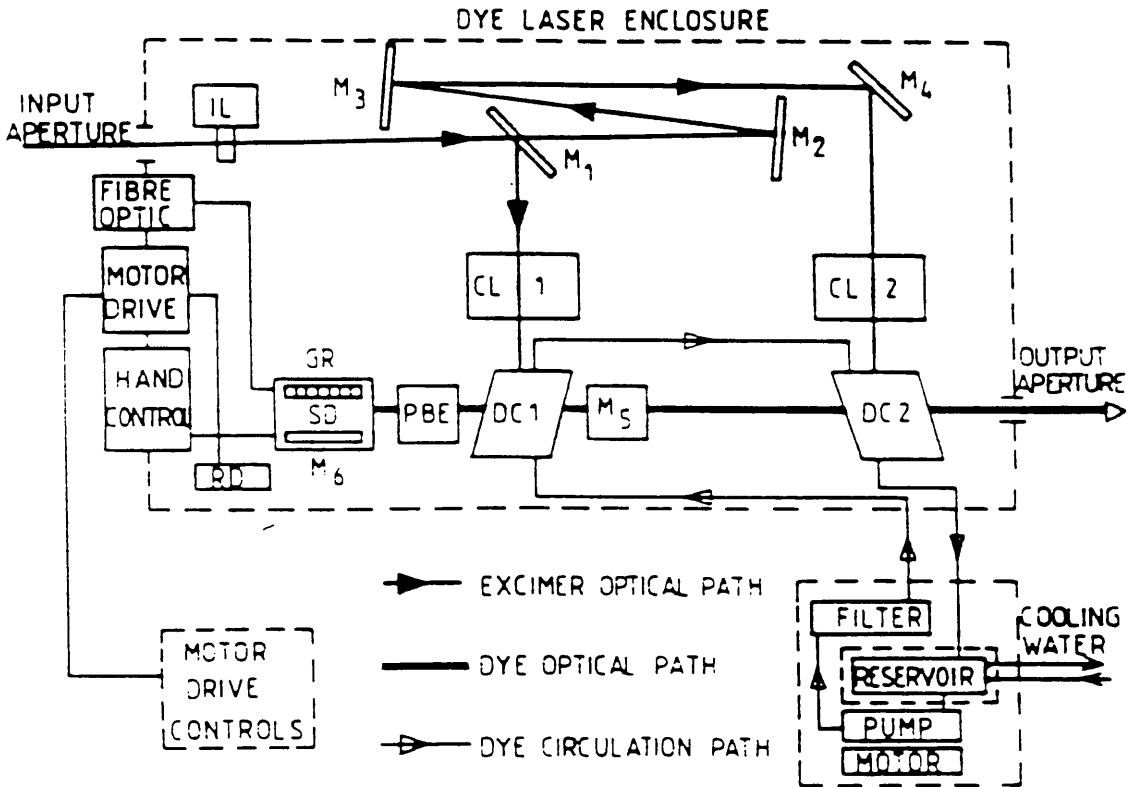
to be diffracted back into the laser cavity.

The laser used in this research was a Lumonics EPD-330 dye laser, pumped by the Lumonics XeCl excimer previously described. The high pump power available from this laser allows sufficient population inversion, even in dyes with low quantum efficiencies. A diagram of the optical arrangement inside the laser cavity is given in Figure 2.5.

The incoming 308nm excimer beam is used to transversely pump both the oscillator dye cell and the single pass amplifier (see Figure 2.6). The pump beam is passed through a beam splitter, with one portion of the beam directed into the oscillator cell using a cylindrical lens, and the remainder strongly focussed through the amplifier cell. This allows rapid alignment and simple operation without loss of efficiency. In addition, a separate amplification region avoids damaging the diffraction grating. The output coupler acts as a cavity mirror with a transmission of around 2% (see Figure 2.7).

A holographic diffraction grating is used to tune the output and is controlled by a Lumonics Compuscan EPD-60 electronic scanner. The laser linewidth can be improved by introducing a prism beam expander which has the effect of increasing the number of lines illuminated by the laser beam. Because the resolving power of a grating is proportional to its number of lines, the more lines hit by the laser, the better the resolution and the smaller the resulting linewidth. The beam expander is often removed, however,

Figure 2.5 Lumonics EPD - 330 dye laser



KEY	CL _{1,2}	Cylindrical lenses	M ₅	Output coupler
	DC _{1,2}	Dye cells	PBE	Prism beam expander
	GR	Grating	RD	Readout
	IL	Interlock	SD	Sine drive
	M ₁ , M ₄ , M ₆	Reflectors		

as it results in a considerable reduction in laser fluence.

The dye laser has a line width of 0.003nm at best with the beam expander in position, and a width of 0.05nm without. The power output ranges from 3%-14% of the pump power, depending on the dye being used - longer wavelength dyes tend to have a higher efficiency than those in the near UV. The pulse width was 2ns less than that of the excimer ie. 6ns-10ns (FWHM) with a spot size of around 1mm x 2mm. The beam divergence was less than 1mR, and the beam was almost completely (95%) vertically polarised.

The system may suffer losses as a result of absorption and heating losses in the dye, and by scattering of light from the dye cells. These may be reduced by the rapid removal of dye molecules from the lasing region by efficient dye circulation.

2.5 Nd:YAG Laser

A Nd:YAG laser is one of the most versatile high powered lasers available. The active medium for this laser is the rare earth Nd^{3+} ion doped into the host insulating material yttrium aluminium garnet at a level of about 1%. It is in some respects similar to the ruby laser, but has better efficiency due to the use of a four level pumping system rather than the ruby laser's three level system which requires very strong pumping. This is due to the final state of the laser transition being the ground state, so that more than half the ground state atoms must be pumped to the upper level to achieve population inversion.

A diagram of the four level system is shown in Figure 2.8. Optical pumping by flashlamps causes excitation from the ground state to level 3. From this level, the atoms decay to the metastable state 2 and the population of this state grows rapidly. Moderate

Figure 2.6 Oscillator cell

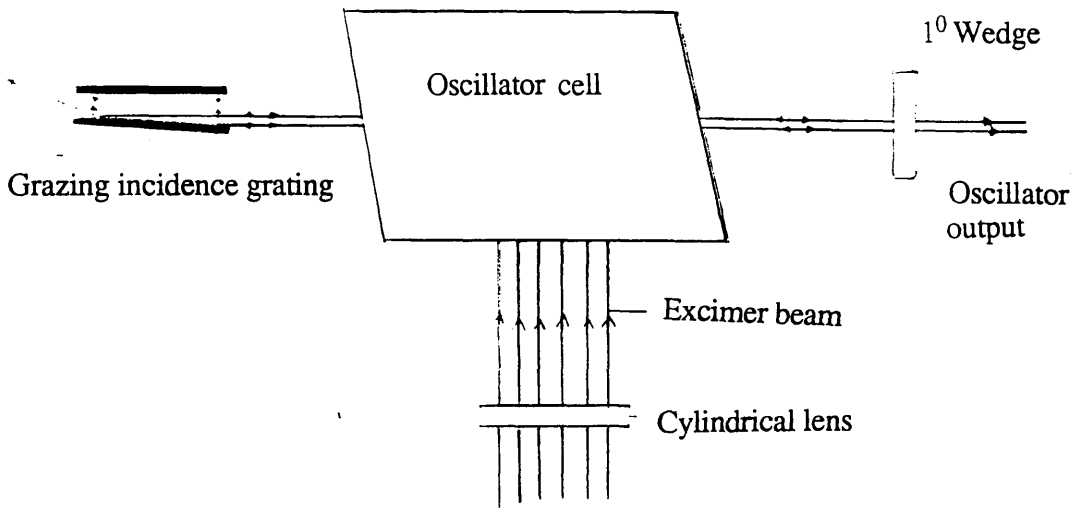
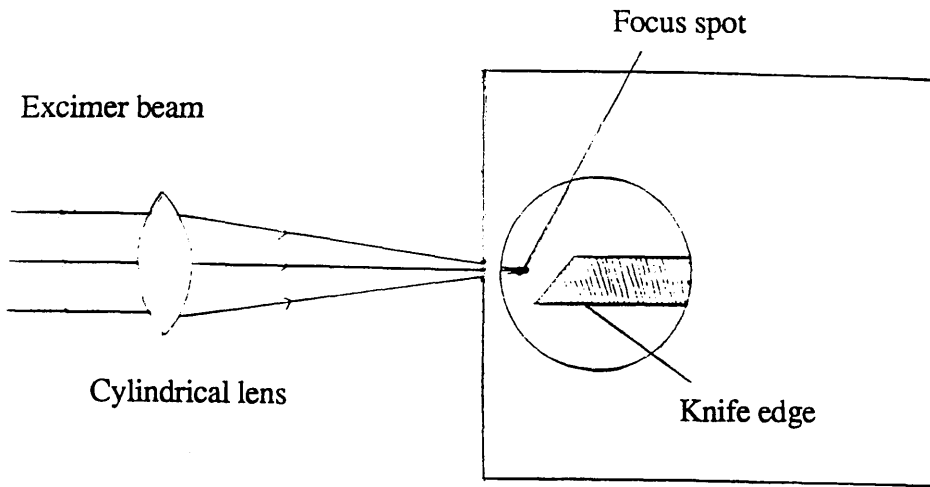
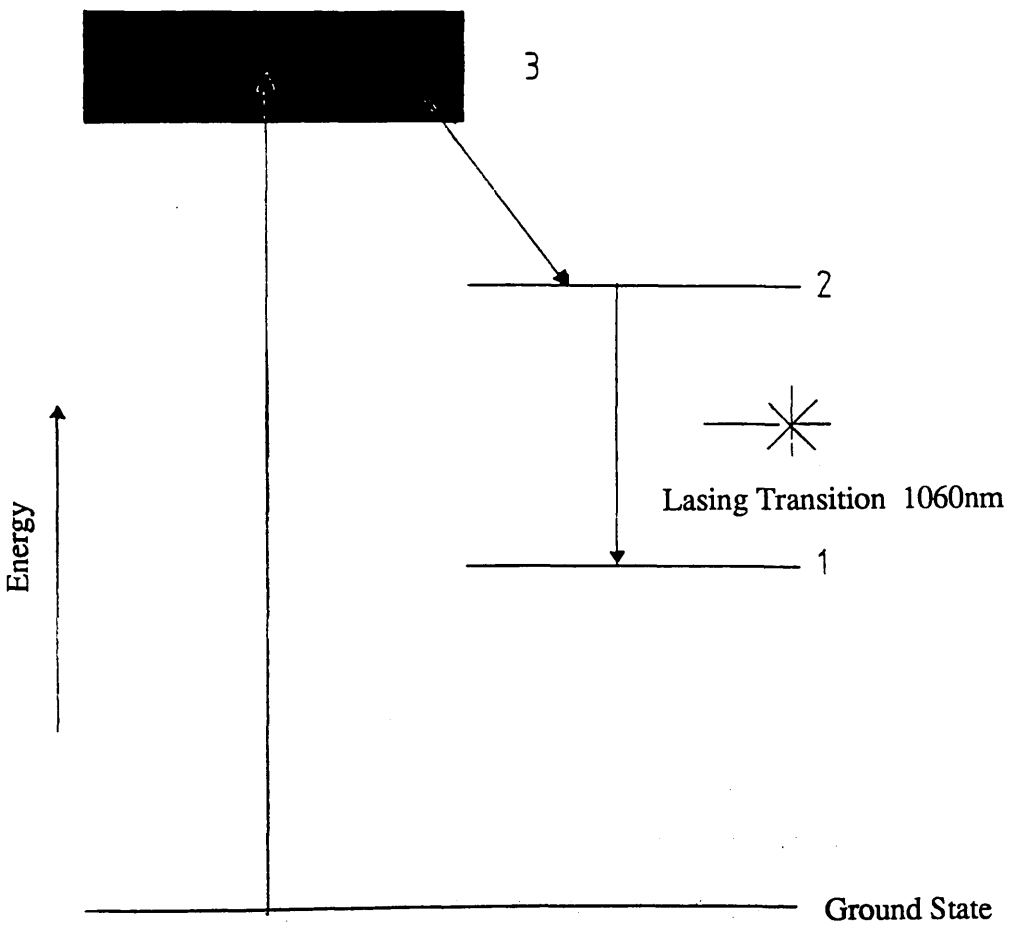


Figure 2.7 Dye laser cavity

Figure 2.8 Four level diagram for Nd: YAG laser



pumping is required if the lifetimes of the (3-2) transition and the (1-0) transition are short and that of (2-1) is long. The populations of energy levels 3 and 1 remain essentially unchanged after the onset of pumping, and only a small number of atoms need to be added to level 2 to make $N_2 > N_1$.

Because the ground state is not the lower level of the population inversion, the ground state population may be large, yet the pumping required to achieve inversion need not be intense. Lasing from level 3 to level 2 gives an output in the infrared region of the spectrum at $1.06\mu\text{m}$.

The Nd:YAG laser used in this research is built by Spectron and is shown in Figure 2.9. It uses flashlamps to pump both the oscillator and the amplifier YAG rods. The oscillator contains a Q switching mechanism to produce very intense short pulses. The quality factor Q of the laser cavity is determined by the losses suffered by the modes of the cavity - the smaller the losses, the higher the Q value. The Q switch operates by altering the cavity Q value from a low level during pumping to a much higher level at the onset of the laser pulse. Losses are incurred mainly as a result of the finite reflectivities of the cavity mirrors, and scattering and absorption in the active medium.

The laser is initially pumped continuously while the Q value of the laser resonator is kept low. When the population inversion has increased sufficiently, the Q value of the resonator is suddenly switched to a high value, with the result that the energy accumulated in the upper level is released as a laser output in a very short pulse. The peak power of the laser pulse obtained by this method is considerably higher than obtainable from normal pulsed oscillation, and the process can be thought of as essentially a means of storing energy until it is required.

In the Spectron Nd:YAG laser, the Q switching is brought about by means of a

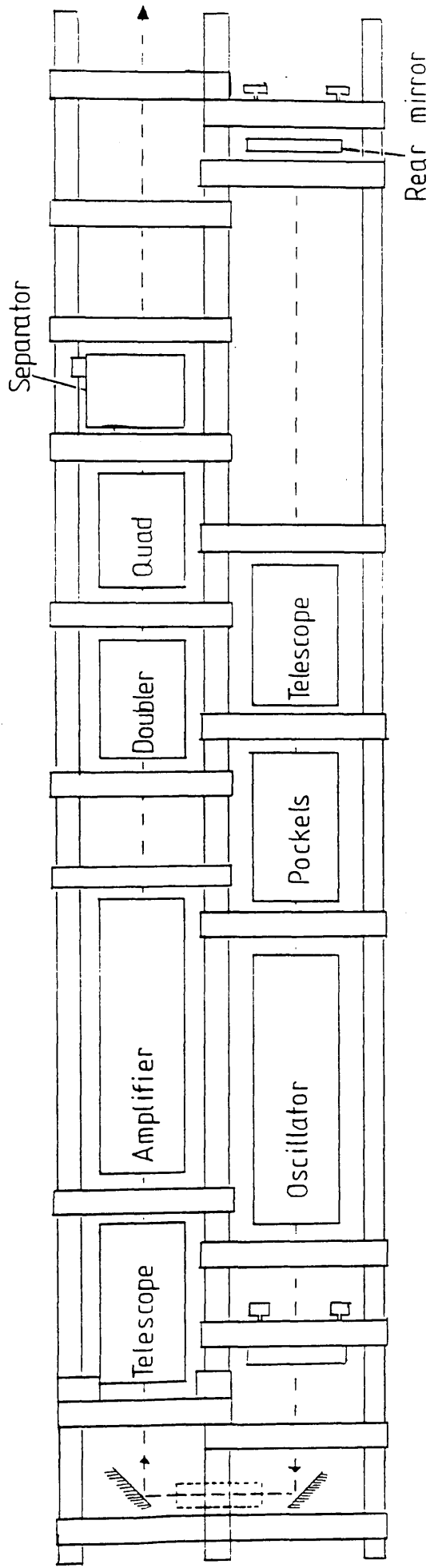


Figure 2.9 Schematic diagram of Spectron Nd: YAG laser

Pockel cell. Pockel's effect is the linear dependence of the refractive index of an electro-optic material with the applied electric field. A Pockel cell is an electronic shutter consisting of a polariser and a birefringent material which is placed in front of one of the mirrors in the laser cavity. The combination is adjusted so that when a voltage is applied to the cell, a double pass through the electro-optic material rotates the linearly polarised light through 90° thus preventing passage through the polariser. In this position, the cavity losses are high and the Q value low. On removing the voltage, the cell does not rotate the polarisation. This corresponds to an open shutter position with small losses. A Pockel cell generally requires several kilovolts for operation.

2.6 Second Harmonic Generation

The Nd:YAG laser makes use of a striking effect in non-linear optics, second harmonic generation, in which a beam of frequency ω generates a beam with frequency 2ω by interaction of a high powered laser beam with a suitable non-linear crystal.

For weak intensities of the incident light beam, the polarisation induced in the crystal is proportional to the oscillating electric field associated with the light beam, ie.

$$P = X E$$

where X is the polarisability of the material. However, in the case of an intense focussed beam, the electric fields can be very high, non-linear effects become significant, and the distorted nature of the induced polarisation wave leads to the production of harmonics of the incident light. In such cases, P is no longer proportional to E and must be expressed in the form

$$P = X_1 E + X_2 E^2 + X_3 E^3 + \dots$$

where X_1 and X_2 are the non linear polarisabilities, and will, in general, be tensors unless the medium is isotropic. For X_2 to be non zero, the medium must exhibit some anisotropy, ie. its physical properties such as index of refraction varying with direction. Crystals having a centre of symmetry, therefore, cannot generate second harmonics.

Assuming the incident field has the form $E = A \sin \omega t$, the polarisation can be expressed

$$P = X_1 A \sin \omega t + 1/2 X_2 A^2 - 1/2 X_2 A^2 \cos 2\omega t - 1/4 X_3 A^3 \sin 3\omega t$$

Non linear polarisabilities are dependent on the polarisation of the electric field and on the optic axis of the crystal. The $2\omega t$ and $3\omega t$ terms represent dipole moments induced in the medium with oscillation frequency two and three times the original wave frequency (see Figure 2.10).

In order to generate a significant proportion of frequency doubled light, the incident wave and the frequency doubled wave must maintain a proper phase relationship. Both the incident wave and the doubled wave will be coherent at the initial point of harmonic generation. As the incident wave propagates through the crystal, it continues to generate contributions of second harmonic light which will combine constructively only if they maintain a constant phase relationship.

The phase velocity of the frequency doubled wave is normally different from that of the incident wave, therefore the newly emitted second harmonic periodically falls out of phase with some of the previously generated waves. The distance required for the second harmonic wave and the incident wave to become completely out of phase is called the coherence length. This is typically around 10^{-3} cm for most crystals. Crystals with a much greater thickness than the coherence length tend to be susceptible to interference

Figure 2.10 Second harmonic generation

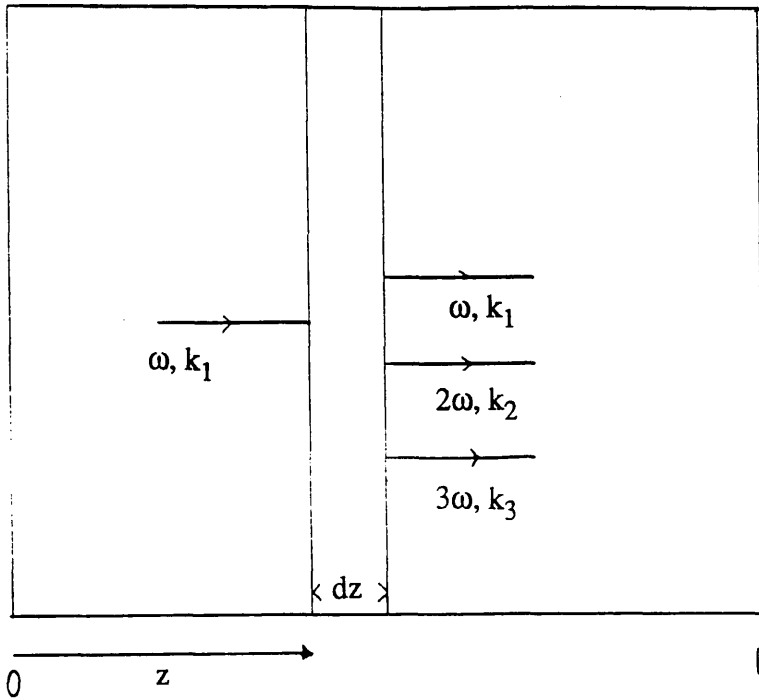
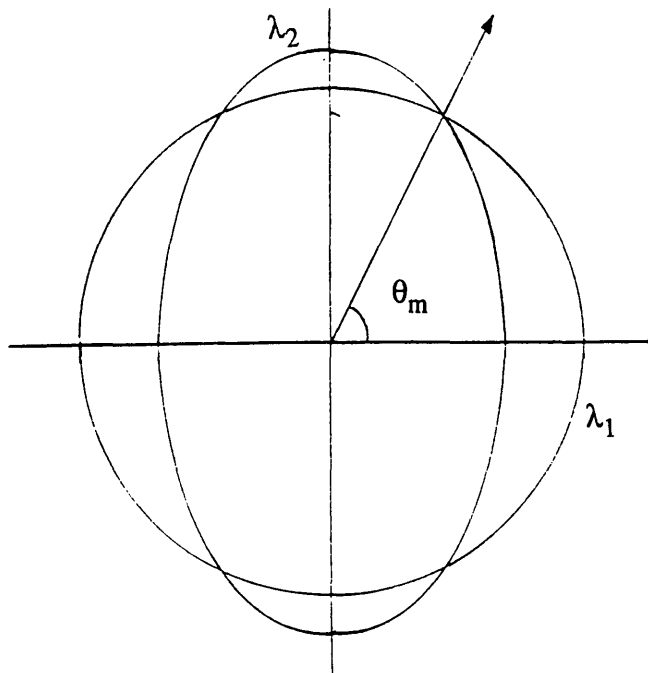


Figure 2.11 Ray velocity diagram for a second harmonic generating crystal



effects which reduce the harmonic output considerably.

Effective second harmonic generation was achieved by a procedure known as phase matching. This can be achieved by using a doubly refractive crystal in which light of a particular wavelength can propagate at two different velocities, known as ordinary and extraordinary, which vary with the propagation direction. Figure 2.11 shows that at a certain angle of incidence, the ordinary incident light will have the same phase velocity as the extraordinary SHG light resulting in a greatly increased coherence length. The second harmonic waves will then interfere constructively thereby increasing the conversion efficiency by several orders of magnitude to around 20%, depending on the incident power density. Commercial second harmonic generators are simply appropriately cut and oriented crystals.

Efficient frequency doubling requires precise orientation of the crystal with respect to the incident laser beam. Hence, the required angle of incidence changes as the wavelength changes. This problem was overcome by use of an auto tracking system (INRAD model 5-12), which maximises the doubling efficiency of the crystal as the dye wavelength is scanned (see Figure 2.12). A fraction of the crystal output was directed onto two photodiodes, and the crystal orientation was continually adjusted by means of a servo controlled motor. A conversion efficiency of around 10% could be achieved. In this research, KDP (potassium dihydrogen phosphate) crystals were used to frequency double the dye laser output to give a wavelength coverage of 260nm - 330nm.

The Spectron Nd:YAG laser used in this research has a fundamental output wavelength of 1064 nm with frequency doubling (532nm), tripling (355nm) and quadrupling (266nm) facilities. The third harmonically generated signal is relatively small, and hence tripling is achieved by frequency summing of the fundamental and doubled beams. The laser has a pulse repetition rate of 10 Hz and a pulse duration of

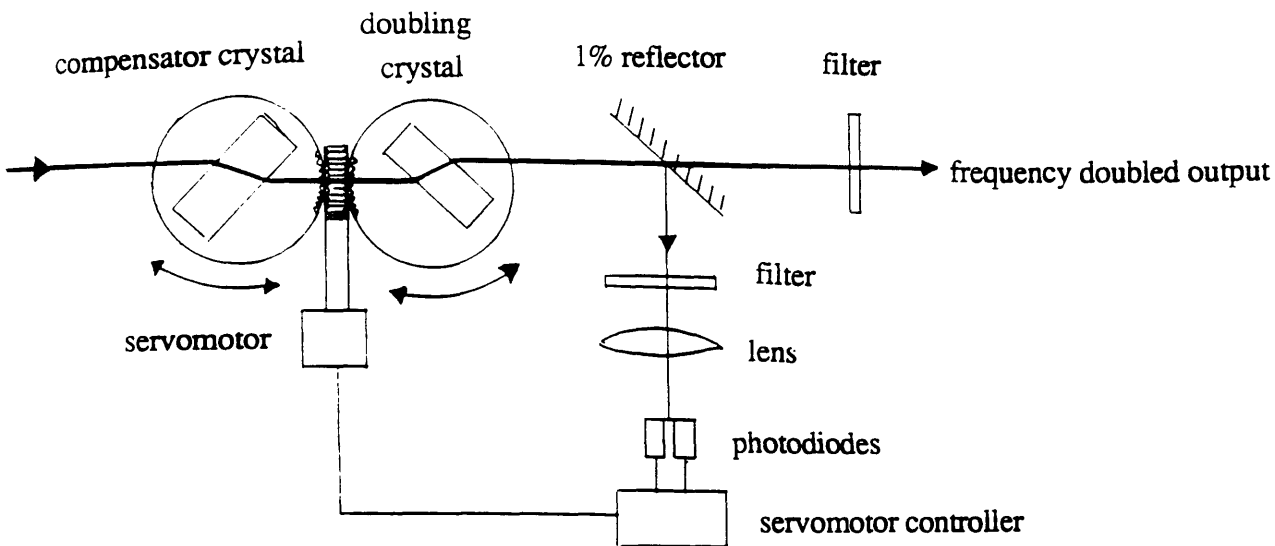


Figure 2.12 Auto tracking system

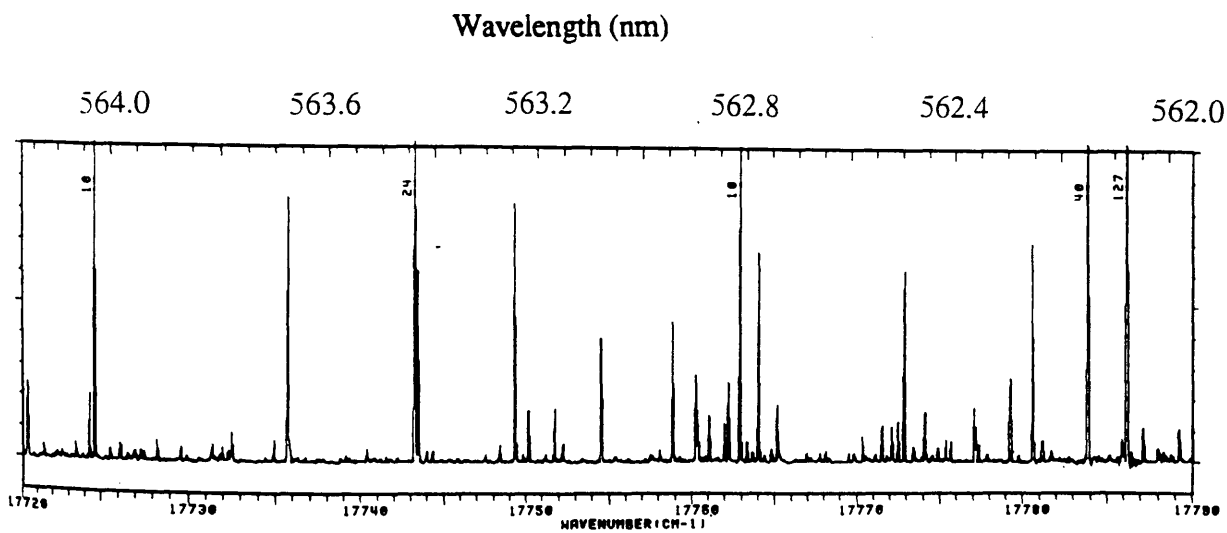


Figure 2.13 A section of a uranium hollow cathode spectrum used for wavelength calibration

15ns. The doubled and tripled outputs have energies of 300mJ / pulse and 80 mJ / pulse respectively. These outputs can be used to pump two different dye lasers, each having slightly different characteristics. The first has a wavelength range of 540nm -700nm with a bandwidth of 0.1 cm^{-1} and a power of 20 mJ / pulse. The second has a slightly wider wavelength span of 400nm - 700nm with a 1 cm^{-1} and energy of 1 mJ /pulse. Frequency doubling crystals can extend this range down to wavelengths of between 270nm - 350nm. The dye lasers can be accurately calibrated using uranium hollow cathode spectra (see Figure 2.13).

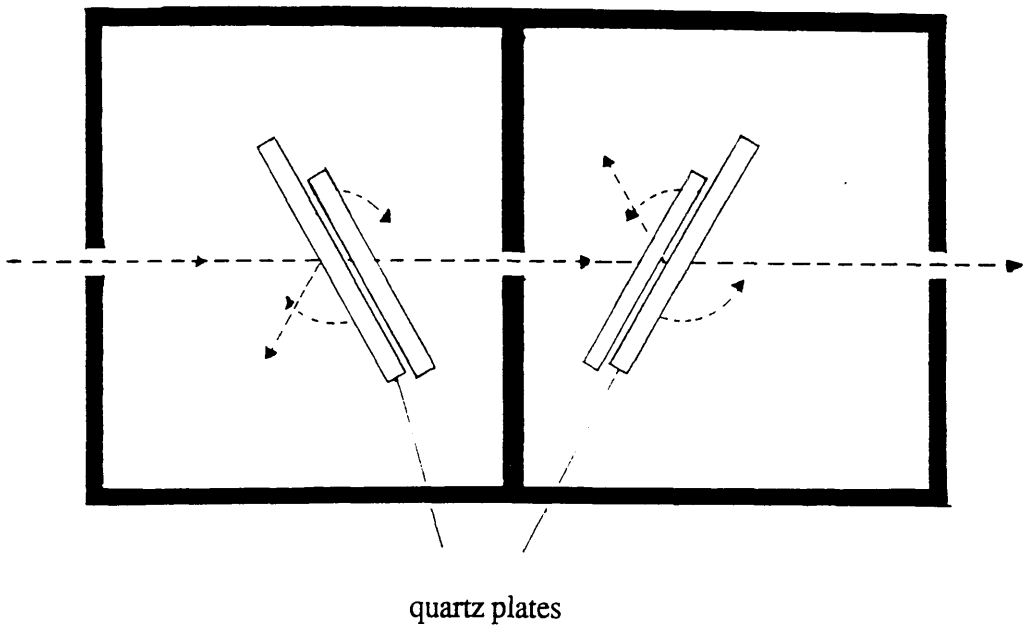
2.7 Measurement and Attenuation of Laser Power

Two different types of joulemeter were used for monitoring the laser fluence. A GENTEC joulemeter was used for measurement of high powers and a Molelectron J3 pyroelectric joulemeter measured the output from the dye lasers. The laser output could be varied if necessary by using a Newport corporation model 935-5 variable attenuator (see Figure 2.14). The attenuator consists of four inclined quartz plates which partially reflect and partially transmit the laser beam. The amount of light transmitted is a function of the angle of inclination of the plates to the beam. The relative positions of the plates compensates for the refractive beam displacements.

2.8 Proportional Counter

A proportional counter is basically an ion chamber which uses a high field strength to give the electrons produced sufficient energy to produce secondary ion pairs which then create further ion pairs, resulting in a Townsend Avalanche, where the original charge deposited by the ionising radiation is multiplied by a factor m , called the gas amplification factor, and may be as large as 10^5 .

Figure 2.14 Newport variable attenuator



The basic cylindrical geometry of a proportional counter is shown in Figure 2.15. The anode is a thin wire ($20\mu\text{m} - 50\mu\text{m}$) situated along the axis of a hollow cylindrical cathode. The electric field between the wire anode and the cathode decreases with radial distance, r , from the axis of symmetry according to the equation,

$$E = \frac{V}{r \ln\left(\frac{b}{a}\right)}$$

where V is the applied potential, b is the radius of the cylinder and a is the radius of the wire. Ion pairs produced in such a detector move apart in the E field. The electrons drift towards the anode wire and as they approach close to the wire, the E field strength increases rapidly. Close to the wire, the electrons gain sufficient energy to cause secondary ionisation and a Townsend avalanche develops. In a uniform field,

$$I = I_0 \exp(\alpha x)$$

where α is the Townsend coefficient. Provided these avalanches do not interfere with each other, the resulting voltage signal is proportional to the initial number of ion pairs produced.

In general, avalanches are only produced within a certain critical radius where the field strength is sufficiently large. This critical radius may be as small as $100\mu\text{m}$. The majority of the initial ion pair production takes place in the remaining volume, and the primary electrons created drift towards the anode wire. Almost all the avalanching starts at the critical radius. Thus the applied field need only be a fraction of the size which would be required to maintain the proportional counter conditions over the entire sensitive volume. In addition, the amplification is independent of the position of the primary ion pair. The electrons finally hit the wire and are detected as a charge pulse with a fast amplifier.

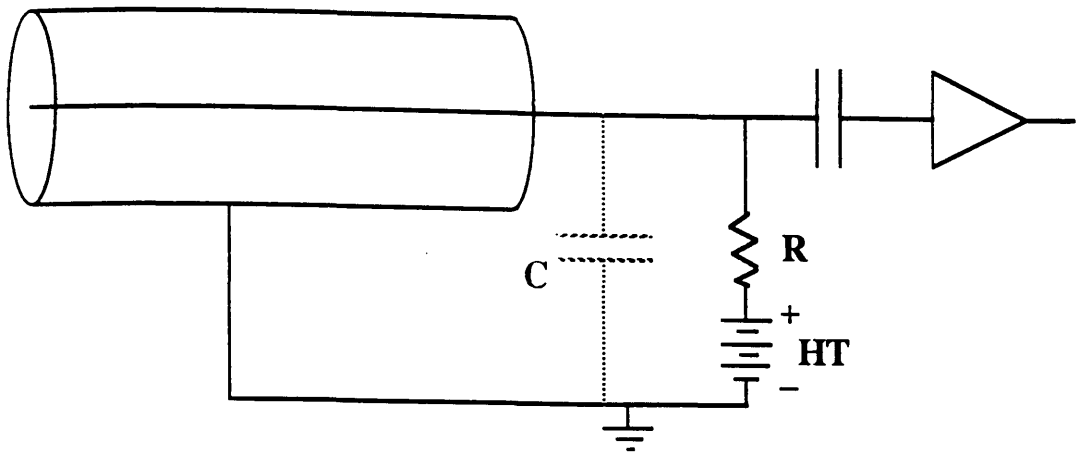


Figure 2.15 Proportional counter

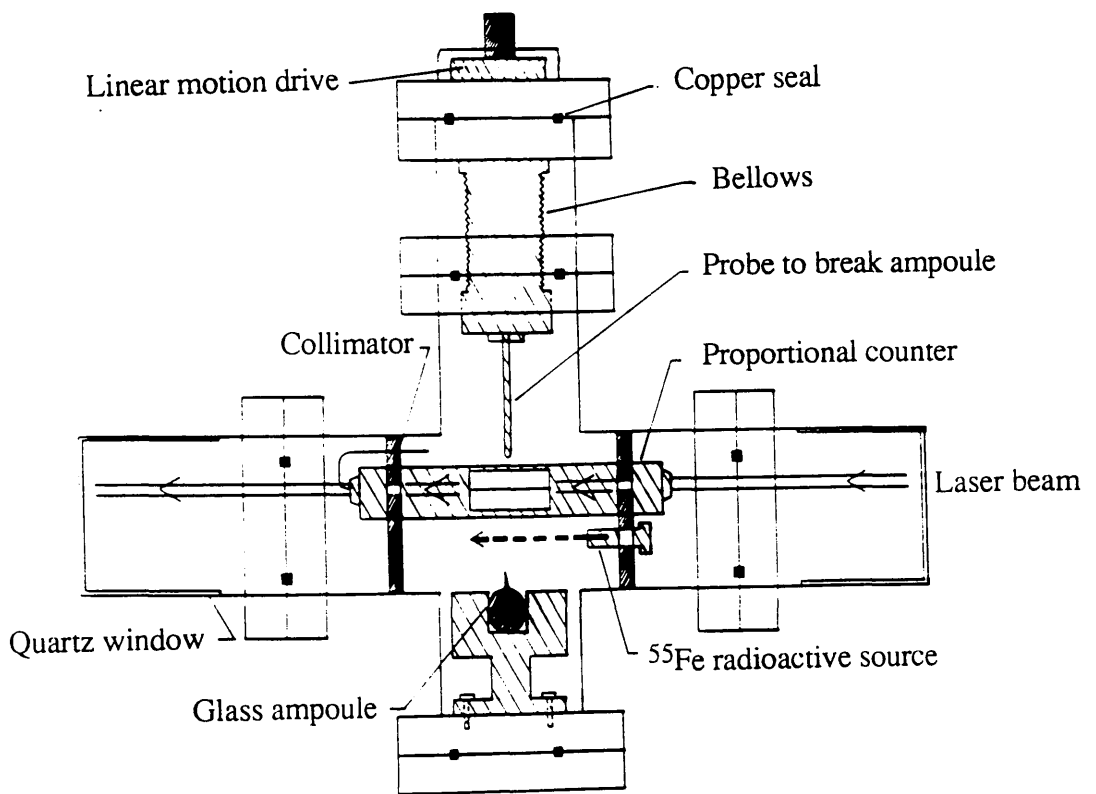


Figure 2.16 Proportional counter housing

2.9 Counter Gas

The gas used in the proportional counter was the standard P10 gas containing 90% argon and 10% methane. The argon acts as a non-reactive buffer gas. The methane gas acts as a quenching agent. Excited atoms can be formed in the avalanche discharge, which then de-excite emitting photons of sufficient energy to create further ion pairs which spread the discharge indefinitely. The addition of an organic gas such as methane stops the discharge lasting indefinitely by absorbing the extra photons. The organic molecules have lower excitation potentials than the argon atoms, and so the photons they emit after excitation have insufficient energy to cause further avalanching.

The counter was usually filled with P10 gas to a pressure of 30 torr. Before filling, the counter was always baked out under vacuum (1×10^{-5} torr) to reduce the ionisation resulting from impurities. It is desirable to operate at a fairly low pressure in order to reduce the background ionisation signal to a minimal level. Background ionisation arises from two main sources - photo-electrons and organic impurities - and is independent of laser wavelength. Photo-electrons are liberated from light scattered off the gas molecules which then ionise the condensed caesium metal on the inner surfaces of the counter. Organic impurities also contribute to the laser induced background signal and may react with the caesium metal reducing its active lifetime.

Operating at low pressures also has the advantage of reducing the collisional broadening of the caesium transition widths. In the caesium experiments, it was important to introduce a higher percentage of quenching gas to avoid instability in the electron avalanches. A mixture of 70% argon/ 30% methane gas was chosen and proved an effective solution.

2.10 Proportional Counter Housing

The chamber was specially designed to incorporate some necessary features. Firstly, the counter must be very clean to avoid initiation of reactions with the caesium metal. The counter must be easily dismantled for cleaning or repair. In addition, it should be constructed from non - contaminating materials such as stainless steel which will not contribute to the background ionisation signal. It should be able to sustain high temperatures (around 200°C) in order to bake out the counter under vacuum to remove contaminants. In order to satisfy these requirements, the chamber was constructed from standard ultra - high vacuum components purchased from Vacuum Generators Ltd. A six way cross chamber was used with two quartz windows mounted on flanges serving as laser entrance and exit ports (see Figure 2.16).

The anode of the proportional counter was made of 0.025mm stainless steel wire and isolated from the earthy cathode by glass insulation. A high voltage of 800V was applied to the anode, one end of which was attached to a thicker nickel wire connected to a high vacuum feedthrough via stainless steel tubing. The resultant signals were passed through a pre - amplifier (ORTEC 142) and finally to the data acquisition system.

The caesium or rubidium sample was contained in a glass ampoule to prevent reaction with air, and was placed in a stainless steel holder located at the base of the six way cross. A stainless steel probe controlled by a linear motion drive was used to break open the capsule and distribute the metal vapour into the ionisation region via a collimator at the top of the sample holder. In practice, it was found that most of the ionisation originated from metal vapour on or around the tip of the probe.

Calibration of the proportional counter was achieved by mounting an ^{55}Fe source in such an orientation as to produce X - rays in the same direction as the laser

beam. Hubricht (1985) stated that these X - rays of energy 5.9 KeV produce approximately 227 ion pairs in P10 gas.

As caesium is a relatively reactive metal, it was imperative that the chamber was kept as clean as possible. Before the caesium ampoule was introduced into the counter, a rigorous process of ultrasonic cleaning and baking was carried out to ensure the lowest possible background ionisation level. A vacuum system containing a diffusion pump backed by a rotary pump was constructed for evacuation and baking of the chamber.

The proportional counter was ideally suited for analysis of caesium vapour as there exists only one stable isotope of caesium. The experimental work on rubidium metal, however, required mass separation to distinguish between the two stable isotopes of rubidium, ie. ^{85}Rb and ^{87}Rb . This was achieved by use of a quadrupole mass spectrometer.

2.11 Quadrupole Mass Spectrometer

The spectrometer contains two main parts - the quadrupole filter and the detector. Diagrams showing the basic principles of operation are shown in Figures 2.17 and 2.18. The quadrupole mass filter consists of equally spaced cylindrical metal rods positioned at the four corners of a square, which act as a mass filter tuned to a specific molecular weight. Application of a Radio Frequency (R.F.) voltage focusses all the ions on the axis of the filter towards the detector.

A proportion of D.C. voltage can be superimposed onto the RF field to introduce a selective acceptance condition. If a particular RF/DC voltage is applied, only the ions with a specific mass/charge ratio remain in stable oscillation along the axis of the filter to the detector. All other ions suffer oscillations of increasing amplitude until they hit the

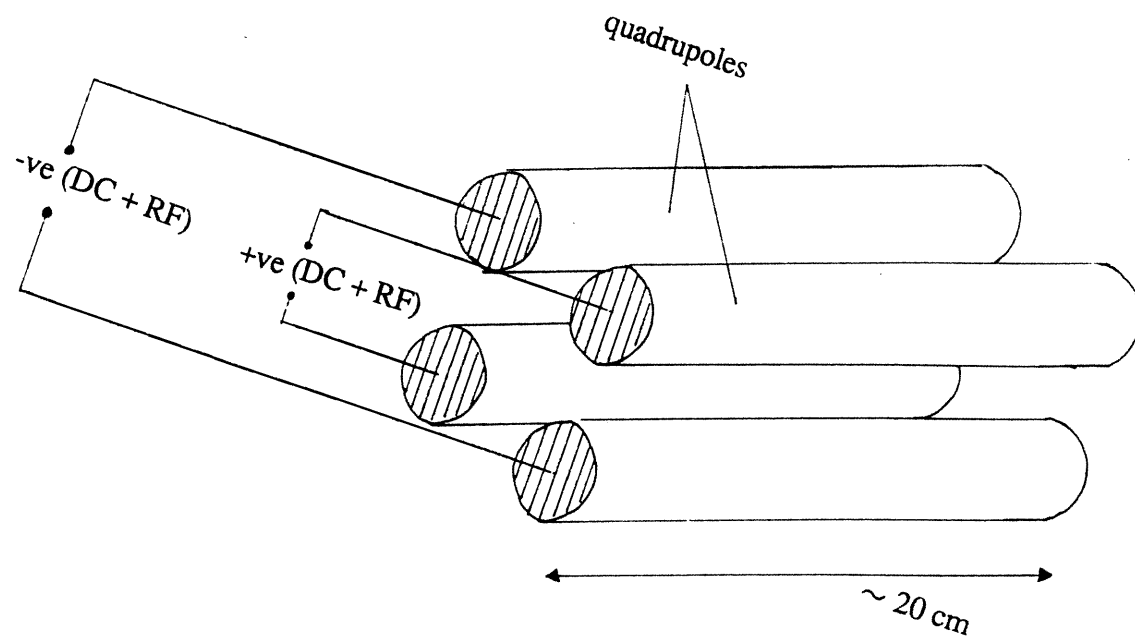


Figure 2.17 RF and DC fields for mass selection in a quadrupole

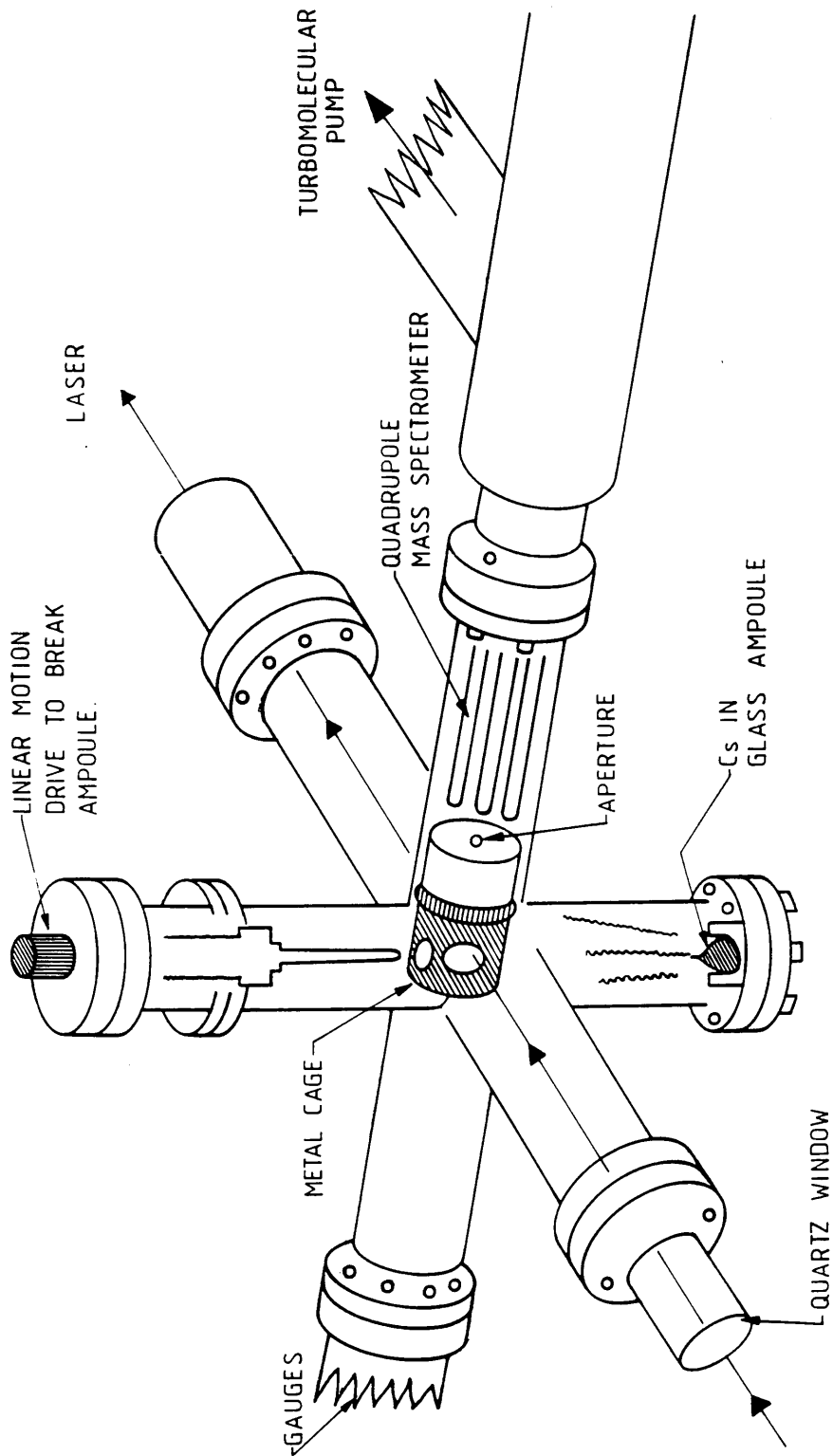


Figure 2.18 Schematic diagram of the quadrupole mass spectrometer

quadrupole rods where they discharge. A single mass/charge value can be chosen by variation of the DC signal. An important feature of the mass filter is its lack of dependence of the filtering action on the axial energy. A quadrupole mass spectrometer has a typical mass resolution of around 1000.

The quadrupole used in this research was a VSW Mass Analyst. It was necessary to adapt this in order to detect as many laser induced ions from the ionisation region as possible. The required modifications are shown in Figure 2.19. A stainless steel extension section of length 25mm was added to the ion cage to ensure that the ions were created in the centre of the ion cage. This cage was set at a slightly positive voltage to encourage the ions to pass into the quadrupole filter. Collimating discs were mounted on the ends of the extension piece to improve the resolution.

The detection system makes use of either a Faraday detector or a secondary electron multiplier (SEM). The Faraday detector is basically a flat metal plate onto which the ions collide. This is connected to a sensitive amplifier since the signals produced here are relatively small. The SEM is a Galileo 4771 channeltron with high gain (10^3 - 10^6) and is mounted off axis to reduce background signals from neutral particles. A negative voltage of 3000V is applied to the SEM. The SEM was used for most of the experimental work in preference to the Faraday plate.

The coating on the inside of the channeltron promotes secondary electron avalanches, and this electron current is then amplified before entering the data acquisition system. The quadrupole has a mass range of 0 - 200 amu and a typical resolution of 1000. It also has a mass scanning facility which is achieved by automatic DC voltage variation.

The pressure in the quadrupole mass spectrometer was kept below 10^{-5} torr by a

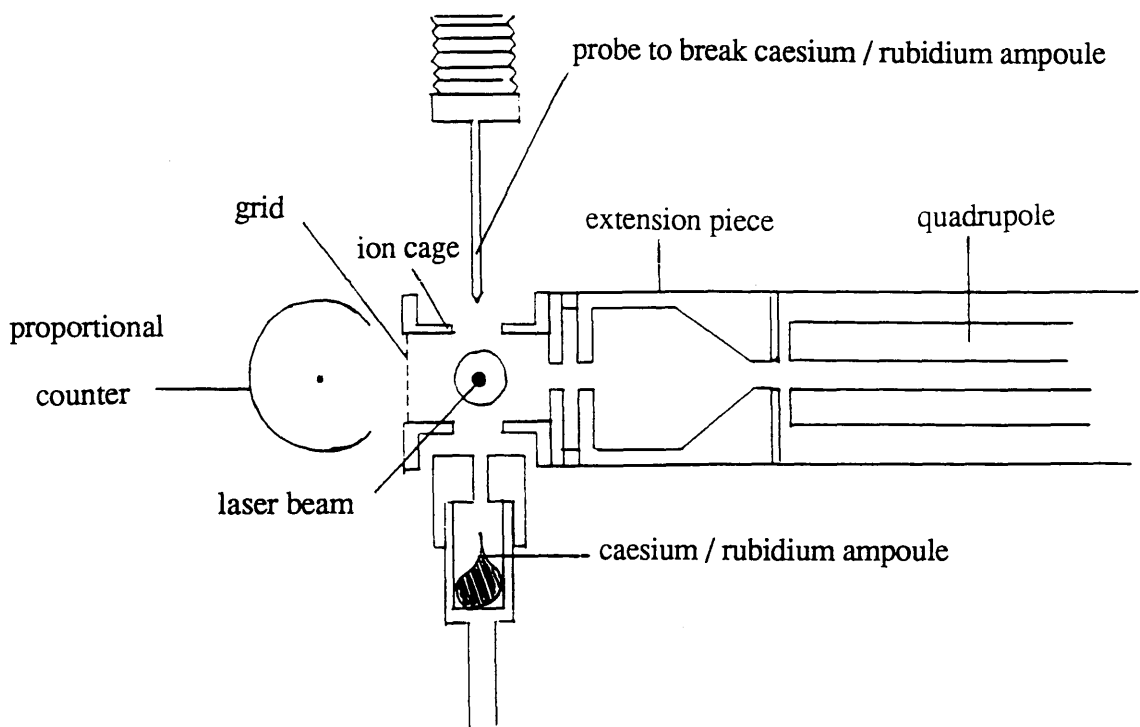


Figure 2.19 Modification of quadrupole mass spectrometer for resonant ionisation and operation with proportional counter.

turbomolecular pump backed by a rotary pump. It is often necessary to heat up the rubidium sample in order to increase the number of neutral atoms entering the ionisation region. Careful monitoring of the temperature and pressure is essential as a pressure of greater than 5×10^{-5} torr could result in damage to the quadrupole.

One major drawback of the quadrupole is its limited detection efficiency. The collection efficiency of ions into the quadrupole may be very low, as most of the ions created will drift towards the quadrupole at fairly large angles and will not be transmitted. An increase in the extraction voltage on the ion cage would increase the collection efficiency but would also bring undesirable Stark shift effects into play. The transmission efficiency through the quadrupole is at best 15%. A detection efficiency of around 50% is expected from the channeltron. The combination of these efficiencies is a total efficiency of around 7.5%. The performance of the quadrupole is usually a compromise between sensitivity and resolution, with the transmission efficiency improving if the resolution is lowered.

The quadrupole mass spectrometer has the severe limitation that only one mass can be recorded for each pulse of the laser. An entire mass spectrum (0-200 amu) can only be recorded by using a large number of laser shots. In this case, comparison of isotopic ratios is extremely difficult due to pulse to pulse fluctuations in the laser power output. It would be of great advantage to be able to accumulate data from the entire mass range for each laser pulse. The solution to this problem lies in the use of a Time of Flight mass spectrometer.

2.12 Time of Flight Mass Spectrometer

This relatively simple device utilises the different velocities of ions with different mass/charge ratios. The mass spectrometer consists of three parts - an ionising region, a

drift tube and an ion detector. The ionisation region contains a series of electrodes at voltages of a few kilovolts which accelerate the ions produced by the laser into the drift tube. This is essentially a field free region of around one metre in length where the ions travel at different velocities according to their mass/charge ratios. Thus the lighter ions arrive at the detector before the heavier ones, resulting in a time of flight spectrum usually in the μ second range with each mass temporally separated according to its flight time.

Two laser time of flight mass spectrometers have been constructed at Glasgow. The first was designed in Glasgow and constructed by Kratos Analytical / Cambridge Mass Spectrometry with ultra trace element analysis in mind, although it could be easily adapted to suit other applications such as depth profiling. Figure 2.20 shows a schematic diagram of the Glasgow RIMS instrument. The sample chamber exhibits spherical geometry with nine ports facing into the central ionisation region. Each port can be adapted for a specific function, eg. ion gun housing or laser ports. UHV conditions ($< 10^{-8}$ torr) are maintained by a combination of diffusion, sublimation and turbo molecular pumps. The turbo molecular pump is situated near the far end of the drift tube and has a pump rate of 200 l/s. The residual pressure in the spherical chamber is maintained at 10^{-9} torr by a cold trapped diffusion pump and a titanium sublimation pump with a combined pumping speed of more than 88 l/s.

The solid sample can be vaporised either by ion gun ablation or by laser desorption. The neutral atoms produced are then irradiated by selectively tuned dye lasers to ionise a particular element. A reflectron time of flight system provides mass separation with energy focussing. Laser induced ions are accelerated into the field free region by a bias voltage of between 2000V and 3000V on the sample stub. Ion focussing optics close to the sample stub ensure a high transmission of ions down the drift tube. Small adjustments in the ion trajectories may be made by varying the voltages on the x-y deflection plates. The reflectron system is employed to provide energy focussing. The

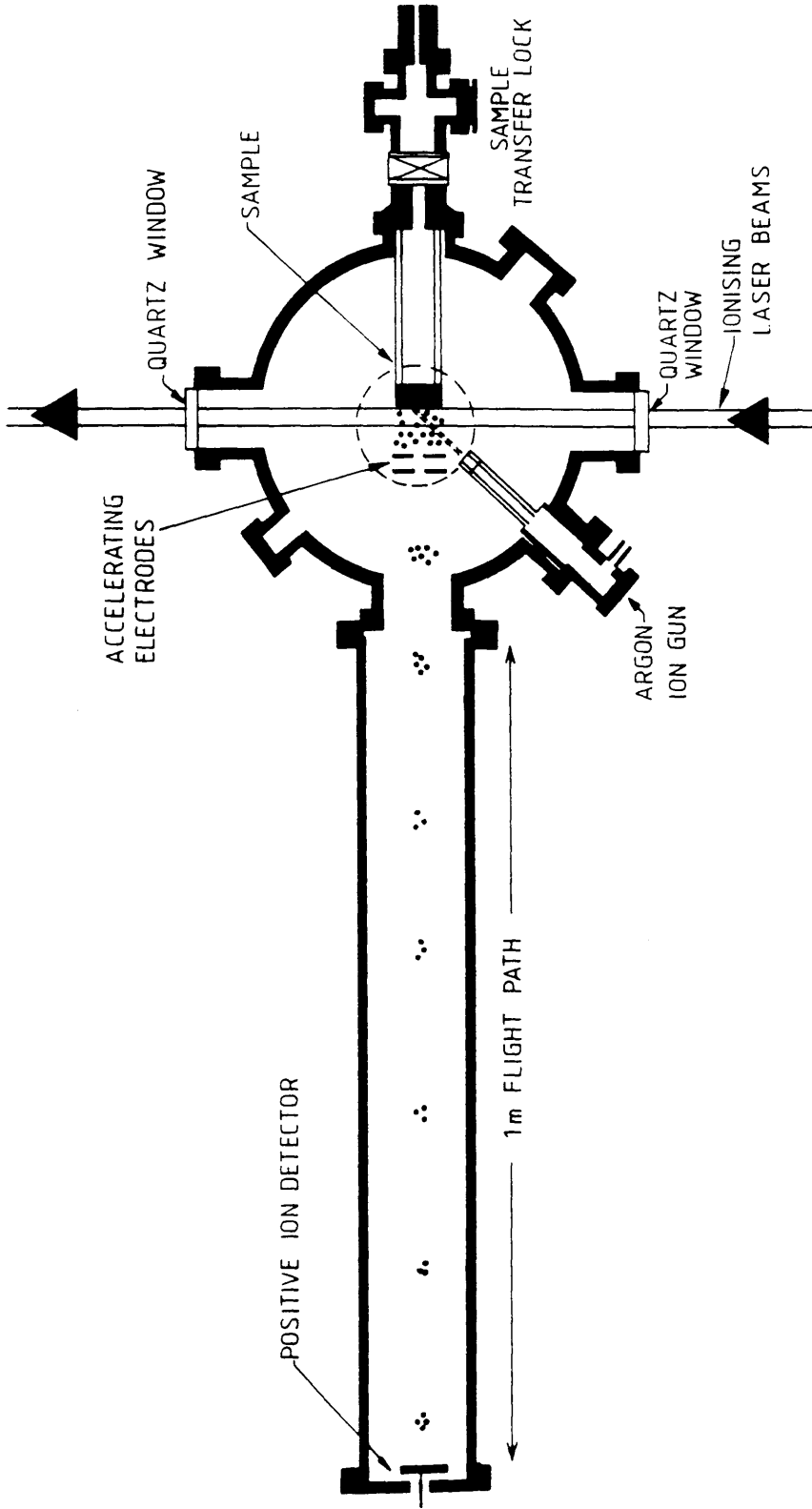


Figure 2.20 Schematic diagram of the RIMS instrument

resolution of a TOF mass spectrometer will be discussed in detail in Chapter 5.

2.13 The Reflectron

A reflectron is basically an electrostatic ion reflector consisting of a series of closely spaced stainless steel discs connected by a resistor chain. A basic diagram of the reflectron is shown in Figure 2.21. For ions with the same mass/charge ratio, those with a higher energy penetrate deeper into the ion reflector than do lower energy ions. As a consequence, the faster more energetic ions have a longer flight time through the reflector than do the slower less energetic ones. This effect compensates for the opposite behaviour along the linear flight path.

The voltages on the reflectron can be optimised so that the fast and slow ions reach the detector together. This gain in resolution, however, is at the expense of sensitivity. Typically, only about 10% of the ions entering the reflectron reach the electron multiplier.

The reflectron can also be used to remove the background signal from secondary ions (SIMS). The secondary ions have a higher energy than the laser induced ions due to their production closer to the accelerating voltage on the sample stub. If the reflectron voltage is less than the accelerating voltage, the secondary ions will be unaffected and will pass through the reflectron and be undetected.

The reflectron is a method of energy focussing and compensates for the initial spread in the kinetic energy of the laser induced ions. It cannot, however, improve the space resolution resulting from ions created in different positions in the ionisation region. This is a consequence of the finite width of the laser beam. Those ions created closer to the accelerating voltage on the sample stub will receive more energy than those further

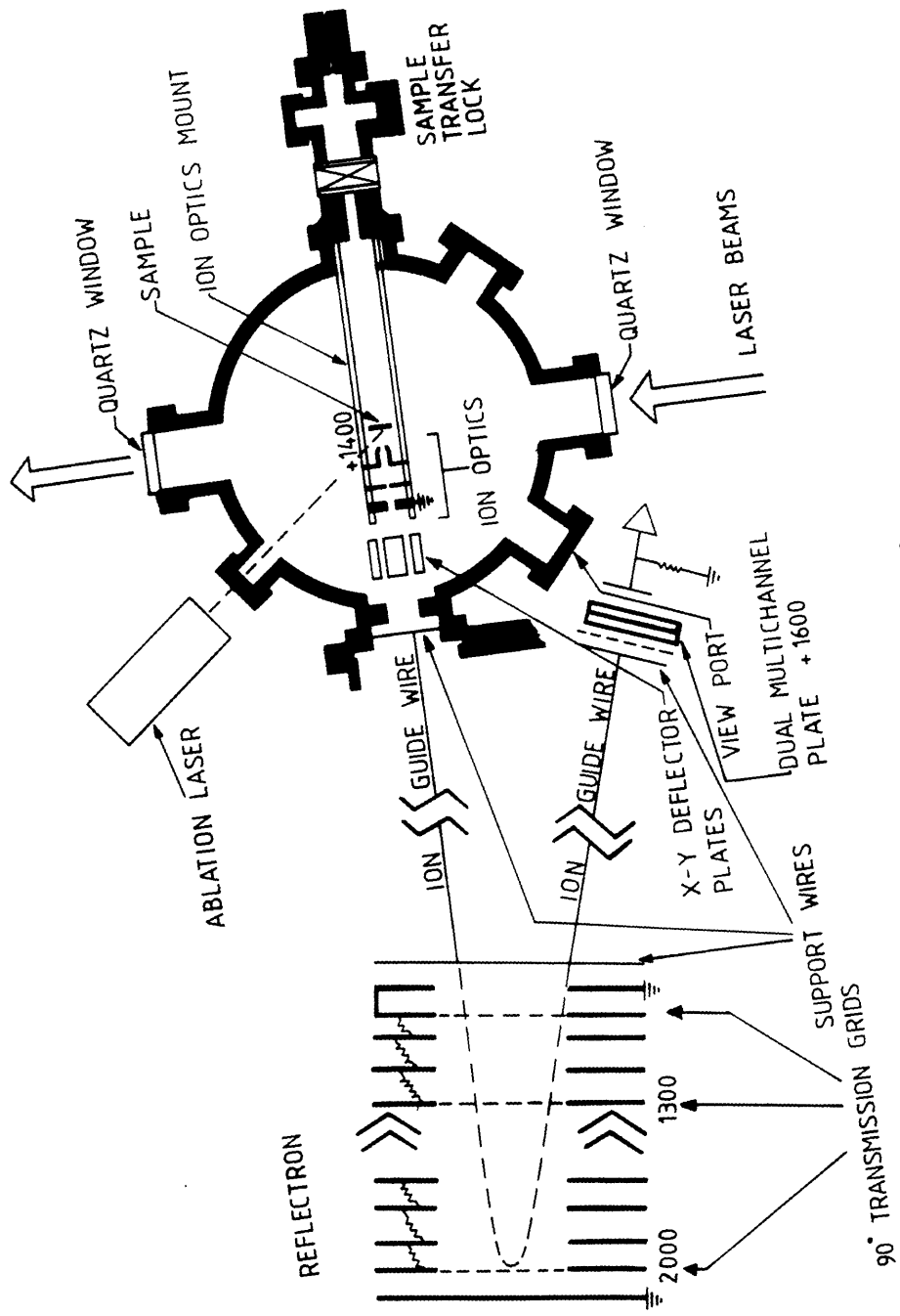


Figure 2.21 The reflectron

away from the stub. It is therefore advantageous to keep the finite width of the laser beam as small as possible. The time spread also results from the initial velocity distribution of the laser induced ions. Those ions travelling towards the sample stub must be stopped, turned around, and accelerated towards the drift tube. An increase in the voltage of the extraction region would reduce this effect considerably. The space resolution can be optimised by careful choice of extraction voltage (see Wiley and McLaren). Diagrams of the ion optics showing typical voltages are given in Figures 2.22 and 2.23.

If all the ions were formed in a plane parallel to the source electrode and with zero initial velocity, the flight time would be the same for all the ions with the same mass/charge ratio and the resolution would be limited only by the detecting equipment. Space resolution and energy resolution place opposite requirements on several system parameters. The best overall resolution, therefore, is a compromise between the two different resolution factors. More details of resolution of time of flight mass spectrometers are given in Chapter 5.

The Glasgow RIMS machine makes use of a thin stainless steel wire to provide an electrostatic particle guide for charged particles. This helps to increase the transmission efficiency of the Time of Flight mass spectrometer. A DC voltage of around 10V is kept on the wire and encourages the ions to follow a spiral course towards the detector.

The detector used in the Glasgow RIMS system is a Kratos double Micro Channel Plate (MCP) detector of the Galileo Chevron type (see Figure 2.24). A micro channel plate consists of an array of $10^4 - 10^7$ electron multipliers each approximately 10 - 100 μm wide and orientated parallel to each other. Two plates with a 150 μm separation were used to increase the effective gain. Micro channel plates have a distinct

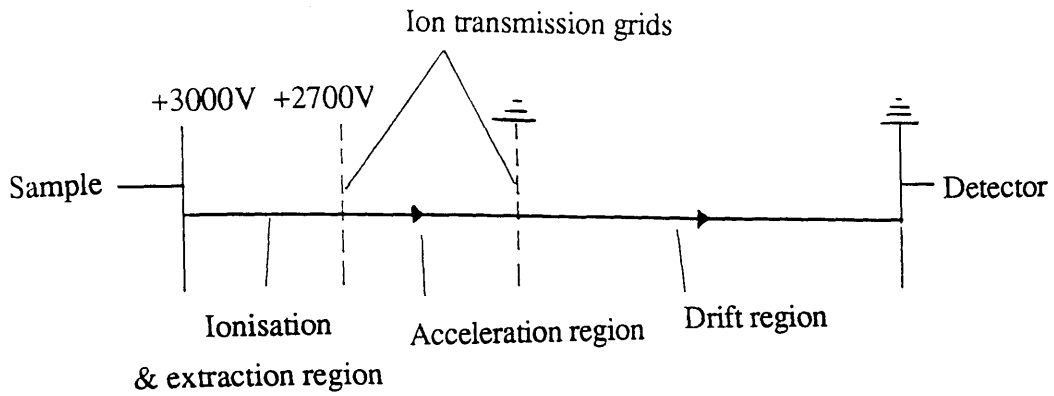


Figure 2.22 Operation of the time of flight mass spectrometer

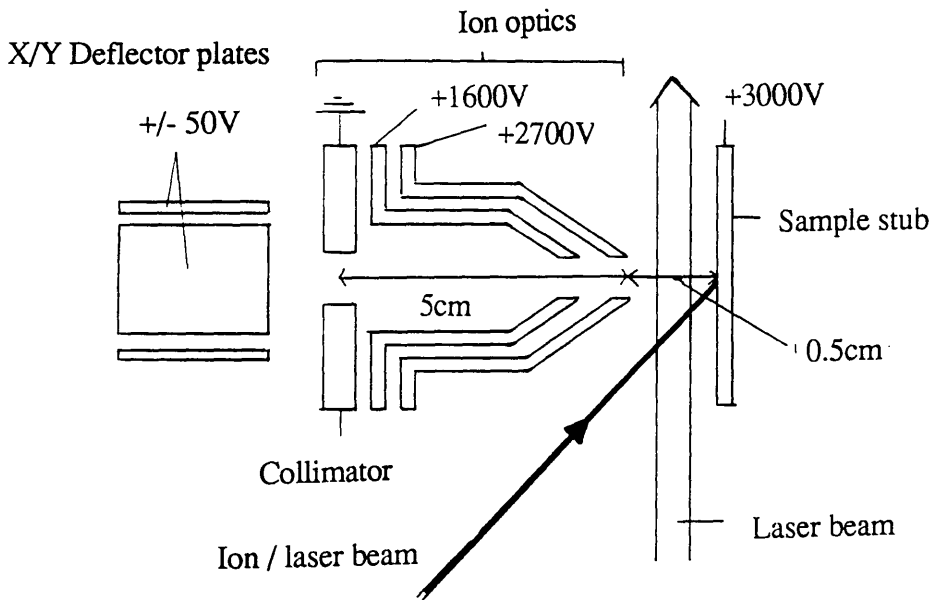


Figure 2.23 Existing ion optics used in the time of flight mass spectrometer

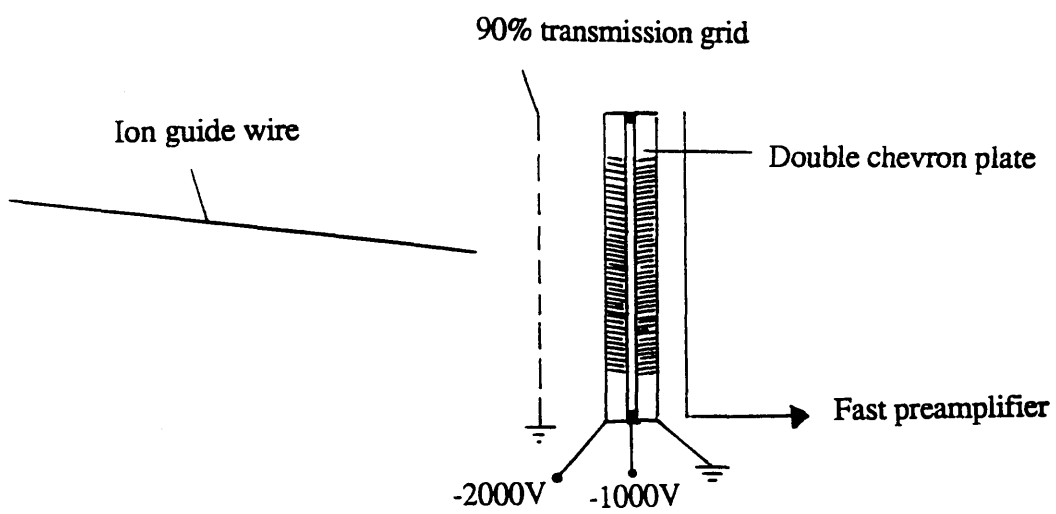


Figure 2.24 Micro channel plate (MCP) detector

advantage over electron multipliers because of their fast response time. It is important to maximise the speed of response of the detector as this can have a significant effect on the resolution of the system.

The sample stub is attached to an xyz θ manipulator to allow three dimensional variation of sample orientation. Rapid sample exchange without disruption of the main chamber pressure is carried out using a fast insert probe. Samples can be exchanged by this method in around five minutes.

2.14 LSI 11 Data Acquisition System

A systematic diagram of the data acquisition system and associated electronics used for the study of laser spectroscopy of caesium and rubidium vapours is shown in Figure 2.25. Ionisation signals from the proportional counter or quadrupole mass spectrometer and corresponding laser power signals from the joulemeter were separately amplified and fed into peak sensing ADCs (Analogue to Digital Convertors). It was usually necessary to delay one or both signals in order to ensure that the pulse peaks were coincident with the gate generated signal (ORTEC 427 delay amplifier).

The timing signals used for the data acquisition are shown in Figure 2.26. The ADCs had 7 input channels with an 11 bit resolution over a two volt dynamic range. A timing reference signal for gating the ADC was provided by directing a fraction of the laser pulse down a fibre optic cable onto a photodiode.

The gate generation follows a number of stages. Firstly, the LSI 11 computer signifies readiness to accept data by switching on the gate generator with a NIM pulse from the output register. The gate generated signal together with the photodiode signal are fed into a coincidence unit which generates a NIM pulse if both signal are present.

This pulse is then used to stop the gate generator and also to produce the gate pulse. The delay on this gate pulse can be varied to ensure coincidence with the ionisation and joulemeter peaks. A gate generator increases the width of the gate from 10ns to 600ns - the operating width of the ADC. This triggering system ensures that the signals entering the ADC were only recorded on floppy disc when the laser was fired.

Ionisation and joulemeter signals were stored event by event on floppy disc and were displayed on line on a Tektronix 611 display unit. Five different output graphs were displayed simultaneously on the screen; ionisation and joulemeter signals versus time and versus channel number and also a plot of ionisation versus joulemeter signal. It was also possible to normalise the data linearly or quadratically to a constant laser fluence. The joulemeter display graph was useful for monitoring the steadiness of the laser power which could be altered if necessary using a variable attenuator. The ionisation versus time graph allowed observation of peaks as they occurred in real time.

The dependence of ionisation on laser power could be determined at particular wavelengths from log / log plots of ionisation versus joulemeter with joulemeter values being fixed between 0 - 2 Volts using the variable attenuator. The data stored on floppy disc can be transferred to an IBM mainframe computer where the experimental data can be analysed, and resultant graphs can be plotted.

2.15 Data Acquisition for the Laser Time of Flight Mass Spectrometer

The existing data acquisition system records and stores time of flight mass spectra on a pulse to pulse basis (see Figure 2.27). The system hardware consists of an IBM - AT computer, equipped with a GPIB card, an EGA graphics card, extended memory and colour graph plotting facilities. A Stanford digital delay generator and a Le Croy GPIB to CAMAC interface are connected to the GPIB port. A Le Croy CAMAC

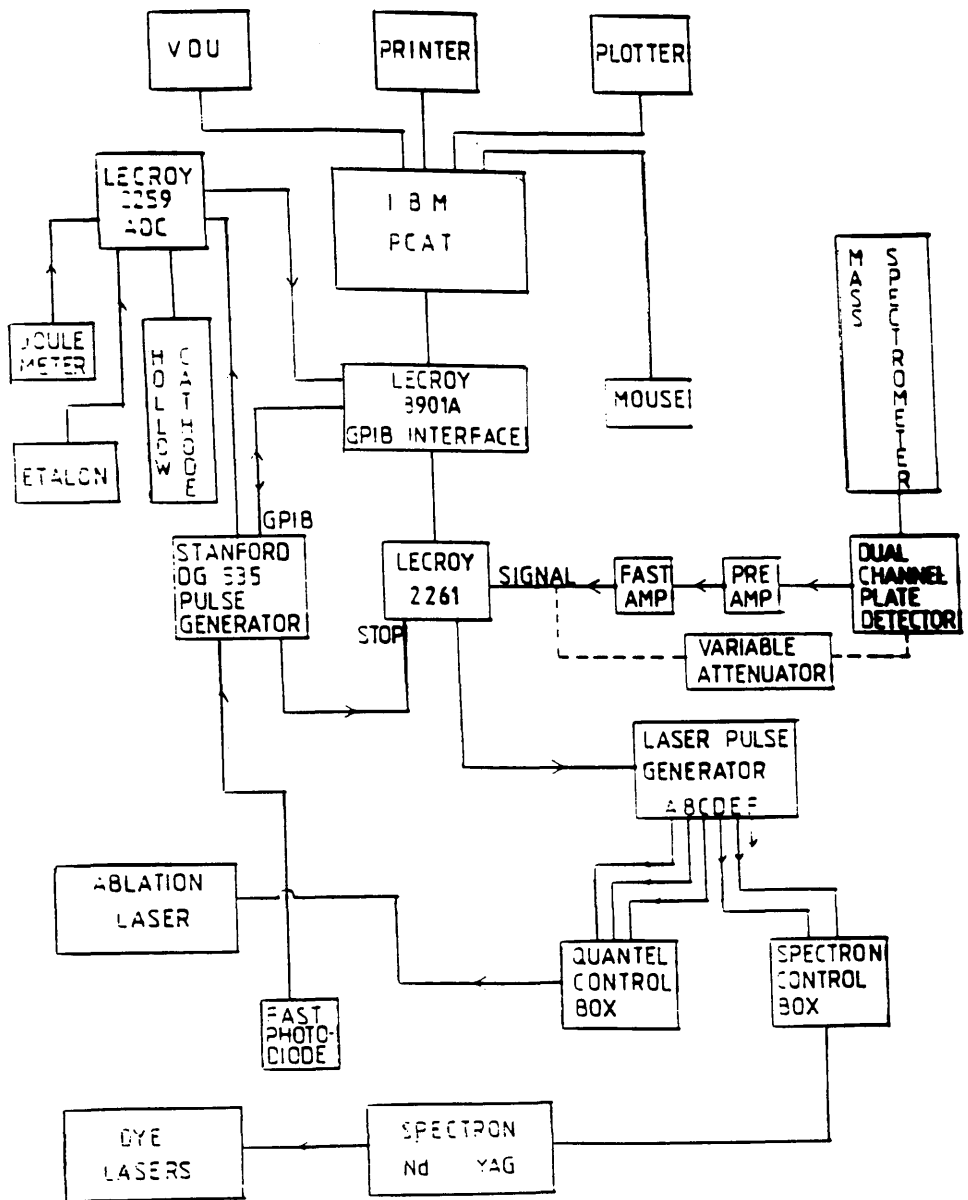


Figure 2.27 Data acquisition system for the time of flight mass spectrometer

crate houses this interface, a 12 channel ADC and a 2261 transient data recorder. Ion signals from the microchannel plate recorder are fed into the transient recorder which provides up to 1040 time channels each of 10ns width. The operating speed is 10 Hz and is controlled by the repetition rate of the laser.

A software program written in IBM Fortran for the IBM-AT reads data from the transient recorder, corrects the readings for background noise, and displays the results on the screen, completing a spectrum every 64 events. A plotting program allows the acquired data to be output to the printer or the plotter.

Chapter 3 RIS OF CAESIUM VAPOUR

3.1 Introduction

This chapter describes the results obtained of the spectroscopy of caesium metal using the resonance ionisation technique in a proportional counter. Caesium was deliberately chosen for initial spectroscopy studies for a number of reasons :-

1) The atomic structure of alkali metals is similar to hydrogen, ie. possessing full electron shells plus one outer electron, and is well understood. Also, all alkali metals have low ionisation potentials (4 - 5 eV) allowing two photon ionisation to be easily achieved using a single dye laser (photon energy of around 4 eV).

2) Caesium metal is liquid at room temperature and has a high vapour pressure (10^{-6} torr) thus allowing a sufficient number of gaseous atoms to be available for laser spectroscopy studies.

3) It was initially proposed to use NBS coal samples with various caesium concentrations as calibrations standards for the Glasgow RIMS instrument. It was therefore important to study various ionisation pathways for caesium metal.

4) Initial work on RIS was carried out by G.S. Hurst in America using caesium metal. There has been a considerable amount of experimental work since then on multiphoton absorption in caesium vapour by a number of authors, in particular, Hurst et al (1977), Popescu et al (1974) and Christian et al (1984). This work investigated mainly photon transitions to Rydberg levels from the atomic spectroscopy viewpoint.

5) RIMS may be used as a method of monitoring reactor produced isotopes of caesium in the environment. At present, two isotopes of caesium, ^{134}Cs and ^{137}Cs , are routinely monitored by nuclear establishments. Another isotope of caesium, ^{135}Cs , is a low energy beta particle emitter produced by thermal fission of the principal fuel nuclides, but it is subject to no discharge restrictions. It is difficult to detect by conventional

radiometry techniques, but can be detected using existing RIMS technology. Before progressing to isotopically selective caesium detection, or to environmental material, detection at an elementally selective level was required.

An energy level diagram for caesium is shown in Figure 3.1. The main transitions studied were two photon (one photon resonant excitation, one photon ionisation) and three photon (two photon resonant excitation via a virtual state, one photon ionisation) processes. In addition, many ground state to Rydberg level transitions were observed. Table 3.1 gives some physical properties of the element caesium.

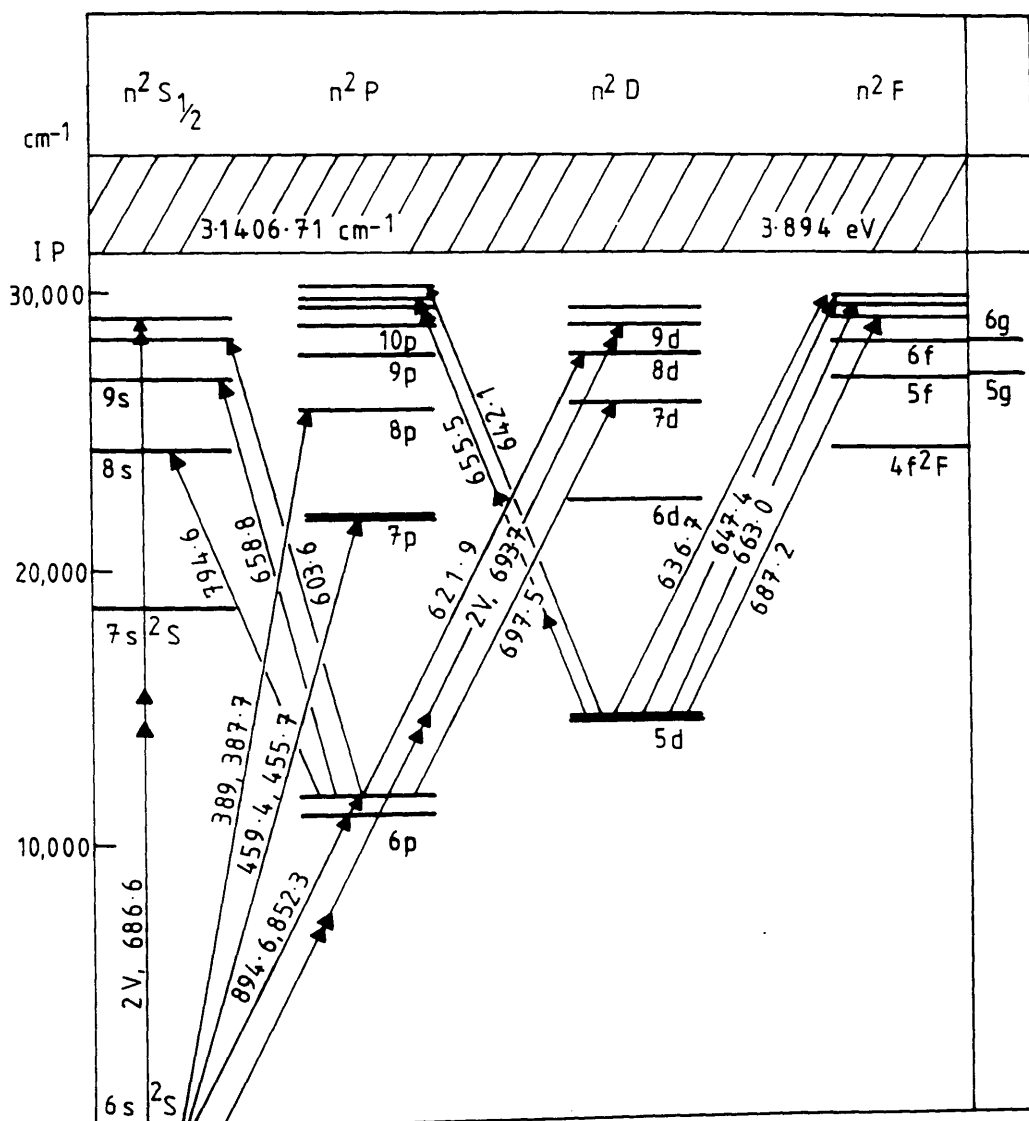
The design of the stainless steel chamber used for the spectroscopy of caesium is described in detail in chapter 2, and a diagram of the chamber is given in Figure 2.16. After extensive cleaning and baking, this chamber produced substantially lower levels of background ionisation than the previous glass counters.

Table 3.1 Properties of Caesium

Ionisation Potential	3.893 eV
Atomic Weight	132.91
Stable Isotopes	^{133}Cs
Vapour Pressure	10^{-6} torr at 300K
Boiling Point	669.3 °C
Melting Point	28.4 °C

An ^{55}Fe source was situated within the chamber as a means of calibration. The counter was normally filled with 70% argon / 30% methane gas to a pressure of around 30 torr. The stainless steel probe mounted on the linear drive mechanism was used to pierce the sealed glass ampoule containing the caesium metal. It was initially thought that the breaking of the ampoule allowed caesium vapour to enter the ionisation region in

Figure 3.1 Energy level diagram for atomic caesium



the proportional counter. It was noticed, however, that the resonant caesium signal disappeared if the probe was fully retracted. It was therefore deduced that the ionisation was occurring in gaseous caesium atoms around the tip of the probe. This is a reasonable assumption as the tip of the probe is covered in caesium liquid as a result of breaking the ampoule. It was necessary to recoat the probe with caesium after about a day by redipping it into the caesium reservoir. The exit laser beam from the chamber could be checked to make sure it passed cleanly through the chamber and avoided hitting the tip of the probe.

3.2 Two Photon Transitions

The main transitions studied were the ground state, $6s_{1/2}$, to the $7p$, $8p$ and $9p$ levels in order to investigate saturation and power broadening effects on the transitions. In each case, the transition doublet peak is shown at various laser power intensities along with the corresponding power dependence graphs. Conclusions about saturation effects can be drawn directly from the graphs.

From the saturation conditions described in Chapter 2, the ratio of the peak intensities of a doublet is given by

$$\frac{I(1)}{I(2)} = \frac{\sigma_1 \sigma_{I(1)}}{\sigma_2 \sigma_{I(2)}}$$

Thus, for the caesium ground state to $7p$ transition, the ratio of peak intensities is

$$\frac{I_{455.5 \text{ nm}}}{I_{459.3 \text{ nm}}} = \frac{\sigma_{(6s_{1/2} - 7p_{3/2})} \sigma_{(7p_{3/2} - \text{continuum})}}{\sigma_{(6s_{1/2} - 7p_{1/2})} \sigma_{(7p_{1/2} - \text{continuum})}}$$

Figures 3.2, 3.3, and 3.4 show the doublet transition $6s$ to $7p$ at laser power

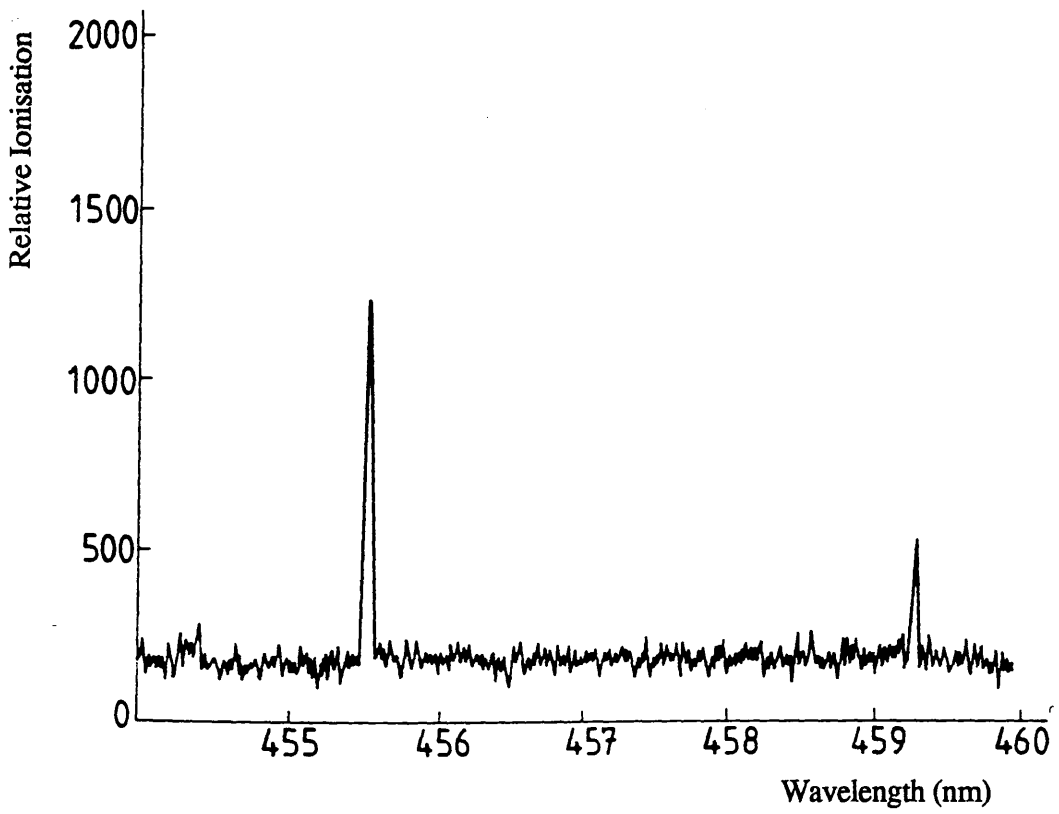


Figure 3.2 6s - 7p doublet transition ($0.8 \mu\text{J}/\text{mm}^2$)

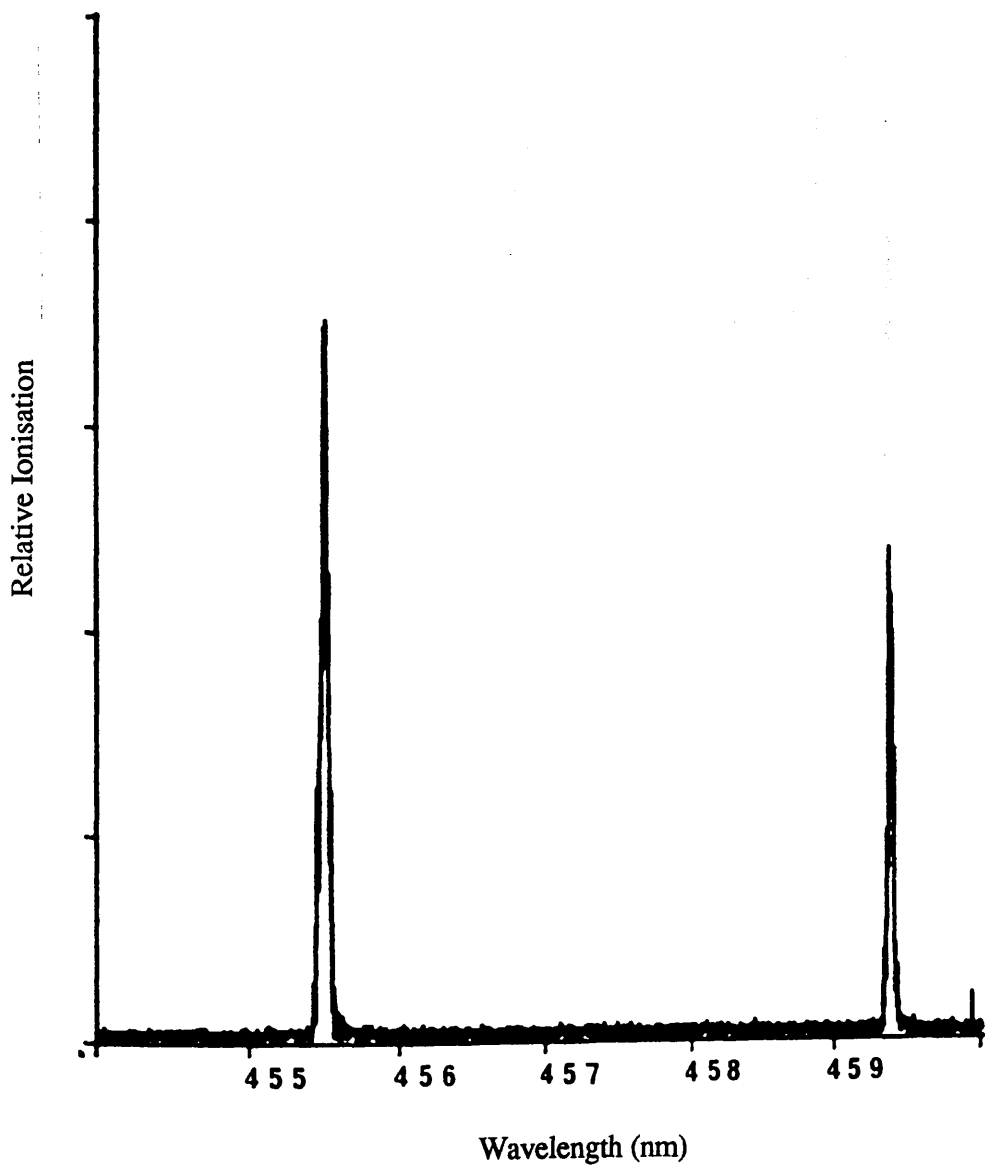


Figure 3.3 6s - 7p doublet transition ($8 \mu\text{J}/\text{mm}^2$)

Relative Ionisation

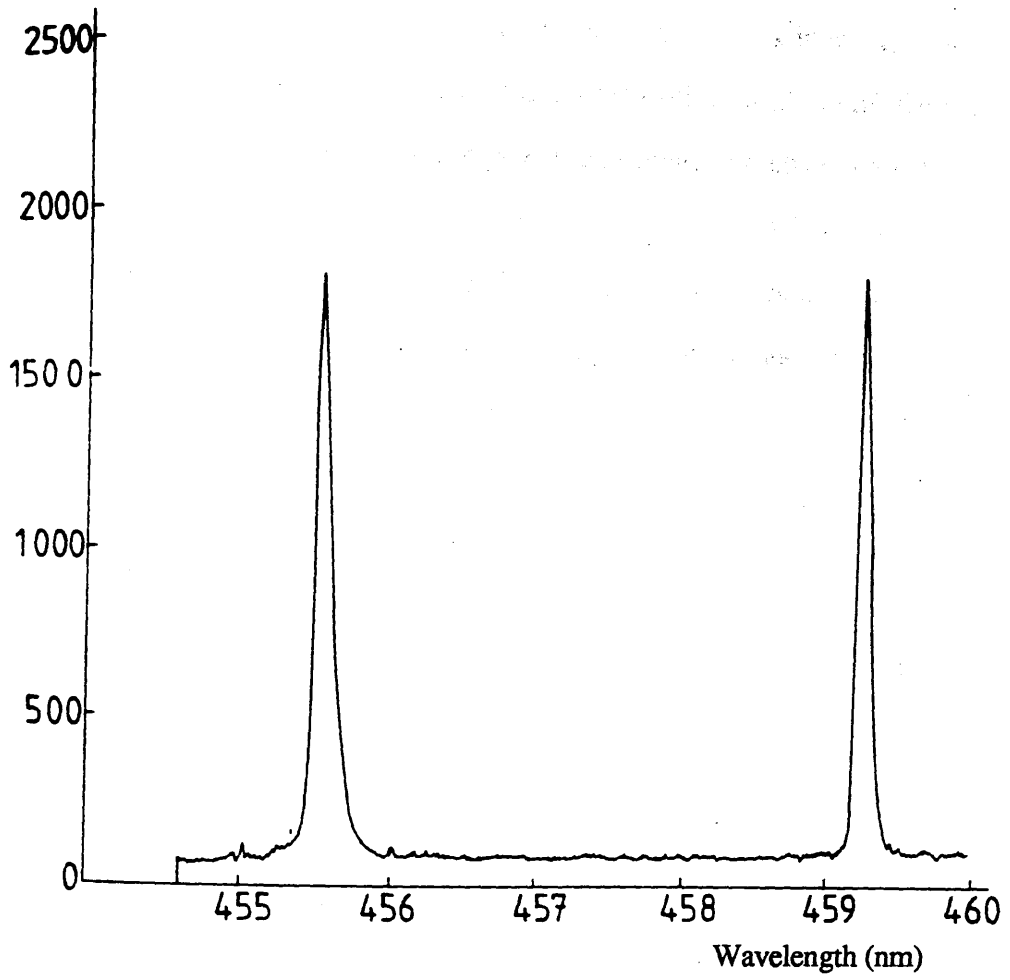


Figure 3.4 6s - 7p doublet transition (1.18 mJ/mm²)

levels $0.8 \mu\text{J} / \text{mm}^2$, $8 \mu\text{J} / \text{mm}^2$ and $1.18 \text{mJ} / \text{mm}^2$ respectively. The first photon resonantly excites the 6s electron to a $p_{1/2}$ or $p_{3/2}$ level, and the second photon from the same laser pulse ionises this electron into the continuum with subsequent detection of the electron in the proportional counter. Scans were taken between wavelengths 454nm and 460nm using Coumarin 47 laser dye. It was seen that the peak intensity ratio decreases with increasing laser fluence. At the highest power level, $1.18\text{mJ} / \text{mm}^2$, the peaks are of similar intensity. The corresponding power dependence graphs demonstrate the near approach to saturation. A background power dependence graph (see Figure 3.5) shows a linear dependence of ionisation on laser fluence. At low laser fluence, the dependence of ionisation on fluence is almost quadratic, indicating an unsaturated two photon process (see Chapter 2). Medium power ($8\text{mJ} / \text{mm}^2$) gives a linear dependence of ionisation on fluence. The highest power level shows the ionisation approaching independence on fluence. Total saturation, however, was not achieved, owing possibly to the interference of the background ionisation or to the wings of the laser beam profile. Increasing laser fluence also has a significant broadening effect on the peaks. Using an ^{55}Fe X - ray calibration source, the saturated caesium signal was calculated to correspond to detection of around 6×10^4 caesium atoms within the laser volume.

Figure 3.6 gives evidence of the power broadening effect on the 455.5nm peak at three fluences, $8\text{mJ} / \text{mm}^2$, $32\text{mJ} / \text{mm}^2$ and $400\text{mJ} / \text{mm}^2$. The observed widths were 0.05nm, 0.1nm and 0.13nm respectively. A noticeable shoulder is seen on the blue wing of the 455.5nm peak. A possible explanation for this is the distortion of the caesium 7p levels by collisions with argon atoms in the gas (Nayfeh et al 1978).

Similar graphs were obtained for the ground state to 8p and 9p levels. In both cases, as the laser fluence was increased, the two photon resonance ionisation approached saturation. The possible laser power available prevented the achievement of saturation. Again, power dependence graphs showed an initial quadratic dependence at low power,

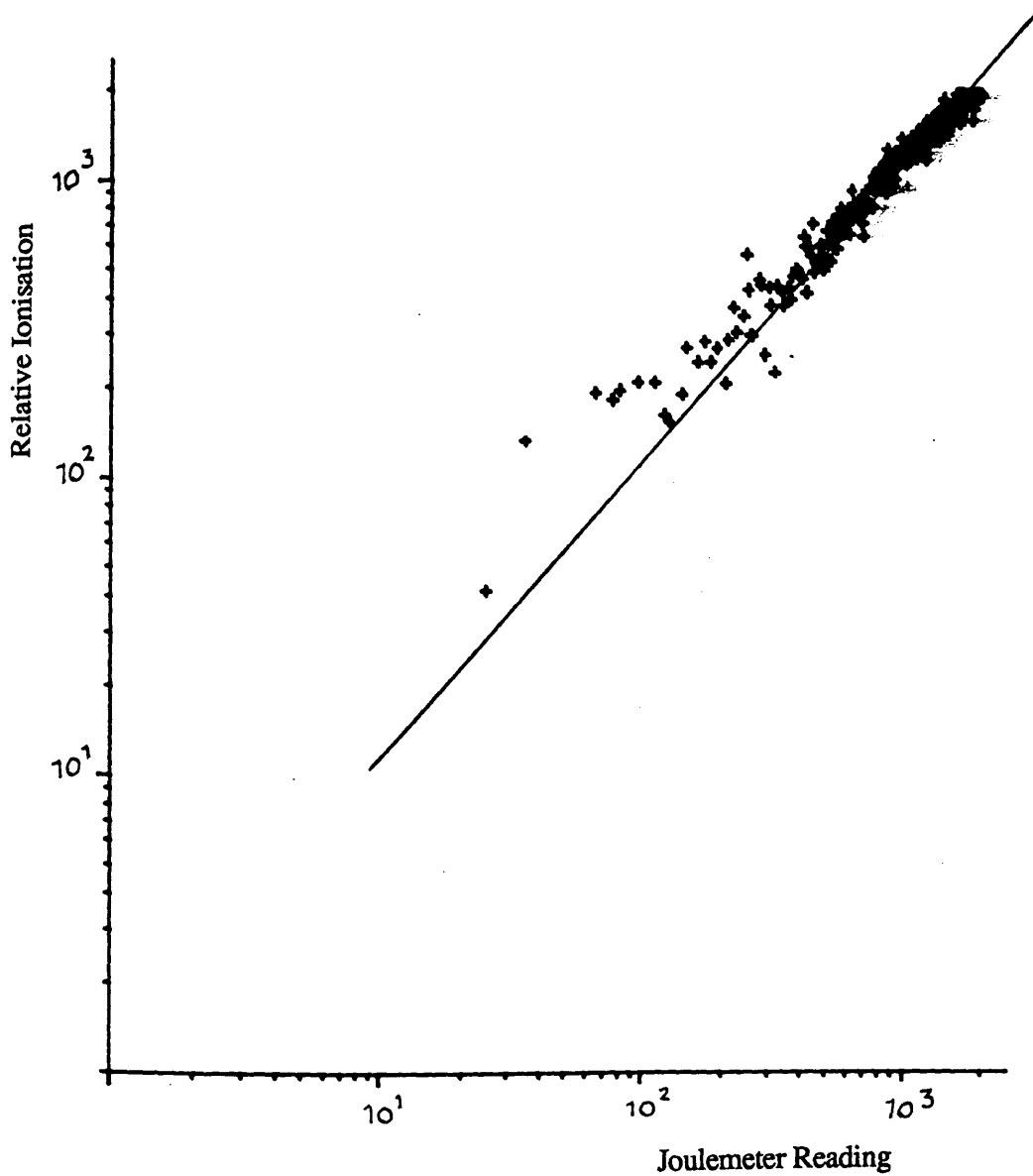


Figure 3.5 Power dependence graph of background at 454.0 nm

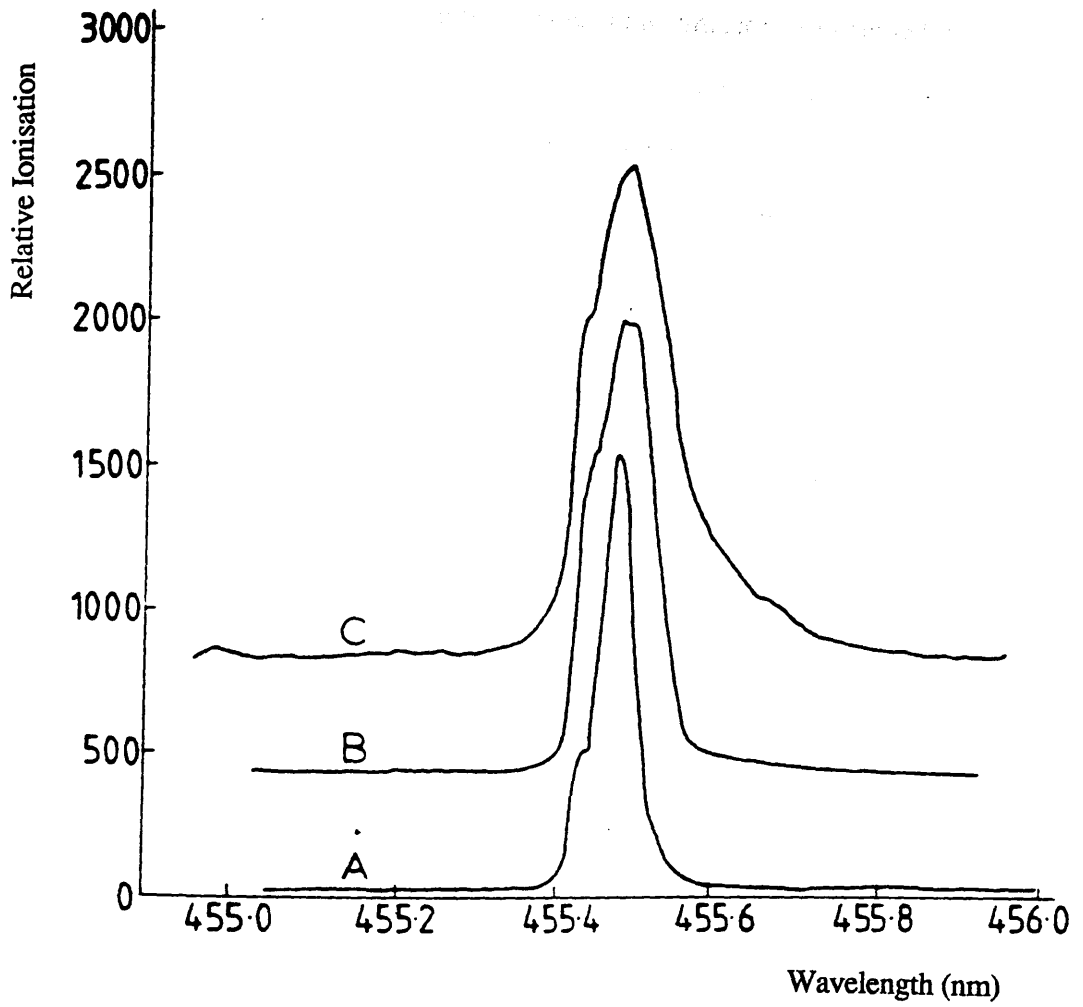


Figure 3.6 Power broadening

becoming linear at medium power levels, and at high power being sub - linear and approaching saturation. The ionisation never quite becomes independent of fluence because of the small component of scattered photon induced ionisation which is always linearly dependent on laser fluence. This is thought to arise from photoelectrons released from caesium deposited on the windows and walls of the ionisation chamber.

It was found that as the principal quantum number was increased, higher laser power was required to saturate the transitions. This implies that the single photon absorption cross section is smaller for higher p levels in the atom. This is in agreement with the published transition probabilities of Table 3.2 (Wiese and Martin 1980), absorption cross sections being directly proportional to transition probability.

Table 3.2 Some 6s - np Transition Probabilities.

<u>Transition</u>	<u>Probability (s⁻¹)</u>
6s - 7p	1.8 x 10 ⁶
6s - 8p	0.38 x 10 ⁶
6s - 9p	0.15 x 10 ⁶

The minimum number of caesium atoms detectable within the focussed laser volume at saturation was 7200 and this represents a detection limit of 0.04ppb. This limit could be improved by reduction of the background signal and by reduction of the laser linewidth. The linewidth used in these experiments was 0.05nm compared with the collision and Doppler broadened caesium transition linewidth of 0.0005nm. Therefore, most of the photons contributing to the fluence were not resonant with the caesium transition.

3.3 6s - Rydberg Transitions

Rydberg levels are high energy orbitals close to the continuum (within $1/40$ of an electron volt) exhibiting long lifetimes and large cross sections. The cross sections of Rydberg levels for excitation and ionisation decrease rapidly with increasing principal quantum number; the excitation cross section is proportional to $1/n^3$, and the ionisation cross section to $1/n^5$. The two photon ionisation cross section for resonant transitions to Rydberg states is therefore proportional to $1/n^8$. Rydberg states have large diameters and long lifetimes, and are therefore susceptible to collisional ionisation.

The single photon absorption edge in caesium lies at 318.4nm (Moore 1952) and the Rydberg transitions can be seen at slightly longer wavelengths. DCM dye was used in the dye laser and was frequency doubled into the ultra-violet. Figures 3.7 and 3.9 show Rydberg levels 6s - np up to around $n = 40$ for two different laser power levels. In Figure 3.7, the laser power was $1\text{mJ}/\text{mm}^2$ which is equivalent to 2.7×10^{27} photons/ cm^2/s . The increase in the density of transitions as the wavelength is decreased is indicative of the decrease in separation of the Rydberg atomic levels as the ionisation limit is approached. The ionisation mechanism occurring in the first step is photon excitation to the high lying Rydberg levels. The ionisation stage is likely to be dominated by the effect of collisions. The collisional ionisation in the second stage is brought about by collisions of Rydberg atoms with the argon atoms in the counter gas. This collisional ionisation is a highly probable effect due to the large dimensions of these atoms. Thus the contribution to the signal resulting from photoionisation will be very small. In order that a Rydberg atom may be ionised, it is necessary for a collision with an argon atom to transfer sufficient energy to the Rydberg atom to raise it above the energy level of the continuum. Hence, as the n value of the atom increases, the amount of collisional energy for ionisation is reduced, and a larger fraction of the collisions will lead to ionisation. The collisional ionisation cannot increase indefinitely, as a stage will

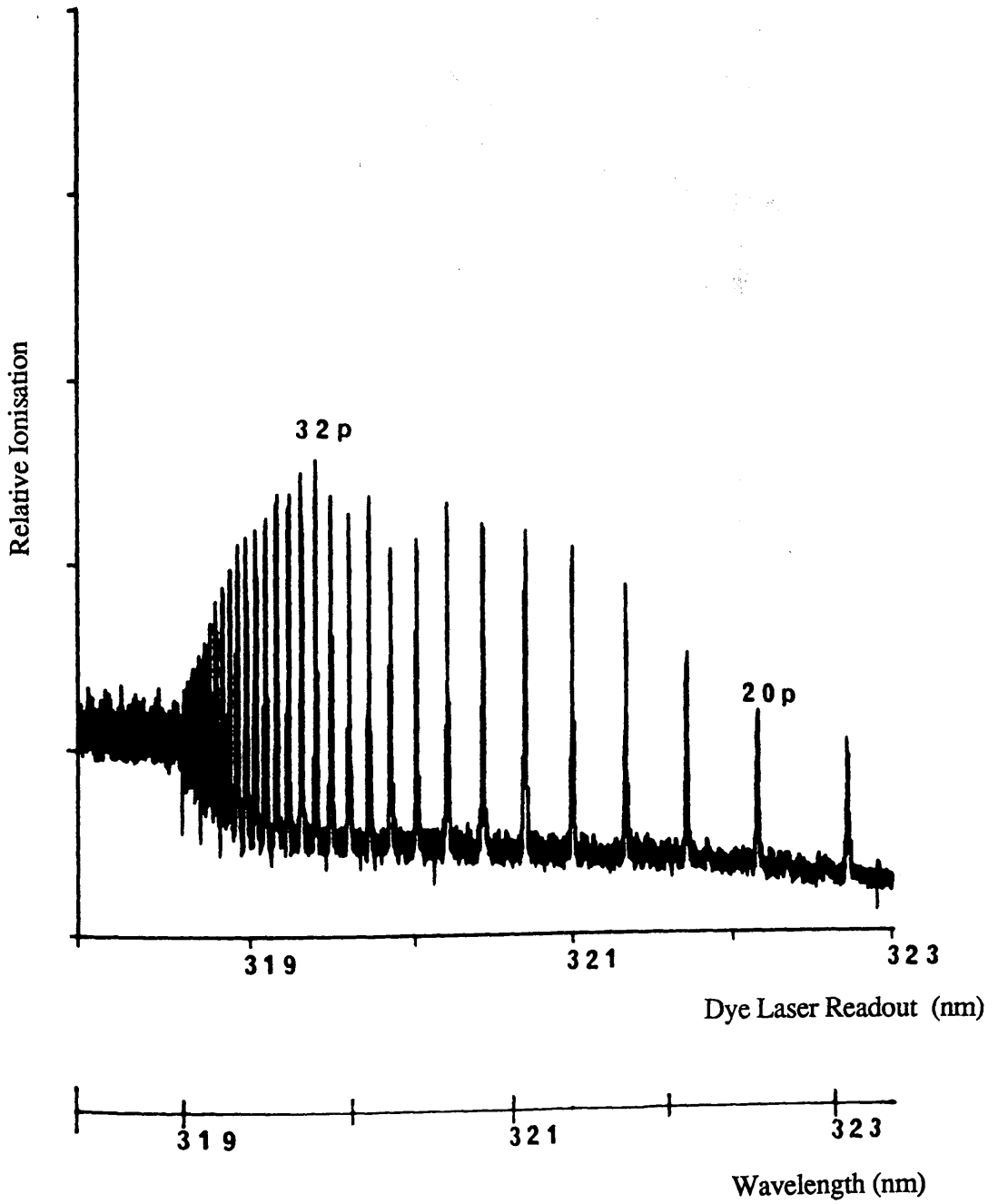


Figure 3.7 6s - np Rydberg transitions ($1\text{mJ}/\text{mm}^2$)

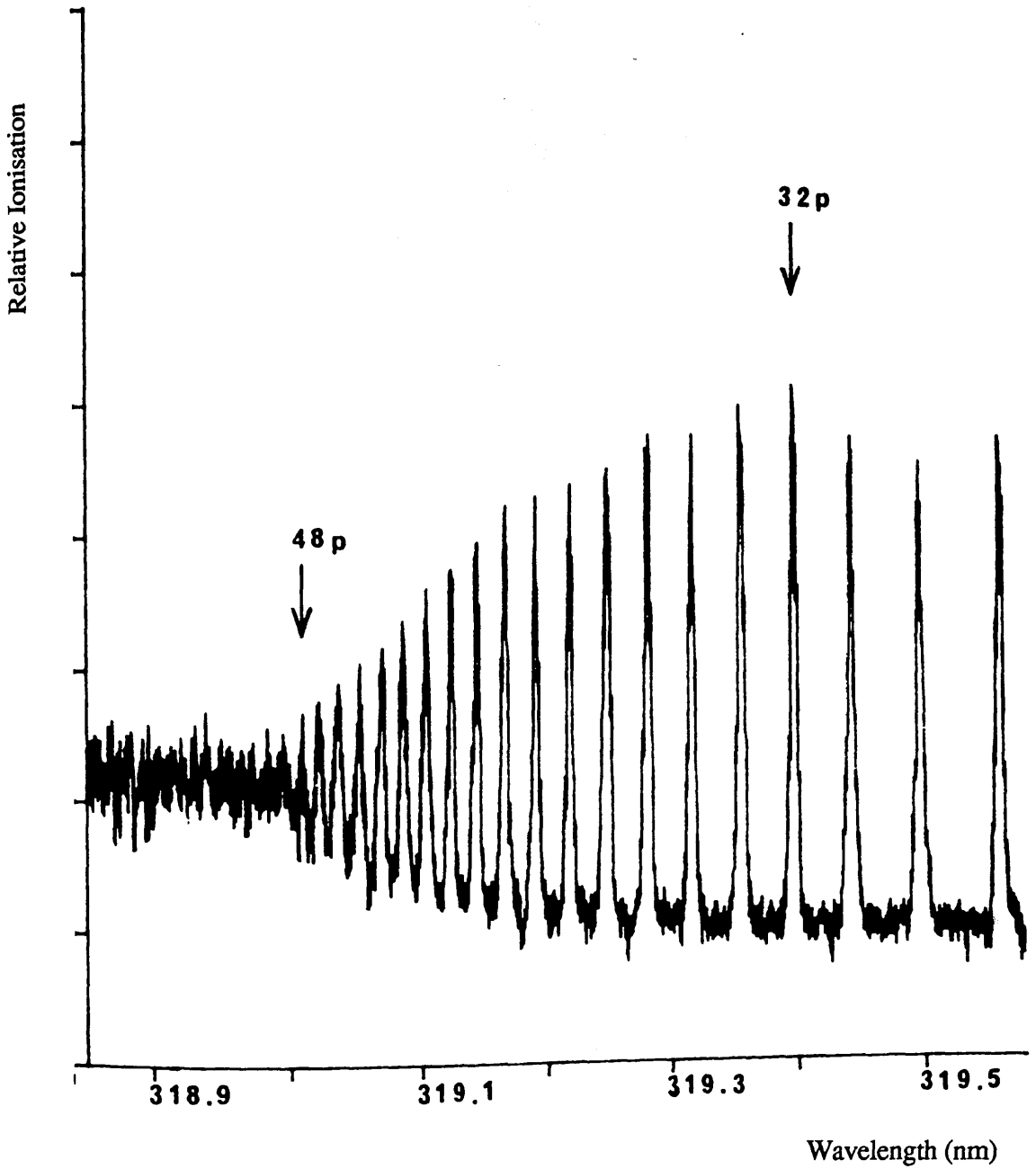


Figure 3.8 6s - np Rydberg transitions ($1\text{mJ}/\text{mm}^2$) - expanded view

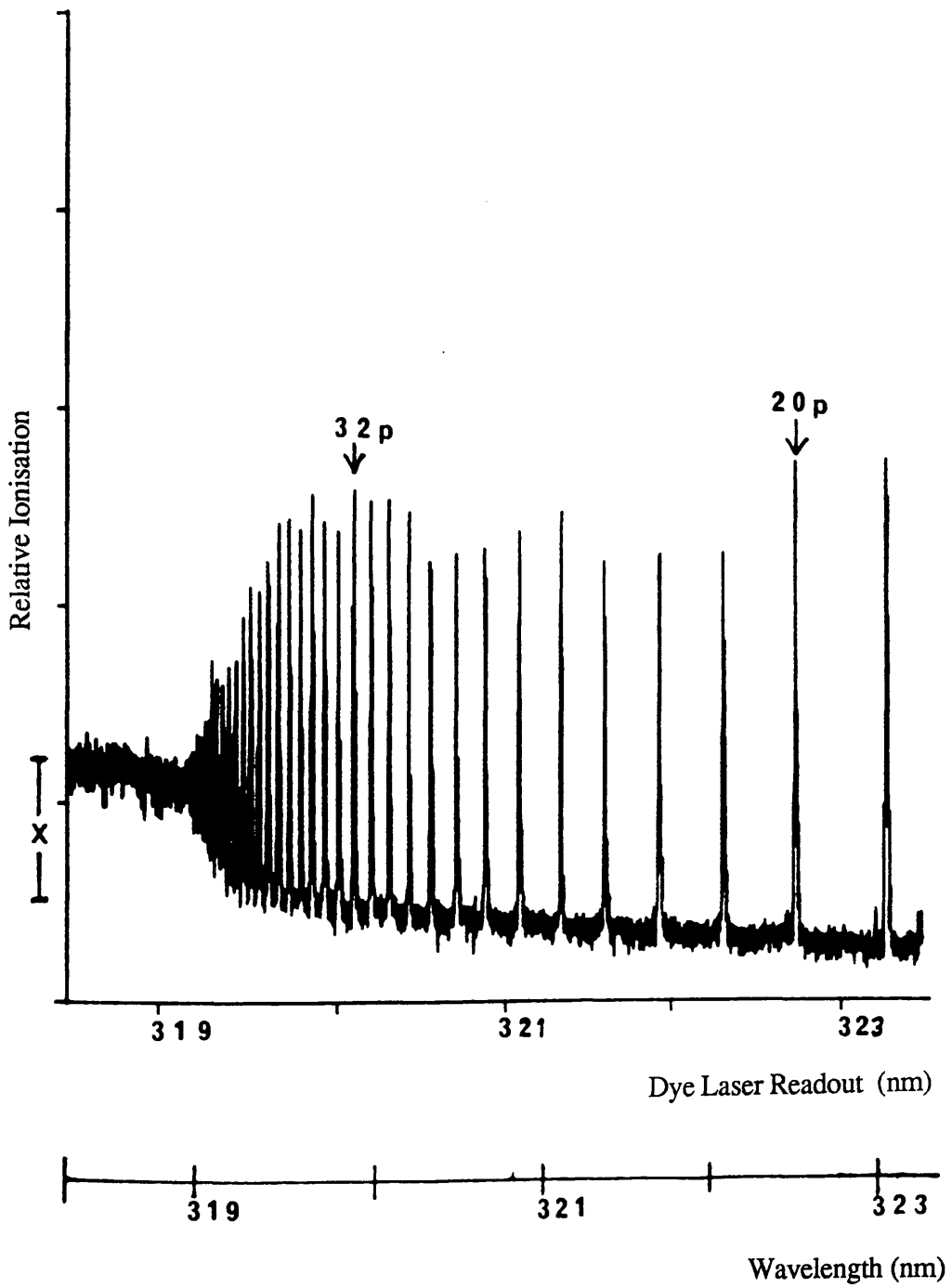


Figure 3.9 6s - np Rydberg transitions (6.3 mJ/mm^2)

be reached where every Rydberg atom has been ionised - this is referred to as collisional saturation. When this condition is reached, the rate of ionisation is determined by the rate at which the Rydberg level is populated from the ground state. This rate is proportional to $1/n^3$ (Letokhov 1983). The n values are assigned to the peaks by comparison of their doublet splitting with the literature values of separation of p level doublets (see Moore's tables 1952).

The lower power scan, Figure 3.7, has maximum ion yield at $n = 32$, indicating that the collisional process has been saturated. For $n > 32$, the size of the signal is dependent on the excitation step $1/n^3$ relation. For $n < 32$, the effect of collisional ionisation is smaller, and the peaks decrease in size. An expanded view of this spectrum is shown in Figure 3.8. Rydberg levels up to $n = 48$ can be seen.

Figure 3.9 shows the effect of an increase in laser fluence to 6.3 mJ/mm^2 . For $n > 20$, the two spectra are very similar. The background signal in both spectra is due to fluctuations in the output intensity of the frequency doubled laser. The section of the graph for which $n > 20$ shows an increase in the intensity of the peaks due to the new saturation of the excitation step. At this level of laser power, the low lying Rydberg levels can be partially saturated. There is insufficient power, however, to saturate the higher levels, and therefore the intensity of these levels decreases with n^3 in accordance with theory.

One noticeable feature of both spectra is that the single photon absorption edge is located at 319.1 nm , and not at the calculated value of 318.4 nm from the ionisation potential. This can be explained by the presence of the electric field which, by the Stark Effect, shifts the wavelengths of the peaks by an amount proportional to the applied field.

The effect of the collisions on the ion yield can be roughly calculated. A possible method is the comparison between experimental and theoretical ratios of the intensities of the 20p and 32p peaks. Weber and Sansonetti (1987) give a value for the quantum defect such that the effective quantum number

$$n^* = n - 3.595$$

Thus, in the absence of collisions, the theoretical ratio for the 20p and 32p peaks is 81:1. Experimentally, the ratio was calculated to be around 0.48 (at 1mJ/mm²). Collisional processes, therefore, result in an enhancement in the 20p yield of around 170 times. It was not possible to operate the proportional counter at a sufficiently low pressure to measure the ion yield in the absence of collisions. The quadrupole mass spectrometer, however, can operate at low pressure, and the pressure dependence of the ion yield could be studied when the mass spectrometer was installed (see Chapter 4).

3.4 6s - ns and nd Transitions

Ground state to p levels are accessible by single photon excitation. By the law of conservation of angular momentum, it requires two photons to reach an s or a d level from the caesium ground state, ie. as the spin of a photon is 1, a change in angular momentum of 0 or 2 requires angular momentum addition of two photons (l = 0 for an s state, l = 2 for a d state).

In order to study the higher s and d transitions, it was necessary to use the red DCM dye without the frequency doubling stage, giving a wavelength coverage for the 635nm to 665nm range. This two photon excitation requires an intermediate virtual state (Scheme 5 of Hurst's RIS schemes), and hence requires a higher laser power for saturation. This was achieved by focussing the laser beam into the ionisation region.

Figure 3.10 shows a spectrum taken between the wavelengths 635nm and 660nm. The laser fluence for this scan was 52.8mJ/mm^2 . This scan shows the two distinct sets of peaks, one set being approximately six times as intense as the other. The caesium two photon absorption edge is just visible at around 637nm. In field free conditions, the two series of transitions converge to the same limit located at 636.81nm. The various s and d peaks have been assigned by comparing their separation with literature values. In verification of these assignments, fine scans were taken which show evidence of doublet structure of the d levels and only singlet states in the s levels. The suppression of the 12d peak is a direct result of the drop in laser fluence as the limit of the dye is reached. There is a major difference in the heights of the s peaks in comparison with the d peaks, the d peaks being approximately six times more intense than the s transitions.

Pindzola (1984) deduced from Hartree - Fock approximations that this difference can be attributed to the variation in photoionisation cross sections of the two types of levels. Furthermore, Pindzola calculated a value of 0.008 for the 12s / 12d ratio. This increase in probability for ionisation of a d level over an s level can be explained in terms of electron orbital distributions. Thus, the potential overlap between a plane continuum wavefunction and a d type orbital wavefunction is greater than that of a plane continuum wavefunction and a spherically shaped s orbital, leading to an increased photo-ionisation cross-section. The experimental results presented here show much enhanced s levels, eg. the ratio between the 15s and 15d peaks is calculated to be 0.25. The enhancement can be attributed to collisional ionisation of the excited caesium atoms. Whitaker and Bushaw (1981) have studied collisionally induced ionisation of rubidium atoms in Rydberg states, and have proved the collisional nature of the ionisation of the Rydberg states by considerably reducing the pressure of the buffer gas with a resultant removal of the majority of the ionisation signals. Calculations of thermally induced collisions disprove the theory of ion formation by a simple exchange mechanism via thermal collisions. The more likely mechanism is associative ionisation

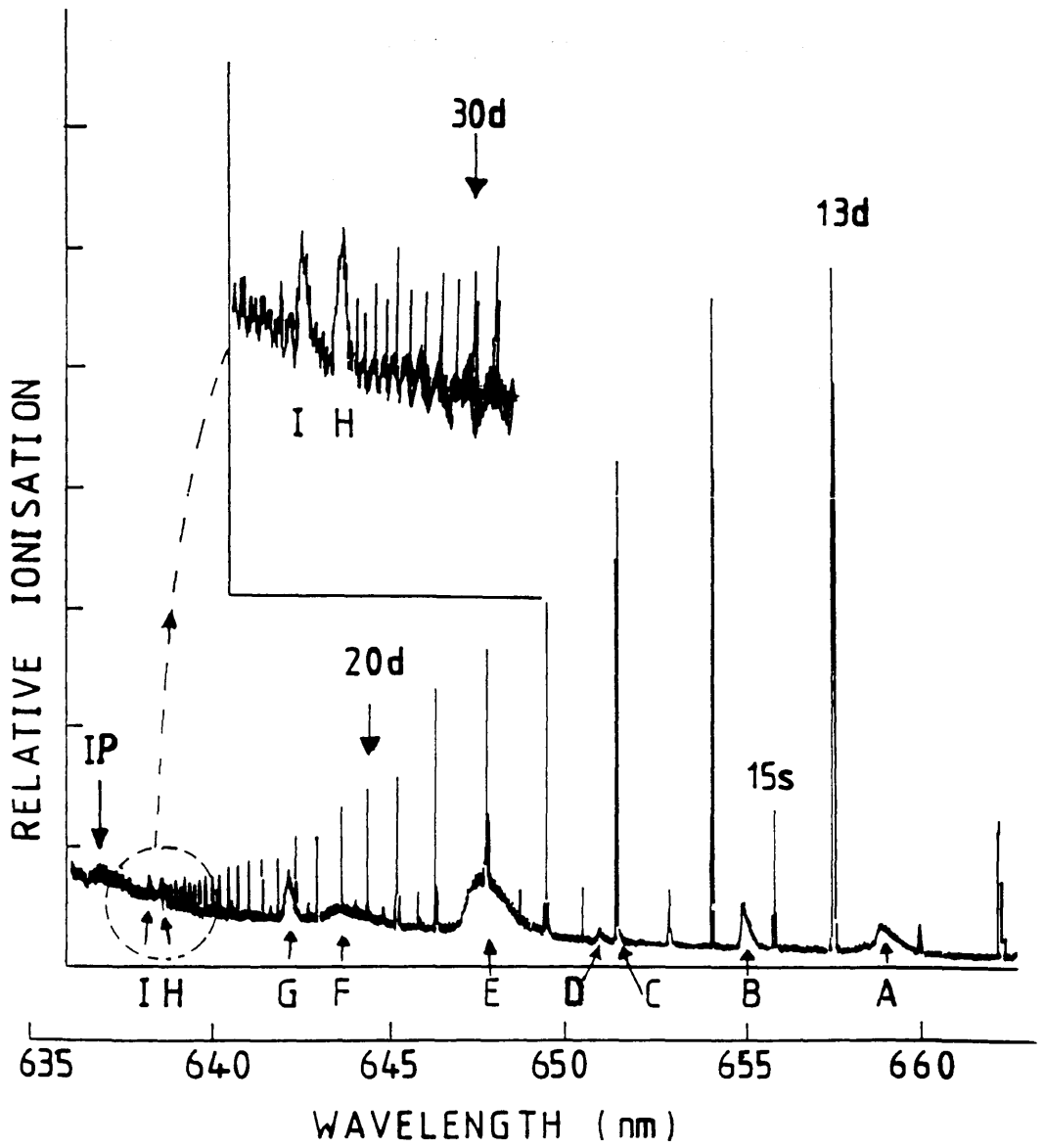


Figure 3.10 6s - ns / 6s - nd transitions

or a collisional redistribution of energy in the Rydberg levels followed by either collisional or photoionisation. Thus an electron in an s state could be collisionally transferred to a p state or a d state with a correspondingly higher ionisation cross section. The result of this would be an enhancement in the intensity of the s peak.

One other interesting feature of the graph is the presence of a number of broad resonances appearing intermittently throughout the spectrum. These resonances are too broad to represent atomic transitions and are only present after the introduction of the caesium vapour, indicating that they are not background signals.

One possible explanation is that the broad peaks may be due to molecular processes. Recently, photolytic spectroscopy of caesium molecules during multiphoton absorption processes has been studied by Collins et al (1981, 1981b). It was found that multiphoton absorption could occur with high probability in caesium molecules through a resonant intermediate state which was electronically excited and easily dissociated. Resonances occur in the multiphoton ionisation spectra for the absorption to a dissociative state followed by absorption from an excited state of a product caesium atom. These resonances were described by Collins as hybrid resonances - partly molecular and partly atomic. The dissociation can occur over a large spectral range (Christian 1984).

Figure 3.11 shows the potential curves for the excited states of Cs_2 (Collins 1976). The broad hybrid resonances can be explained with reference to Figure 3.12. Initially, the caesium molecule absorbs a photon from its single or triplet ground state $X^1\Sigma_g^+$, $^3\Sigma_u^+$, thus making a molecular transition to any of the $^3\Sigma_u$, $^1\Sigma_u$, or $C^1\Pi_u$ states. These unstable excited molecular states then dissociate to a ground state atom and an excited atom at levels $d_{3/2,5/2}$ or $p_{3/2}$. From this state, the excited atom may absorb a further photon to make a transition to the high lying Rydberg states. A third photon

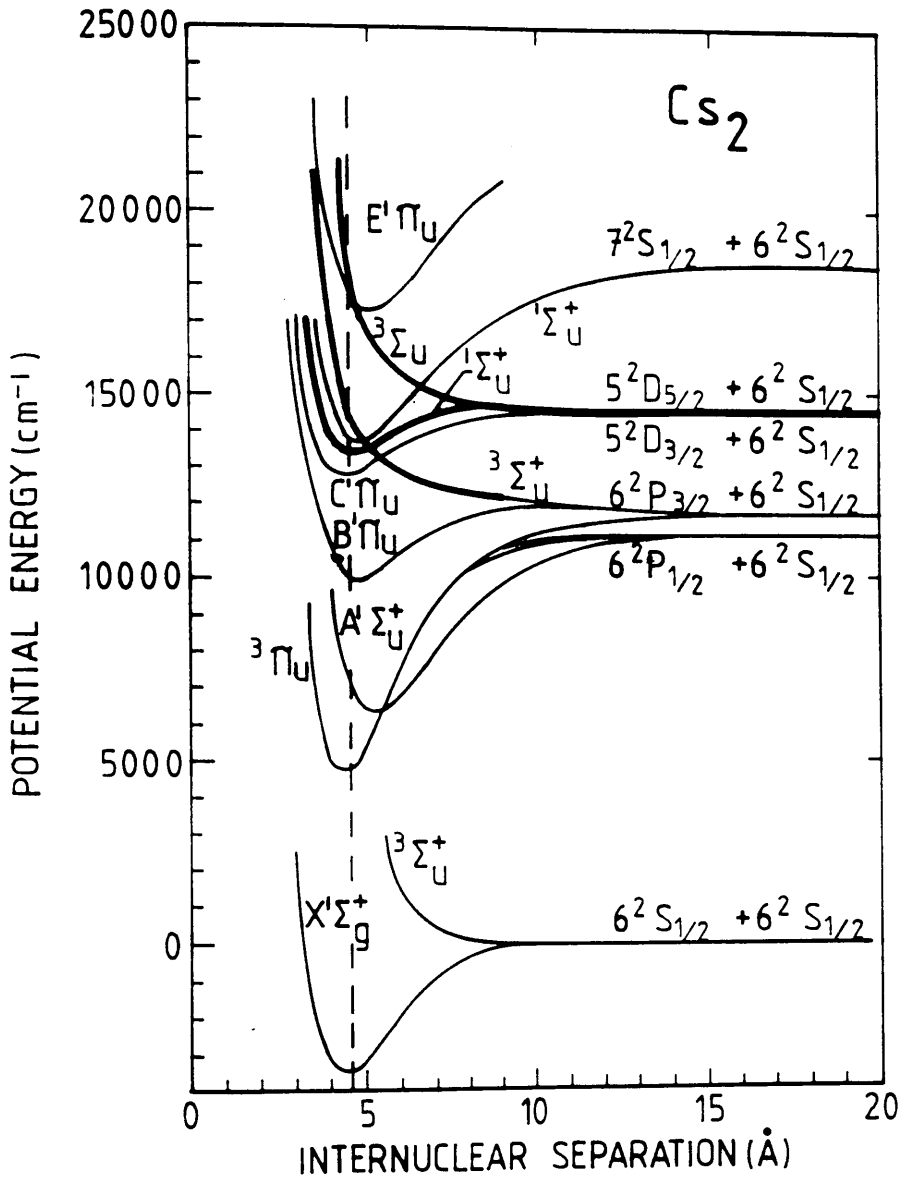
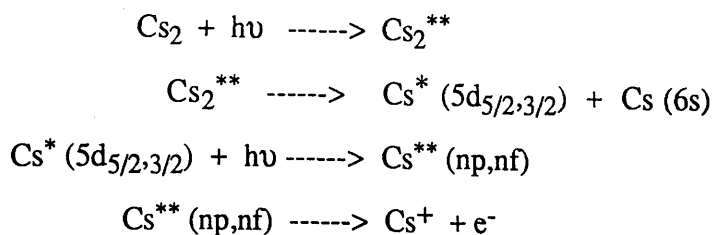
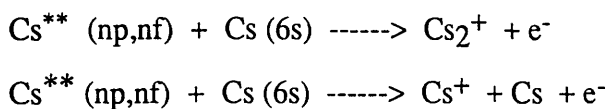


Figure 3.11 Potential curves for Cs_2 excited states (Collins 1976)

can then be used for the final ionisation stage. The process can be written:-



The final ionisation step could also occur by associative or Penning ionisation, ie,



This method of ionisation via Rydberg levels has been proven very effective (Collins 1984) as the caesium atom in the high lying Rydberg states has essentially unit probability for undergoing collisional ionisation through associative ionisation.

Table 3.2

<u>Hybrid Resonance</u>	<u>Corresponding Transition</u>	<u>Calculated Wavelength(nm)</u>	<u>Experimental Wavelength(nm)</u>	<u>Resonance Width (nm)</u>
A	5d _{5/2} - 8f _{5/2,7/2}	663.04	663.0	1.2
B	5d _{3/2} - 8f _{5/2}	658.78	658.9	1.0
C	5d _{5/2} - 12p _{3/2}	655.00	655.0	0.2
D	5d _{3/2} - 12p _{1/2}	651.32	651.3	0.05
E	5d _{3/2} - 12p _{3/2}	650.82	650.9	0.1
F	5d _{5/2} - 9f _{5/2,7/2}	647.44	647.4	0.6
G	5d _{3/2} - 9f _{5/2}	643.37	643.2	0.5
H	5d _{5/2} - 13p _{3/2}	641.95	642.1	0.2
I	5d _{3/2} - 13p _{1/2}	638.30	638.2	0.1
J	5d _{3/2} - 13p _{3/2}	637.96	637.9	0.1
K	5d _{5/2} - 10f _{5/2,7/2}	636.73	636.6	1.0

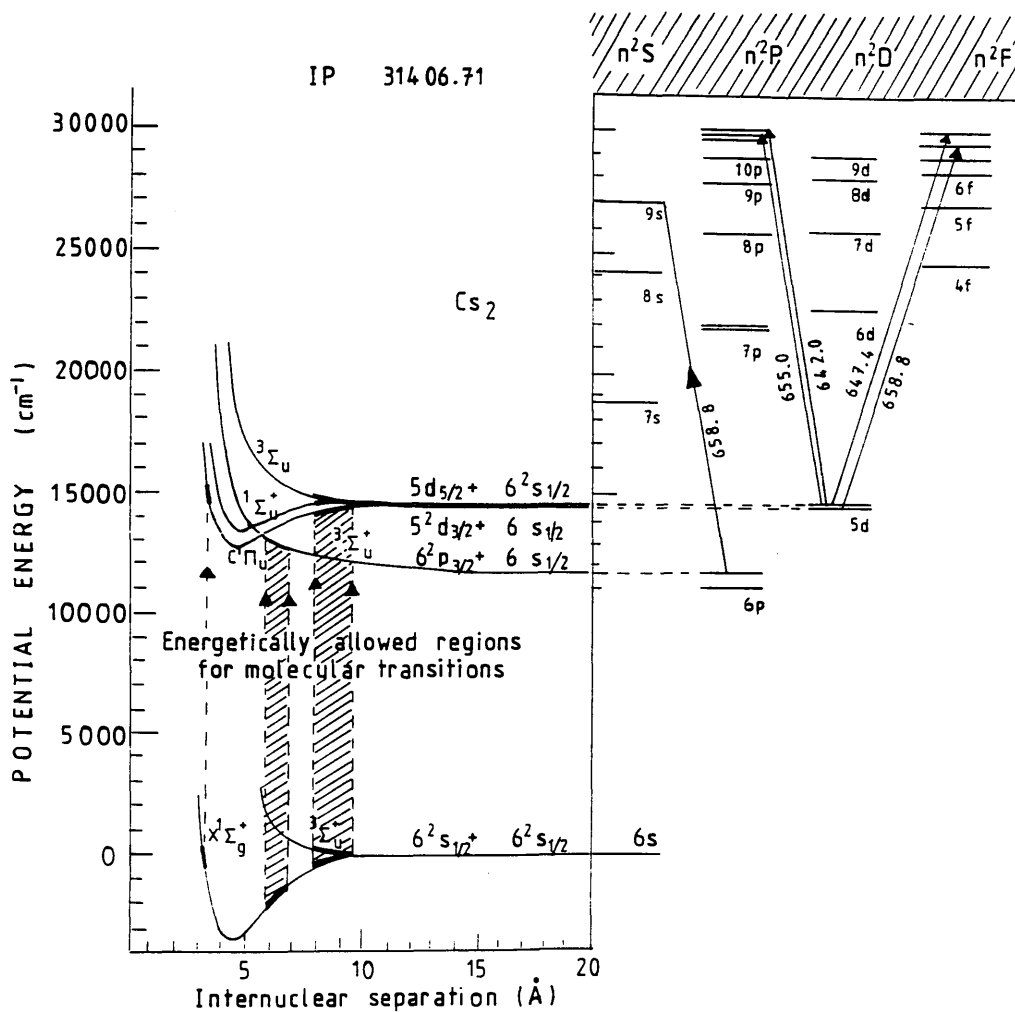


Figure 3.12 Dissociation of Cs_2 molecules to $5d_{5/2}$, $5d_{3/2}$ and $6p_{1/2}$ excited state atoms at 630nm - 660nm

Table 3.2 compares the calculated values of the hybrid resonances with the peaks obtained in Figure 3.10. The corresponding width of each resonance is also given, and the width appears to be an order of magnitude larger than the width of an atomic transition (around 0.02nm). This could be due partly to the increase in the width of the excited atomic state, as a result of fast dissociation of the caesium molecules. There is a noticeable increase in the width of the peaks resulting from 5d to f transitions compared with the width of the 5d to p transitions.

Another feature of Figure 3.10 is the large intensity of the hybrid resonance peaks considering the ratio of atoms of caesium to molecules at room temperature is around 50000 : 1. The ionisation via molecular states is a resonant process through a real intermediate state. The atomic ionisation, however, is occurring through a virtual state and hence has a probability of around six orders of magnitude smaller than the molecular process. Thus the signals from both processes are of similar size. In a proportional counter, it is impossible to distinguish caesium atoms from caesium molecules, and hence the fraction of caesium molecules in the ionisation signal was not known.

CHAPTER 4 RIS OF RUBIDIUM VAPOUR

4.1 Introduction

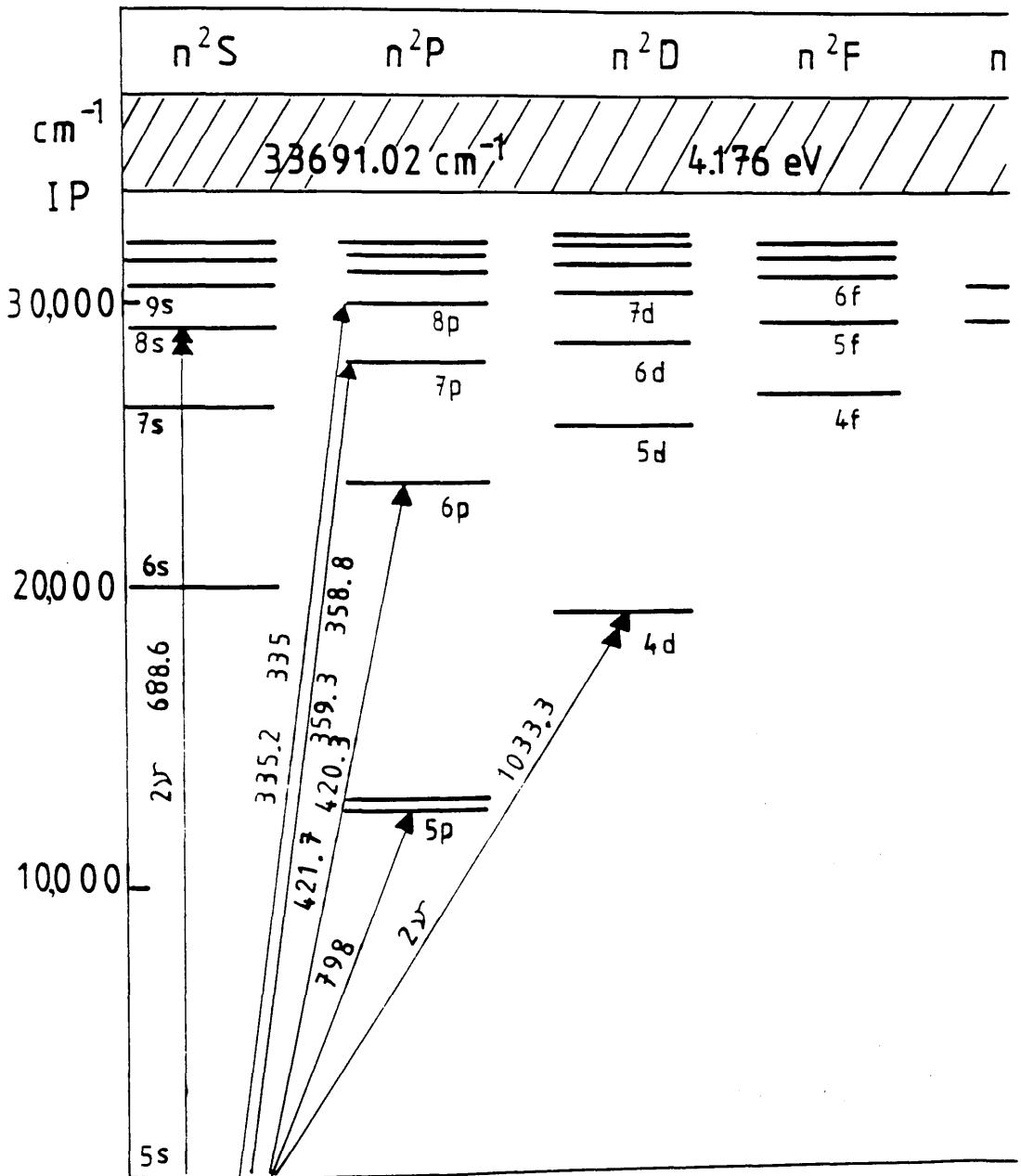
After initial studies on the spectroscopy of caesium vapour (Chapter 3) it was decided to continue spectroscopic studies using rubidium vapour. This was seen as a natural progression, as the detection of rubidium is slightly more complex as it has two naturally occurring isotopes, ^{85}Rb and ^{87}Rb . Initial studies were carried out using the proportional counter as in the caesium experiments. Using this arrangement, however, it was impossible to distinguish the two isotopes. The apparatus was therefore adapted to house a quadrupole mass spectrometer.

The proportional counter was used to study the two and three photon ionisation spectra of the ground state to s, p, and d states, and to the high lying Rydberg states. The quadrupole mass spectrometer was then used to study the effect of buffer gas pressure on the three photon transitions, the identification of the two isotopes, ^{85}Rb and ^{87}Rb , and the contribution from molecules. Table 4.1 gives the physical properties of elemental rubidium, and Figure 4.1 gives the Grotrian diagram for the atomic energy levels.

Table 4.1 Properties of Rubidium

Ionisation Potential	4.176 eV
Atomic Weight	85.47
Stable Isotopes	^{85}Rb , ^{87}Rb
Vapour Pressure	10^{-7} torr at 300K
Boiling Point	688 °C
Melting Point	38.89 °C

Figure 4.1 Grotrian diagram for rubidium



Rubidium metal is slightly less reactive than caesium, but still requires storage in glass ampoules to avoid exposure to air or moisture. The quadrupole mass spectrometer head was incorporated into the apparatus as shown in Figures 2.17, 2.18 and 2.19. The operation of the spectrometer is described in detail in Chapter 2. As rubidium has a slightly lower vapour pressure than caesium, it was necessary to heat up the sample to around 40°C - 50°C in order to produce sufficient atoms for ionisation. At this temperature, rubidium atoms are present at a pressure of around 4×10^{-4} torr, and rubidium dimers at 1.6×10^{-7} torr (Samson 1966). Thus, in an unfocussed laser beam (dimensions $1\text{mm}^2 \times 20\text{mm}$) there are 2.8×10^{11} atoms and 1×10^8 molecules. The rubidium vapour pressure, however, tends to drop after a few days as a result of interaction of rubidium with impurities from the buffer gas or from the counter surfaces. A heat gun was directed onto the chamber arm containing the rubidium ampoule in order to increase the rubidium vapour pressure. A careful check was kept on the pressure within the chamber, as damage could occur to the quadrupole mass spectrometer if the pressure rose to beyond around 5×10^{-5} torr.

One major disadvantage involved in the heating of the sample was the shortened lifetime of the counter between cleanings. This was due to the windows and the inside of the chamber becoming progressively more coated with condensed rubidium metal. This caused an increase in the background ionisation signal, and, if allowed to progress, blocked the passage of the laser beam through the quartz windows.

4.2 Two Photon Ionisation of Rubidium in a Proportional Counter

Transitions between the ground state 5s level and the Rydberg p levels were obtained by scanning the dye laser between 290nm and 300nm, using the frequency

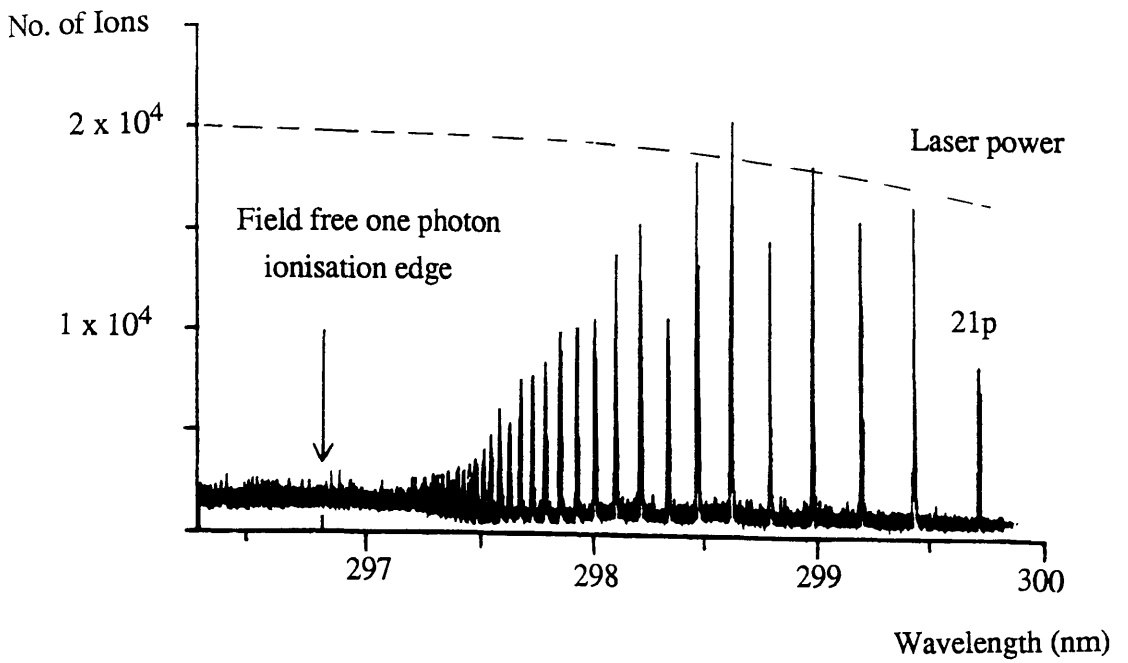


Figure 4.2 Two photon transitions ($5s - np$) in rubidium (6×10^{22} photons/cm²/sec)

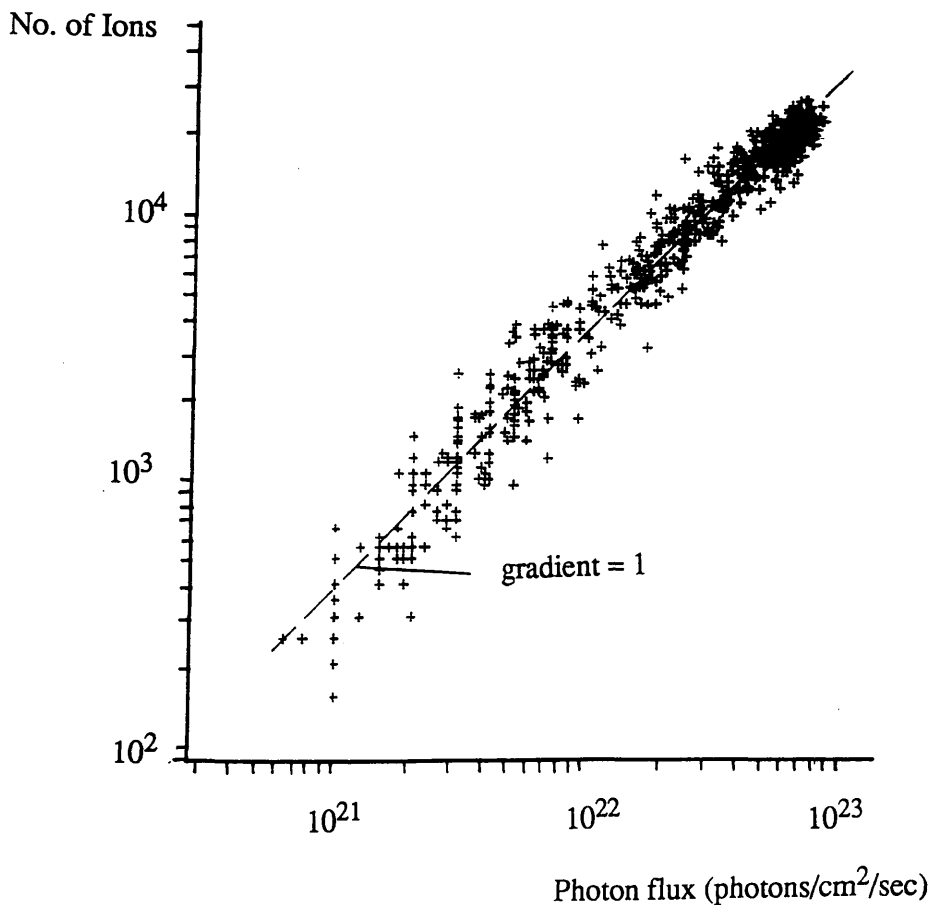


Figure 4.3 Power dependence curve for 20p peak

doubled output of the Rhodamine 6G dye. The spectrum obtained is shown in Figure 4.2. This was taken using an unfocussed laser beam at a flux of 6×10^{22} photons/cm²/second. Figure 4.3 shows the power dependence curve taken on the 20p peak. This shows a linear dependence of the ionisation on laser flux, indicating that the collisional ionisation of the high lying states has been saturated, and the ionisation rate depends only on the single photon excitation rate. It is unlikely, at this power level, that the excitation stage of the process could be saturated. According to Singhal et al (1988), the flux required to saturate a transition is given by $(2\tau \sigma_{exc})^{-1}$, where the excitation cross-section is defined in the theory section as

$$\sigma_{exc} = g_1 / g_2 (\lambda^2 A_{12} / 8 \pi \Delta\nu_1)$$

From the above calculation, the flux required for saturation would be of the order of 10^{26} photons/cm²/second, assuming a pulse length of 10^{-8} seconds. A power dependence curve was taken at 296nm, just above the ionisation limit (Figure 4.4) and shows a linear power dependence caused by single photon ionisation of rubidium atoms. Figure 4.5 shows an unexpected result of power dependence taken off-resonance at 299nm. At this wavelength, the non-resonant ionisation is expected to be dominated by rubidium molecules, exhibiting a linear dependence of ionisation on fluence (the ionisation potential for rubidium molecules is 3.9 eV). The quadratic dependence seen here is indicative of an excitation / dissociation process, and is entirely analogous to the process for caesium molecules described in Chapter 3.

Figure 4.6 shows the effect on the spectrum of an increase in laser flux to 4.5×10^{24} photons/cm²/second. Although the atomic transitions are still visible, the ratio of background signal to atomic ionisation has increased considerably, due to the increased molecular and possibly organic signals.

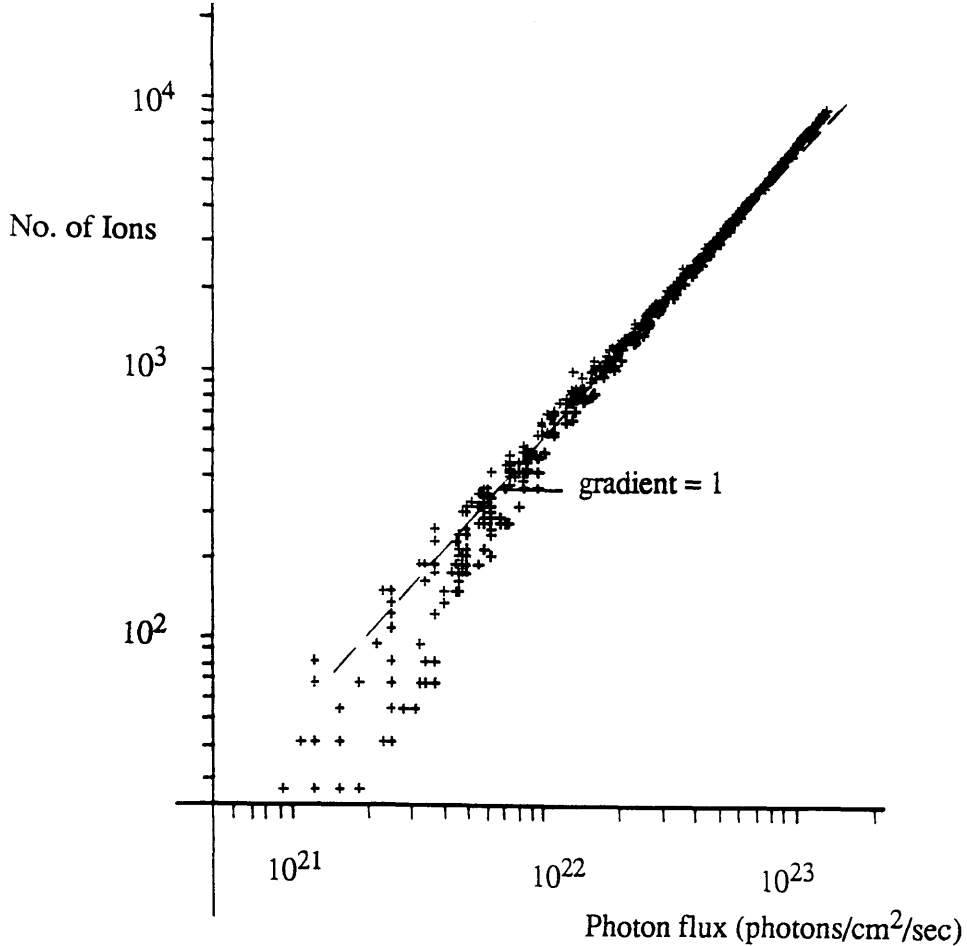


Figure 4.4 Power dependence curve at 296 nm

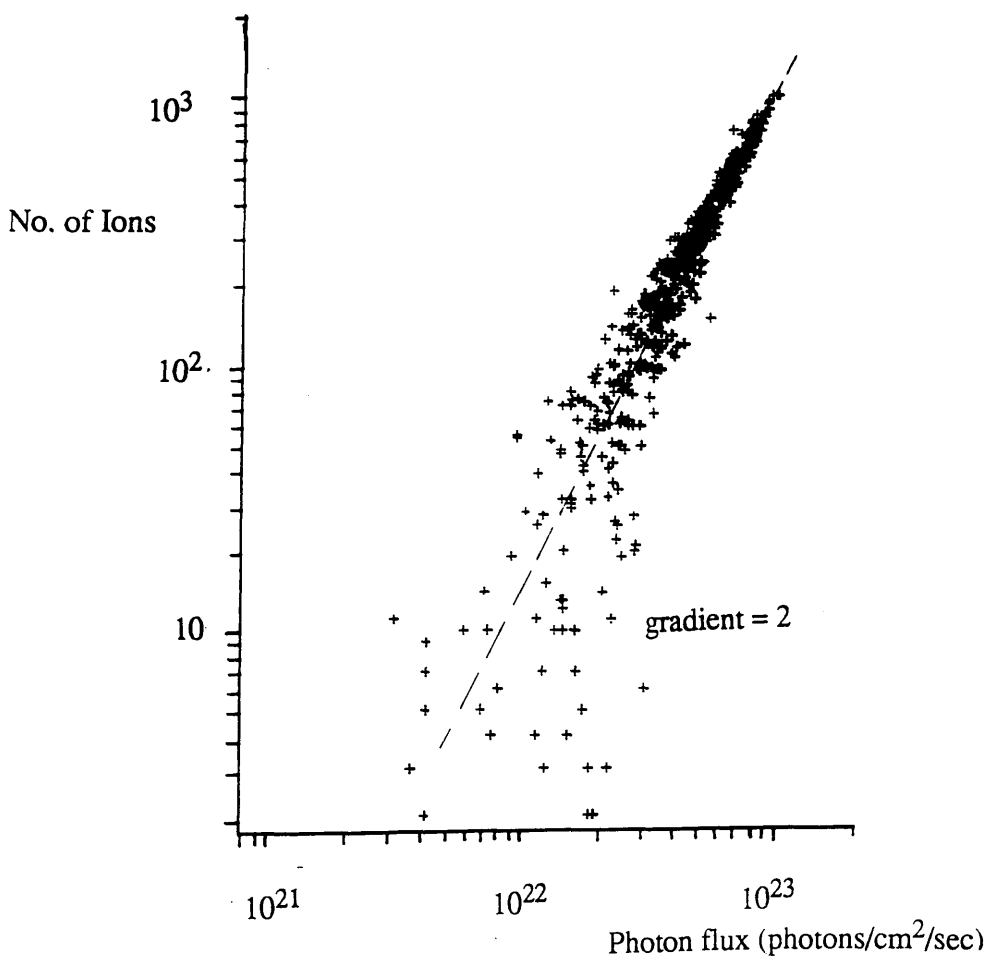


Figure 4.5 Power dependence curve taken off resonance at 299 nm

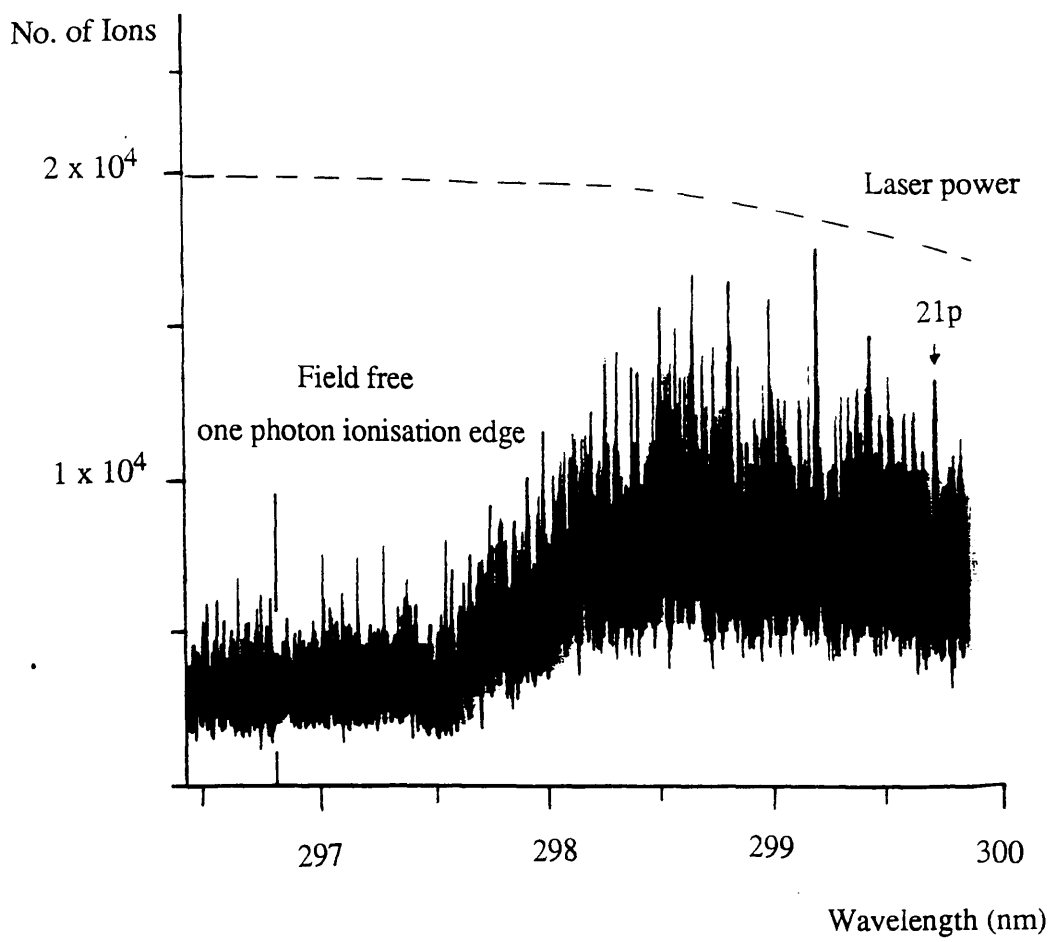


Figure 4.6 Two photon transitions ($5s - np$) in rubidium (4.5×10^{24} photons/cm²/sec)

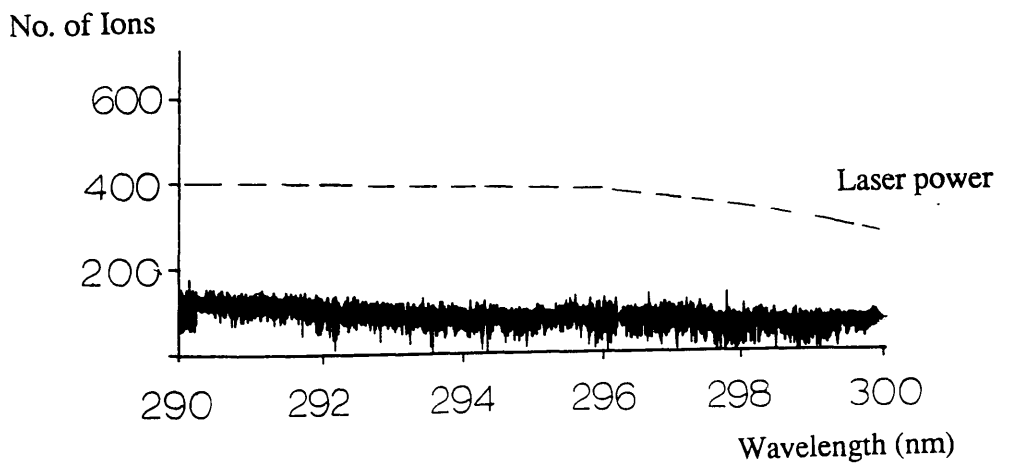


Figure 4.7 Background ionisation

For comparison, Figure 4.7 shows a spectrum of the background ionisation before the breaking of the rubidium ampoule. The ionisation due to organic impurities in this graph decreases by a factor of two over the wavelength range, in agreement with Drysdale et al (1986) which shows background ionisation in the region 260nm - 330nm dropping rapidly as wavelength is increased. This strongly suggests that the ionisation seen in Figure 4.6 is not due to organic impurities.

Figures 4.8 and 4.9 give two power dependence graphs taken on resonance at 295.5nm and off resonance 299nm respectively. Figure 4.8 shows a gradient of $3/2$ flattening off to a linear power dependence at higher laser fluence. The ionisation here is made up of three components; the single photon ionisation of rubidium atoms, the two photon resonant ionisation of organic impurities and the ionisation / dissociation of the rubidium molecules. The change to linear dependency indicates the saturation of the molecular process. Figure 4.9 is a power dependence curve taken off resonance at 299nm. The ionisation at this wavelength will be dominated by the molecular component, which, at higher flux, begins to saturate giving a gradient of $3/2$.

4.3 Three Photon Ionisation of Rubidium

The proportional counter was again used to take three photon spectra of rubidium vapour. Figure 4.10 shows the two series of sharp and diffuse transitions similar to those seen with caesium. Peaks were seen corresponding to Rydberg levels from the $n = 20$ level for the s transitions and $n = 19$ for the d transitions. Under field free conditions, these two series converge to the two photon ionisation edge at 593.6nm.

The power dependence graphs for the ground state ($5s - ns$) transition and the

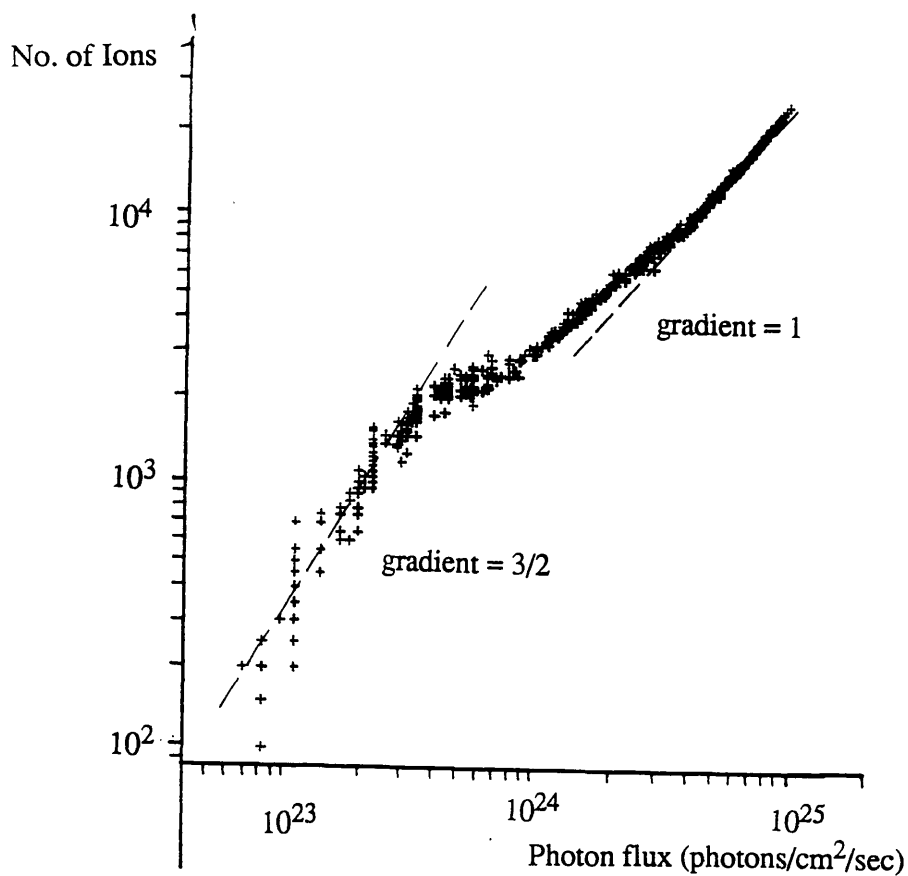


Figure 4.8 Power dependence curve on resonance at 295.5 nm

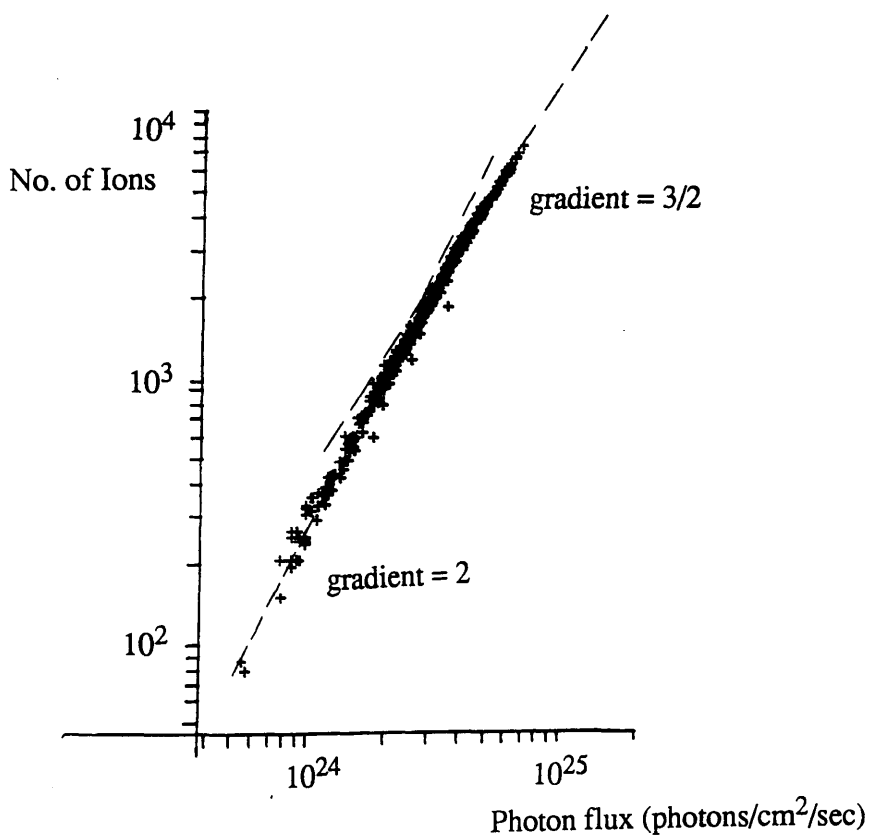


Figure 4.9 Power dependence curve off resonance at 299 nm

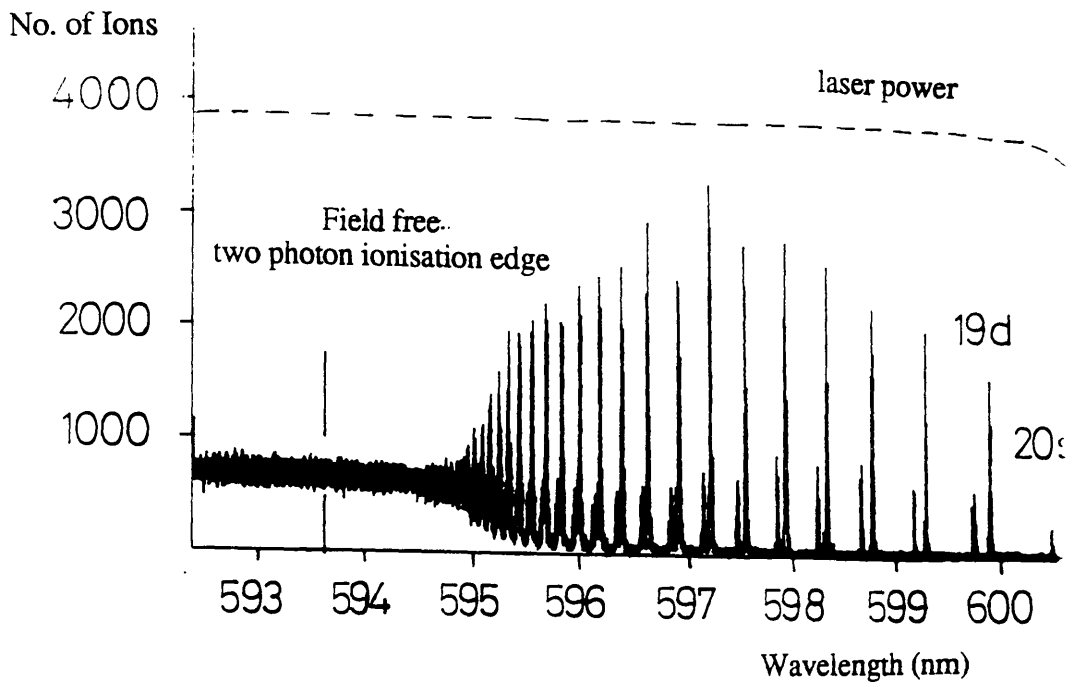


Figure 4.10 Three photon ionisation ($5s - ns, nd$) in rubidium

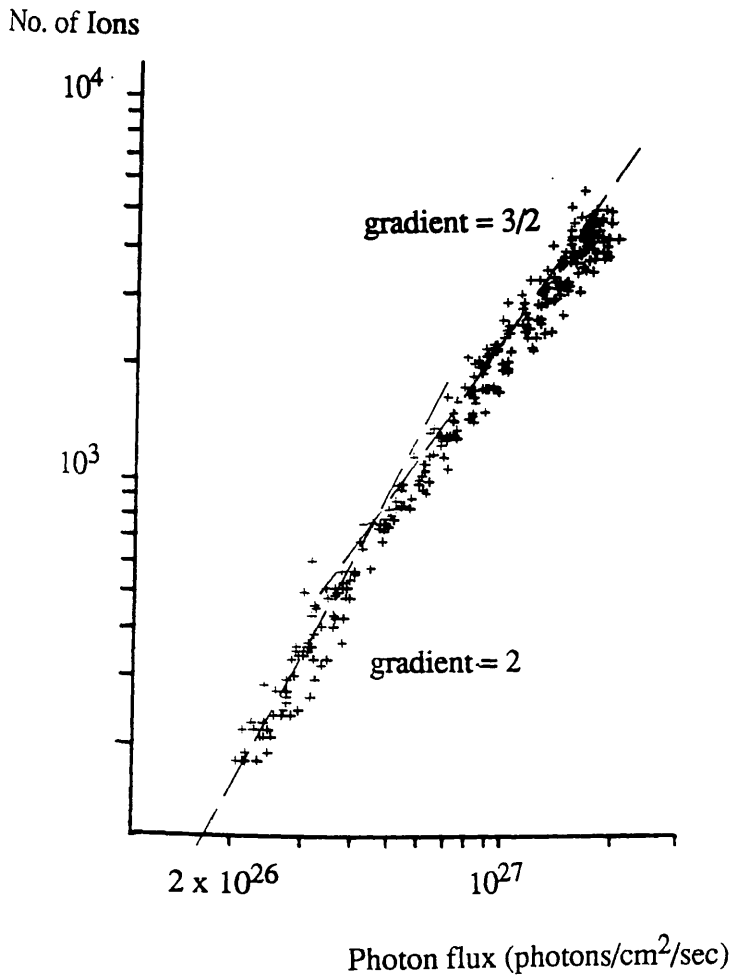


Figure 4.11 Power dependence curve ($5s_{1/2} - 28s_{1/2}$)

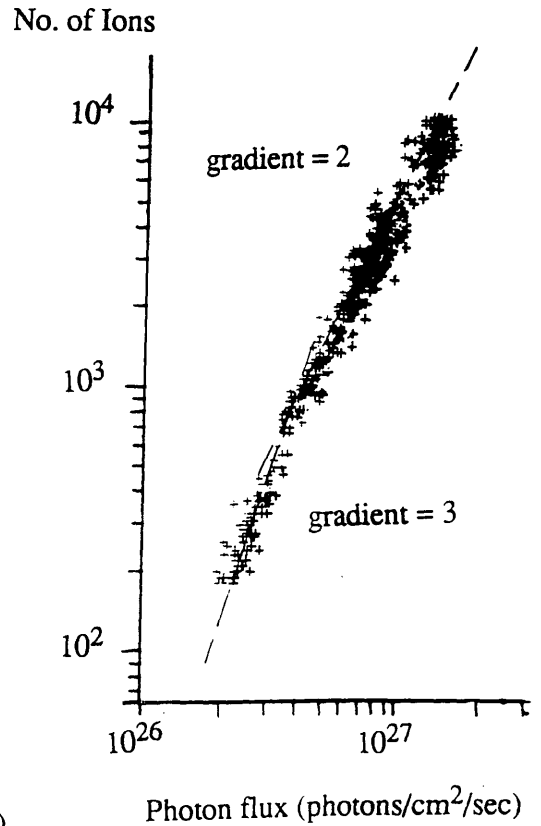


Figure 4.12 Power dependence curve ($5s_{1/2} - 20d_{5/2}$)

ground state ($5s - nd$) transition are shown in Figures 4.11 and 4.12. The $5s_{1/2} - 20d_{5/2}$ transition shows a cubic dependence at low flux (see Figure 4.12). At higher flux levels, the ionisation step becomes saturated as a result of increased collisional enhancement of the signal through collisions with the buffer gas or with ground state rubidium atoms, and the dependence becomes quadratic. The $5s_{1/2} - 28s_{1/2}$ transition, however, shows a quadratic dependence at low power, which decreases to $3/2$ as the power is increased (Figure 4.11). A purely light induced process would show a cubic dependence, and therefore collisional effects must be significant. It would therefore appear that whereas ionisation through d levels occurs by pure photoionisation, s levels are ionised without photons. At this high s level, $n=28$, collisional ionisation will be very probable (Niemax 1983). Photoionisation of d states can be explained by the much higher probability for photoionisation compared with s levels (Pindzola 1984). Further evidence for the importance of s - s collisional enhancement is the increase in the expected ratio of s / d peak intensities. This effect was also seen in caesium spectra contained in Chapter 3.

A power dependence graph was also taken above the two photon edge, and showed a quadratic dependence as expected at low flux, becoming linear as saturation effects start to occur (Figure 4.13). Two other power dependence graphs show the dependence of non resonant ionisation on the photon flux. Figure 4.14 was recorded using an unfocussed laser, whereas in Figure 4.15, focussing was employed. Figure 4.14 has a gradient of 2, and implies a two photon ionisation of rubidium molecules. This process is thought to occur via a real molecular electronic level (Gupta et al 1978). Figure 4.15, however, with focussing employed, shows a gradient greater than 1 at lower fluxes, becoming linear at higher levels of flux. This is an indication of the molecular two photon ionisation step becoming saturated at one of the stages.

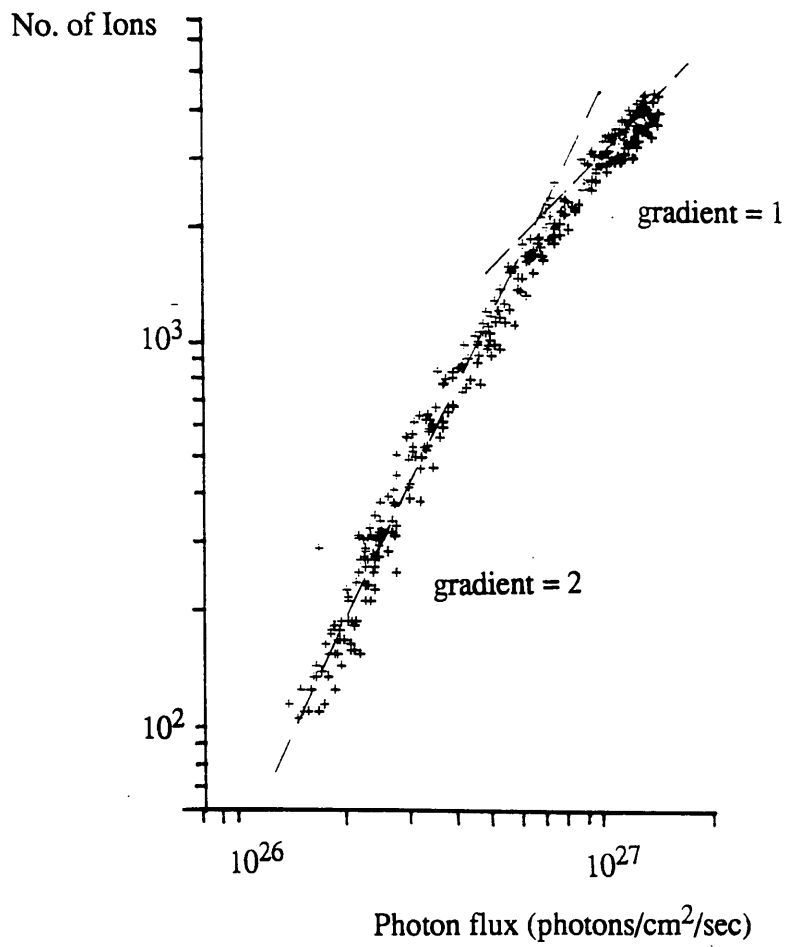


Figure 4.13 Power dependence curve above two photon edge

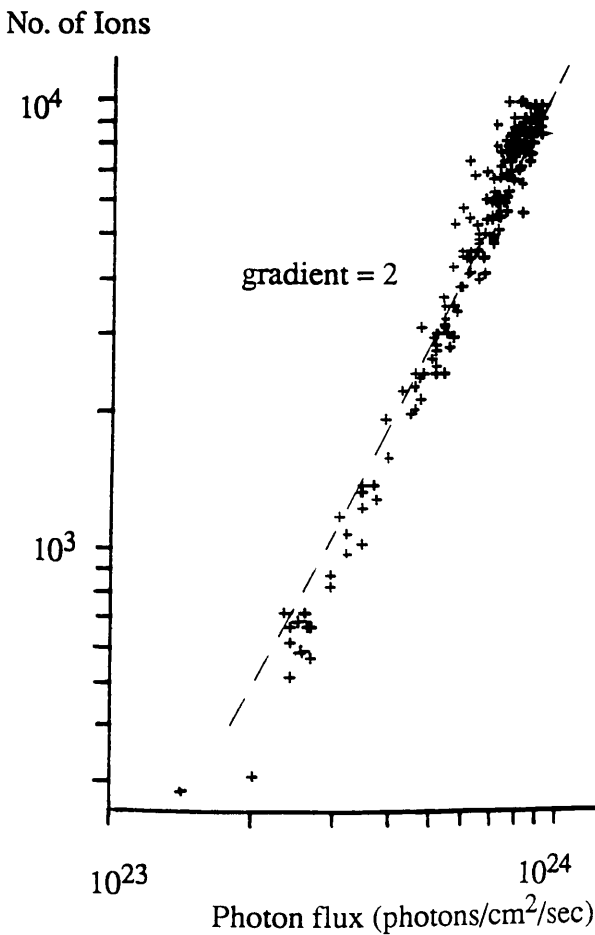


Figure 4.14 Power dependence curve off resonance (unfocussed)

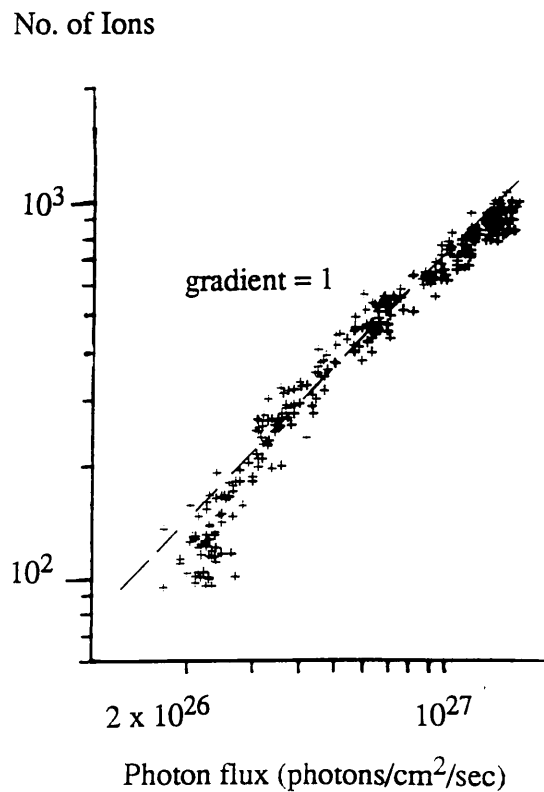


Figure 4.15 Power dependence curve off resonance (focussed)

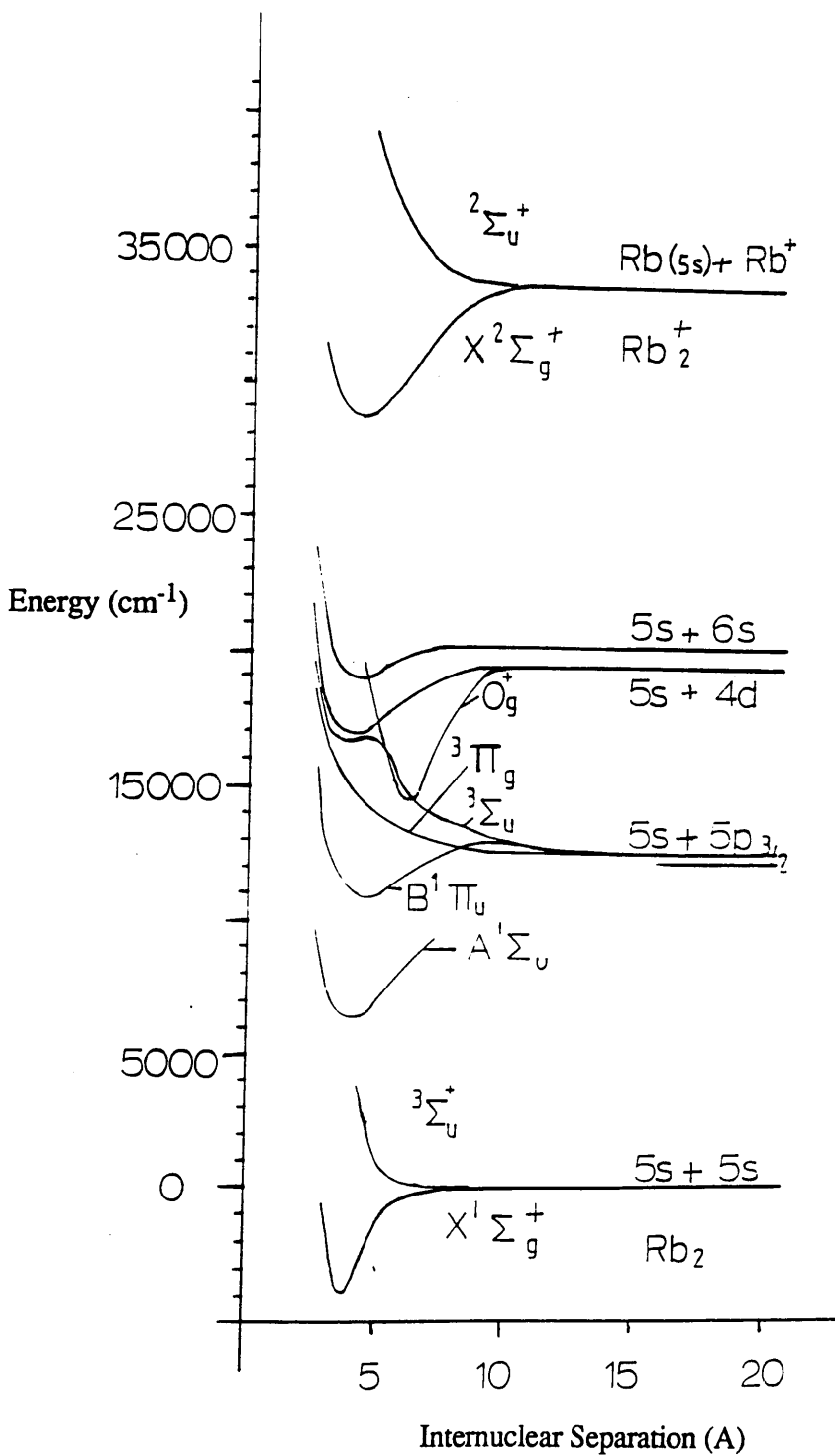
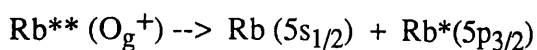


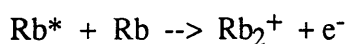
Figure 4.16 Energy levels for rubidium molecules (Collins et al 1976)

There is no evidence of the hybrid resonance structure in this three photon ionisation spectrum, as was observed with caesium. The excited rubidium molecular state, the O_g^+ state, can dissociate to form a ground state atom and an excited $5p_{3/2}$ atom, as shown in Figure 4.16 (Collins et al 1976), ie.



where the double asterisk indicates a state unstable against dissociation. This would then be followed by absorption of a second photon if its energy corresponded with a resonance of the s or d series in absorption.

The final step would occur by one of the two mechanisms below,



A simple explanation for the absence of broad resonances is the fact that over the particular wavelength range of the scan (590nm - 600nm) there are no transitions from the $5p_{3/2,1/2}$ level to s or d levels. As a result, no broad resonances are seen in this rubidium spectrum.

An expanded view of Figure 4.10 is given in Figure 4.17, and shows evidence of the existence of peaks corresponding to the parity forbidden two photon s - p transitions. These become increasingly evident as wavelength is decreased, and are visible up to the 48p level. It was further noted that parity forbidden transition peaks became less evident as the voltage on the proportional counter was reduced (see Figure 4.18). The external electric field has the effect of mixing together near degenerate levels,

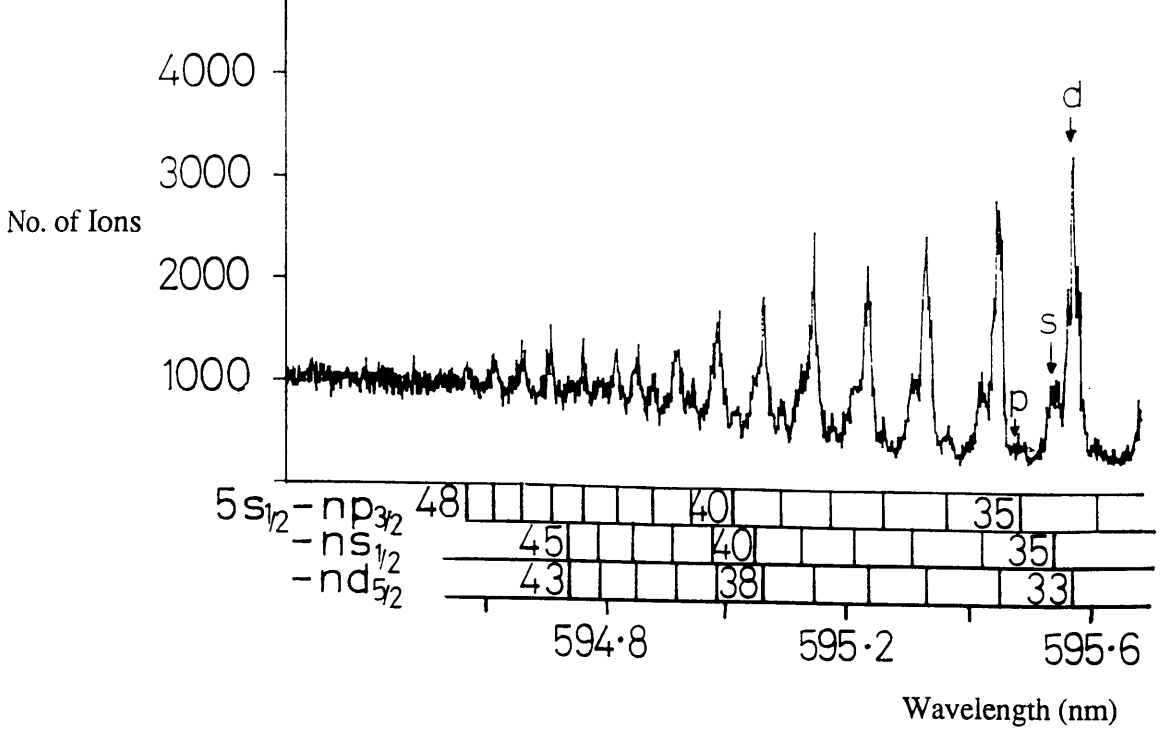


Figure 4.17 Expanded view of Figure 4.10 showing parity forbidden s - p transitions

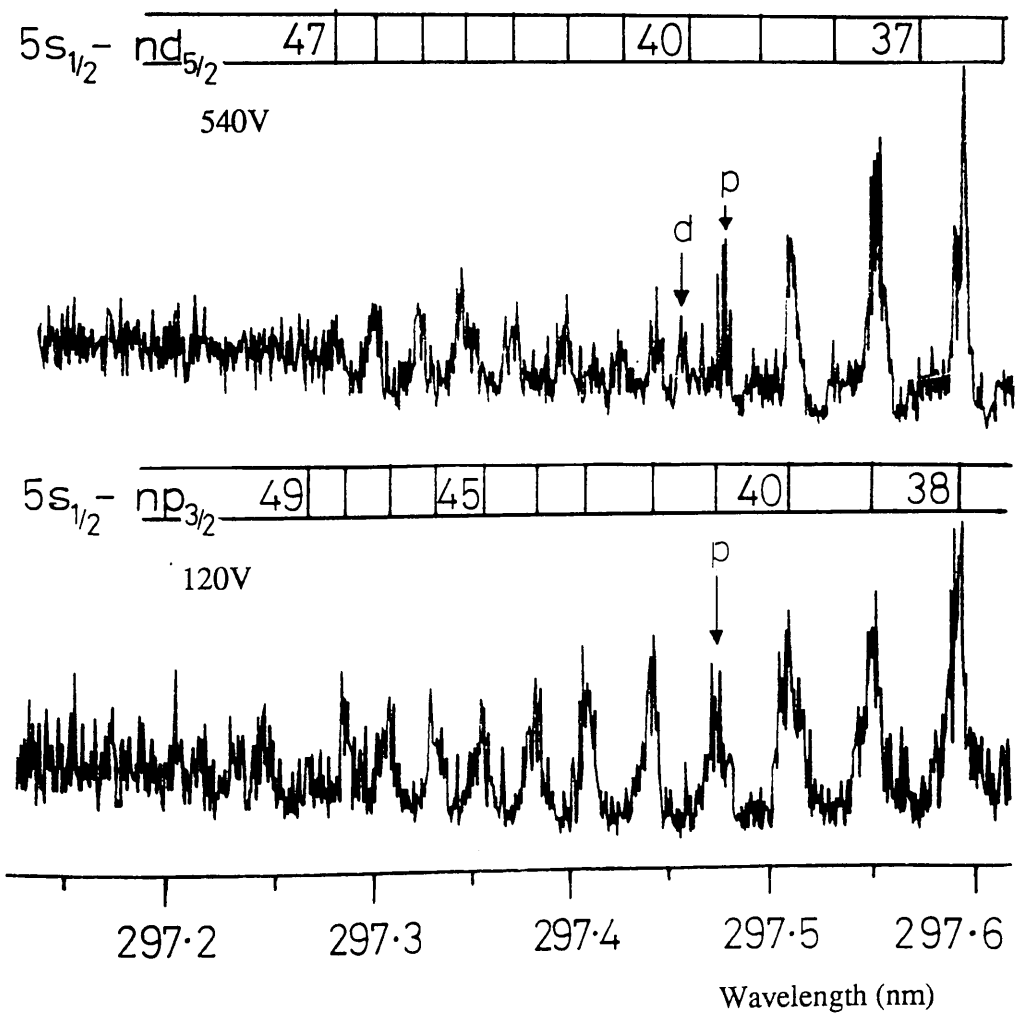


Figure 4.18 Dependence of parity forbidden transitions on external field

causing a breakdown in the parity selection rules, and allowing normally forbidden transitions to occur. As the principal quantum number increases, the corresponding levels become progressively more degenerate, and hence the mixing of levels is increased, leading to an increase in the size of the forbidden transition peaks.

Whitaker and Bushaw (1981) have demonstrated the efficiency of collisional ionisation for Rb - Kr collisions. As the photoionisation from Rydberg levels has a low cross section, high laser power would be required to saturate this transition. An improvement in ionisation signals by two orders of magnitude over photo-ionisation efficiency is estimated.

4.4 Pressure Dependence of Three Photon Ionisation of Rubidium

Both the proportional counter and the quadrupole mass spectrometer were used in this experiment to study the dependence of buffer gas pressure on the collisional ionisation of rubidium. For direct comparison, two graphs were taken over the same wavelength range (620nm - 660nm), one at a pressure of 100 torr in the proportional counter, and the other with the quadrupole mass spectrometer operating at a pressure of around 5×10^{-6} torr (Figures 4.19 and 4.20). In both cases, the laser beam was focussed, giving a flux of approximately 7×10^{26} photons/cm²/second. In the low pressure graph, the s peaks are barely distinguishable from the background ionisation. At 100 torr, however, the s states are greatly enhanced. As explained in Chapter 3, Pindzola (1984) calculated s / d ratios for caesium atoms, eg. 12s/12d ratio of 0.008, and deduced that although two photon excitation cross sections from the ground state to s and d levels were of similar magnitude, the photoionisation cross sections of d levels were orders of magnitude larger than s levels. On the assumption that rubidium behaves in a similar manner to caesium, the ratio of s to d levels obtained at low pressures is as

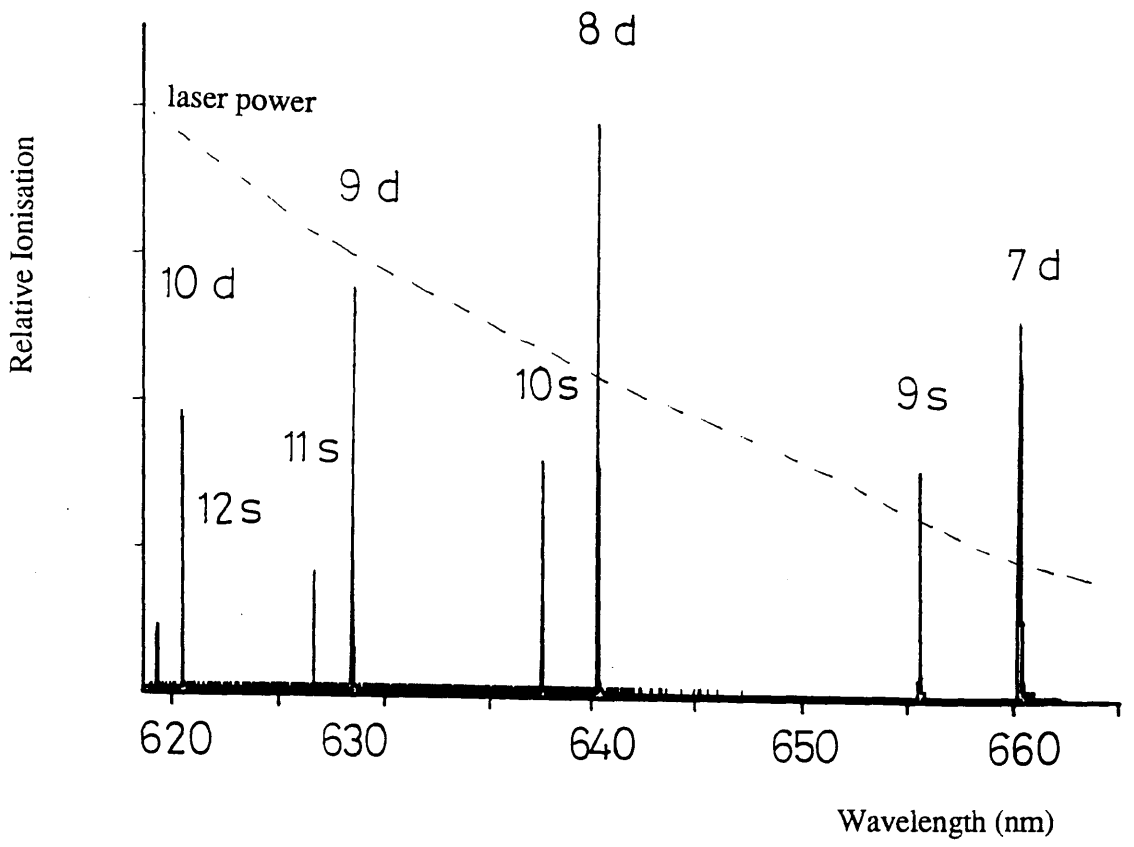


Figure 4.19 Three photon ionisation of rubidium at 100 torr

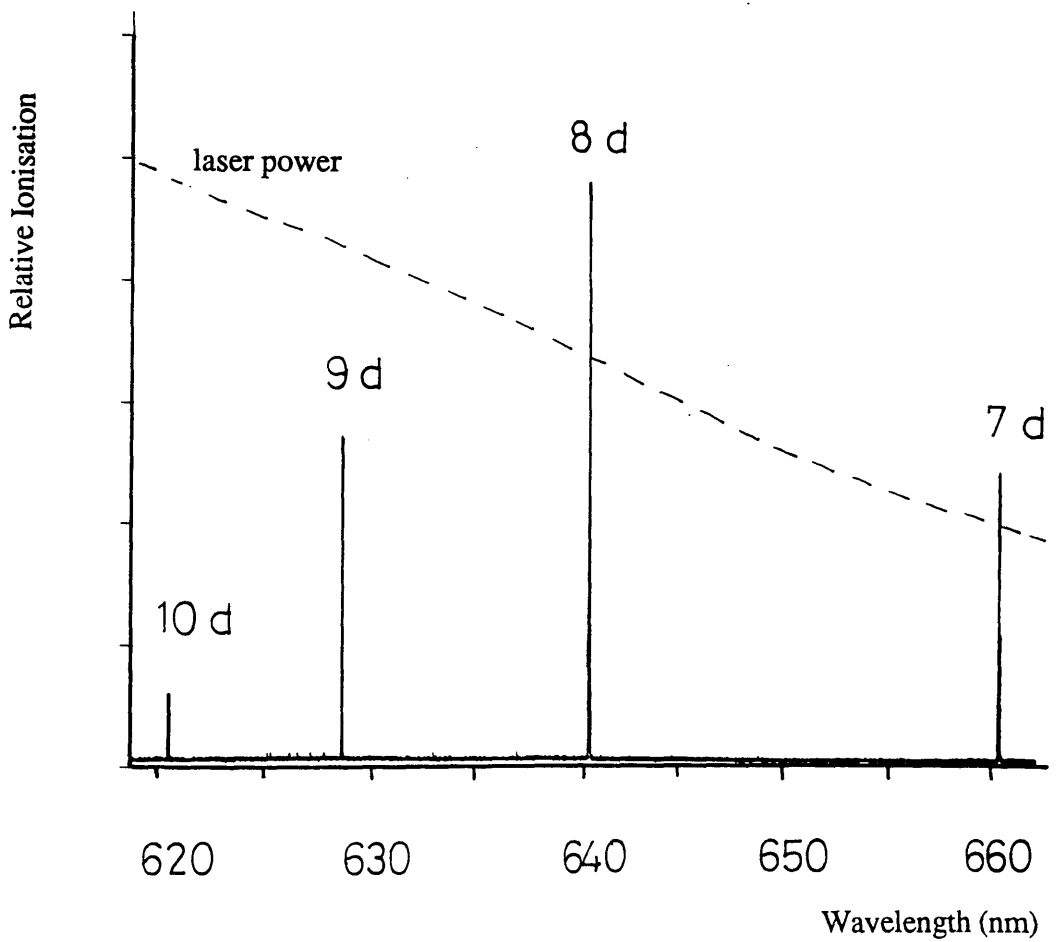


Figure 4.20 Three photon ionisation of rubidium at 2×10^{-6} torr

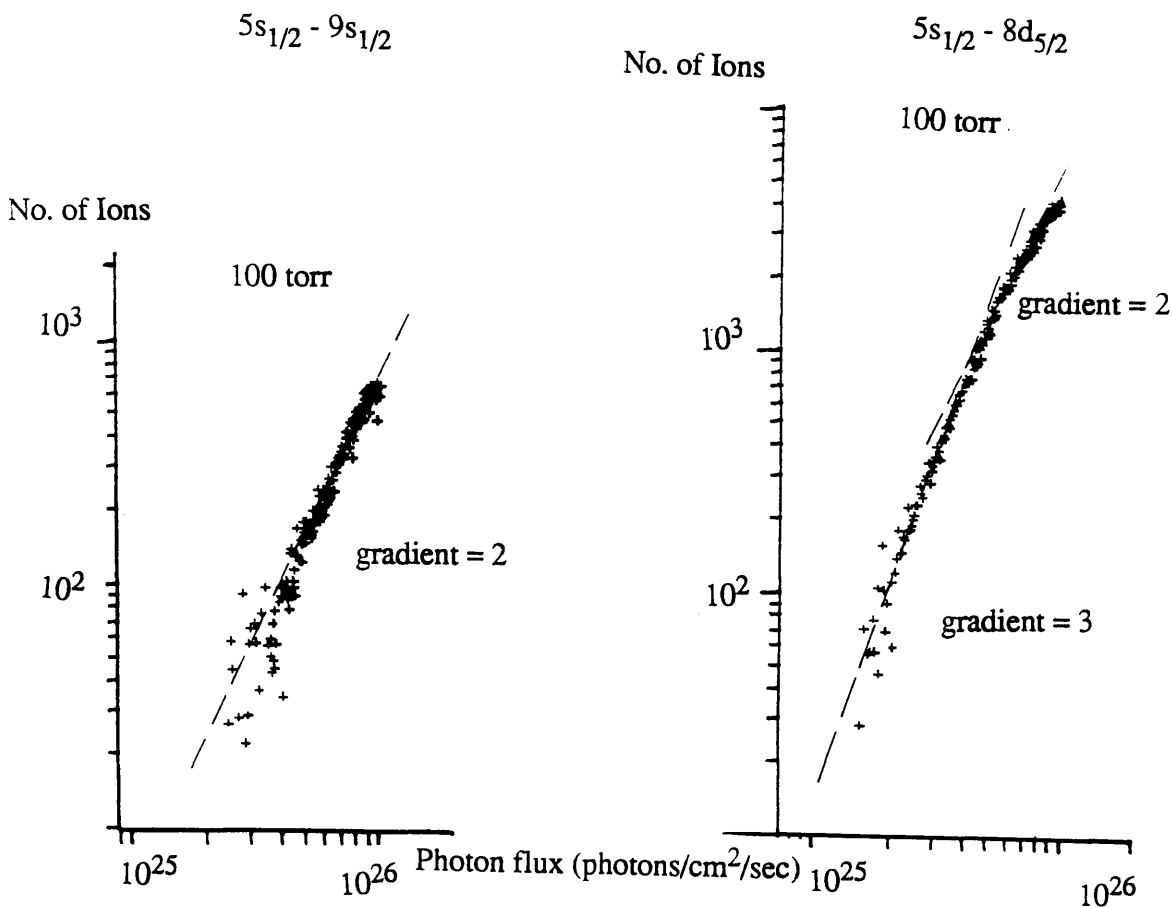


Figure 4.21 Power dependence curves for s and d transitions at 100 torr

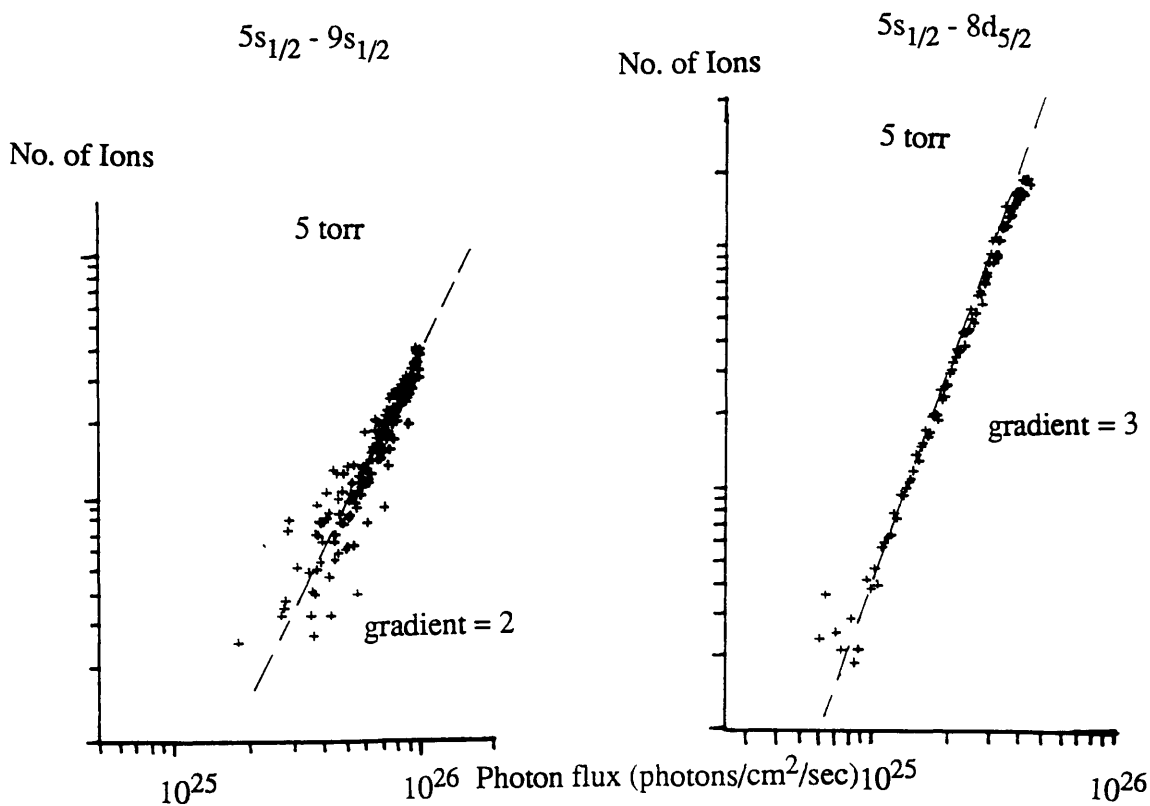


Figure 4.22 Power dependence curve for s and d transitions at 5 torr

expected, ie. the ratio of $9s / 7d$ was 4.6×10^{-3} and $10s / 8d$ was 1.7×10^{-3} .

The enhanced ratio of s / d levels shown in Figure 4.19 would therefore appear to be collisionally induced. Further evidence for this is shown in the power dependence graphs. Figure 4.21 shows the power dependence of both s and d transitions at 100 torr. The $5s - 9s_{1/2}$ transition ($\lambda = 655.76\text{nm}$) shows a purely quadratic dependence, whilst the $5s - 8d_{5/2}$ transition ($\lambda = 640.56\text{nm}$) shows a cubic dependence which begins to saturate at high powers. Thus the s transition appears to be dominated by collisional effects more than the d transition. Figure 4.22 shows the power dependencies at a much lower pressure of 5 torr. The s transition still shows a purely quadratic behavior, whereas the d transition is cubically dependent except at the very highest laser power. This suggests that collisional ionisation is still the dominant mechanism for s states at 5 torr, and photoionisation for d states is the major effect. Niemax (1983) studied the effect of noble gas collisions on the intensities of rubidium principal series lines ($5s - np$) in a thermionic diode. Figure 4.23 (Niemax 1983) shows the collisional ionisation probability of rubidium atoms as a function of principal quantum number for three different buffer gas pressures. The probability value of 1 is reached for all three cases at around $n = 25 - 30$. From the graph, for a constant n value of, for example, 15, the collisional ionisation increases from 0.1 at 0.12 torr to 0.4 at 12 torr. The collisional ionisation at 100 torr is therefore highly likely, even at n values as low as 10 - 15. It is likely that s and d states of rubidium would be susceptible to collisions in the same manner. It can be assumed, therefore, that the s states in Figure 4.19 have been collisionally ionised. The corresponding d states are already close to saturation as a consequence of their higher photoionisation cross sections compared with s states (Pindzola 1984). The effect of collisions on these levels is therefore less noticeable.

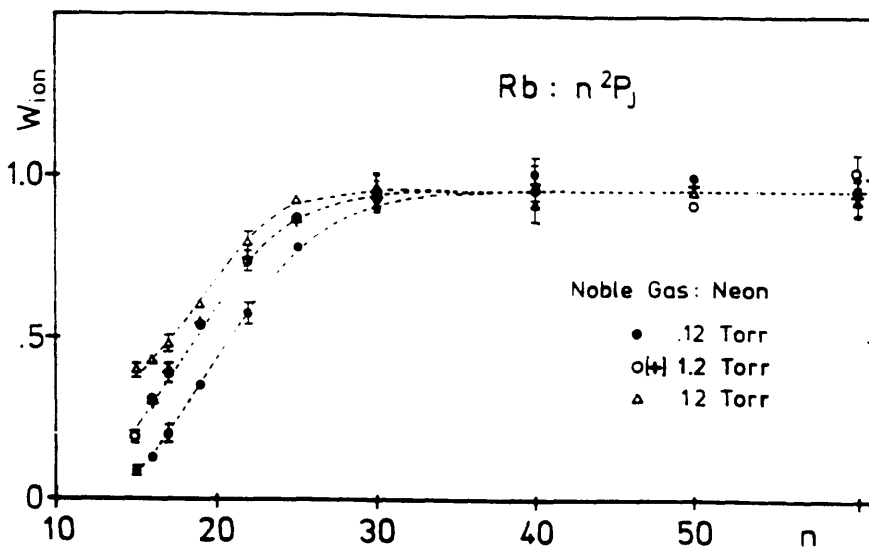


Figure 4.23 Collisional ionisation probability as a function of principal quantum number (Niemax 1983)

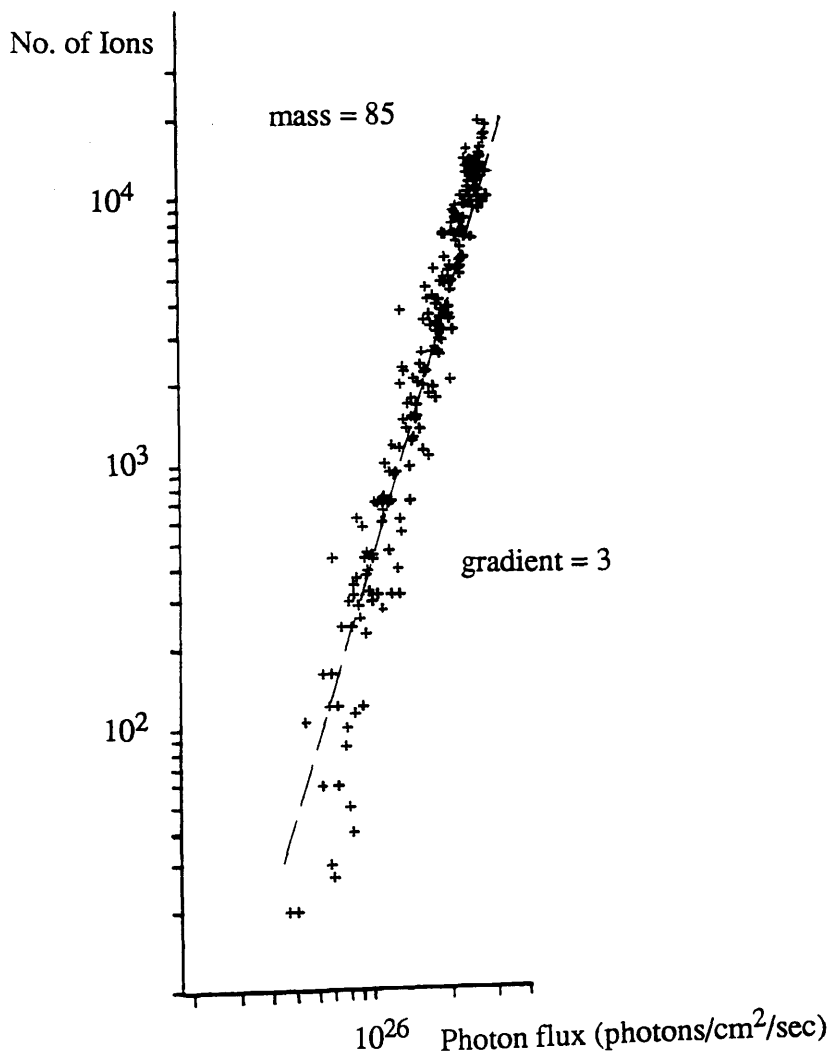
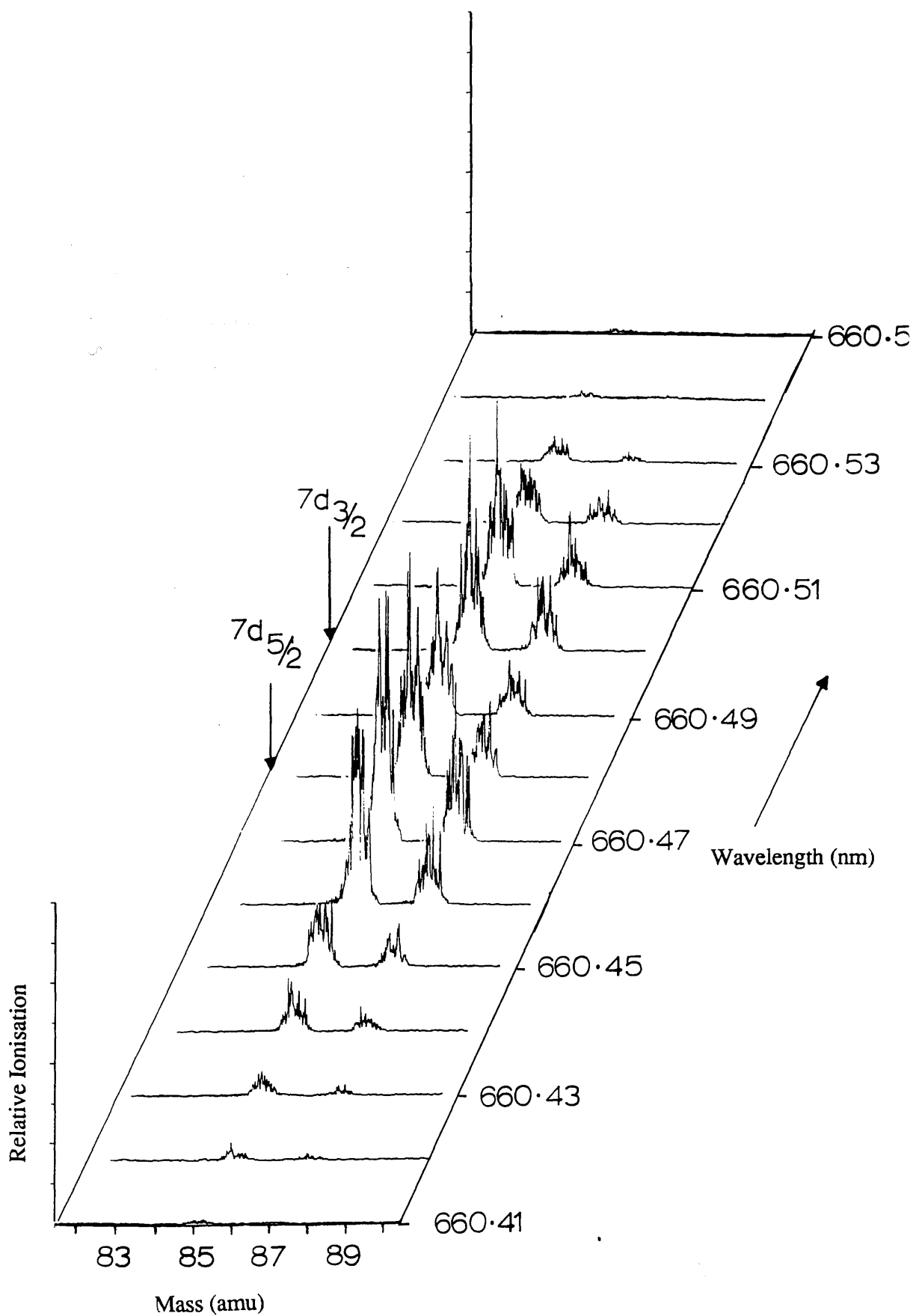


Figure 4.24 Power dependence curve for d transition at 2×10^{-6} torr

Figure 4.25 Relative ionisation as a function of both mass and wavelength over the 5s - 7d doublet transition in rubidium



A further decrease in pressure incurred when using the quadrupole mass spectrometer (2×10^{-6} torr) resulted in a purely cubic dependence for the d transition (Figure 4.24) implying little or no collisional ionisation at this pressure.

Figure 4.25 shows a scan of both mass and wavelength in order to determine the change in the isotopic ratio of rubidium over an atomic transition. The wavelength range included the 5s - 7d doublet transition. This doublet structure, in addition to the two isotopes of rubidium, is evident from the graph. Furthermore, within the accuracy of the experiment, the $^{85}\text{Rb} / ^{87}\text{Rb}$ ratio remains constant as the wavelength is incremented. The laser here has a linewidth of around 2.5 cm^{-1} compared with the isotopic splitting of the 5s level of 0.05 cm^{-1} . It was not expected, therefore, to observe any isotopic selectivity.

4.5 Atomic Mass Spectra

The quadrupole mass spectrometer was used in this experiment to study mass spectra of atomic and molecular rubidium. Initially, the quadrupole was set for transmission at mass 85 amu, and a wavelength scan between 419nm and 422nm was recorded showing the $5s_{1/2} - 6p_{3/2,1/2}$ doublet transition (see Figure 4.26). This was carried out at a relatively low power value of 5×10^{21} photons/cm² /sec. Laser power dependence graphs were taken on each peak of the doublet in order to assess the positions of saturation (Figures 4.27 and 4.28). In both cases, the saturation of the excitation step began at around 4×10^{22} photons/cm² /sec. The arrow on each graph indicates the power level of 5×10^{21} photons / cm² / sec for the wavelength scan, showing that neither the excitation nor the ionisation stages were near saturation.

A mass scan of rubidium taken off resonance at 430nm is shown in Figure

Relative Ionisation

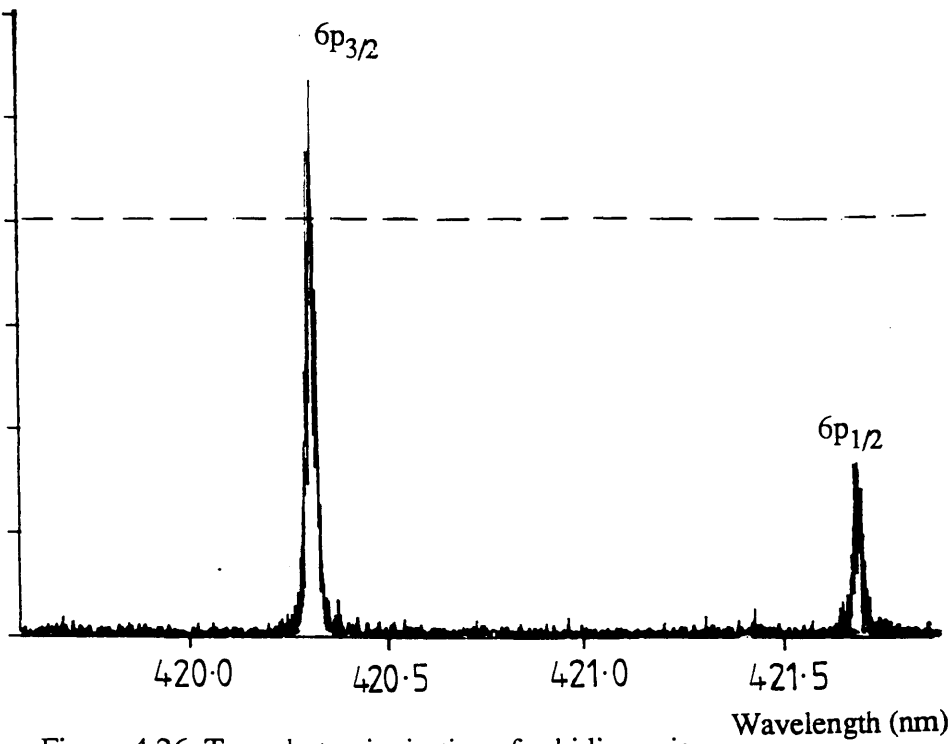


Figure 4.26 Two photon ionisation of rubidium via the $5s_{1/2} - 6p_{3/2,1/2}$ transition (5×10^{21} photons/cm²/sec)

No. of Ions

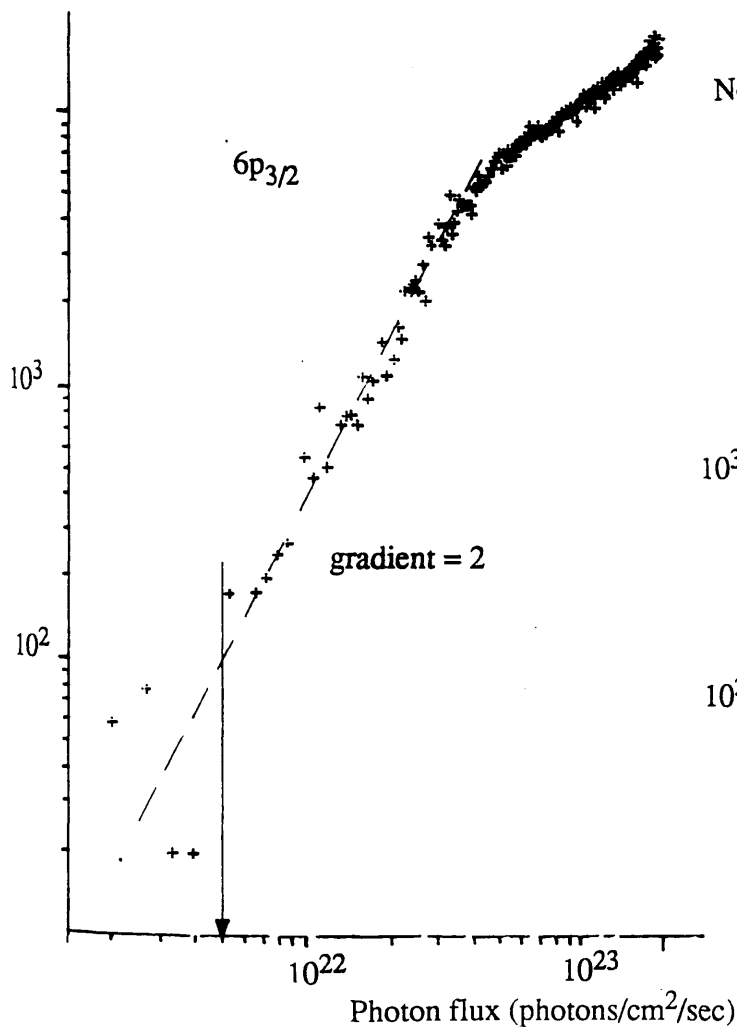


Figure 4.27 Power dependence curve for $5s_{1/2} - 6p_{3/2}$ transition

No. of Ions

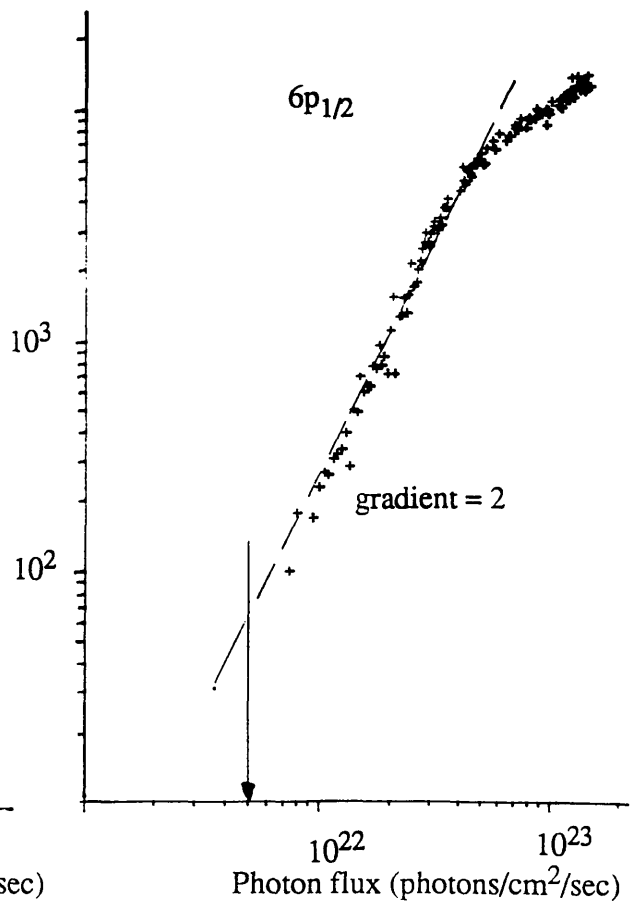


Figure 4.28 Power dependence curve for $5s_{1/2} - 6p_{1/2}$ transition

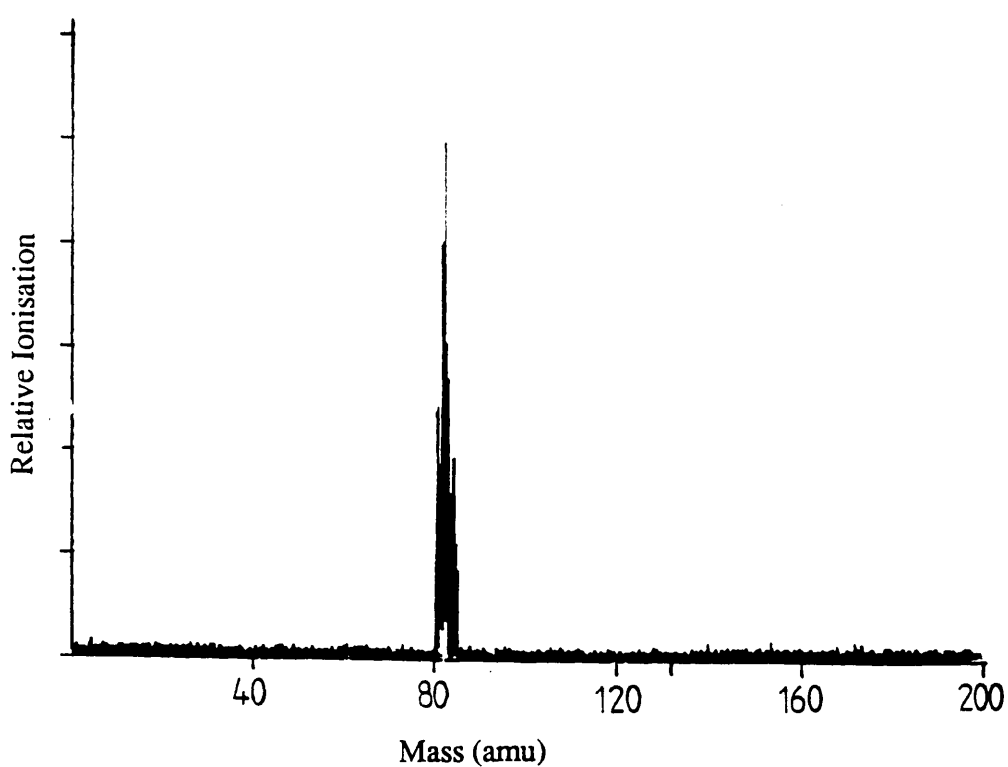


Figure 4.29 Mass spectrum off resonance at 430 nm (6.5×10^{25} photons/cm²/sec)

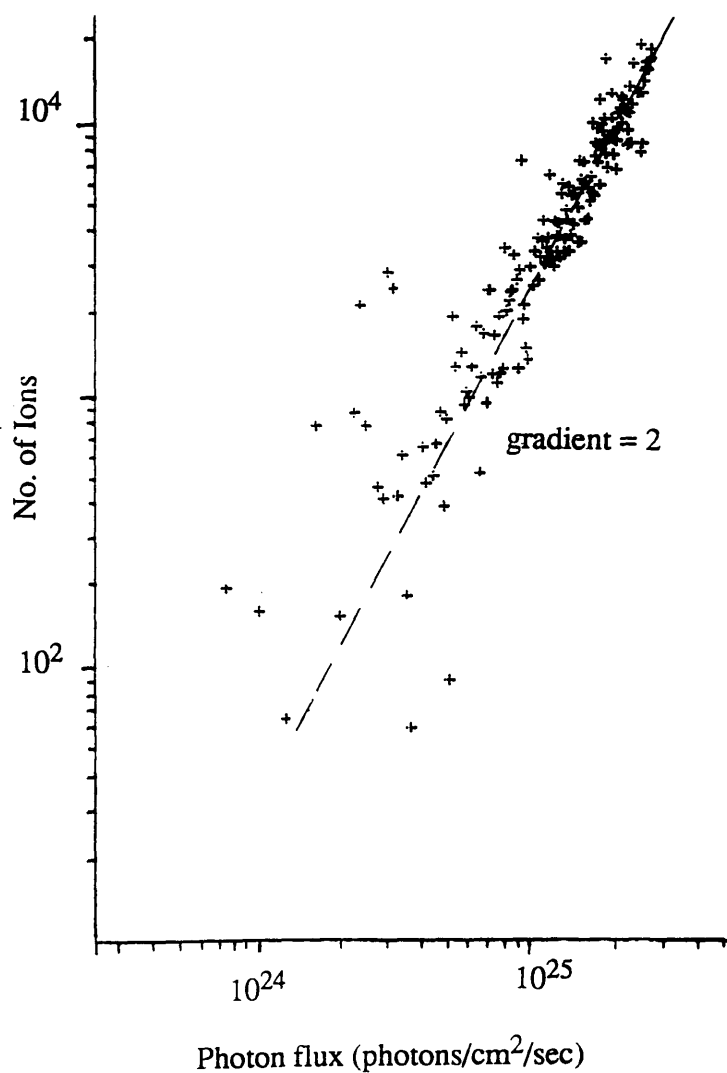


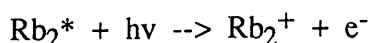
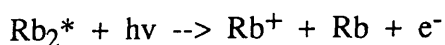
Figure 4.30 Power dependence curve for rubidium using a focussed laser beam at 430nm

4.29. In this scan, the laser power was increased by focussing to 6.5×10^{25} photons/cm² /sec in order to distinguish the non resonant ionisation from noise. A power dependence graph at 430nm shows a quadratic dependence of ionisation on power (Figure 4.30). There was no indication of a molecular rubidium signal.

4.6 Molecular Mass Spectra

There are three possible combinations of rubidium atoms within a dimer, namely $^{85}\text{Rb} + ^{85}\text{Rb}$ (170 amu), $^{85}\text{Rb} + ^{87}\text{Rb}$ (172 amu) and $^{87}\text{Rb} + ^{87}\text{Rb}$ (174 amu). In an attempt to observe molecular dimers, mass spectra were taken at low resolution in order to maximise the transmission of the quadrupole. Figure 4.31 shows a mass spectrum taken at wavelength 420.78nm in which there is no evidence of the existence of dimers. The two isotopes of rubidium can just be resolved. (The laser flux was 5×10^{21} photons/cm² /sec). An increase in laser power to 5×10^{22} photons/cm² /sec still produced little evidence of dimer signal (see Figure 4.32).

Granneman et al (1976) suggested two possible methods of ionisation of the rubidium dimer, ie. absorption of one photon by the ground state molecule $X^1\Sigma_g^+$ followed by absorption of a second photon to produce either a rubidium atomic ion Rb^+ and a neutral atom or a molecular ion Rb_2^+ .



where Rb_2^* denotes an excited molecular dimer. The first method here would not, in fact, produce a molecular signal, but would contribute to the atomic signal. The absence of a molecular signal in this case was due to three main factors:-

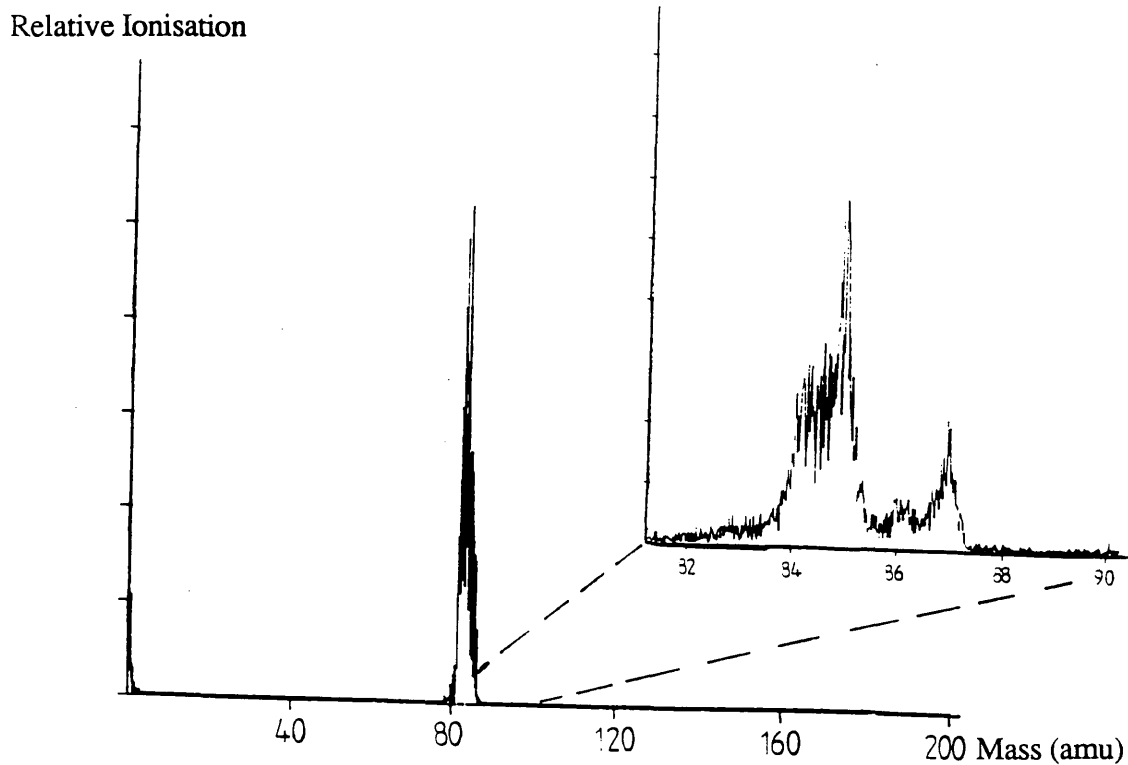


Figure 4.31 Mass spectrum of rubidium on $5s_{1/2} - 6p_{3/2}$ transition at 420.78nm (5×10^{21} photons/cm²/sec)

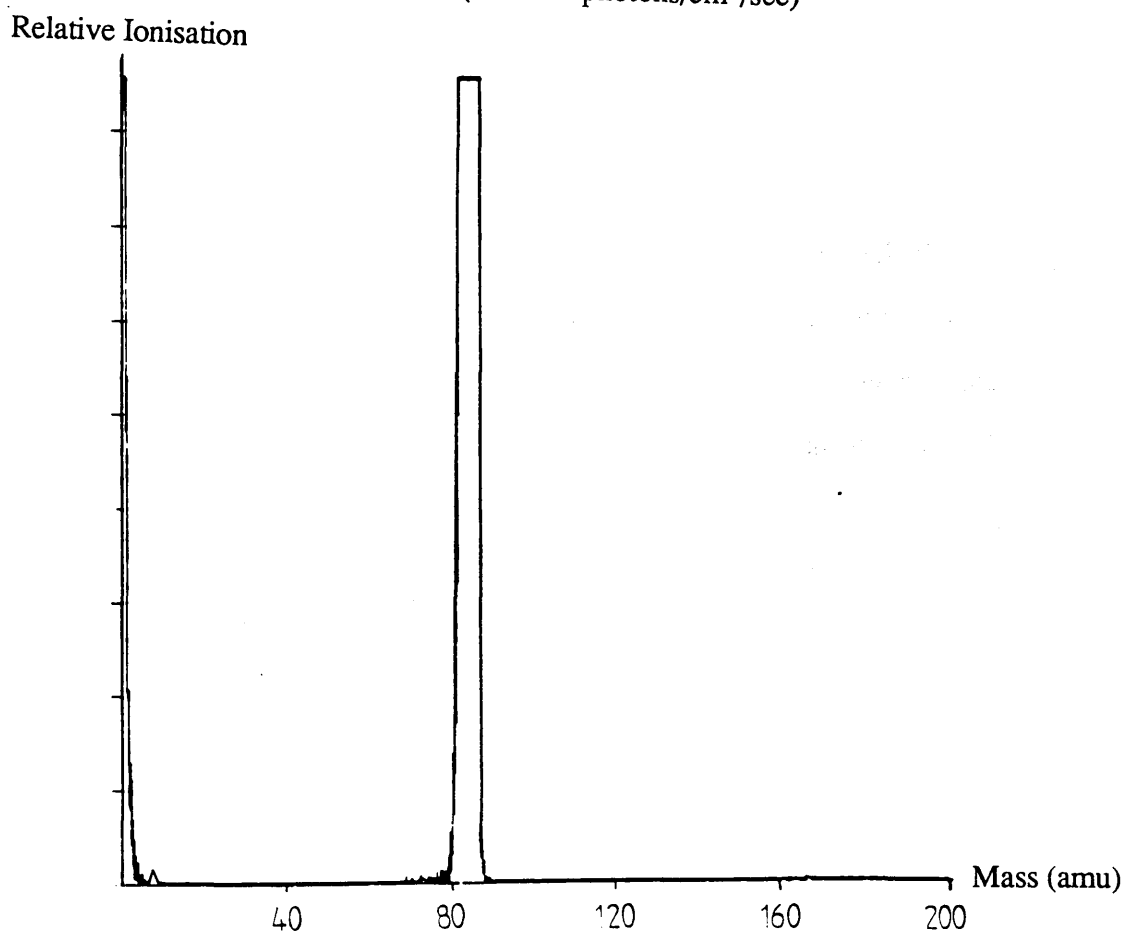


Figure 4.32 Mass spectrum of rubidium on $5s_{1/2} - 6p_{3/2}$ transition at 420.78nm (5×10^{22} photons/cm²/sec)

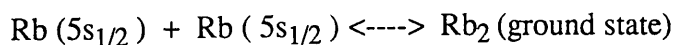
1) The low transmission efficiency of the quadrupole - only around 1% of the ions are detected.

2) The overall cross section is fairly small ($2 \times 10^{-43} \text{ cm}^4 \text{ sec}$), and consequently, little ionisation would occur at the power levels used.

3) The interaction region will contain a very small number of atoms (2×10^4). Focussing the laser would further reduce this - a focussed beam of dimensions $0.13\text{mm}^2 \times 10\text{mm}$ is likely to contain less than 100 molecules.

It was therefore decided to increase the dimer population by heating the rubidium reservoir. The temperature was raised to 410K and was carefully monitored as a pressure of more than 5×10^{-5} torr may cause damage to the quadrupole. At this temperature, the vapour pressure of atomic rubidium is 5×10^{-4} torr (2×10^{13} atoms / cm^3) and that of molecular rubidium is 2×10^{-7} torr (7×10^9 molecules / cm^3).

This increase in temperature resulted in the detection of a molecular signal. Figure 4.33 shows a wavelength scan at mass 170 using a focussed laser. The spectrum shape reflects the tuning curve of the laser dye. Gupta et al (1978), however, report a broad absorption band for the rubidium molecule, centred at wavelength 430nm. The two prominent dips in the spectra correspond to the atomic rubidium doublet transition $5s_{1/2}$ to $6p_{3/2,1/2}$. Thus when the laser is tuned to an atomic resonance, the molecular signal drops to approximately background level. This effect can be explained in terms of the equilibrium between atomic and molecular formation, ie.



On an atomic resonance, most of the ground state rubidium atoms will become excited, and as a result the equilibrium will shift as to favour dissociation of the

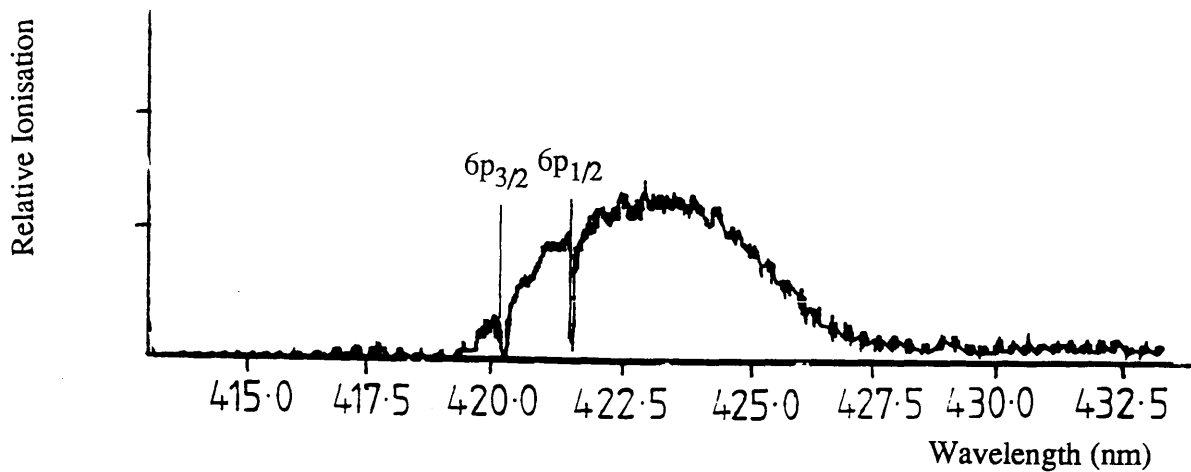


Figure 4.33 Wavelength scan at rubidium dimer mass 170 amu using a focussed laser

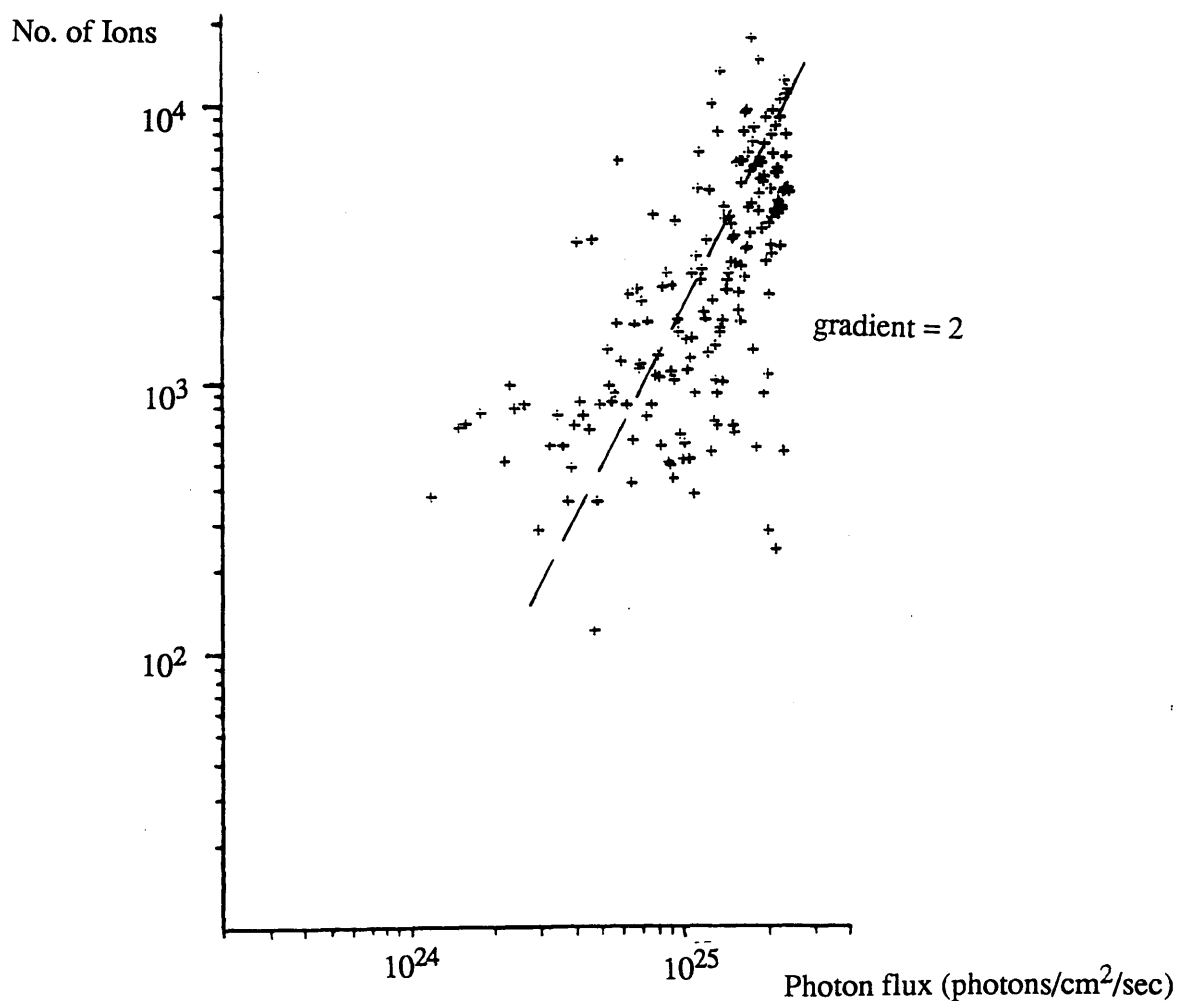
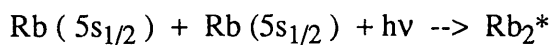


Figure 4.34 Power dependence curve for focussed laser at 427.1 nm

rubidium molecule (assuming sufficient laser power). There will therefore be few ground state molecules available for ionisation. As the laser is tuned off an atomic resonance, the molecular excitation process will approach saturation (depending on laser power) and the equilibrium will shift in favour of creation of the rubidium molecules.

This result could also be explained in terms of the effect of the radiation field on the formation of the excited state molecule, ie.



In this process, the formation of the excited molecule is dependent on the intensity of the laser flux. As in the previous explanation, the depletion of the number of ground state atoms available is directly responsible for the sudden drop in molecular ionisation yield at the atomic resonance wavelength. Figure 4.34 shows a power dependence curve taken at 427.1nm using a focussed laser. The large spread in ionisation is indicative of a small number of ions being formed.

From the above results, it is clear that at room temperature, the molecular component of the ionisation is negligible. Techniques such as laser ablation and ion sputtering, however, may result in a considerable increase in the molecular population. Kimock (1984) suggested that dimers and other large molecular components may account for up to 10% of the sputtered particles during the process of ion ablation. This could have a substantial effect on the sensitivity of RIMS as an analytical technique.

CHAPTER 5 LASER TIME OF FLIGHT MASS SPECTROMETER

5.1 Introduction

Resonance ionisation mass spectrometry has been demonstrated to be a very sensitive and selective analytical technique (Fassett et al 1984, Tembreull and Lubman 1986). This chapter describes the study at Glasgow of laser resonant ionisation in time of flight (TOF) mass spectrometers. The increasing importance of this technique is reflected in the interest shown by several commercial firms to manufacture RIMS instruments. The laser TOF mass spectrometer at Glasgow has been developed in collaboration with Kratos Analytical / Cambridge Mass Spectrometry Ltd. and has been designed and constructed specifically to be suitable for the commercial market. The instrument's main purpose is ultra - trace analysis, although profiling can also be carried out. A second laser ionisation mass spectrometer has been built primarily for depth profiling studies of semiconductors, and is described in more detail in Appendix 2. The main part of this research has involved the ultra - trace analysis instrument.

The ultra - trace analysis process can be divided into three main sections. Firstly, the solid sample is vaporised. The ionisation process then involves the use of precisely tuned dye lasers to selectively ionise an element of interest. The ionised atoms are then detected in the TOF mass spectrometer. Each section will be discussed in detail.

5.2 Vaporisation of Sample

The RIS process is applied only to atoms in the gaseous phase, and therefore the analysis of solids requires a vaporisation technique. There are currently four main methods of evaporation :-

1) Thermal Vaporisation

Initial studies of RIS tended to utilise thermal vaporisation (Donahue et al 1984, Nogar et al 1984, Travis et al 1984). By this method, electrically heated filaments are coated with minute quantities (microgrammmes- nanogrammes) of the required sample. A layer of graphite is often used as an overcoating to effect the reduction of metals deposited as salts, thereby encouraging the evaporation of free atoms instead of molecules.

2) Ion Beam Sputtering

A source of noble gas ions eg, Ar^+ , Kr^+ , is used to form an ion beam which can generally operate in pulsed or continuous mode. Winograd (1984), Becker and Gillen (1984), and Pellin et al (1984) emphasise the importance of ion beam sputtering for surface studies.

3) Glow Discharge

This method has been demonstrated by Harrison et al (1984) and by Savickas et al (1984). Here, the sample is adapted to form a cathode, with argon gas maintaining the glow discharge. Improved sample utilisation may be achieved by pulsing the discharge.

4) Laser Ablation / Desorption

This has been developed mainly by Becker and Gillen (1984) and by Williams et al (1984). Pulsing the laser results in a high sample utilisation for pulsed RIS

analysis. Low powered laser evaporation is generally referred to as desorption, and the term ablation is used for higher laser powers ($>10^9$ W/cm²).

The Glasgow RIMS instrument has been designed such that either ion gun sputtering or laser ablation may be carried out. Both techniques will be described in greater detail in the following sections. Ion gun sputtering is currently used widely in the SIMS technique applied to surface analysis and depth profiling.

5.3 Use of SIMS as an Analytical Technique

Secondary Ionisation Mass Spectrometry (SIMS) is used to obtain information on the compositional and structural state of a sample surface. The technique is based on the fact that charged atomic or molecular species are ejected from the surface of a liquid or solid under heavy particle bombardment. The removal of surface material can be attained by two different SIMS processes - static and dynamic SIMS. In static SIMS, information on the composition of the uppermost monolayer is obtained with as little disturbance of the composition and structure as possible. This can be achieved by use of a very low primary ion current density (around 10^{-9} Acm⁻²). This technique is often applied to monolayer analysis, as the rate of removal of a monolayer can be as long as several hours. Static SIMS can be used as a complementary technique to Auger Electron Spectroscopy, X - ray Photoelectron Spectroscopy, Ion Scattering Spectroscopy or Thermal Desorption Mass Spectroscopy in surface studies. Dynamic SIMS uses a high primary ion current of a few Acm⁻² for fast surface erosion thereby shortening the lifetime of a monolayer to around 10^{-3} seconds. This technique is used to supply information on the originally deeper layers of the sample. Depth profiling requires dynamic SIMS to determine elemental concentration with high sensitivity down to parts per billion level. Dynamic SIMS is used widely in semiconductor and integrated circuit analysis.

During this bombardment by ions or neutral particles - normally in the range of a few KeV - surface particles are sputtered and the primary bombarding particle may be embedded into the target sample. The impact of the primary particle on the surface causes an energy and momentum transfer to a limited area around the point of particle impact, resulting in :-

- 1) a change of the lattice structure
- 2) loss of surface material by sputtering

The ion bombardment induced emission processes include electron and photon emission as well as emission of surface particles (atoms or molecules) in a charged or uncharged and possibly excited state. The secondary ion emission includes all emitted ionised surface particles in the ground state as well as the excited state - these ions can be separated by use of one of the many types of mass analyser.

One of the most important features of SIMS is the analysis of the uppermost monolayer of a solid. Application of a focussed primary particle beam scanned over the surface of the solid will enable information about the lateral surface distribution of the secondary ion emission to be obtained and hence the chemical composition can be determined. If the sputter yield and the ionisation probability of the emitted species are known, this supplies direct information about the lateral elemental distribution.

The type of mass analyser used is determined by the required application. Static SIMS requires a mass spectrometer with a high overall transmission for ions originating from a relatively large area. Quadrupole mass spectrometers are generally used for this application. The detection of elements present in low concentration with the

additional requirement of high lateral resolution requires maximum use of all secondary ions produced. Two types of mass analyser are most suited for this type of high performance SIMS - the Time of Flight Mass Spectrometer and the ion cyclotron analyser. Both instruments have been applied successfully in static and dynamic SIMS studies.

A major drawback of SIMS is the lack of quantification (this is described in greater detail in Section 5.5). This may be achieved, however, by the additional application of analytical techniques such as Auger Electron Spectroscopy, X-ray Photoelectron Spectroscopy or Rutherford Backscatter Spectroscopy. Complementary use of static SIMS and such surface analytical techniques is considered to be the optimum approach to quantity studies.

A more recent development in surface analysis is the use of emitted neutrals. On average, over 99% of the particles emitted from a surface are uncharged (Robinson 1984, Winograd, 1984). The separation of these neutral particles from the emitted ions by means of laser photons results in a SIMS modification which improves the quantitative accuracy. This is the basis of the resonant ionisation technique as discussed in Chapter 1. Experiments comparing the SIMS analysis with resonant ionisation techniques are described in Chapter 6.

5.4 Sputtering Mechanism

It was initially assumed that the primary ion beam had the sole effect of localised heating of the solid around the point of contact. After experimental evidence to the contrary, this explanation was abandoned in favour of a momentum transfer approach resulting from the observation of preferred direction ejection in sputtering of single crystals. The collisional cascade model of Sigmund (1972) quantitatively explains the

features of sputtering. The energy and momentum transfer of primary particles to the target are explained by the concept of "cascades" of energetic collisions between ion and target particles and between recoil and stationary particles.

The sputtering of surface atoms can be explained as a consequence of collision cascades intersecting the surface, and in a binary collision, transferring enough energy and momentum to a surface atom to overcome the surface binding forces of the solid. A large amount of experimental data on total yields and energy distributions is available to support this collisional cascade theory. Sputtered atoms are mostly neutral atoms ejected in a broad angular distribution, which may contain significant structural information about the solid. Neutral atoms sputtered from a solid sample have an energy distribution that extends to several hundred electron volts. Fortunately, the distribution is sharply peaked and most of the neutral atoms are centred about an average energy of about 10 eV. Some ejected atoms are in excited states; they are accompanied by small numbers of atomic and molecular ions and by a few neutral molecules. The yield of ions and excited atoms is strongly influenced by surface contaminants, especially oxygen. Figure 5.1 shows results obtained by Townsend et al (1976) on the variation of sputter yield with increasing incident energy of noble gas ions.

5.5 Matrix effects

The SIMS technique suffers the disadvantage of the ion signal being dependent upon the composition of the surface. This is known as the matrix effect. The change in surface composition can be a result of a number of different processes:-

- 1) Interactions between the primary ions and the matrix, for example, primary ion implantation into the sample or recoil implantation of surface adsorbed species by the primary ions.

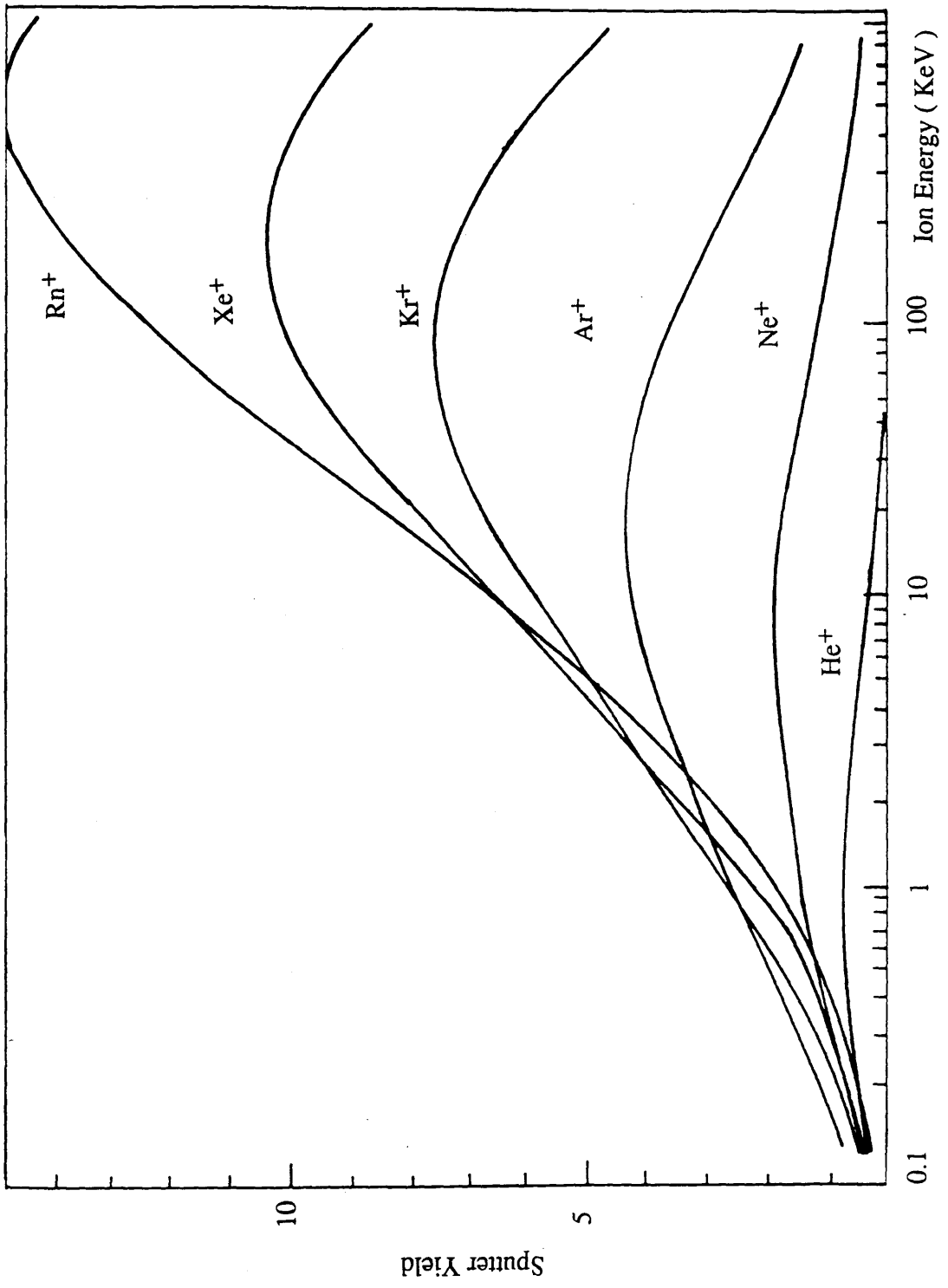


Figure 5.1 Variation of sputter yield with ion energy for noble gas ion beams

2) Incorporation of elements in the analysed surface or in the near surface layers caused by redeposition.

3) Diffusion or migration of an element on the surface can take place due to vacancy or implant induced stress, electrical charging or temperature gradients.

4) Physisorption (caused by weak van der Waal's forces at the surface) or chemisorption (a result of chemical bonding with the surface) may take place either from the residual gas atmosphere or as a result of directing a beam of neutral gas onto the surface.

These matrix effects are the main drawback to using SIMS as an accurate quantitative analytical technique. SIMS is, however, a very useful technique for surface analysis because of its high detection power, and its capacity to detect all elements (including hydrogen) and their isotopes and also to detect both organic and inorganic compounds. Although the sputtering/ionisation process can be highly controlled by varying the energy, current density, and composition of the sputtering ion beam, the ionisation efficiency is low and is greatly affected by the chemistry of the sputtering region. The main difference between SIMS and RIMS is that the latter analyses the neutral vaporised atoms instead of the positive ions, with the resultant reduction in matrix effects.

Other surface analytical techniques which are presently applied enable at least a semi - quantitative determination of the element concentration, but cannot detect hydrogen. With the exception of XPS and AES, identification of compounds is not possible. A combination of SIMS with the resonant ionisation technique would result in high power detection with the added selectivity stage to give improved quantification.

5.6 Minibeam Ion Gun

Sputtering is carried out in the laser TOF mass spectrometer using a minibeam argon ion gun. The ion gun is an ultra high vacuum (UHV) device which contains an ion source, an ion extractor section, an electrostatic lens section for beam focussing and deflection plates to control the ion beam. A diagram of the ion gun components is shown in Figure 5.2.

The gun used for sputtering in the RIMS machine is a Kratos Minibeam ion gun. The gun is mountable on a standard 70mm UHV flange and can be operated at voltages up to +5000V and at pressures up to 10^{-4} torr. The ion gun control unit contains power supplies to provide an ion beam voltage ranging from 0V to +5000V, deflection voltages in the range 0V to 250V (either polarity), a grid voltage 50V to 300V. The filament current can be varied between 0 and 2.5A with a maximum 7.5V. This filament current is controlled using a feedback system to maintain a constant electron emission current.

This ion gun is usually filled with argon gas, and can be operated in either pulsed or continuous mode. Pulsed dye lasers are needed to achieve the high laser power requirements, and therefore, the best sample utilisation is achieved if the ion gun is also pulsed. Currently available continuous dye lasers have insufficient power to saturate a transition and also do not operate in the required near UV regions. Pulsing the ion gun also has the advantage of increasing the life of the sample - continuous operation quickly erodes away the sample.

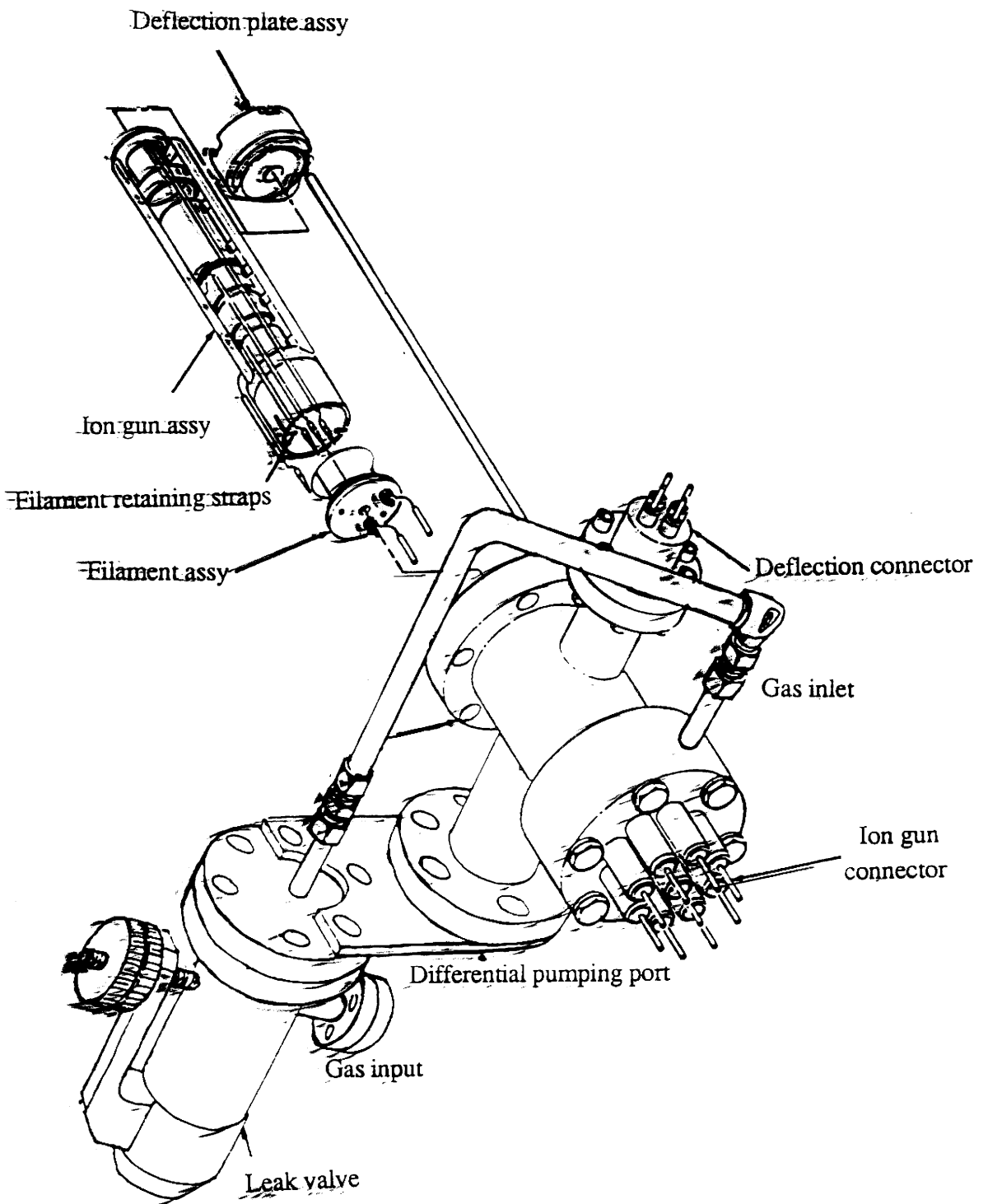


Figure 5.2 Ion gun components

5.7 Laser Desorption

The use of pulsed lasers with continuous sample evaporation can result in substantial loss of analyte because of the low effective duty cycle. The use of pulsed lasers to desorb the sample can substantially increase the sample utilisation efficiency (Apel et al 1986).

Recently, laser ablation and desorption have become very popular as a method of vaporising solid samples for RIMS technology. The use of laser desorption coupled with RIMS detection of sputtered neutrals has a number of advantages:-

1) The duty cycle for analytical samples is vastly improved relative to thermal evaporation (Miller et al 1982).

2) Laser desorption can be applied to any material, can be used as a microprobe, and is simple to implement and operate.

3) No background is introduced due to bulk heating of the sample.

4) Spatial resolution is limited only by diffraction (typically 1 μ m in diameter).

5) Little sample preparation is necessary.

6) Sensitivity is excellent, with detection limits in the sub ppb range. (Nogar et al 1988)

The process involved in the interaction between laser and solid differs from

the ion beam sputtering mechanism. The amount of evaporated material is determined by the basic physical properties of the sample such as surface reflectivity of the laser wavelength, density, specific heat, thermal conductivity, melting point and heat of vaporisation.

As a laser beam strikes a solid surface, the energy is absorbed by conduction electrons and is quickly transferred to the lattice. There are two possible mechanisms for the production of vaporised species (Ready 1971), depending on the incident power intensities.

For low power densities ($< 10^9$ W/cm²), the material simply heats and evaporates, creating a relatively small number of ions. This is generally referred to as laser desorption. Higher power densities initiate the recoil of vaporised surface material, creating a shock wave which propagates through the solid, causing melting and vaporising of the material as it passes. This higher power technique is normally classed as laser ablation.

If the pressure and temperature of the material exceed the thermodynamic critical point, there is no longer a distinction between liquid and vapour. Vaporisation then takes place as the explosive expansion of the highly compressed, highly ionised plasma. The plasma can absorb laser radiation directly, producing net ionisation of up to 100%. This plasma may reach high local temperatures in the 10^4 - 10^5 K range (Mayo et al 1982).

Unfortunately, large thermal gradients in the sample can produce large mechanical stresses and the resulting effluent from the crater may contain a significant fraction of clusters in addition to the expected free atom, ion, and molecule content (Kelly and Rothenberg 1985). For most analytical purposes, high sample utilisation efficiency

is required, making it important to suppress the formation of particles and clusters in favour of free atoms. Beekman and Callcott (1984) have measured the kinetic temperature of a laser ablated vapour cloud of samarium, and have obtained values of around 1200K. This was compared with a calculated excitation temperature of approximately 1600K. The significant difference between the two values was attributed to a lack of equilibrium between the population of atomic energy levels and the kinetic energy of neutral atoms, resulting from recombination and de-excitation processes.

Using this desorption technique, synchronised ionisation laser pulses can be applied close to the heated spot to catch the desorbed atoms, thus alleviating the low efficiency problem caused by the poor temporal duty cycle of the pulsed dye laser. The laser used for desorption in this research has been a Quantel Nd:YAG laser with outputs at four possible wavelengths: 1064nm, 532nm, 355nm and 266nm. In Chapter 6, experiments are described in which a dye laser has been used for both desorption and ionisation of the sample in a similar manner to the SIMS technique, thus allowing the process of laser desorption to be studied in greater detail.

5.8 Resonant Ionisation

Having created a vapour cloud in the ionisation region of the mass spectrometer, the next stage in the analysis process is the selective ionisation of the required atom or molecule. The five basic ionisation schemes have already been described in Chapter 1. The efficiency of this stage is very much dependent on the ionisation scheme chosen. Saturation of the resonant ionisation process, ie. every atom of the required type is ionised, is more easily achievable by using single photon steps rather than multiphoton ionisation.

RIS is a spectroscopic technique, but differs from other spectroscopic

techniques in that the detection of the absorption of light depends on ion or electron detection and does not depend on a direct measurement of the absorption of photons. Thus, RIS detection suffers no photon background effects as compared with normal spectroscopic methods which must deal with a photon background.

The RIS process involves the sequential absorption of photons having energies which match the bound - bound transitions, followed by a bound - continuum transition which yields an ion pair. The final transition may be achieved by a number of mechanisms other than photoionisation, eg. field, Penning or collisional ionisation via Rydberg states (A more detailed explanation is given in Chapter 1). These methods have the advantage of requiring a fairly low laser power (around $0.1\text{mJ}/\text{cm}^2$), resulting in a reduction of the background signal. A direct photoionisation process requires high power of greater than $100\text{mJ}/\text{cm}^2$ for the photoionisation step. Another possibility would be photoionisation into autoionisation levels in the continuum, which would reduce the required laser power.

5.9 Detection using Time of Flight Mass Spectrometers

In this research, time of flight mass spectrometers have been chosen as the most suitable for ultra trace analysis using RIS. A general description of the TOF mass spectrometer has been given in Chapter 2. This section explains the advantages of TOF systems over other mass spectrometers and discusses methods of optimising the resolving power.

Time of flight mass spectrometers have three main advantages over other types of mass spectrometers. One advantage is the ease of design and construction compared with other mass spectrometric methods (eg. Fourier Transform, magnetic sector, etc.). A second feature of the TOF mass spectrometer is that the entire mass

spectrum can be recorded for each laser pulse. It is therefore possible to accurately measure the relative intensities of mass peaks and also isotope ratios, even with unpredictable changes in source conditions or laser power. The third main advantage of the TOF mass spectrometer is that its accuracy is dependent on electronic circuitry rather than precise mechanical alignment. The main disadvantage of the TOF mass spectrometer is the limited resolution. Basic TOF mass spectrometers may have a useful resolution of only a few hundred amu. The resolution may be improved by methods described later in this chapter.

5.10 Resolution of the TOF Mass Spectrometer

In theory, if all ions were formed in a plane parallel to the source electrodes with zero initial velocity, then all ions having the same mass / charge ratio would have identical flight times and the resolution would be virtually unlimited. In practice, however, the resolution of a time of flight mass spectrometer is limited basically by time broadening caused by the inevitable initial space and kinetic energy distributions of the ions in the ionisation region.

Resolution in a time of flight mass spectrometer is defined as the largest mass M for which the adjacent masses are completely separated, i.e. the mass for which the time spread for ions of the same mass equals the time between adjacent masses. Measurement of mass may be proportional to either the peak area or the peak height. In general, measurements of peak heights are much more sensitive to variations in peak shape and therefore, in this research work, measurement of peak areas has been used. Improvements in the resolution may be brought about by three different methods - time, space and energy focussing.

"Time focussing" refers to methods for ensuring that ions of the same mass /

charge ratio, leaving the ionisation region at a given moment, all reach the detector simultaneously, despite an inevitable energy spread. In the ionisation process, the length of the ionising laser pulse is around 6 nanoseconds, and hence the temporal distribution of the created ions is very small. The term "space resolution" refers to the spread in arrival times at the detector caused by spatial distribution at ionisation. "Energy resolution" concerns the spread in initial kinetic energy of the ions. The effects of the initial kinetic energy distribution can be minimised by use of very high accelerating voltages. For ions in the gas phase, however, the problem is more complex since "space focussing" is best achieved when low voltages are imposed across the ionisation region. The best resolution, therefore, is a compromise between space and energy resolution.

Wiley and McLaren (1955) observed that ions having the same mass / charge ratio have a spread of arrival times at the detector due to the spatial distribution at ionisation and also the initial kinetic energy distribution of the ions. A pulsed two grid ion source was therefore designed by Wiley and McLaren with its dimensions optimised for space and energy resolution.

The number of vaporised atoms present in the ionising laser beam is dependent on a number of factors. These include the diameter of the desorbing laser beam and the time delay between the desorbing and ionising pulses. Desorption of the sample by laser or sputtering by ion gun creates a plume of neutral and excited atoms with a wide range of kinetic energies. The ionising laser pulse is of the order of 10ns. Only a fraction of the desorbed atoms will be interrogated by the laser beam - those with velocities too great or too small will be outside the beam dimensions. The ionising laser beam can be expanded to cover a larger number of vaporised atoms - this can be important for ultra trace analysis. Expanding the laser beam has, however, the effect of decreasing the laser flux and hence the probability of ionisation is reduced. It also increases the spatial distribution of the atoms with a resulting decrease in resolution.

While the temporal width of the laser pulse can be made so that it does not affect the TOF-MS resolution, even a tightly focussed laser has a non-negligible diameter. Since electrostatic potential varies with position in the ionisation region, ions formed at different positions are accelerated to different final velocities. This leads to a spread in ion flight times which is dependent on the size of the focal spot. Focussing the laser beam would increase the laser flux and increase the resolution, but decrease the interaction volume. Hence, the size of the laser beam used is essentially a compromise between optimising the resolution and the sensitivity of the system. In trace element analysis, an unfocussed laser is normally preferable to maximise the interaction volume.

The magnitude of the accelerating voltage used also affects the resolution. A high electric field in the ionisation region tends to minimise broadening due to the initial kinetic energy distribution, but it amplifies broadening due to the spatial distribution of the ions. It is therefore necessary to optimise grid spacings and applied potential in order to attain the highest mass resolution.

A number of methods have been proposed in the last few years to increase resolution by eliminating or compensating for ion kinetic and spatial distributions. Wiley and McLaren originally introduced the idea of space focussing which makes the flight time almost independent of initial position. Space focussing depends on the fact that ions initially produced closer to the detector acquire less energy from the electric field, and therefore are eventually overtaken by ions which have larger initial velocities.

Energy focussing can be brought about by either time lag focussing or by use of an ion reflector. The concept of time lag focussing was first demonstrated by Wiley and McLaren. By this method, there is a variable time delay between the ionisation

pulse and the ion acceleration pulse. During the time lag, the ions having different velocities move to new positions in the ionisation region. When the ion acceleration pulse is turned on, the ions closer to the exit grid are given a smaller voltage potential than those further away from the exit grid. Consequently, ions further from the grid will have larger final velocities than those closer to the grid. It is therefore possible to adjust the length of the time lag so that while the ions are in flight to the detector, the initially slower moving ions can catch up with the originally higher velocity ions, and all ions with the same mass can be made to arrive at the ion detector at the same time. Wiley and McLaren reported a significant increase in energy resolution using this technique.

The reflectron mass spectrometer was introduced as a means of energy focussing by Mamyrin et al, and causes the ions to be reflected once by a reverse electric field. Relatively fast ions penetrate deeper into the reflecting field and take a longer time to return than slow ions. This compensates for their faster velocity in the drift tube. Thus fast or slow ions with the same mass / charge ratio can be temporally focussed at the detector. The time and velocity distributions of ions leaving the first acceleration region depends on both the spatial and kinetic energy distributions. Unfortunately, the reflectron can focus only one of these distributions and not both simultaneously. Resolution and signal to background ratios are better than in a linear instrument. A reflectron system has been incorporated into the ultra-trace RIMS instrument (see Chapter 2), and has proved very effective in improving the energy resolution. Mass resolving powers with Reflectron TOF instruments of 10,000 or better have been achieved (Boesl et al 1987).

5.11 Laser Mass Spectrometer for Ultra-Trace Analysis

The ultra-trace analysis instrument has been designed and constructed in Glasgow, and has previously been described in Chapter 2. It incorporates a reflectron

system for energy focussing, and an electrostatic particle guide to improve the ion transmission efficiency. This takes the form of a fine wire stretched along the axis of the drift tube. A small voltage of around 10V is applied to the wire, and the ions follow a spiral orbit down the length of the tube. There is no perturbation of the flight time due to the spiral trajectory. A reduction of the applied voltage results in a reduction of the effective ion acceptance cone, thereby enhancing the resolving power at the expense of sensitivity. Voltage potentials on the sample stub and extraction optics are carefully chosen to optimise the space focussing effect.

The desorbing laser or ion gun is incident at an angle onto the solid sample surface. It has been established that the most effective angle of incidence for ion sputtering is between 45° and 60° to the sample normal (Townsend et al 1976). The ion beam is incident at a 55° angle to the normal of the sample surface. Laser ablation may take place at incident angles of either 45° or 55° to the normal, depending on the port used.

5.12 Preliminary Results

Initial results from this machine were taken of laser desorption and ionisation of rubidium. Rubidium was chosen as its spectroscopy had been previously studied in detail. The initial results were taken in order to physically align the system and to optimise its performance.

A sample of rubidium chloride salt was used instead of rubidium metal which would have been difficult to introduce into the mass spectrometer. The concentration of rubidium in the sample was a few percent. This was used to coat the surface of a conducting graphite substrate. A conducting sample was necessary in order to avoid a build up of charge on the sample stub, which could affect the electric field in

the ion optic extraction region. Variation in this electric field could result in a time jitter in the detector signal.

Figure 5.3 shows the results obtained using the dye laser to both desorb and resonantly ionise the rubidium atoms. The gate of the ADC was set to coincide with ion signals from the rubidium isotope at mass 85. A desorption dye laser, with a tuning range between 415nm - 430nm was focussed onto the rubidium chloride sample at a grazing incidence of approximately 5 J/cm^2 . Resonant structure was observed with the two major peaks assigned to the resonant two photon ionisation of rubidium through $5s_{1/2} - 6p_{3/2}$ and $5s_{1/2} - 6p_{1/2}$ transitions. The background structure is thought to be from resonance ionisation and dissociation of rubidium molecules. Evidence of a rubidium dimer signal is shown in an ionisation spectrum taken at mass 170 (see Figure 5.4). The dimer signal is a result of the two photon ionisation of Rb_2 molecules and also of the non resonant production of molecular ions. The dimer signals were approximately 10% of the atomic signal.

Figure 5.5 shows the resonant ionisation spectrum of the 5s-6p doublet transition of rubidium. This was obtained using continuous argon ion sputtering combined with ionisation from a blue dye laser. The $6p_{1/2}$ and $6p_{3/2}$ doublet can easily be resolved. The argon ion gun at this stage was operated in DC mode with the laser beam passing directly above the sputter region. The power of the laser was approximately 10 mJ/cm^2 and had a cross section area of 0.06 cm^2 . A TOF mass spectrum was recorded with argon ion sputtering, and the ionising laser set at 420.6nm, coinciding with the $5s_{1/2}$ to $6p_{3/2}$ transition (see Figure 5.6). The two isotopes of rubidium can be seen. The separation of the mass peaks was calculated to correspond to a mass resolution of around 100. Clearly, the resolution of the system at this stage was not optimised. A large background signal is evident; this signal may be obscuring the rubidium dimer signal.

Relative Ionisation

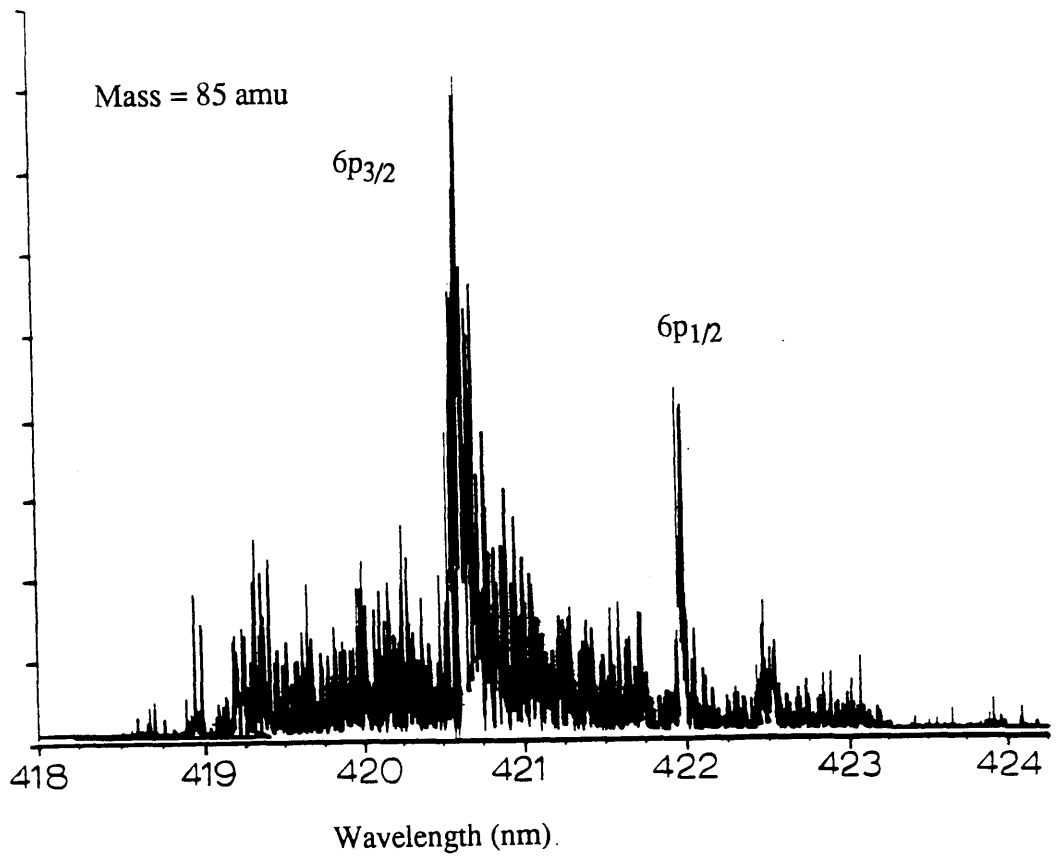


Figure 5.3 Detection of rubidium in TOF mass spectrometer

Relative Ionisation

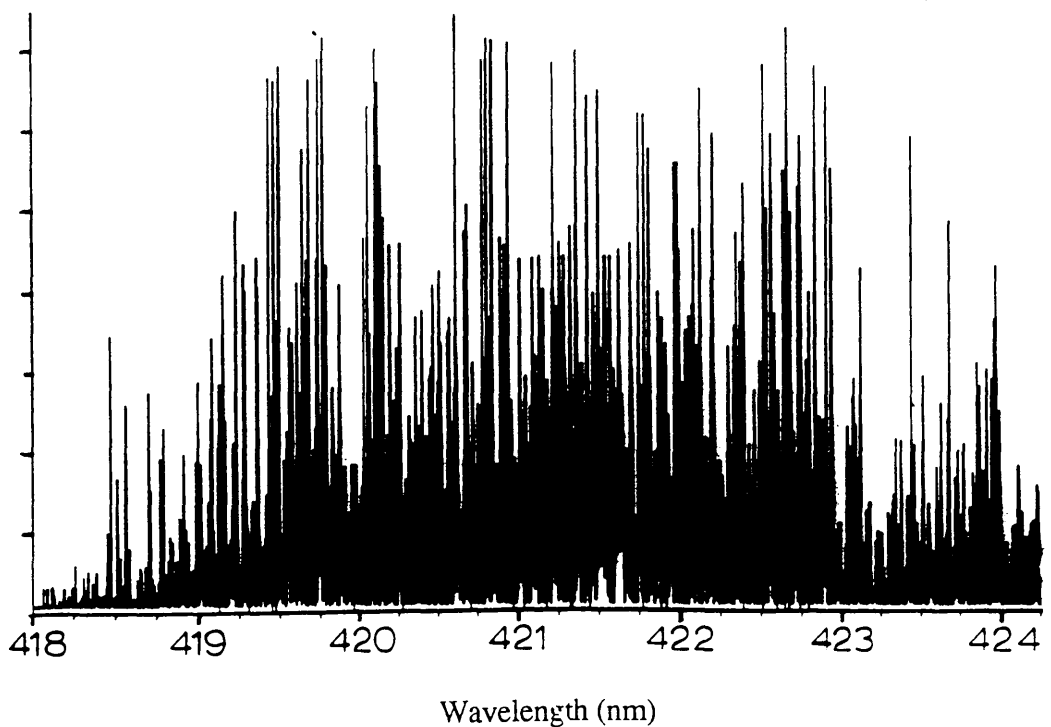


Figure 5.4 Detection of rubidium dimers in TOF mass spectrometer

Relative Ionisation

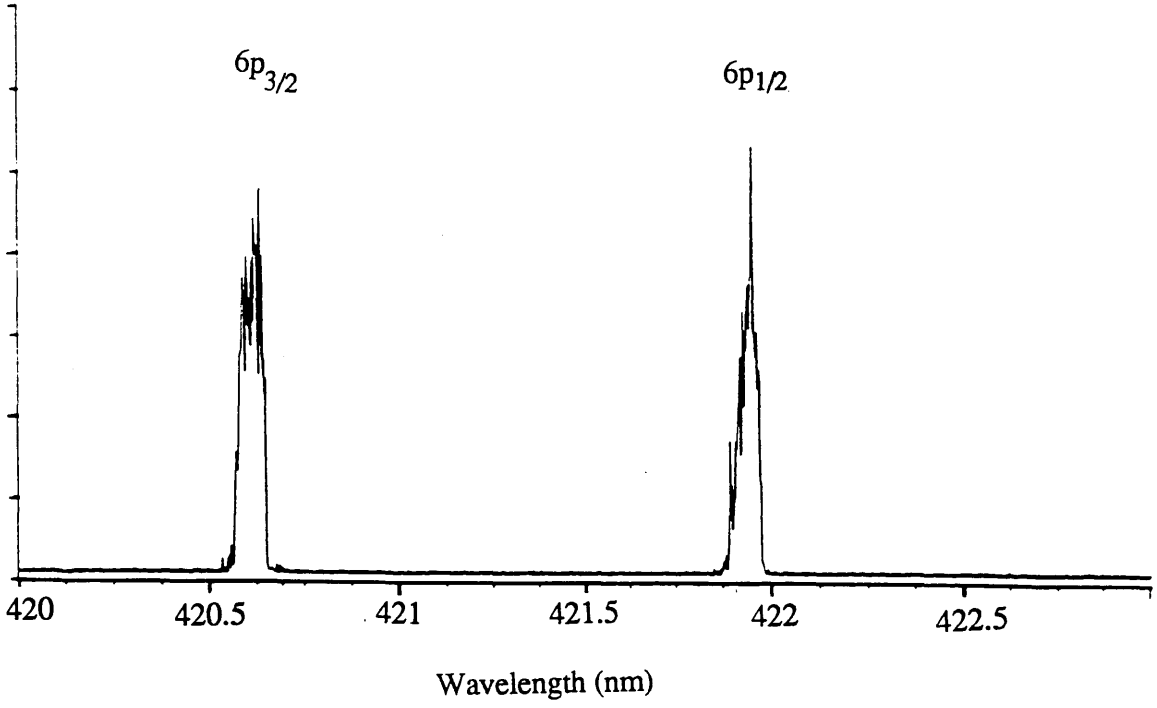


Figure 5.5 Resonant ionisation spectrum of rubidium $5s - 6p_{1/2,3/2}$ doublet

Relative Ionisation

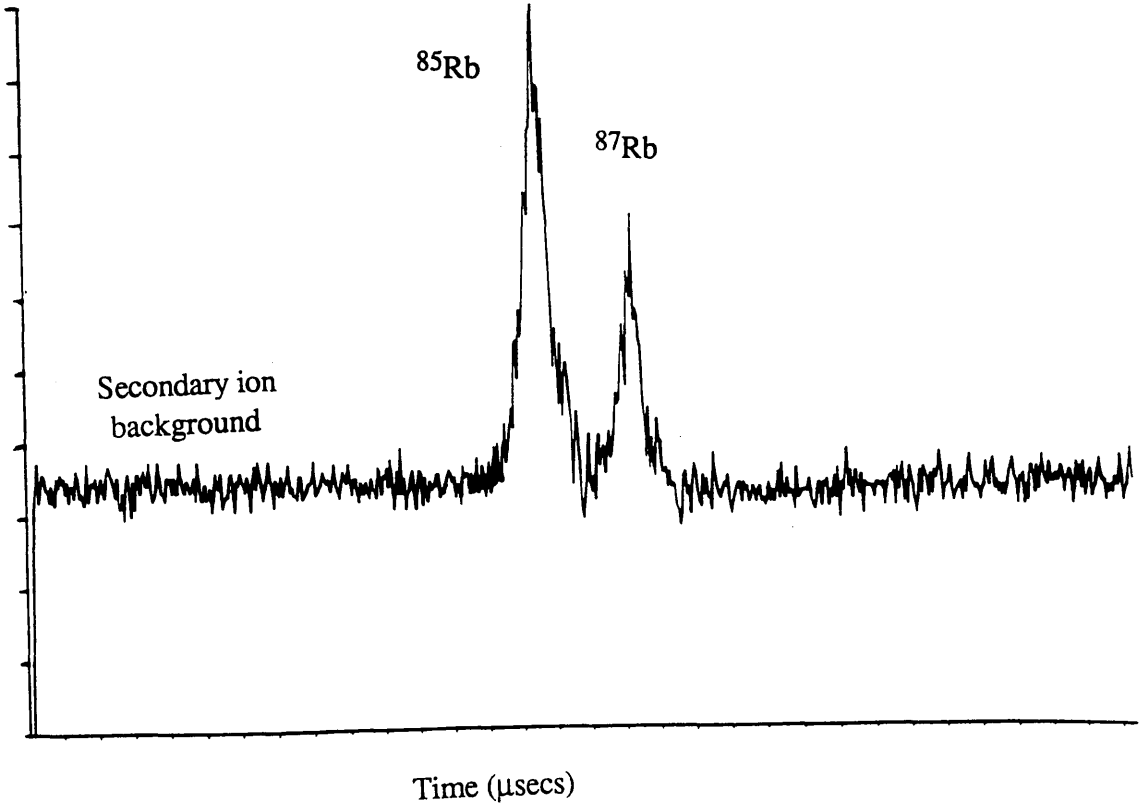


Figure 5.6 Time of flight spectrum at 420.6 nm

Mass spectra were also recorded from a sample of alkali salts (NaCl, KCl, RbCl) in a graphite substrate using laser desorption. The dye laser tuned to 420nm was focussed to a power of around 100 μ J, and was used to both desorb and ionise. The concentration of the alkali metals was estimated at parts per thousand. The individual element's isotopes are clearly distinguishable. There was no evidence of dimer signals.

A laser desorption / ionisation mass spectrum of a solid sample of lead taken at 355nm laser wavelength is also shown (Figure 5.7). The dimer signal was approximately 10% of the atomic signal. This observation is consistent with previous measurements of neutral sputtered particles from clean metal targets which indicated 5-10% of neutral flux may be composed of dimers or small clusters (Oechsner 1974).

Collection of this data allowed optimisation of the various voltage parameters of the system, eg. voltage on the sample stub and on the detector, and ion extraction voltages. It is important to be able to distinguish between the ions produced directly at the surface (SIMS) and those produced by interaction with the photon field. Since the secondary ions and the resonant ions are formed in distinctly different regions of the extraction field, they will have different energies and velocities as they travel down the drift tube. Voltages on the reflectron can be set such that SIMS ions are removed from the signal, ie. the voltage on the reflectron can be adjusted to reflect only RIMS ions, the SIMS having extra energy to pass unaffected through the reflectron.

It is clear from the above results that dimer signals were only evident when the element was present in fairly high concentrations, ie. around a few percent. At lower concentrations, the dimer signal was negligible.

Relative Ionisation

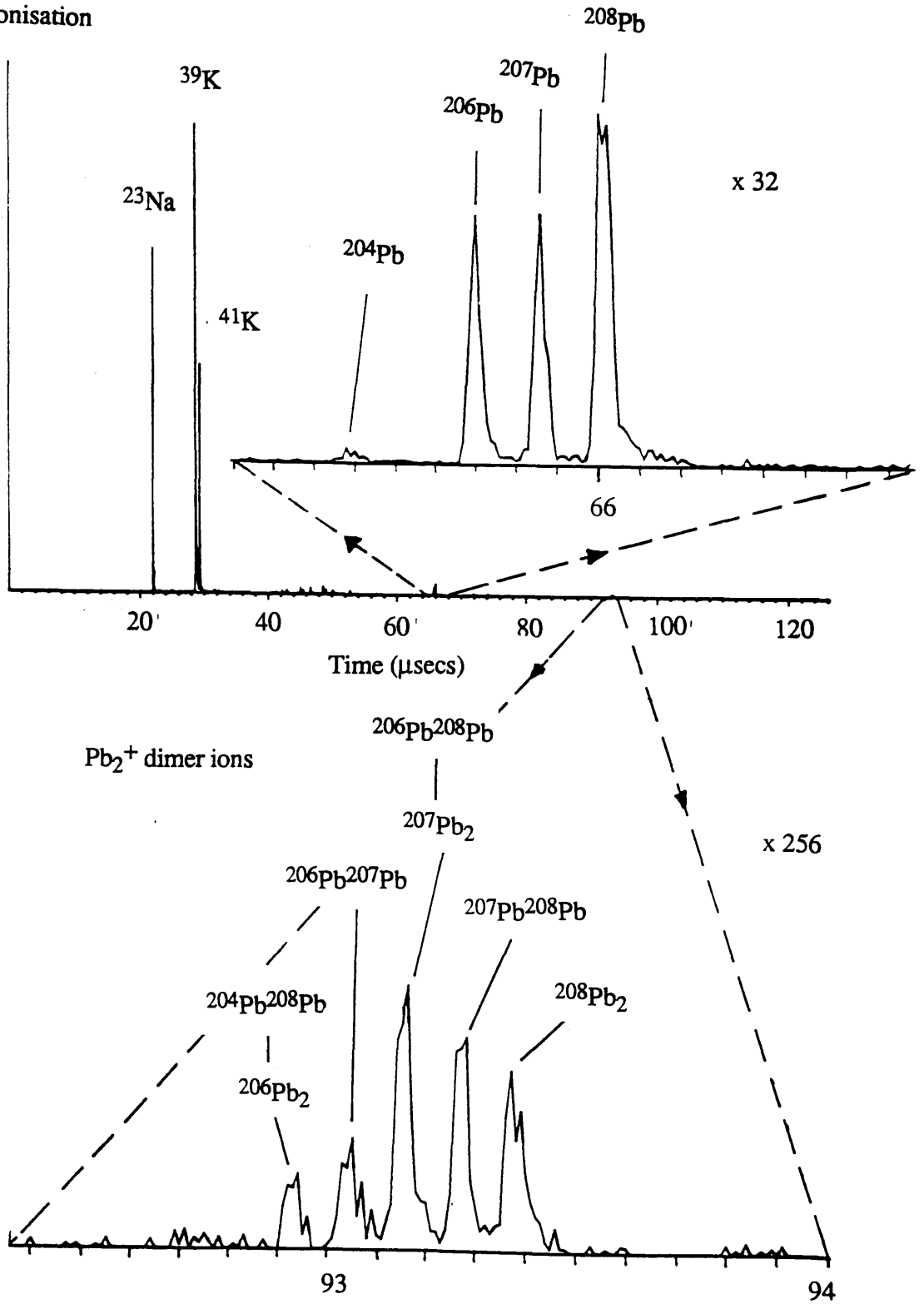


Figure 5.7 Time of flight spectrum showing lead isotopes

5.13 Sensitivity of Laser TOF Mass Spectrometry

This section discusses the anticipated sensitivity of the Glasgow RIMS instrument and proposes possible improvements to the experimental arrangement to improve this limit. The sensitivity is affected by all three main processes in the ultra-trace analysis, namely sample evaporation, ionisation and detection. The sensitivity of each stage contributes to the overall sensitivity of the machine.

The number of atoms evaporated in the first stage is dependent on a number of factors. The argon ion beam contained in the Glasgow RIMS instrument has a sputtering rate of 10^{10} atoms per second when operated at 10Hz with a 3 μ second pulse length (using a 15 μ A beam of energy 3KeV and sputtering rate of 5). To maximise the spatial overlap between the ejected neutrals and the photon field, it is important to use an ion beam spot which is small relative to the diameter of the laser beam. Unfortunately, it is difficult to transfer high ion currents (μ A) to the sample in small spot sizes (<1mm) due to space charge effects.

The excitation state of the evaporated atoms has an effect on the sensitivity. Most resonant ionisation schemes require neutral atoms in the ground state. Therefore, only those atoms in the ground state will be analytically useful. Young et al (1987) suggested that around 50% of the vaporised atoms will be in the ground state. This percentage will be averaged over all elements in the periodic table, as there is a dependence on the type of atom being evaporated.

The ionisation efficiency is dependent on the number of photon steps used. Resonant ionisation by single photon steps, for example, can be 100% efficient and the process can be saturated. A much higher laser flux is required for saturation via resonant

multiphoton ionisation as the ionising steps include virtual states of lower cross section (see Chapter 1). Non resonant multiphoton ionisation would require an even higher flux.

A loss of ions will obviously occur in the ionisation stage as a complete geometrical overlap of the vaporised plume and the ionising laser beam is impossible. Kimock et al (1984) have studied the effect of laser beam size on the number of indium atoms in the photon field. Figure 5.8 shows a graph of calculated number of atoms of In versus primary ion pulse width for three different ionising laser beam widths. Thus for a 10 μ second primary ion pulse, the 1.9 cm diameter beam overlaps around 70 times more atoms than the 0.05 cm diameter beam. An increase in beam size, however, will enforce a decreased laser flux. Therefore, especially for atoms which are difficult to photoionise, a compromise must be reached between maximising the number of atoms in the photon field and maximising the ionisation efficiency.

Also, the number of ions available for photoionisation is increased by positioning the laser beam close to the sample stub. Thus, the number of atoms in the photon field is maximised by using the largest diameter laser beam oriented as close to the sample as possible.

One other drawback affecting the sensitivity is the use of pulsed lasers in order to saturate the ionisation process, resulting in a low duty cycle for the experiment. It has been shown (Miller 1983) that the use of CW lasers can result in total ion yields comparable with pulsed laser yields. The photon flux in CW lasers, however, is considerably reduced, and hence the high degree of ionisation efficiency would be lost. Typically, a laser power of around 100 mJ /cm² is required to saturate the ionisation of atoms. Although the use of short (nanosecond) pulsed lasers can be seen as a disadvantage in terms of duty cycle, the shortness of the pulses leads directly to the positional probability of evaporated ions being independent of particle velocity. The vast

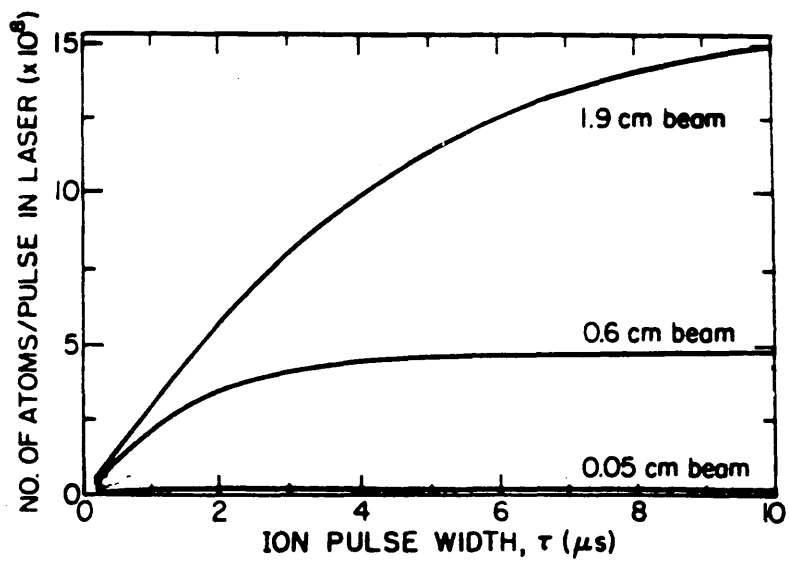


Figure 5.8 No. of In ions versus primary ion pulse for 3 ionising laser beam widths

majority of sputtered or desorbed atoms possess energies of less than 30eV. In effect, most particles are virtually immobile or "frozen" inside the photon field for the duration of the laser pulse.

Finally, the type of detector system used has an influence over the total efficiency of the RIMS process. The multichannel plate ion detector used in this research has an efficiency of around 80%.

The detection efficiency of an instrument can be defined as the ratio of the number of ions arriving at the detector to the number of ions produced at the ion source. Having taken the efficiencies of the individual stages into account, it has been calculated that the lowest concentration at which an impurity in a substrate could be detected is one part in 10^8 (Smyth 1988). This value assumes a 100% efficiency in ionisation, a 10% geometrical overlap between vapour cloud and ionising laser, and a sputtering rate of around 10^{10} atoms per second.

CHAPTER 6 - RESULTS OF LASER INDUCED IONISATION IN A TIME OF FLIGHT MASS SPECTROMETER

6.1 Introduction

This chapter documents the results obtained from the Glasgow Laser Time of Flight Mass Spectrometer of laser desorption spectra of different solid samples and spectra of laser resonant ionisation combined with laser desorption. The first sections contain laser ionisation spectra of the ambient gas within the TOF spectrometer. These results were recorded by strongly focussing a Nd:YAG laser beam into the centre of the ionisation region and analysing the constituents of the gas inside the machine. After recording background spectra, it became important to identify the sources of the background signals. Therefore, spectra of likely contaminants, vacuum pump oils, and spectra of the sample substrate, carbon, were taken. Some very interesting carbon spectra were seen, and as a result, an investigation into carbon clustering effects was carried out (see Sections 6.5 and 6.6). The later sections describe the experiments in which a dye laser was used to obtain both non resonant and resonant ionisation spectra of an NBS coal sample containing rubidium at a level of 15 parts per million. The main purpose of this section was to compare the two techniques and to demonstrate the increased sensitivity possible using resonant ionisation. NBS standard coals and ashes (SRM 1632a, 1633 and 1645) were considered a suitable choice as they contain a range of trace elements at parts per million concentrations (Gladney 1980), and have a matrix problem with carbon clusters being desorbed throughout the mass range (see Section 6.3). Real environmental samples are likely to have a similar composition.

In a time of flight mass spectrometer, the mass, m , is related to the arrival time, t , by the following equation,

$$m = 2 t^2 V e / d^2$$

which is derived from

$$1/2 m v^2 = e V$$

where d is the drift length, V is the accelerating potential and e is the charge on an electron. All masses labelled on the spectra have been assigned using this formula.

6.2 Laser Ionisation of Ambient Organic Vapour

The sensitivity of a laser resonant ionisation mass spectrometer is likely to be limited by the level of background ionisation within the machine. Organic molecules have structures which when fragmented by photodissociation into many different masses may interfere with detection of the sample ion. It was therefore necessary to record spectra of the background ionisation in order to identify possible impurities and reduce them to the minimum possible levels.

All ultra - high vacuum systems suffer from contamination with organic compounds. The RIMS machine at Glasgow operates at a pressure of around 10^{-10} torr which implies that the laser interaction region (volume $2.3 \times 10^{-3} \text{mm}^3$) may be contaminated with around 5×10^4 organic molecules. Organic molecules which are aromatic (benzene - like) have relatively low ionisation potentials (5 - 10 eV) and have UV resonances in the 240nm - 300nm range. They may therefore contribute to the background signal when UV light or two photon transitions are used. Two possible contaminants in the system are diffusion pump and rotary pump oils.

Diffusion pump oil is composed of a polyphenyl ester of mass 446amu which is known to be aromatic. It may also break down into smaller more volatile aromatic molecules. In general, rotary pump oil consists of saturated hydrocarbons which are less likely to be ionised than the aromatic molecules. There may, however, be aromatic hydrocarbons present in the oil as contaminants. It was useful, therefore, to record laser ionisation spectra of organic vapour present in order to determine possible impurities.

A focussed Quantel Nd:YAG 585 laser was used at the four possible wavelengths, 1064nm, 532nm, 355nm and 266nm, with pulse powers of 400, 160, 60 and 25mJ respectively, to study the composition of the gas. The laser had a pulse duration time of 10 nanoseconds and a repetition rate of 10 Hz. At laser fluences of above about 1mJ/mm², the resolution and stability of the time of flight system deteriorates rapidly due to a combination of space charge and collisional effects in the desorption plume as well as saturation in the microchannel plate detector. More organic impurities are expected to be seen at the UV wavelengths, although multiphoton processes using the fundamental (1064nm) or doubled light (532nm) could be possible.

The Nd:YAG laser was strongly focussed into the ionisation region of the RIMS machine. The ions created were extracted into the TOF drift tube and detected at the channel plate. No peaks were seen at the longer wavelengths 1064nm or 532nm even when the laser was strongly focussed. Figure 6.1 is a spectrum at 266nm (400 mJ/cm²) of the background vapour in the mass spectrometer before the introduction of any organics into the system. With the 50cm lens strongly focussed into the chamber, many fragmentation ions were observed. The main peak was C₃⁺, but fragments were clearly visible up to C₈⁺. The distribution shows a number of small clusters of peaks with a maximum signal corresponding to mass 209 amu. Figure 6.2 is a spectrum taken at wavelength 266nm with less focussing (40mJ/cm²), and shows a substantial reduction in fragmentation.

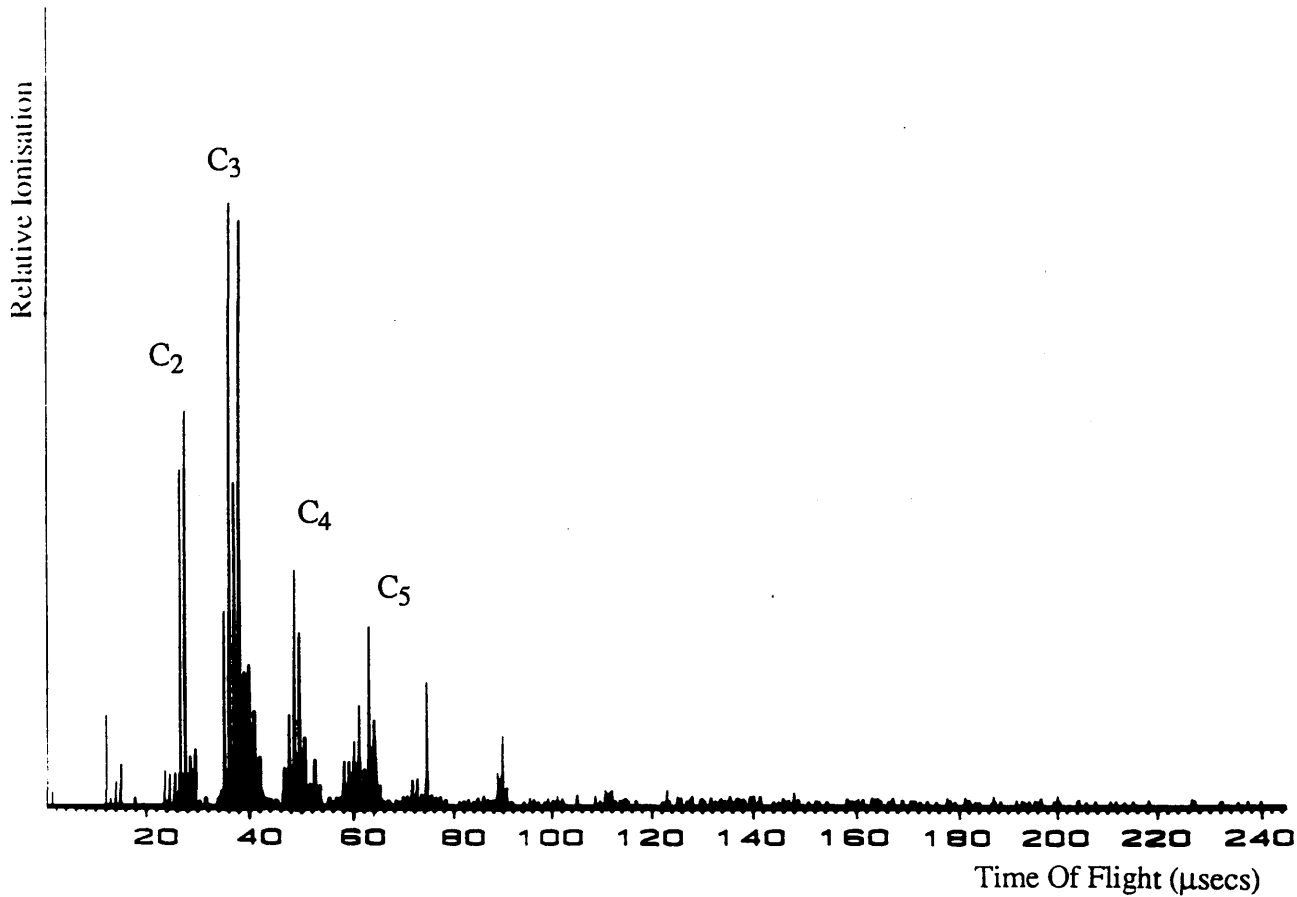


Figure 6.1 Background vapour at 266 nm (strongly focussed)

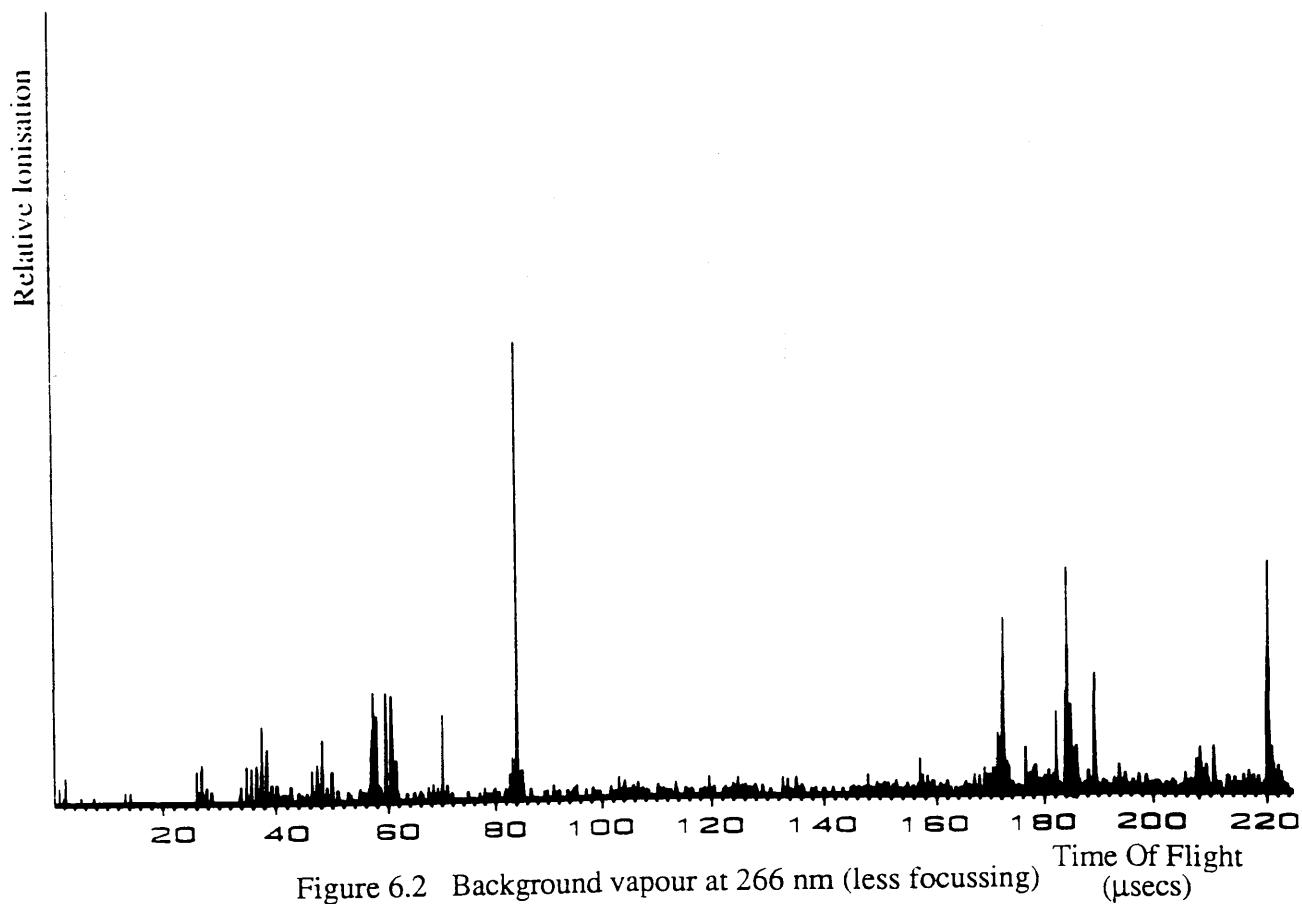


Figure 6.2 Background vapour at 266 nm (less focussing)

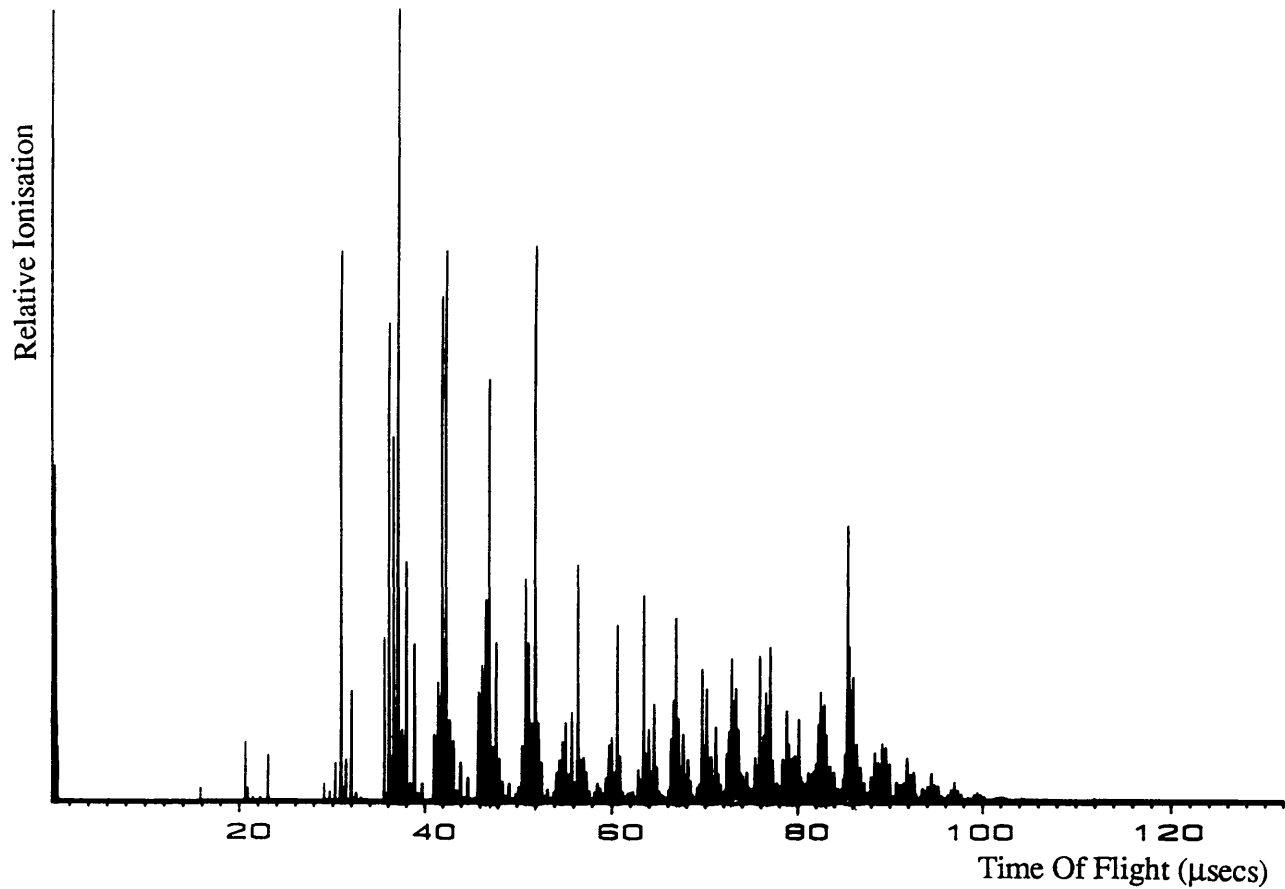


Figure 6.3 Spectrum of diffusion pump oil at 266 nm (400 mJ/cm^2)

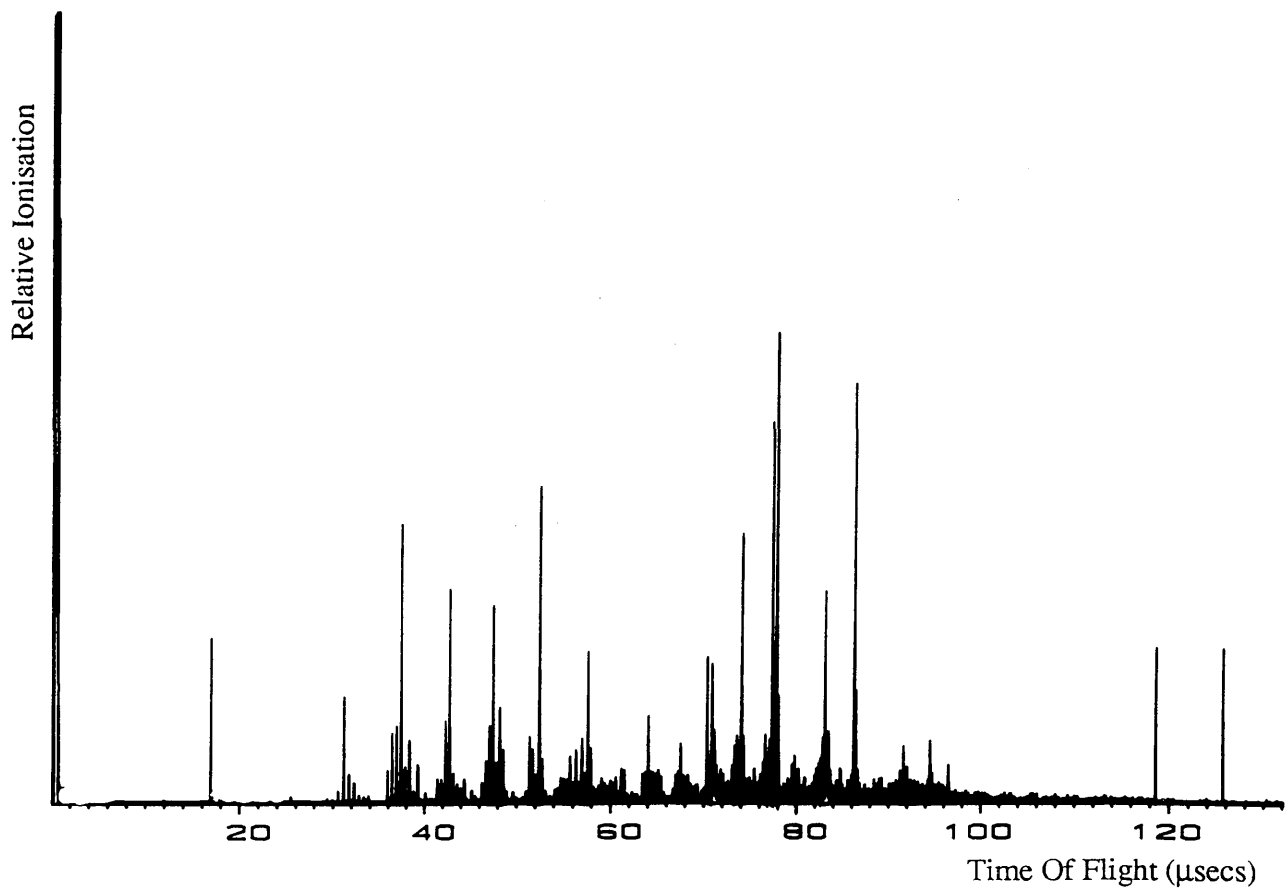


Figure 6.4 Spectrum of diffusion pump oil at 266 nm (40 mJ/cm^2)

In order to investigate the source of this ionisation, it was decided to introduce a small quantity of diffusion pump oil and also rotary pump oil into the ionisation region. Spectra of the pump oils could then be compared with the ambient vapour spectrum. Figure 6.3 shows the 266nm spectrum obtained after introduction of a small quantity of diffusion pump oil. The laser power level is around $400\text{mJ}/\text{cm}^2$. The spectrum shows the large number of organic fragments produced. Figure 6.4 is a lower power scan at $40\text{mJ}/\text{cm}^2$, showing larger molecular fractions. Figures 6.5 and 6.6 are scans taken after the introduction of a small quantity of rotary pump oil into the system. The power levels are $40\text{mJ}/\text{cm}^2$ and $130\text{mJ}/\text{cm}^2$ for Figures 6.5 and 6.6 respectively. As with diffusion pump oil, the higher power scan shows greater fragmentation of organic molecules. It is clear from these graphs that both diffusion and rotary pump oils could be responsible for the peaks seen in the background scans.

Changing to wavelength 355nm decreases the background signal considerably. Figure 6.7 has a power level of $10\text{J}/\text{cm}^2$, but the production of fragments has been very much reduced. Figure 6.8 is a scan taken at wavelength 532nm with a high power level of $25\text{J}/\text{cm}^2$, and is magnified eight times. Very few background signals are seen. No background signals were observed when the laser was tuned to the fundamental wavelength 1064nm.

The results show that the background ionisation will be negligible when using lasers of a longer wavelength, as the ionisation cross section of organic molecules appears to drop rapidly with increasing wavelength. The power levels required for saturation of a RIMS process, when virtual state transitions are not involved, are in the order of a few hundred μJ up to a few tens of mJ. The runs at 355nm, 532nm and 1060nm were carried out with power levels greater than $1\text{J}/\text{cm}^2$. On the other hand, it is very clear that the detection of molecules requires UV light, which may result in some

Relative Ionisation

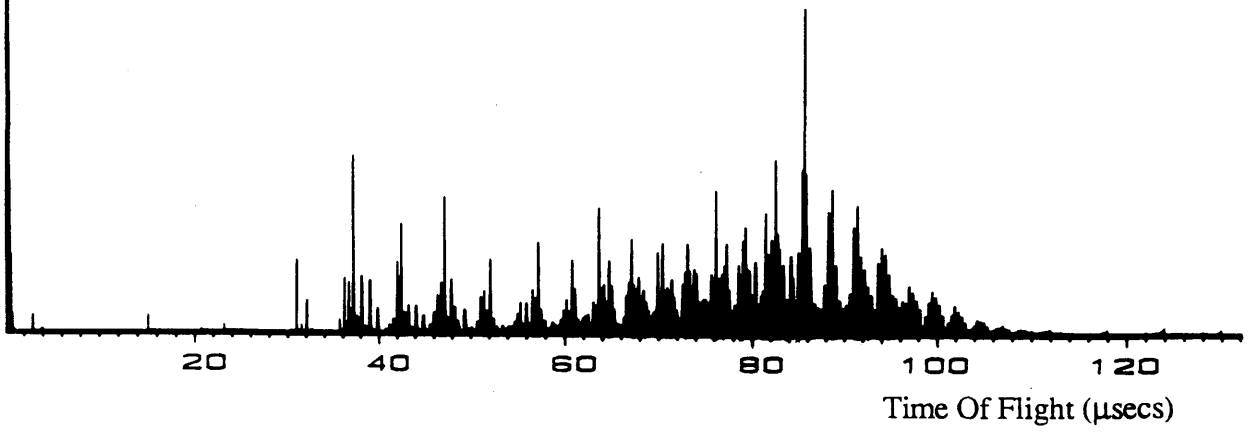


Figure 6.5 Spectrum of rotary pump oil at 266 nm (40 mJ/cm^2)

Relative Ionisation

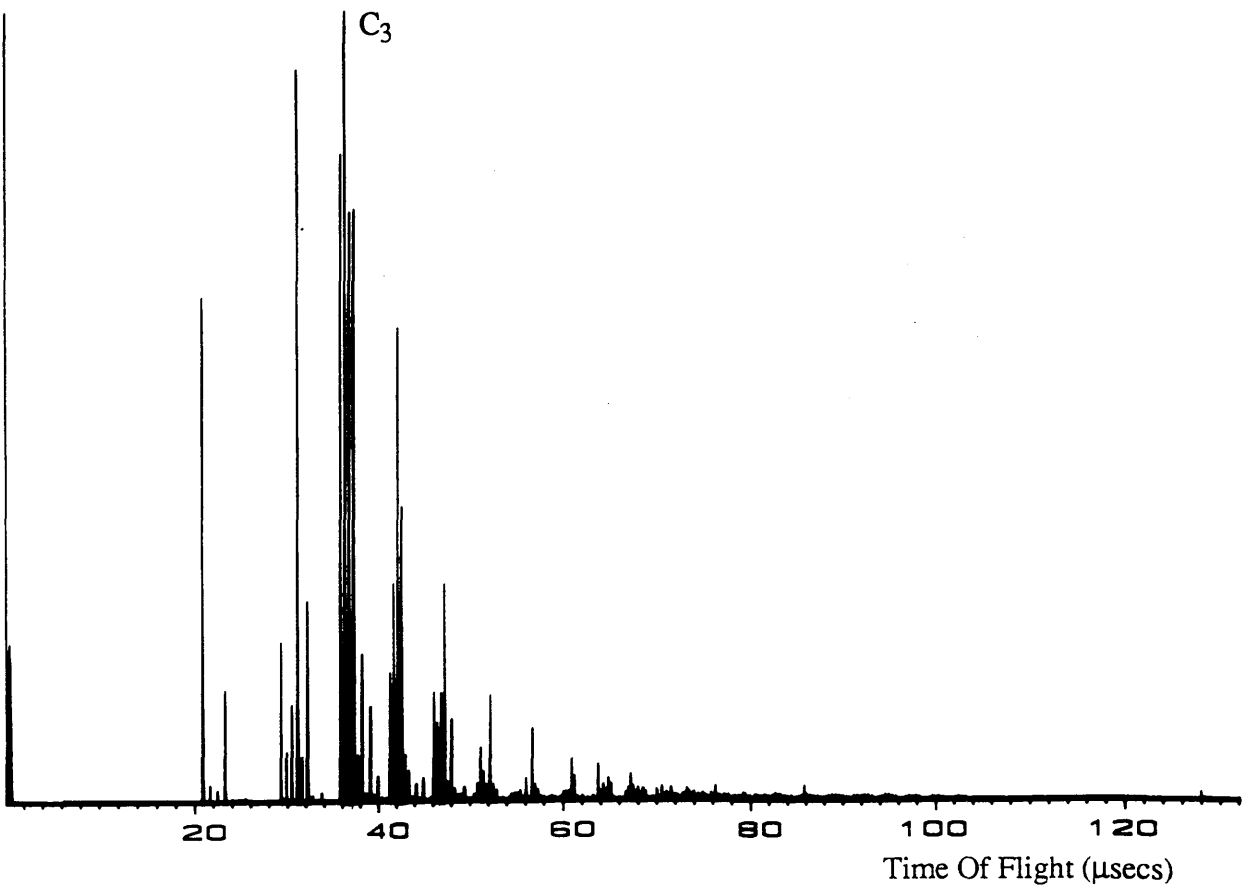


Figure 6.6 Spectrum of rotary pump oil at 266 nm (130 mJ/cm^2)

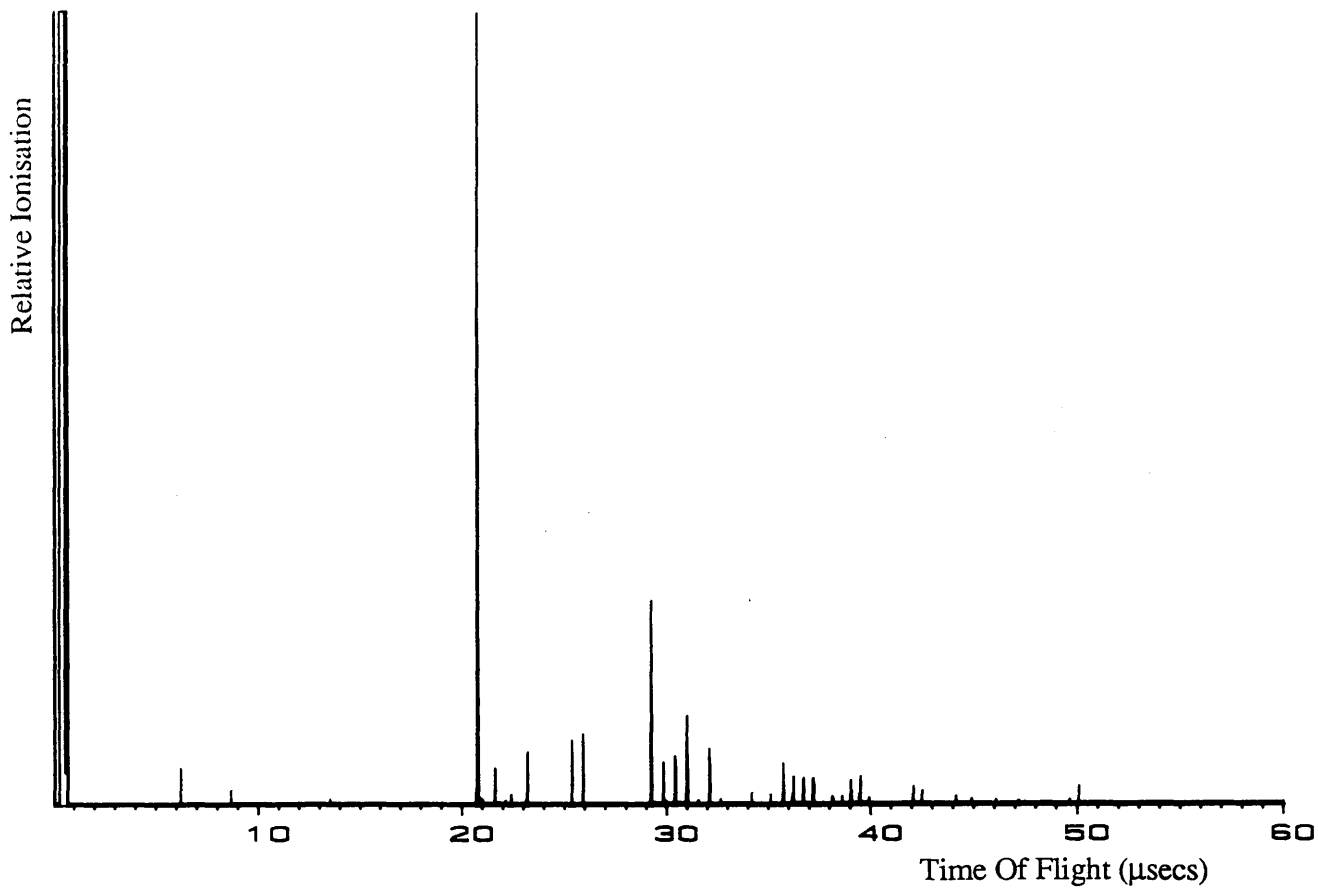


Figure 6.7 Spectrum of diffusion pump oil at 355 nm (10 J/cm^2)

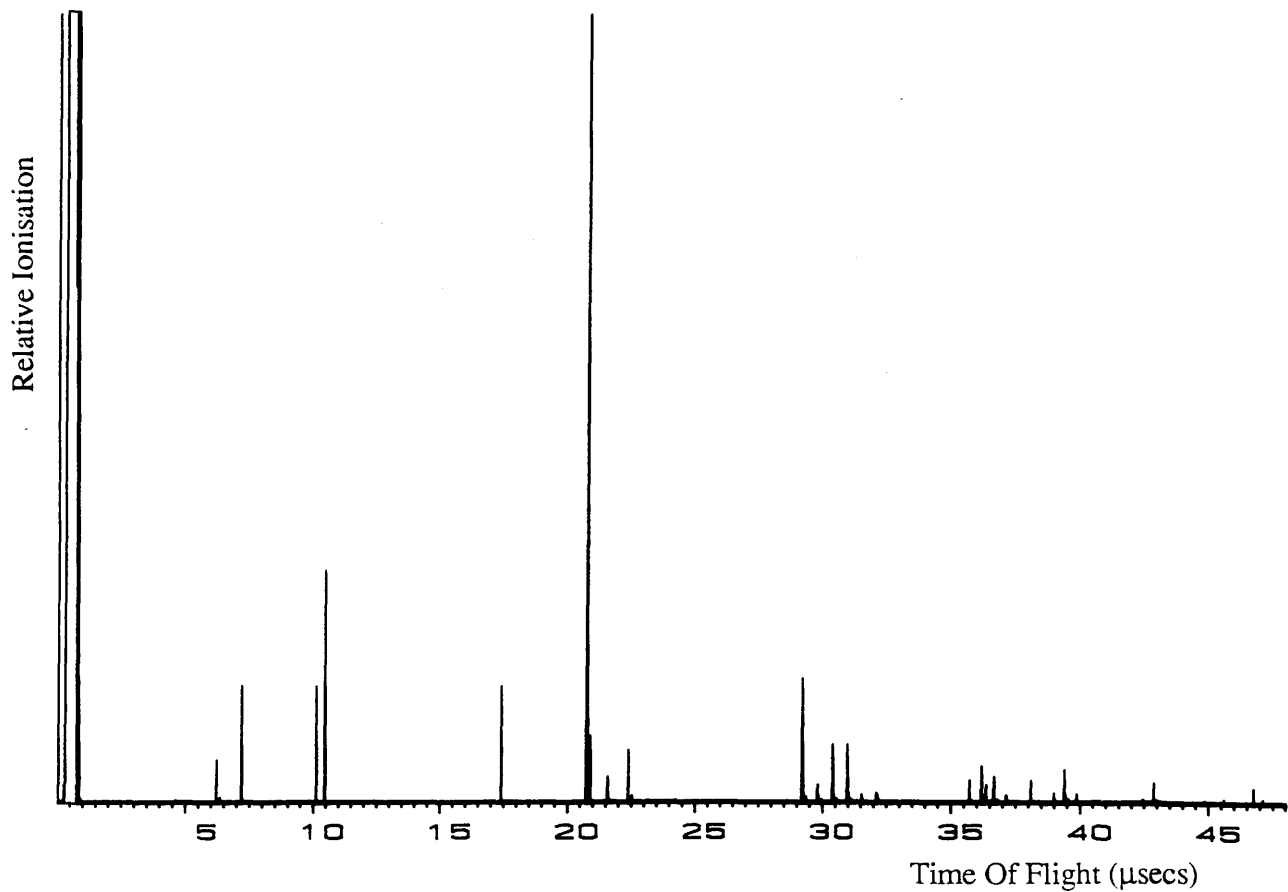


Figure 6.8 Spectrum of diffusion pump oil at 532 nm (25 J/cm^2)

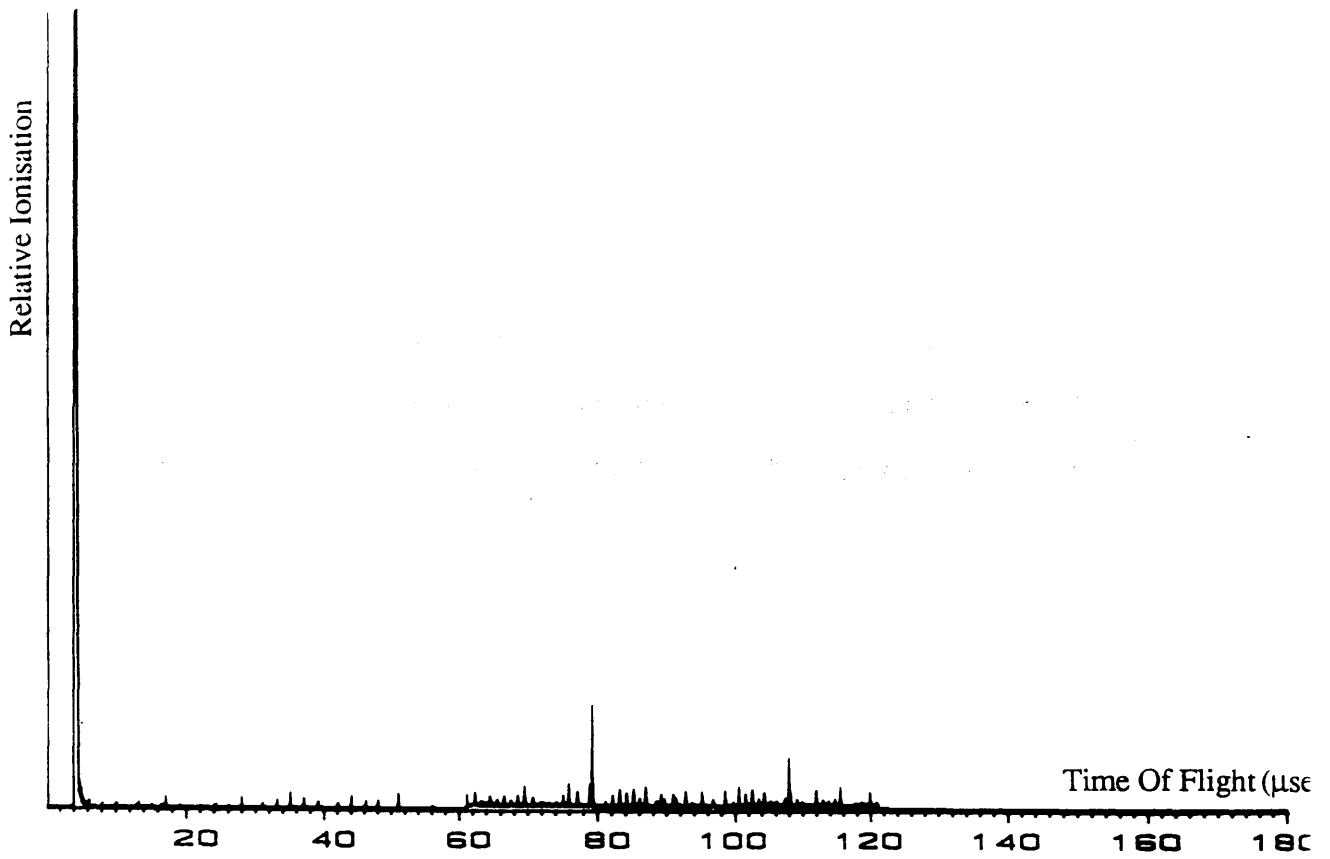


Figure 6.9 Spectrum of diffusion pump oil at 532 nm (2.8 mJ/cm^2)

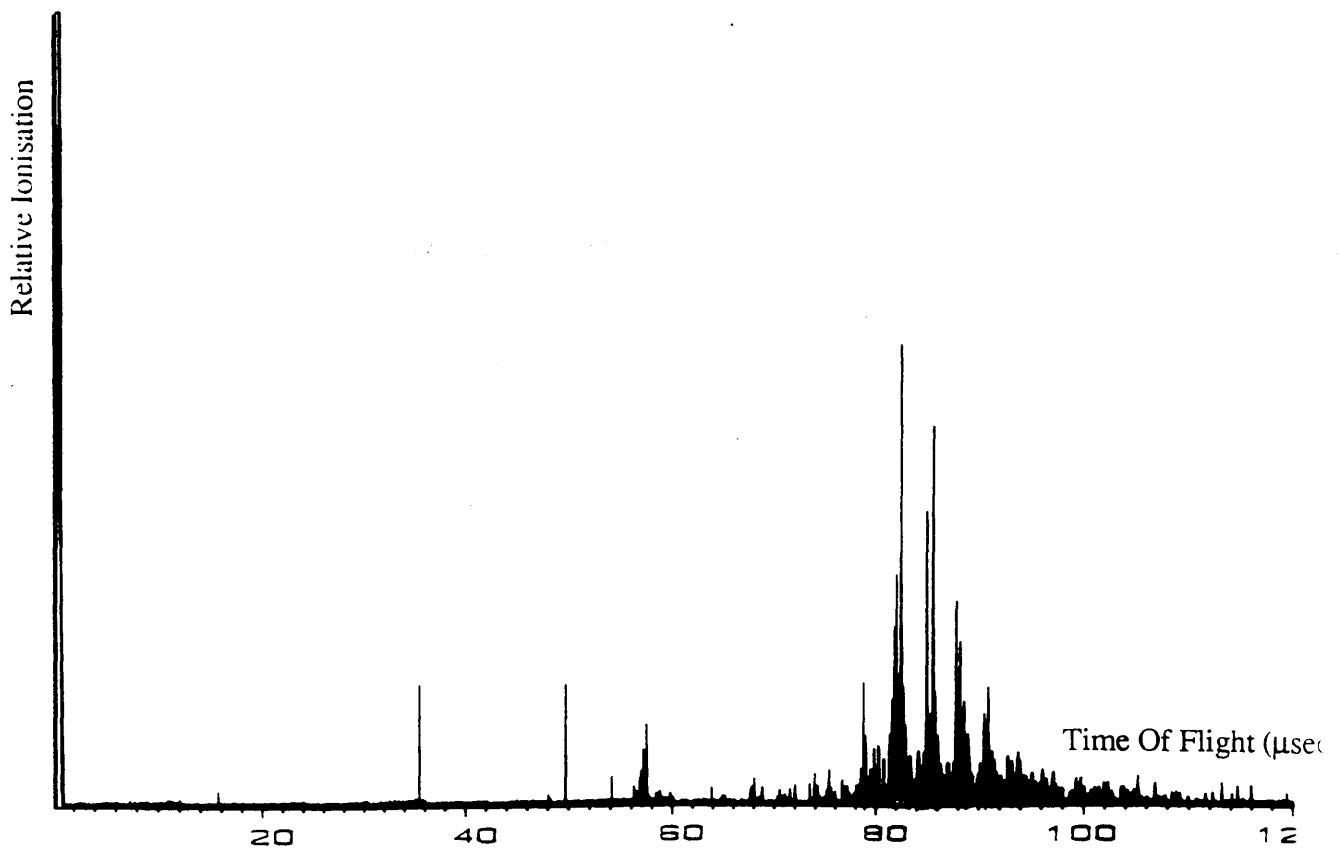


Figure 6.10 Spectrum of diffusion pump oil at 532 nm (8 mJ/cm^2)

interference from background signals. Figure 6.9 is a low power scan (2.8 mJ/cm^2) at wavelength 266nm with a small amount of diffusion pump oil introduced. The background here is negligible. A scan was then recorded at 8 mJ/cm^2 , a laser power value nearer the maximum required for saturation in the RIMS process (Figure 6.10). This spectrum was magnified vertically by a factor of 16, and proves that there is a small but significant amount of organic material ionised which could interfere in the ultra - trace detection. Clearly, this has shown that the background vapour pressure within the instrument should be as low as possible ($< 10^{-10}$ torr).

6.3 Laser Ionisation of NBS Coal Samples

The Glasgow laser ionisation mass spectrometer has been designed primarily for the analysis of impurities in solid samples. The preparation of samples for the TOF mass spectrometer requires the sample to be mixed with an appropriate substrate. There are a number of requirements of a substrate, namely :-

- 1) The substrate should be a conducting material in order to avoid a build up of charge on the sample stub causing space charge effects.
- 2) The substrate should contain as few impurities as possible.
- 3) The substrate should preferably be in pelletable powder form, ie. should compress easily into the sample stub indentation.

Graphite was chosen as a possible substrate as it satisfies all of the above criteria, and is also relatively cheap and easily available. High purity graphite was used to avoid contamination of the sample under analysis. The sample under analysis was generally mixed in equal proportions with the graphite and compressed into the sample

indentation. The NBS coal samples (SRM 1632a, 1633 and 1645) were chosen to simulate real environmental samples, as they contain a range of elements at parts per million concentrations as well as a background of carbon clusters which can form throughout the mass range. Samples of NBS coal ashes were mixed with high purity graphite in a 1:1 ratio to provide conduction, and were compressed into the sample stub inset (diameter 1cm and depth 2mm).

In this experiment, the four wavelengths of the Quantel laser, 1064, 532, 355 and 266nm were used to desorb an NBS coal sample containing trace elements in known quantities. At each wavelength, different laser powers were used to obtain time of flight spectra of the sample.

The ions detected here are produced by desorption and consequent ionisation which occurs during the same laser pulse. There are two likely mechanisms involved. Firstly, the laser striking the sample will produce a cloud of mainly neutral atoms with some positively charged atoms in a ratio of at least 1000 : 1 (Kimock et al 1984), with some of the resultant neutral atoms being ionised in the tail of the same pulse. The amount of ionisation is likely to be dependent on the wavelength of the desorbing laser, with a greater fraction of the neutrals being ionised by higher energy shorter wavelength photons. An alternative explanation involves the formation of a plasma by the laser beam. Andersen and Hinthorne (1973) introduced the hypothesis that a plasma layer is created on the surface of a sample during desorption in which atoms, ions, molecules and electrons are in local thermodynamic equilibrium (the LTE model). It is suggested that the positive ions in this plasma are formed by the dissociation of neutral atoms into positive ions and electrons. At the power levels used in the following experiments, the positive ions are likely to be created by a combination of these two effects. A prediction of the positive ion intensities is given by the Saha - Langmuir equation (Benninghoven et al 1987),

$$\frac{N^+}{N^0} = \frac{Z^+}{Z^0} \exp \frac{(\phi - E_i)}{kT}$$

where Z^+ and Z^0 are the partition functions of positive and neutral particles, respectively, E_i is the ionisation potential, ϕ is electron work function and T is the temperature of the surface.

Figures 6.11 and 6.12 are time of flight spectra at wavelength 1064 nm taken at high power (600mJ/cm²) and lower power (300mJ/cm²) respectively. The two spectra are very similar, with increased intensity of the peaks in the higher power spectrum. Figure 6.13 is an expanded view of Figure 6.12 (600mJ/cm²), and Table 6.1 compares experimental concentrations with calibrated concentrations obtained by Gladney (1980) for the 1632a NBS sample. The area under each peak was calculated using a program on the IBM - PC. The elemental concentrations were then determined by using one element, eg. lithium, as a standard and calculating the other concentrations from the ratio of the areas.

At this longer wavelength, the spectra are virtually free of interference from organic impurities and carbon clusters. As demonstrated in Figure A-1, most organic molecules tend to become ionised only at shorter UV wavelengths, ie. less than 330nm. The results clearly show that those elements having low ionisation potentials are more efficiently desorbed and non resonantly ionised than those with higher ionisation potentials. This is in agreement with the Saha - Langmuir equation. A detection limit of 1.5 ppm for the element rubidium was calculated by measuring the area of the rubidium peak and the corresponding background signal. Although this appears to be a fairly sensitive method of detection, this limit was only possible for elements such as rubidium having particularly low ionisation potentials. At this longer wavelength, there is generally insufficient energy in the photons to induce ionisation in most other elements.

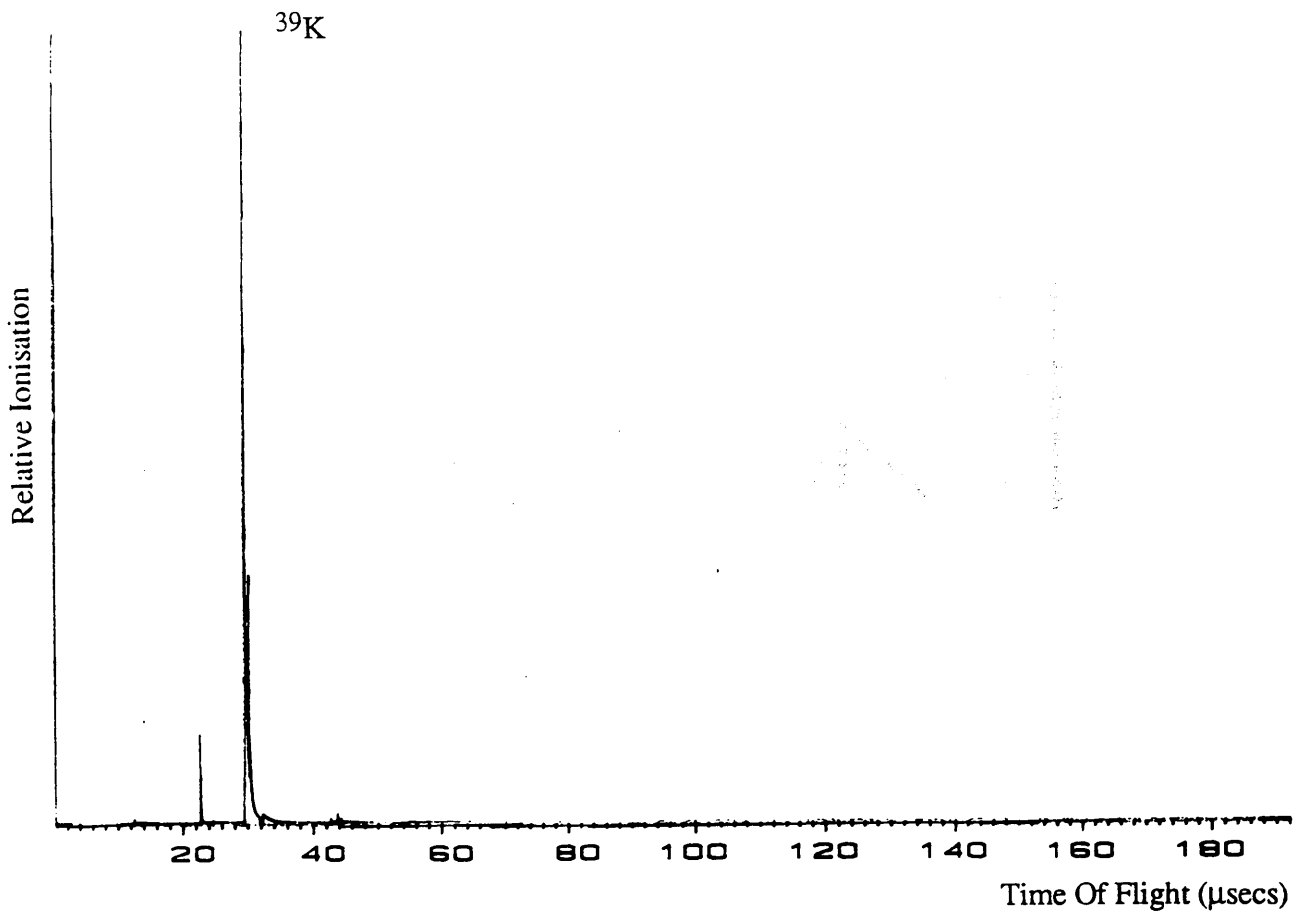


Figure 6.11 Time of flight spectrum at 1064 nm (600 mJ/cm²)

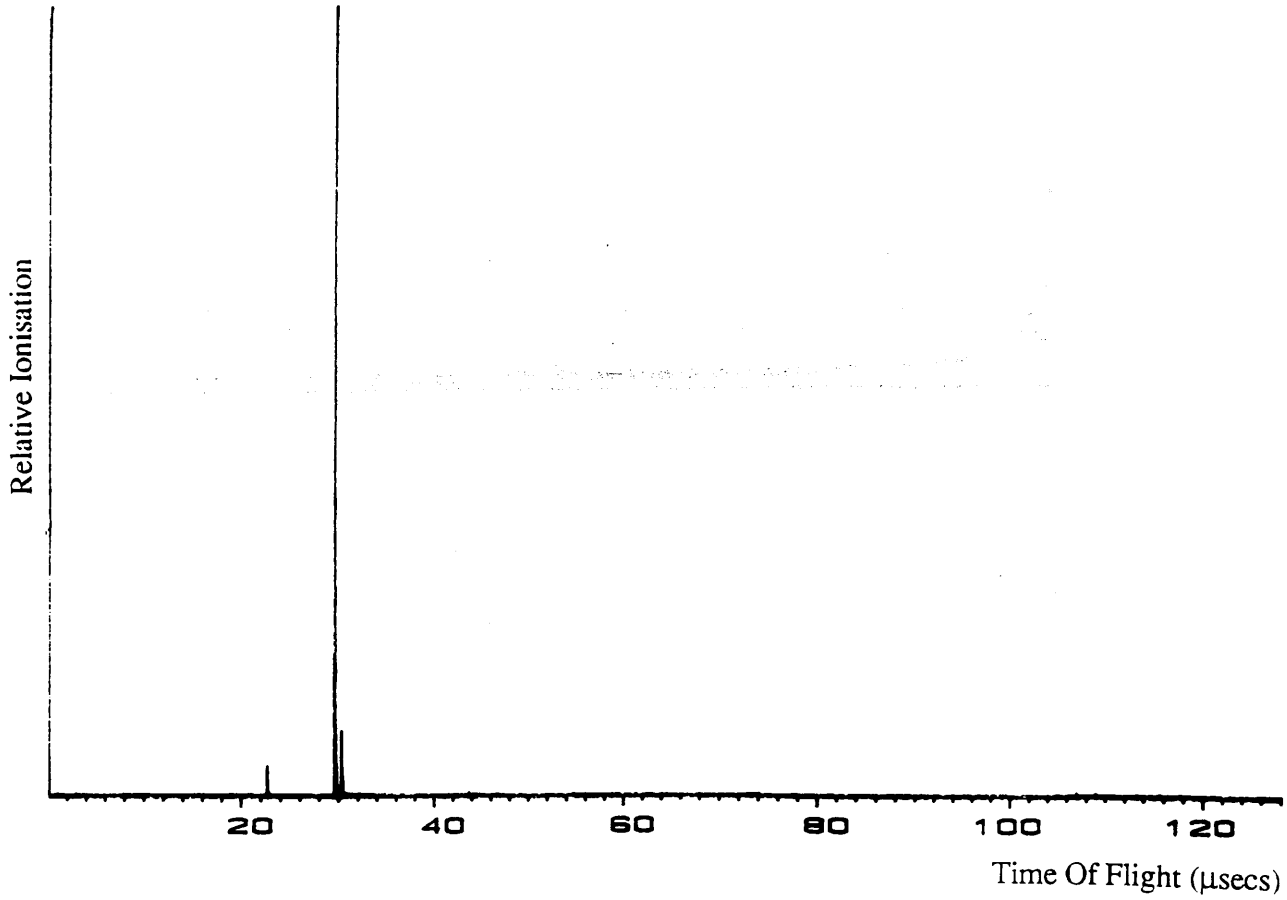


Figure 6.12 Time of flight spectrum at 1064 nm (300 mJ/cm²)

Figure 6.13 Mass spectrum at 1064 nm (600 mJ/cm²)

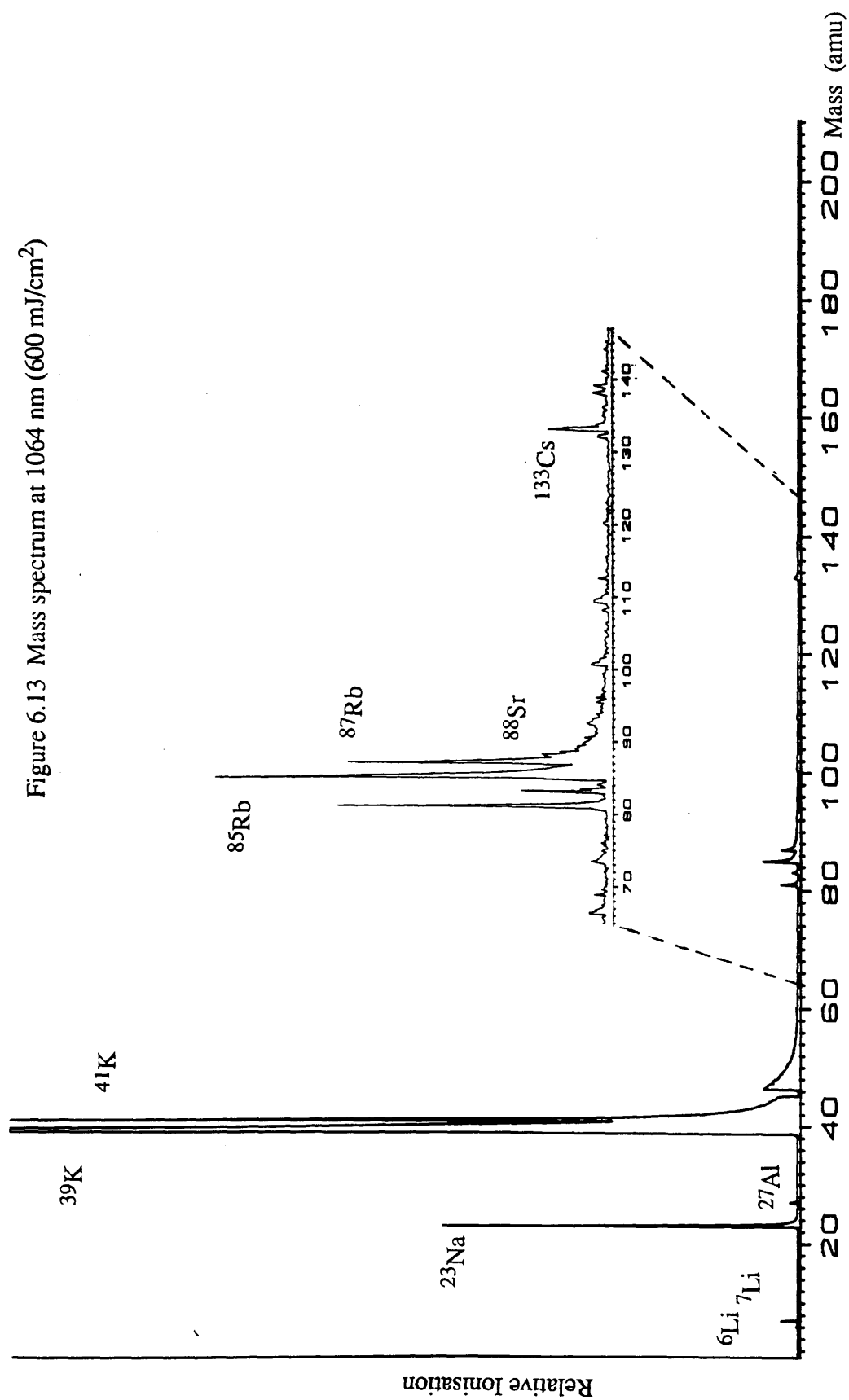


Table 6.1 Results from laser desorption of 1632a NBS sample at 1064 nm

Element	I.P. (eV)	Gladney (ppm)	Experimental (ppm) (+/- 10%)
⁶ Li ⁷ Li	5.3	18.1	18.1
²³ Na	5.138	380	579
²⁷ Al	5.984	1.485%	13.8
³⁹ K ⁴¹ K	4.339	2050	13162.5
⁸⁵ Rb ⁸⁷ Rb	4.176	15	86.2
⁸⁸ Sr	5.692	44	9.0
¹³³ Cs	3.893	1.0	5.1
¹³⁸ Ba	5.21	65	1.5
¹³⁹ La	5.61	8	1.15

Figure 6.14 Mass spectrum at 532 nm (120 mJ/cm²)

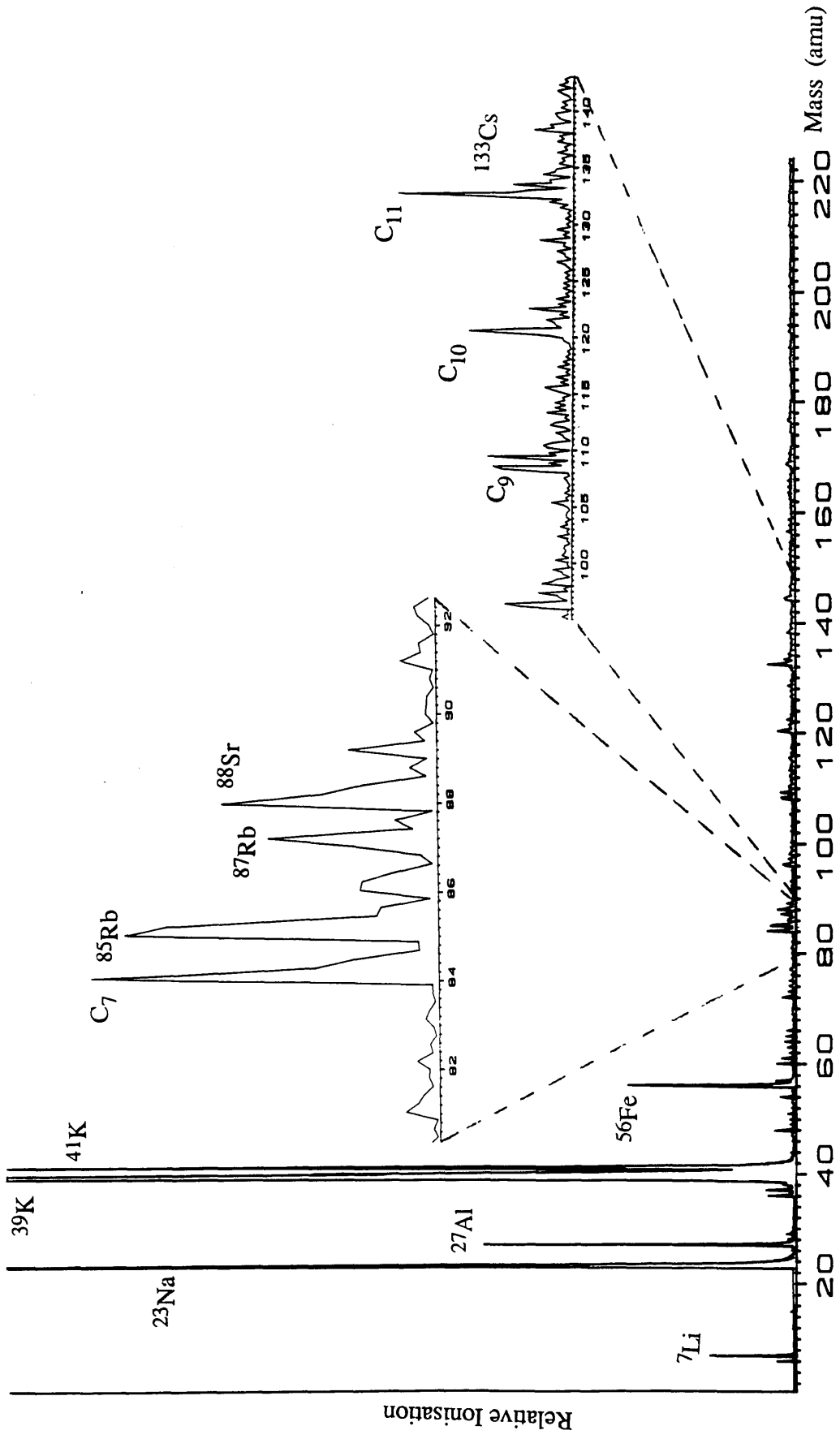


Table 6.2 Results from laser desorption of 1632a NBS sample at 532nm

Element	Possible Contaminant	I.P. (eV)	Gladney (ppm)	Experimental (ppm) +/- 10%
⁶ Li ⁷ Li	-	5.39	18.1	18.1
²³ Na	-	5.138	380	397.5
²⁷ Al	-	5.984	1.485%	36.4
* ³⁹ K * ⁴¹ K	C ₃ H ₃ C ₃ H ₅	4.339	2050	1181.5
* ⁴⁰ Ca	C ₃ H ₄	6.111	1150	25.3
⁵⁶ Fe	-	7.87	0.56%	26.05
* ⁸⁵ Rb * ⁸⁷ Rb	C ₇ H C ₇ H ₃	4.176	15	4.4
* ⁸⁸ Sr	C ₇ H ₄	5.692	44	1.185
* ⁸⁹ Y	C ₇ H ₅	6.3	2.9	0.395
* ¹³³ Cs	C ₁₁ H	3.893	1.0	0.79

Figure 6.14 taken at 532nm (120mJ/cm²) shows a slight increase in the number of elements which can be detected. At this wavelength, carbon clusters and other organic molecules are beginning to become evident in the spectrum. In some cases, they occur at the same mass as an element, causing an anomalous enhancement of the peak intensity. This is known as isobaric interference, and severely affects the accuracy of the calculated concentrations. This is also true for carbon cluster molecules containing one or more hydrogen atoms which result in series of consecutive peaks after the main cluster peak. Those elements affected are marked in the tables with an asterisk, and possible contaminants are given. In particular, the ⁸⁵Rb peak is increased in intensity by C₇H and the ¹³³Cs peak by C₁₁H. These interferences make accurate concentration calculations impossible. Table 6.2 compares the experimental concentrations to Gladney's results for NBS standards (1980).

A lower wavelength scan (Figure 6.15) at 355nm (20mJ/cm²) showed a further increase in the number of peaks obtained compared with 532nm. In this spectrum, carbon is much more evident, and clusters containing up to 15 carbon atoms can be seen. Table 6.3 gives experimental concentrations compared with Gladney's results.

Further evidence of carbon clusters are seen when the wavelength was changed to 266nm. Figure 6.16 was taken at 266nm with a power level of 100mJ/cm² and with 5dB attenuation to prevent damage to the transient recorder. Figure 6.17 is a lower power scan at 266nm (62.7mJ/cm²) with 4db attenuation, and shows less fragmentation of the carbon clusters. Expansion of Figure 6.16 (Figure 6.18) reveals peaks corresponding to almost every mass unit, particularly at higher masses. The carbon clusters are very prominent in this spectrum, and to a large extent engulf the elemental peaks, making elemental determination impossible. Table 6.4 gives the elements and possible contaminants present in the spectrum.

Figure 6.15 Mass spectrum at 355 nm (20 mJ/cm²)

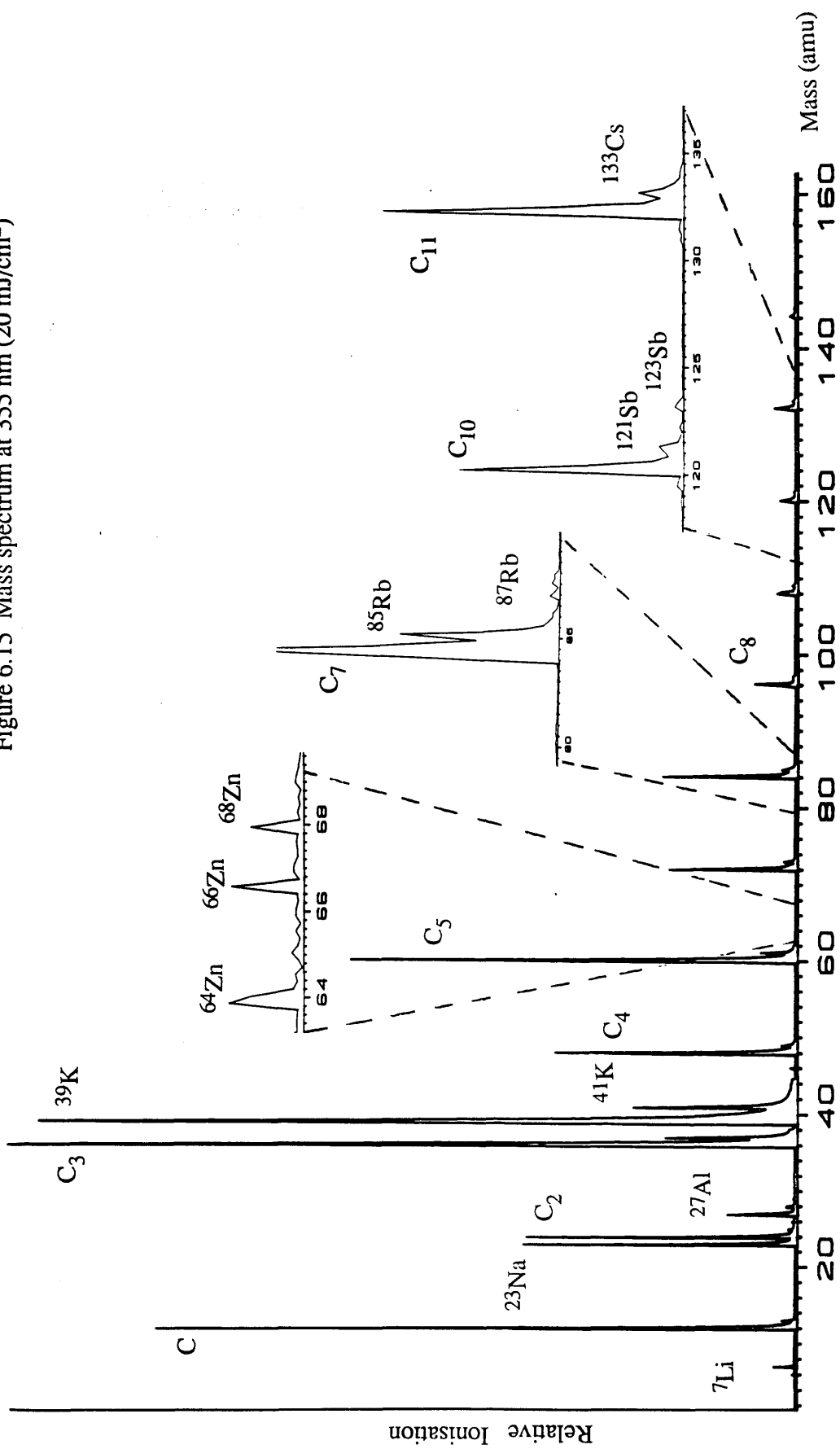


Table 6.3 Results from laser desorption of 1632a NBS sample at 355nm

Element	Possible Contaminant	I.P. (eV)	Gladney (ppm)	Experimental (ppm) +/- 10%
⁶ Li	-	5.39	18.1	18.1
⁷ Li	-			
¹¹ B	-	8.296	26.5	0.127
²³ Na	-	5.138	380	214.36
* ²⁷ Al	C ₂ H ₃	5.984	1.485%	57.7
* ²⁸ Si	C ₂ H ₄	8.149	2.95%	10.72
* ²⁹ Si	C ₂ H ₅			
* ³⁰ Si	C ₂ H ₆			
* ³⁹ K	C ₃ H ₃	4.339	2050	1500
* ⁴¹ K	C ₃ H ₅			
⁵⁶ Fe	-	7.87	0.56%	0.195
* ⁶³ Cu	C ₅ H ₃	7.724	7.95	0.086
* ⁶⁴ Zn	C ₅ H ₄	9.391	14	0.735
* ⁶⁶ Zn	C ₅ H ₆			
* ⁶⁸ Zn	C ₅ H ₈			
* ⁸⁵ Rb	C ₇ H	4.176	15	3.45
* ⁸⁷ Rb	C ₇ H ₃			
* ⁸⁸ Sr	C ₇ H ₄	5.692	44	0.655
* ¹²¹ Sb	C ₁₀ H	8.639	0.35	0.74
* ¹²³ Sb	C ₁₀ H ₃			
* ¹³³ Cs	C ₁₁ H	3.893	1.0	1.4

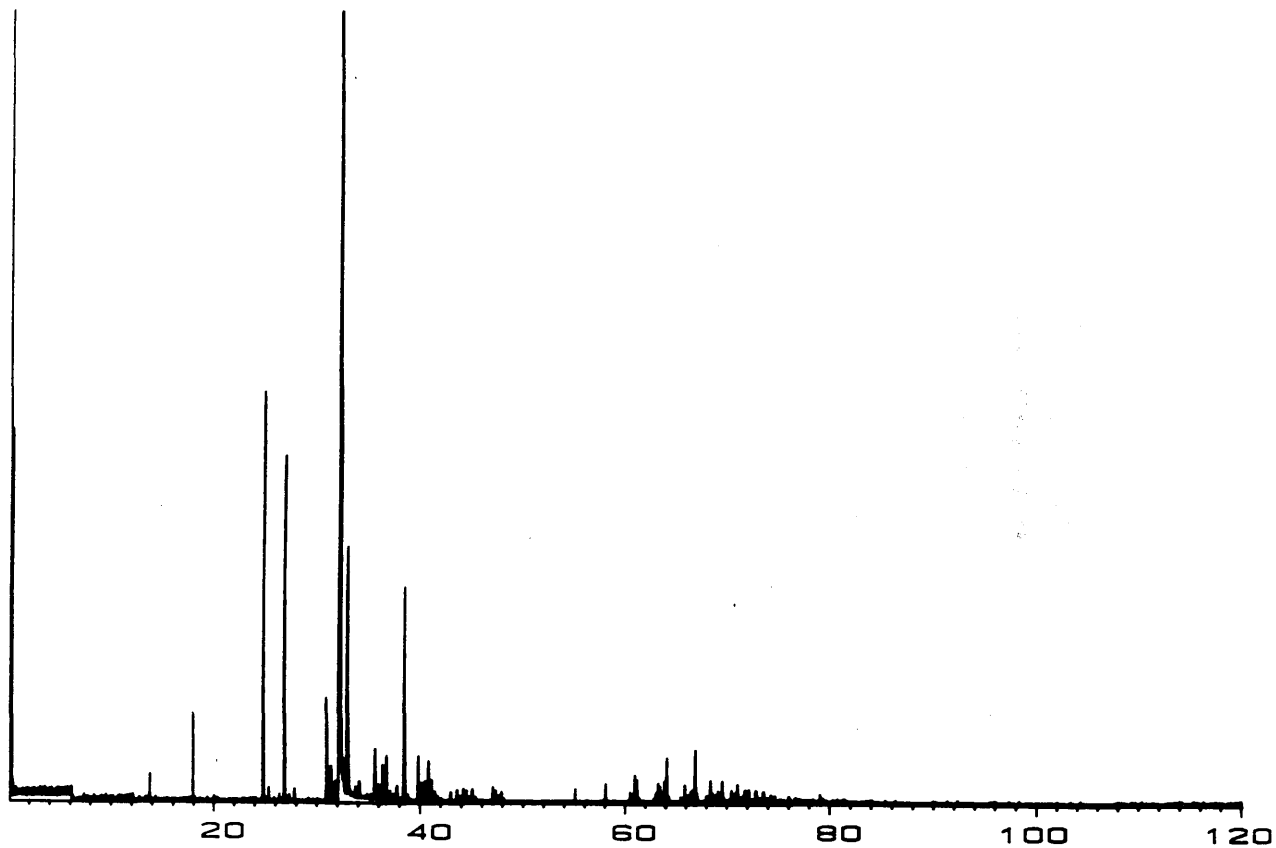


Figure 6.16 Mass spectrum at 266 nm (100 mJ/cm^2)

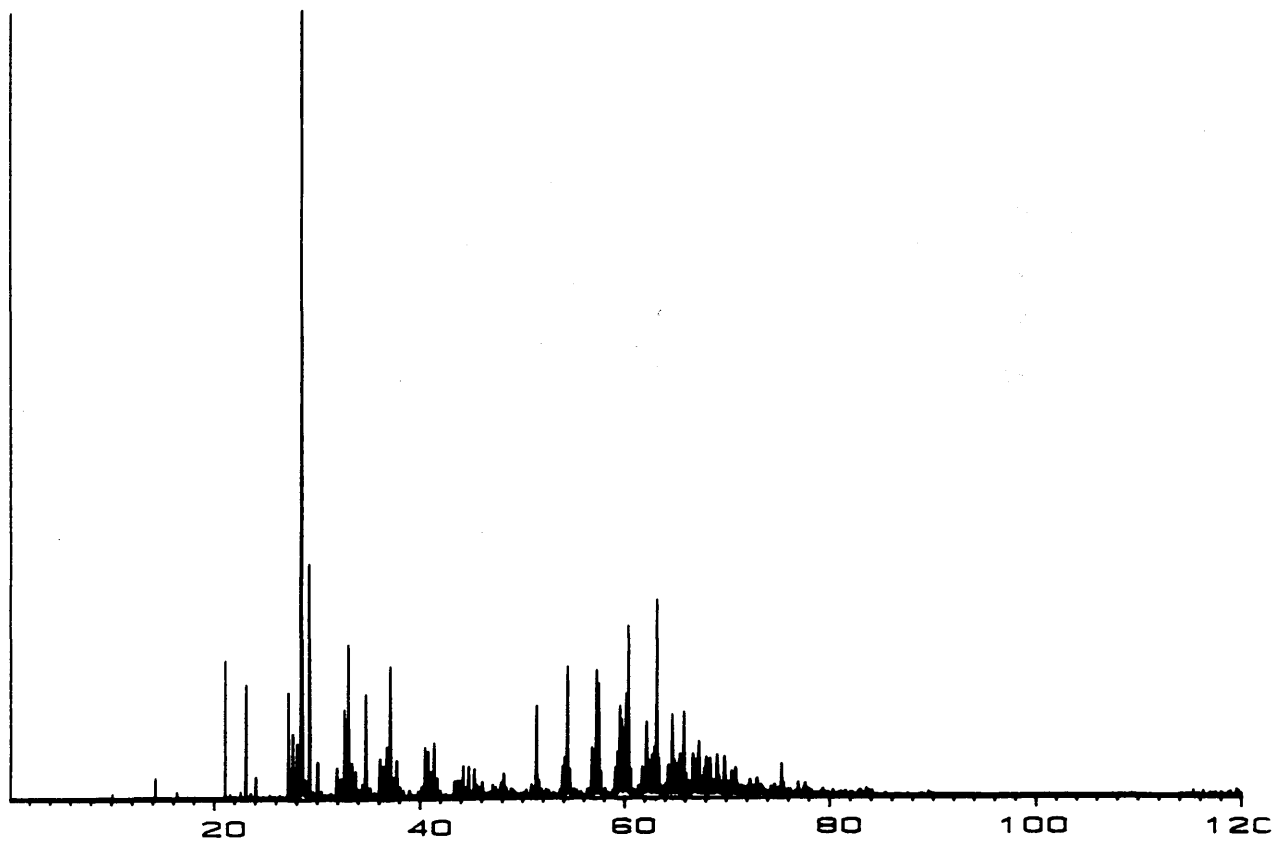


Figure 6.17 Mass spectrum at 266 nm (63 mJ/cm^2)

Figure 6.18 Mass spectrum at 266 nm (63 ml/cm²) - expanded view

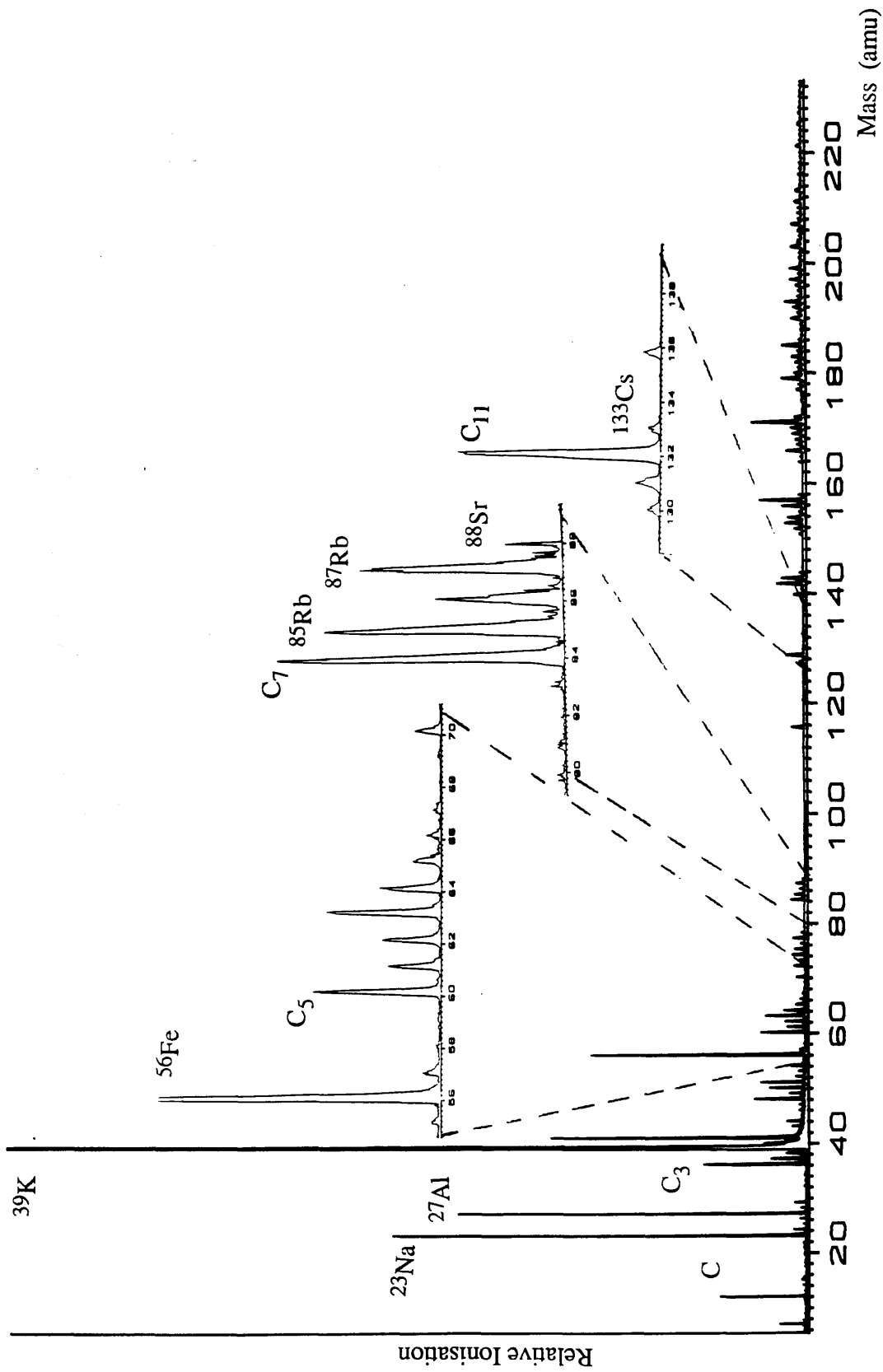


Table 6.4 Results from laser desorption of 1632a NBS sample at 266 nm

Element	Possible Contaminant	I.P. (eV)	Gladney (ppm)	Experimental (ppm) \pm 10%
^6Li	-	5.39	18.1	18.1
^7Li	-			
^{11}B	-	8.296	26.5	1.17
^{23}Na	-	5.138	380	362
^{27}Al	-	5.984	1.485%	331
* ^{28}Si	C_2H_4	8.149	2.95%	18.3
* ^{29}Si	C_2H_5			
* ^{30}Si	C_2H_6			
* ^{39}K	C_3H_3	4.339	2050	6345
* ^{41}K	C_3H_5			
^{40}Ca	-	6.111	1150	24.3
* ^{52}Cr	C_4H_4	6.764	17.5	20.95
* ^{53}Cr	C_4H_5			
^{54}Fe	-			
^{56}Fe	-	7.87	0.56%	325.4
* ^{63}Cu	C_5H_3	7.724	7.95	74.9
* ^{65}Cu	C_5H_5			
* ^{64}Zn	C_5H_4	9.391	14	38.3
* ^{66}Zn	C_5H_6			
* ^{67}Zn	C_5H_7			
* ^{75}As	C_6H_3	9.81	4.9	14.2
* ^{85}Rb	C_7H	4.176	15	33.5
* ^{87}Rb	C_7H_3			
* ^{88}Sr	C_7H_4	5.692	44	1.15
* ^{121}Sb	C_{10}H	8.639	0.35	2.85

The above comparisons of experimental concentrations with Gladney's results are generally *not* in good agreement. Stronger signals are seen for those elements having low ionisation potentials. Although peaks corresponding to a large number of elements within the sample are seen, the intensities of the peaks are *not* a reliable gauge of the actual concentrations. The main purpose of tabulating these results is to demonstrate the very strong dependence of the ion yield on the sample matrix.

Analytical instruments utilising the positive ion fractions are presently commercially available. The LAMMA (Laser Microprobe Mass Analysis) instrument and also the Laser Ionisation Mass Analyser (LIMA) use quadrupled Nd:YAG lasers at 266nm to vaporise samples, followed by time of flight mass spectrometry. The experimental results obtained in this section, however, show that at this short wavelength, organic interference is likely to be severe. This is likely to cause major problems in the study of environmental or biological samples containing high percentages of carbon. Furthermore, although at this wavelength, most of the elements present in the sample will be detected at 266nm by non resonant multiphoton ionisation, the degree of ionisation will be species dependent and will require careful calibration to avoid severe matrix interferences.

It has been suggested (Kimock 1984) that the yield of neutral atoms is less subject to matrix effects than ions because the much larger neutral component is less sensitive to surface properties and surface contaminants (Becker 1984), and therefore measurements on the neutrals would provide a more quantitative measurement of surface concentrations. Figure 6.19 (Kimock 1984) shows the yield of neutral In atoms and In ions as a function of oxygen exposure, which is often observed to enhance positive ion yields by several orders of magnitude. This graph shows that the neutral yield gives a much more direct representation of the surface composition than the secondary ion yield.

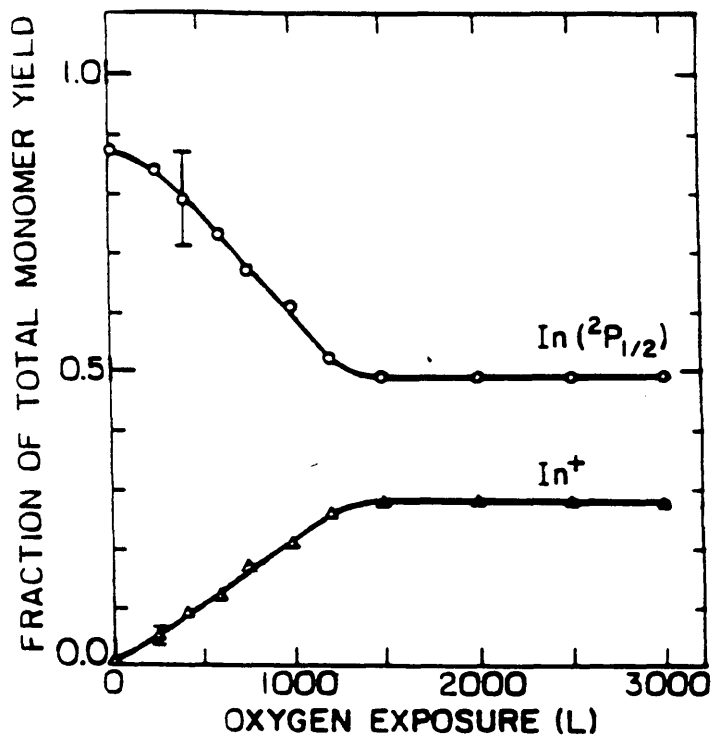


Figure 6.19 Yield of In neutrals and ions as a function of oxygen exposure (Kimock 1984)

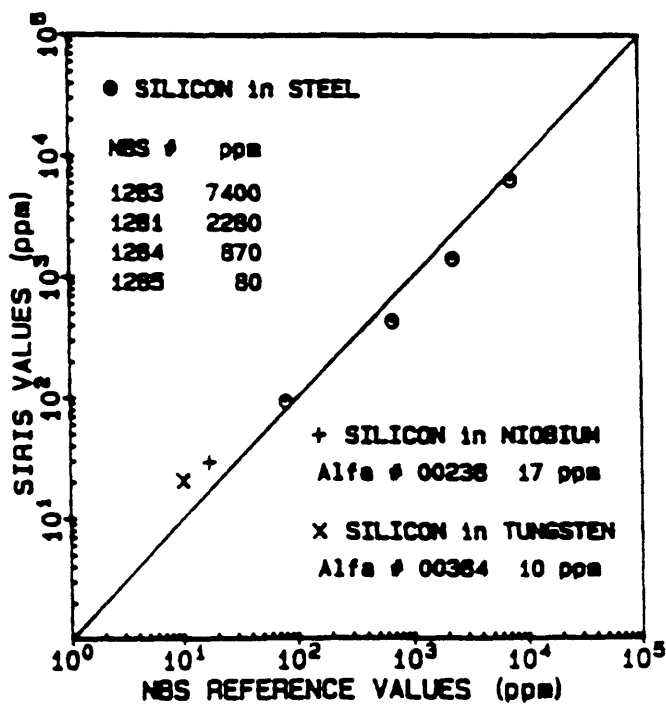


Figure 6.20 Comparison of SIRIS values and NBS reference values of concentrations of silicon in steel, tungsten and niobium (Parks 1986)

Although the neutral yield is not completely free from matrix effects, these are much less serious than those observed in SIMS. The technique of RIMS, in which neutral atoms are created and then resonantly ionised, is therefore likely to be much less matrix dependent. Verification of this is given in Figure 6.20 (Parks 1986) which shows good agreement with certified reference values for concentrations of silicon in niobium, tungsten and steel, using the SIRIS technique which utilises neutrals.

More carbon ions were expected to be seen at shorter wavelengths, since carbon has a fairly high ionisation potential of 11.3eV, and would therefore require more energy in the ionising photons. The carbon peaks were indeed present in the largest quantities in the spectra taken at 266nm and 355nm. The production of large numbers of clusters results in large scale isobaric interference, ie. the obscuring of trace element peaks by carbon peaks. It is clear from the above spectra that at shorter wavelengths the use of graphite as a conducting substrate could cause severe difficulties. However, carbon is the basic constituent of the NBS coal samples and is likely to be present in large quantities in most environmental samples. The use of longer wavelengths in the resonant ionisation process would suppress the production of carbon clusters and other organic background, but may not ionise the required elements. The resonant ionisation stage therefore appears essential for selectivity in the trace element analysis process.

6.4 RIMS of NBS Coal Samples

NBS coal samples were also used in the demonstration of the sensitivity of resonant ionisation in contrast to non resonant ionisation. Figure 6.21 shows a time of flight mass spectrum of a 1632a coal sample containing rubidium at a concentration of 15 parts per million. This is an desorption spectrum using an unfocussed Nd:YAG laser of wavelength 532nm and power 1mJ in a spot size of about 1mm². There is no evidence of the two rubidium isotopes. Figure 6.22 is a resonant ionisation mass spectrum. The

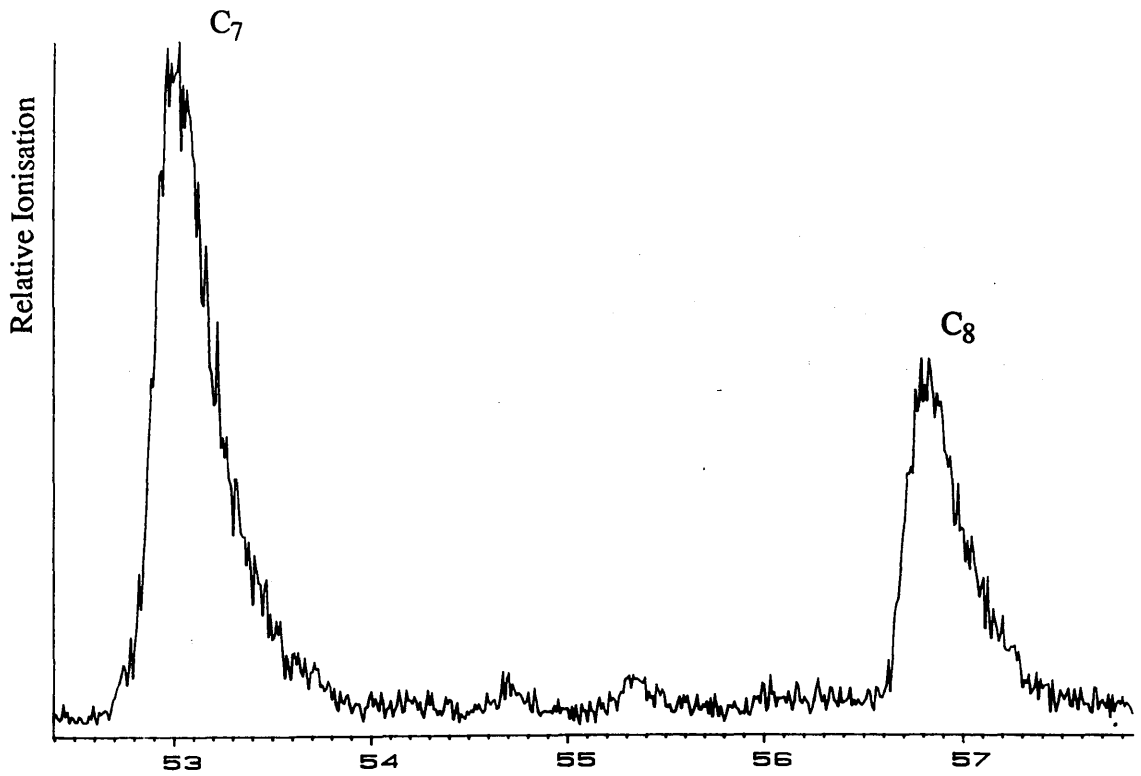


Figure 6.21 Time of flight spectrum of NBS 1632a coal sample using unfocussed ablation laser at 532 nm ($1\text{mJ}/\text{mm}^2$)

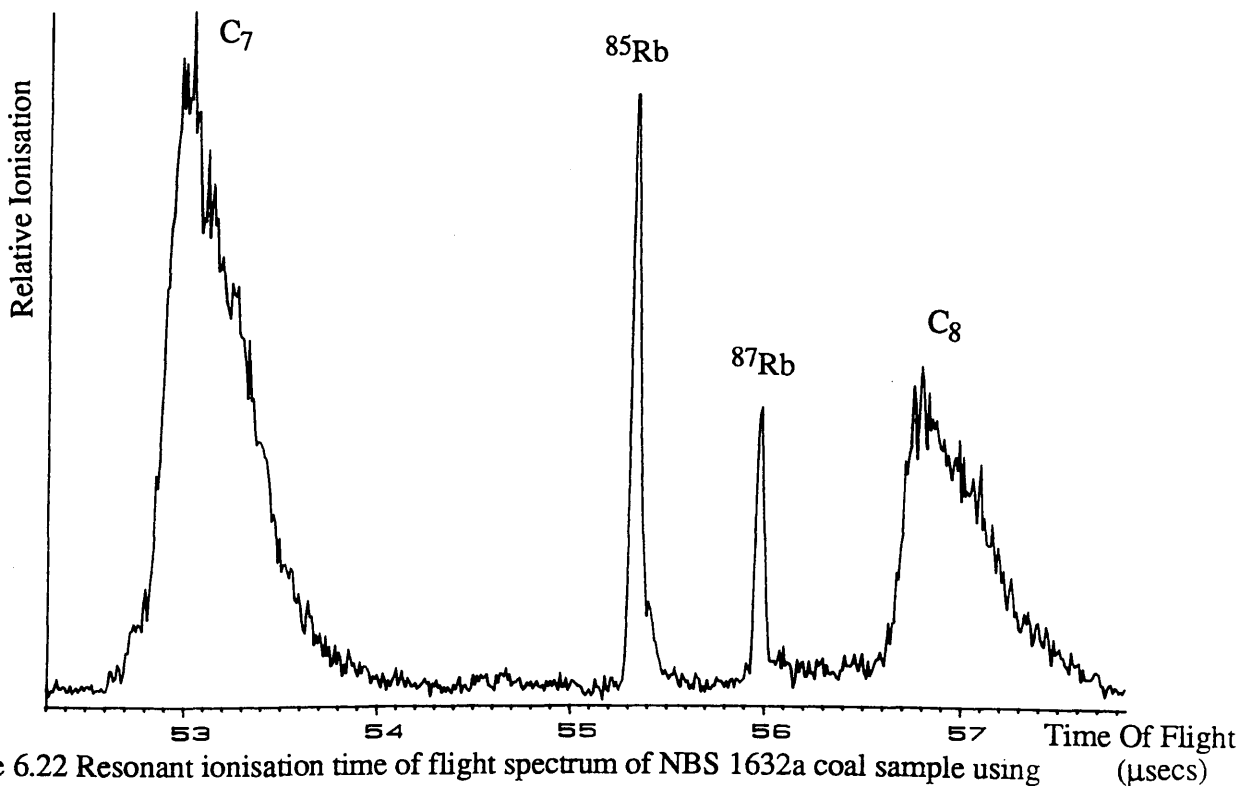


Figure 6.22 Resonant ionisation time of flight spectrum of NBS 1632a coal sample using unfocussed ablation laser at 532 nm ($1\text{mJ}/\text{mm}^2$) and resonant excitation dye laser tuned to rubidium resonance at 420.7 nm. The photoionisation step is brought about using an unfocussed Nd:YAG laser at 532 nm ($7\text{mJ}/\text{mm}^2$).

neutral rubidium atoms produced by the desorption laser were then ionised via a two photon resonance ionisation process, ie. using a blue dye laser for the excitation step tuned to the rubidium transition $5s_{1/2} - 6p_{3/2}$ at 420.7nm and focussed strongly to a power of 120 μ J, and ionising the excited rubidium atoms using an unfocussed Nd:YAG laser at 532nm with a power output of 7mJ. The two laser beams passed collinearly into the interaction region, and were triggered to ionise the neutral plume after a delay of about 1 μ second from the desorption laser pulse. The resonantly ionised rubidium isotope peaks are clearly visible and are noticeably narrower and better resolved than the non resonant peaks. The background level corresponding to a minimum detection limit of rubidium in SRM 1632a coal of less than 1 part per million was determined by calculating the areas of the rubidium peaks and of the corresponding background signal. In this spectrum, the green 532nm laser initiating ionisation was unfocussed. Figure 6.23 shows the effect of blocking the green ionising laser. The non resonant signals are of similar size, but the resonant rubidium peaks are very much diminished. This verifies that the green 532nm laser is responsible for much of the ionisation of the excited rubidium atoms from the 6p level to the continuum.

In Figure 6.24, the green ionising laser is strongly focussed. This has the effect of increasing the intensity of the rubidium peaks, but also shows a ^{88}Sr signal and a hydrocarbon signal at mass 84 amu. Focussing the green ionising laser therefore has the unwanted effect of ionising other species apart from rubidium. Figure 6.25 is a spectrum taken using the green laser unfocussed, and the blue excitation laser slightly detuned to off resonance at 418 nm. No rubidium signals are seen, and this confirms the effectiveness of RIMS in elemental selectivity.

Williams et al (1984) have used a similar RIMS system to detect chromium in stainless steel samples. The isotope ^{54}Cr was detected in their experiment at parts per thousand levels for around 4500 laser shots. It was anticipated, however, that parts per

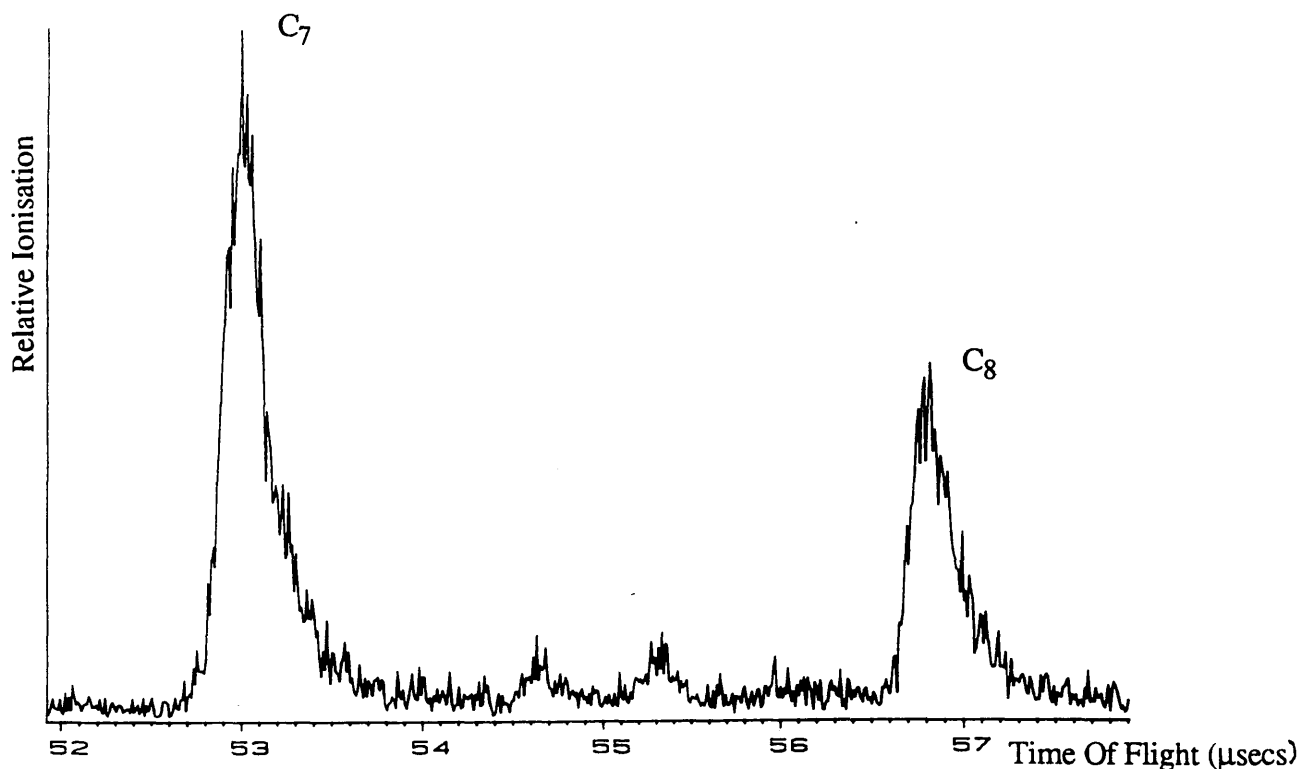


Figure 6.23 Resonant ionisation time of flight spectrum of NBS 1632a coal sample using unfocussed ablation laser at 532 nm ($1 \text{ mJ}/\text{mm}^2$) and resonant excitation dye laser tuned to rubidium resonance at 420.7 nm. The photoionising laser has been blocked.

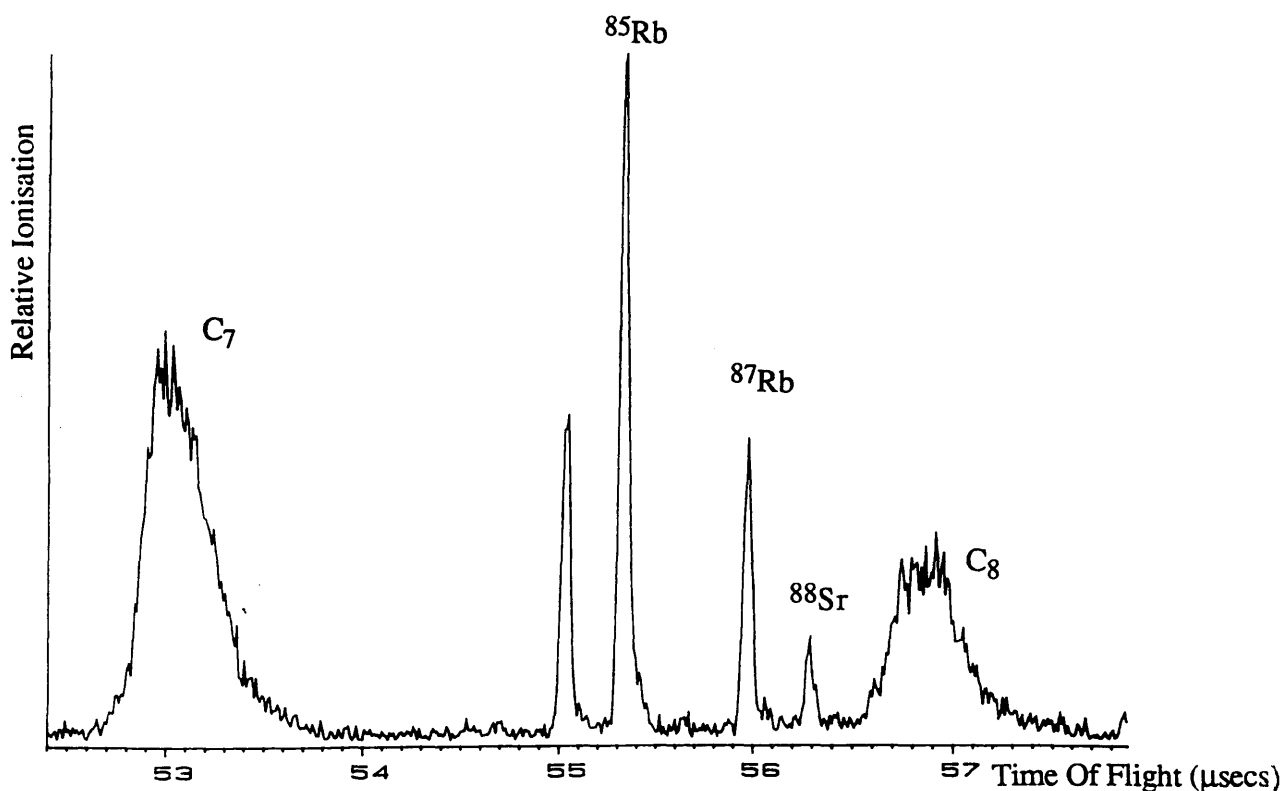


Figure 6.24 Resonant ionisation time of flight spectrum of NBS 1632a coal sample using unfocussed ablation laser at 532 nm ($1 \text{ mJ}/\text{mm}^2$) and resonant excitation dye laser tuned to rubidium resonance at 420.7 nm. The photoionisation step is brought about using a strongly focussed Nd:YAG laser at 532 nm.

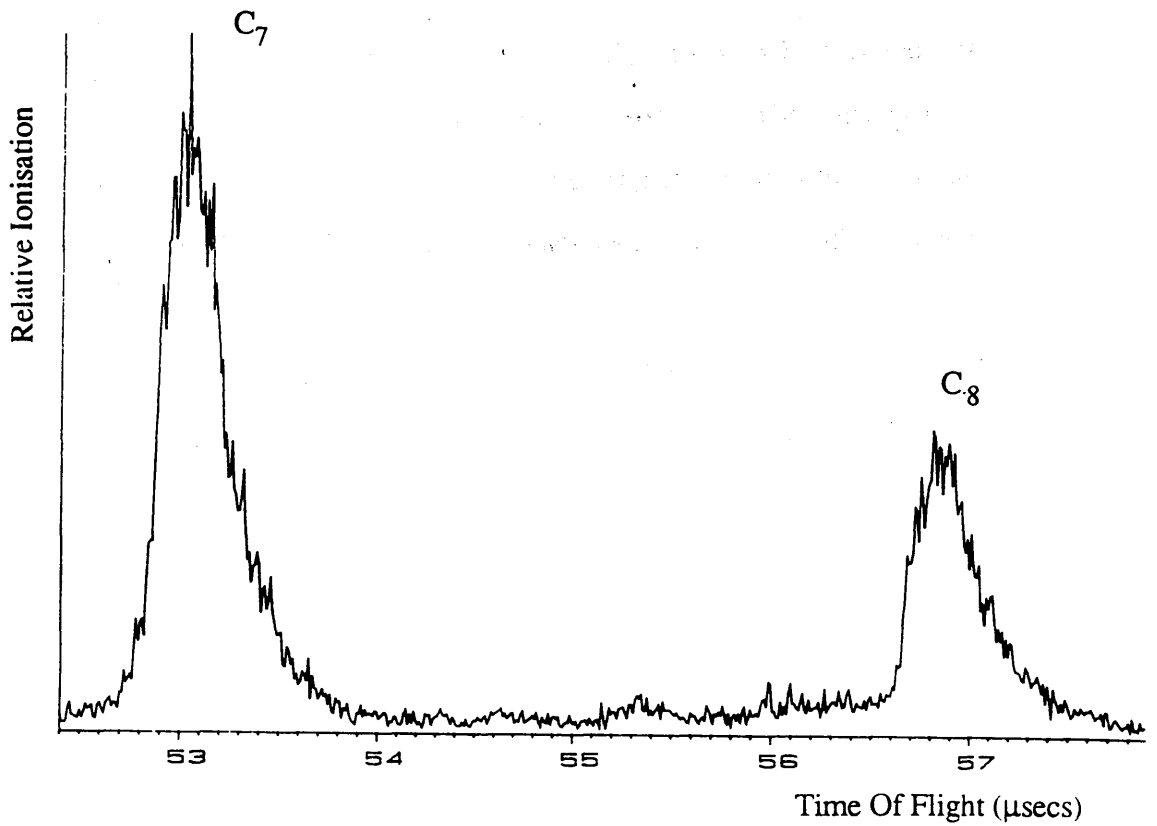


Figure 6.25 Time of flight spectrum of NBS 1632a coal sample using unfocussed ablation laser at 532 nm ($1 \text{ mJ}/\text{mm}^2$) and dye laser off resonance at 418 nm.

million could be detected if the number of laser shots used was increased to around 30000 in order to obtain good statistics. The RIMS results presented above give a much lower detection limit for rubidium of less than 1ppm for only 1000 laser shots. This limit could be further improved by increasing the number of laser shots.

It is clear from Figures 6.22 and 6.25 that the resonance ionisation technique exhibits excellent sensitivity for elemental detection. The broad peaks observed in the resonant spectra, however, are due to C_7 and C_8 clusters which remain at the same intensity when the ionising lasers are tuned off resonance. The clusters of carbon ions are both desorbed and non resonantly ionised during the pulse of the desorption laser, in a similar process to secondary ionisation mass spectroscopy (SIMS). There are at least three possible methods of removing these ions from the RIMS spectra. Firstly, the desorption laser could be operated at the 1064nm wavelength to avoid ionisation of the carbon clusters. Secondly, there is a significant and very useful time difference between the detection of the SIMS like background ions and the RIMS ions. This is due to the fact that the SIMS like ions are liberated from the sample surface, whereas the RIMS ions are formed in the neutral plume at about 1mm from the surface. It is therefore possible to suppress the SIMS like ions by applying a negative voltage onto the sample stub to coincide with the desorption pulse and ending before the RIMS laser pulse, ie. lasting around 1 μ second. A third alternative method for removal of SIMS ions has been suggested by McLean et al (1988), in which the ion extract optics are designed as to create a field reversal in the laser interaction region which does not permit desorption ions to be emitted from the sample surface, but enables RIMS ions created to the right of the null point to experience the extraction field. The optimum condition for RIMS ion transmission is that the null point is as close to the sample surface as possible, ie. to ensure that the geometrical overlap between the RIMS lasers and the desorbed plume is maximised. This condition can be calculated by use of positive ion ray tracing programs, eg. SIMION (Dahl and Delmore).

6.5 Carbon Clustering Effects- Background

Having observed many carbon peaks as contaminants in the coal sample experiments, it became important to analyse the TOF spectrum of a pure graphite sample for use as a control sample. The observed distribution of carbon clusters showed many interesting features which warranted further more detailed studies.

The study of clusters is a relatively recent topic for research; most of the present knowledge regarding clustering effects has been acquired within the last decade. The study of clusters is important in the fields of catalysis and combustion, and is also of interest in astrophysics, as clusters have been identified spectroscopically in the atmospheres of carbon stars and in comet tails. In general, clusters are formed in the gas phase or in a plasma. The exact clustering mechanisms are not completely understood, and, as noted by Rohlfiing et al, the origin of the observed distribution of cluster sizes may depend upon the initial conditions for the formation of the clusters.

The two most widely used methods for the study of clusters are (O'Keefe et al 1986) :-

- 1) Particle bombardment or laser vaporisation of a surface with direct mass spectrometric detection of the ions formed, which is similar to the evolution of carbon clusters in our laser mass spectrometer.

- 2) Laser vaporisation of carbon into a molecular beam, followed by laser photoionisation of the neutral clusters produced, and consequent mass analysis.

Supersonic beams are often used in the study of clusters since the clusters

within the beam are isolated and cooled as a result of the free jet expansion, and are therefore in an ideal state for study of the properties of unsupported clusters.

In the first method, carbon clusters of relatively small sizes are observed (less than 30 atoms). The second method produces a bimodal distribution of C_n^+ , with the first modal maximum at $n = 15$ and the second at $n = 60$. The lower mass distribution contains peaks corresponding to both odd and even clusters, whereas the higher mass distribution contains clusters with only even numbers of atoms. The overall structure of the mass distribution produced by either method is the same. The following sections discuss recent results obtained on carbon clustering effects.

In 1984, Rohlfiing et al studied the clustering of carbon atoms using laser vaporisation of a graphite substrate within a pulsed nozzle. The neutral cluster beam was probed downstream by UV photoionisation and consequent mass analysis. Spectra of carbon clusters containing between 1 and 190 carbon atoms were produced, showing a distinctly bimodal cluster size distribution. Both even and odd clusters were observed up to the 30 atom level. The remainder of the spectrum contained peaks corresponding to only even clusters (see Figure 6.26). O'Keefe et al (1986) observed a similar bi-modal peak distribution with enhanced abundances of C_n^+ at $n = 11, 15, 19, 44, 50, 60$ and 70. This observation was explained by Rohlfiing et al on the basis of carbon cluster formation and stability arguments and led to speculation regarding a proposed new form of carbon, the carbyne form, made up of C_2 units with alternate single and triple carbon bonds. This argument was supported by the fact that the absence of odd clusters appeared to be inconsistent with other theories of ring structures, the diamond lattice sub units or the cumulated double bonds being the primary cluster sub units for these larger clusters.

It has also been observed that some clusters exhibit unusual stability, and in

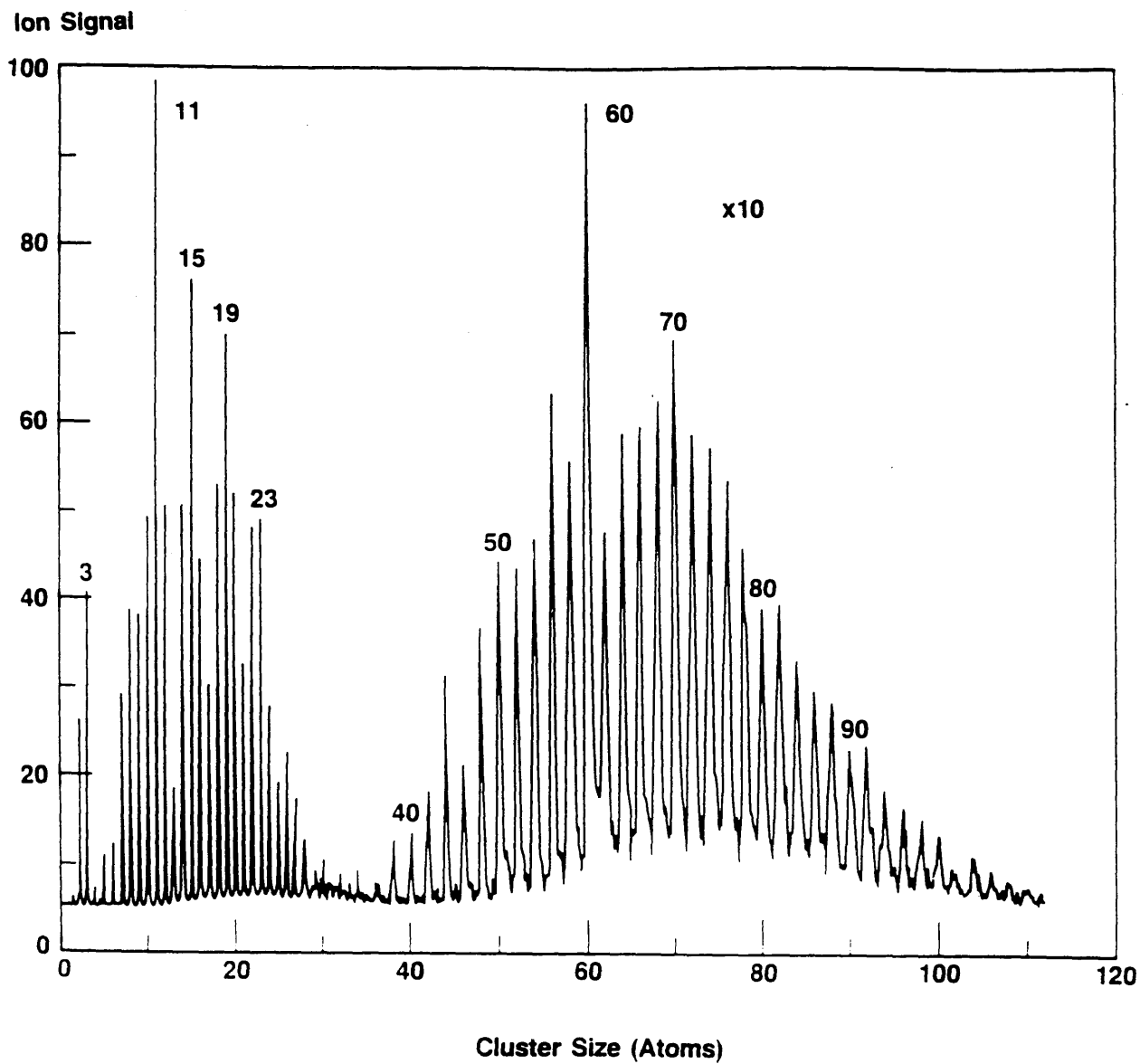


Figure 6.26 Carbon cluster spectrum (Rohlfing et al 1984)

particular, the C_{60} cluster is exceptionally stable. Kroto et al (1985) proposes that the geodesic and chemical properties inherent in a closed hollow spheroidal carbon cage structure can explain the stability of the C_{60} molecule. The structure suggested is a truncated icosahedron (football shape) which is a polygon with 60 vertices and 32 faces, 12 of which are pentagonal and 20 hexagonal. The C_{60} molecule results when a carbon atom placed at each of the 60 vertices has all its valences satisfied by two single and one double bond. This molecule has been given the name Buckminsterfullerene, as a consequence of Buckminster Fuller's architectural studies (see Marks 1960). This football structure (see Figure 6.27) satisfies all valencies, appears to be aromatic and has a diameter of around 7Å. The inner and outer surfaces are covered with a sea of π electrons. In addition to the dominance of the C_{60} peak in the spectrum, Kroto et al observed prominent peaks at C_{50} and C_{70} . Furthermore, the results of Liu et al (1986) support the special stability of even carbon clusters in the range 40 - 80 atoms and the icosahedral structure of C_{60} .

There exists a number of arguments verifying the closed structure theory (Kroto 1987):-

1) It is essential that the carbon valence requirements are satisfied, ie. that each atom is three-connected to other atoms by one double and two single bonds. Thus, only even numbered cages should be stable. Shells containing an odd number of atoms are possible, but all such structures must have several unbonded atoms.

2) Five and six ring networks are abundant in polyaromatic hydrocarbons. Seven membered rings are rare, and those containing three or four atoms are very unstable. This indicates that only five or six ring networks are likely to occur readily. Jones (1966) has stated that the cages must contain twelve pentagonal rings, but the number of hexagonal rings is not restricted.

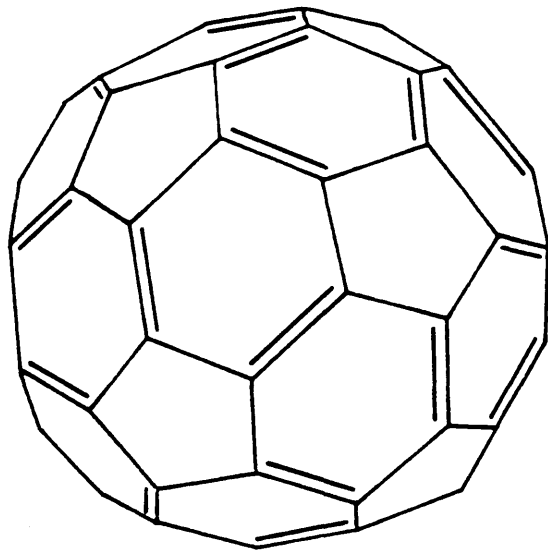


Figure 6.27 The Buckminsterfullerene cluster C_{60}

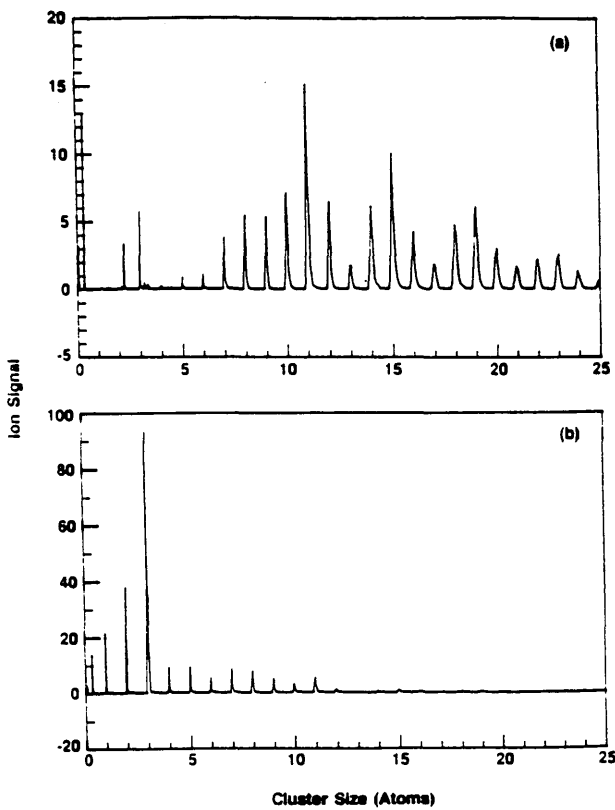


Figure 6.28 TOF spectra of C_n clusters (Rohfing et al 1984) at a) 0.7 MW/cm^2
b) 40 MW/cm^2

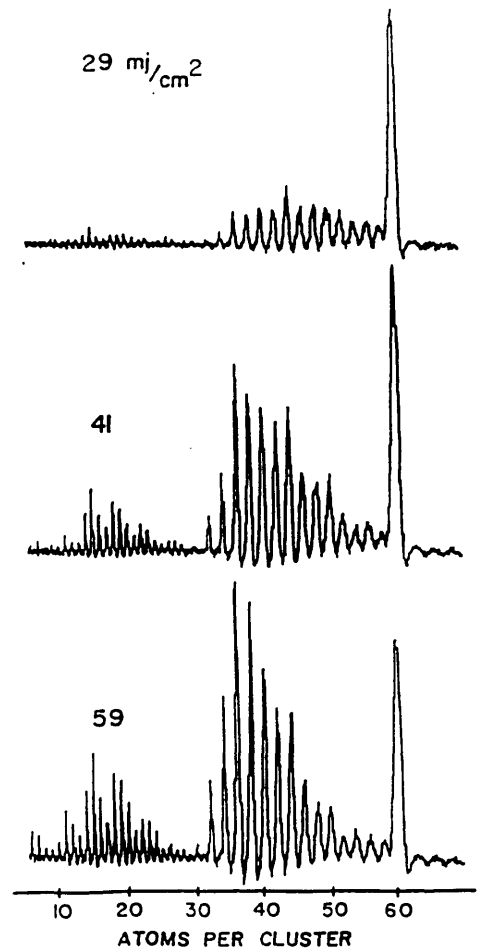


Figure 6.29 C_n clusters at various power levels (O'Brien et al 1988)

3) Barth and Lawton (1971) have established that a structure in which a pentagon is completely surrounded by hexagons is stable. Furthermore, the optimum stability is achieved in a cage in which twelve pentagons are completely surrounded by hexagons (C_{60} structure).

4) Closed spheres are likely to be structurally stable, as the strain from bond angle deformation can be evenly dispersed over the surface.

5) Closed cages are likely to have closed shell electronic structures. (Fowler and Steer 1987).

In addition, Kroto observed that other numbers of carbon atoms exhibited increased stability, namely those clusters containing 20, 24, 28, 32 and 36 atoms.

Rohlfing et al (1984) produced two carbon cluster mass spectra (see Figure 6.28) taken under identical conditions except that one spectrum was recorded using a focussed ionising ArF laser (40 MW/cm^2) and the other using an unfocussed laser (0.7 MW/cm^2). The difference in the two spectra is very obvious - the high intensity mass spectrum is dominated by smaller cluster ions, particularly C_3^+ , resulting from fragmentation of larger neutral or parent ion clusters. Similar results were obtained when using a KrF laser (with photon energy 4.99eV) with the C_3^+ peak dominating the spectrum.

O'Brien et al (1986) observed carbon cluster mass spectra at various ionising laser fluences, and deduced that the relative prominence of C_{60} in comparison with its neighbours diminishes with increasing laser fluence. This implies that C_{60} does not arise as a result of photofragmentation of larger "soot" clusters, ie. clusters containing

more than 200 atoms. In addition, the dependence of the C_{60} peak on ionisation cross section effects can be ruled out by the demonstration of dependence of C_{60} prominence on the conditions at the laser vaporisation nozzle source, and the fact that C_{60} is prominent regardless of whether an ArF or an F_2 laser was used for ionisation.

A later paper by O'Brien et al (1988) describes photofragmentation experiments on the positive ions of C_{60} and other carbon clusters using a dissociation laser. A mass spectrum gives evidence of the existence of two distinct types of cluster. A distinct gap was observed in the carbon cluster mass spectrum between around 28 and 40 atoms. The lower group shows peaks corresponding to both odd and even clusters, whereas the higher group consists of only even clusters. It was observed that clusters containing 34 atoms or more all dissociate to form even numbered fragments. Large even clusters were found to fragment by the loss of the high energy species C_2 , and odd clusters appear to lose only one atom. Clusters having 31 atoms or less, however, all fragment by the loss of C_3 . These two regimes are separated sharply by C_{32}^+ which fragments to produce small cluster ions in the 10 - 19 atom range. These photophysical results were interpreted as consequences of the large even clusters having edgeless, spheroidal cage structures, whilst the smaller ones have linear chain or ring structures. Both theory and experiment agree that small clusters are largely one or two dimensional (Pitzer et al 1959, Heath et al 1987) - smaller clusters form linear chains and larger ones form monocyclic rings.

Figure 6.29 shows mass spectra of C_{60} fragments obtained by O'Brien with various fluences of 353nm laser light. This confirms the bi-modal structure observed by Rohlving and others, and shows there is a gap in fragment cluster ions observed after C_{32}^+ down to around C_{25}^+ . This abrupt change in the fragmentation pattern at 32 indicates that this is the last stable cage structure.

O'Brien et al also conducted experiments providing extensive evidence that large even numbers of clusters, in particular, C_{60} , are particularly stable, and conclude that only one consistent explanation can account for all observations, ie. the large even clusters are closed cages with twelve pentagons and $(n - 20) / 2$ hexagons. The special stability of the C_{60} cluster results from symmetry considerations. The proposed truncated icosahedron, C_{60} , achieves a perfectly even distribution of strains. Strain distribution considerations would then predict C_{70} to be the next most stable cluster in agreement with experiment (Zhang et al 1986, Klein et al 1986).

Experimental results obtained by Seifert et al (1988) on smaller clusters ($n < 20$) support the theory of a transition from linear to cyclic C_n clusters. It was observed that C_7^+ , C_{11}^+ and C_{15}^+ were abundant. From binding energy considerations, it was deduced that clusters with an odd number of atoms seem more stable than clusters with an even number of atoms. The lower stability of small rings is a consequence of a reduced overlap of the p orbitals in the ring plane, compared with the linear arrangement of the atoms. With increasing ring size, this overlap approaches that of a linear system. This can be interpreted as a decrease of ring strain with increasing cluster size in cyclic systems.

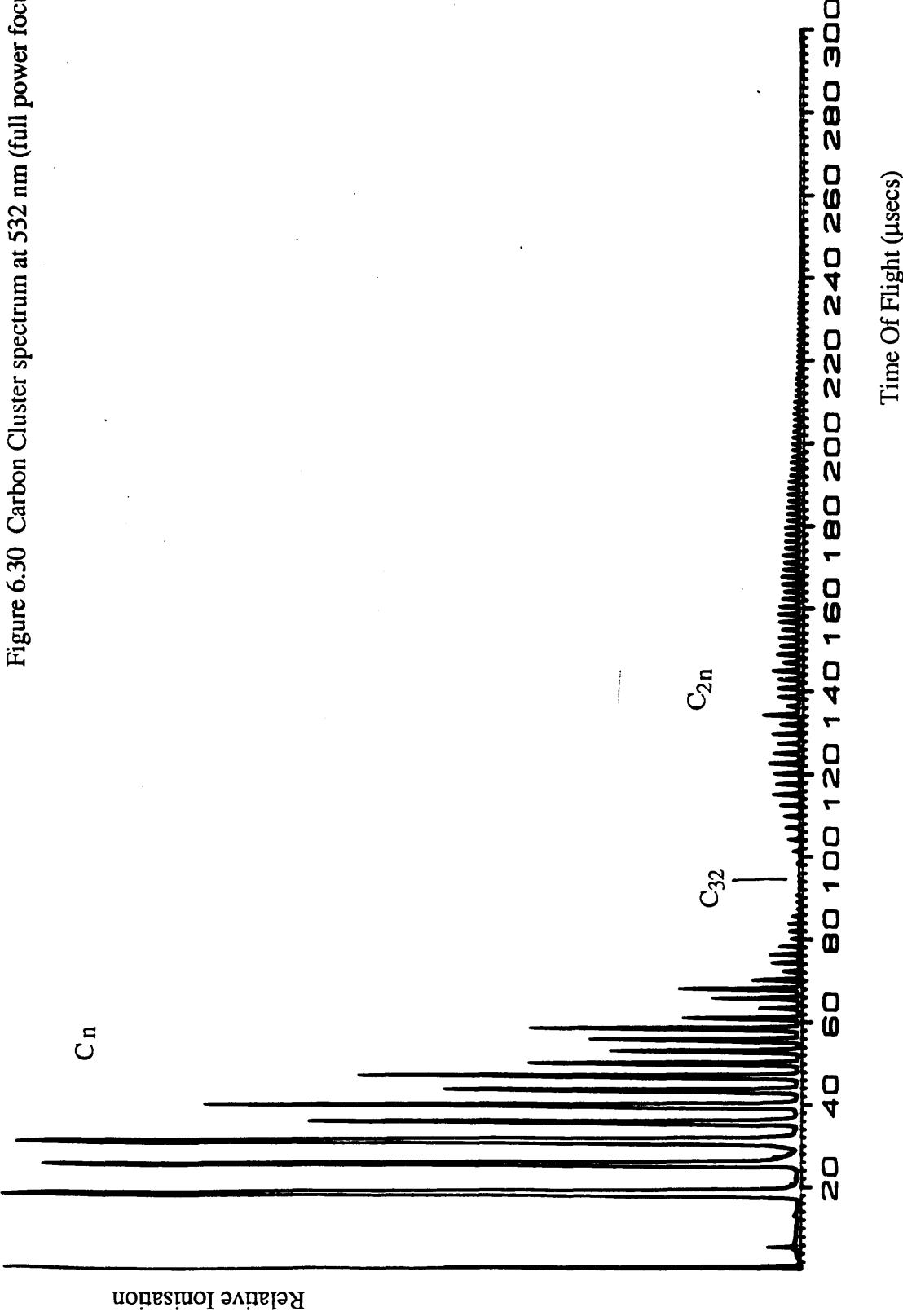
6.6 Carbon Clustering Results from the TOF Mass Spectrometer

Graphite samples were made up by compressing high purity graphite powder into the indentation on the stainless steel sample stub. The sample stub could then be positioned inside the ionisation chamber on the $xyz\theta$ manipulator. Samples could be easily exchanged using the sample insert probe without loss of high vacuum. A Quantel Nd:YAG laser, incident at a 45° angle to the graphite sample was used for desorption and ionisation. The resultant carbon cluster ions were accelerated by the extraction optics into the TOF drift tube and consequently detected at the channelplate.

Figure 6.30 shows a TOF mass spectrum of carbon recorded by laser desorption / ionisation using a graphite sample. The desorption / ionisation was carried out using a fully focussed Nd:YAG laser at a wavelength of 532nm. The bi - modal structure of roughly Gaussian distribution observed in other experiments (Rohlfing et al 1984, O'Keefe et al 1986 and O'Brien et al 1988) is clearly visible. Both even and odd clusters were observed up to around the $n=30$ atom level. This can be attributed to a simple atom addition mechanism for cluster formation. The structure of the C_n^+ clusters is not precisely known. The most probable forms may be linear chains or a diamond - like structure. Figure 6.30 also indicates the relative abundances of the C_n and C_{2n} clusters. Clusters were observed up to around mass 40,000 amu.

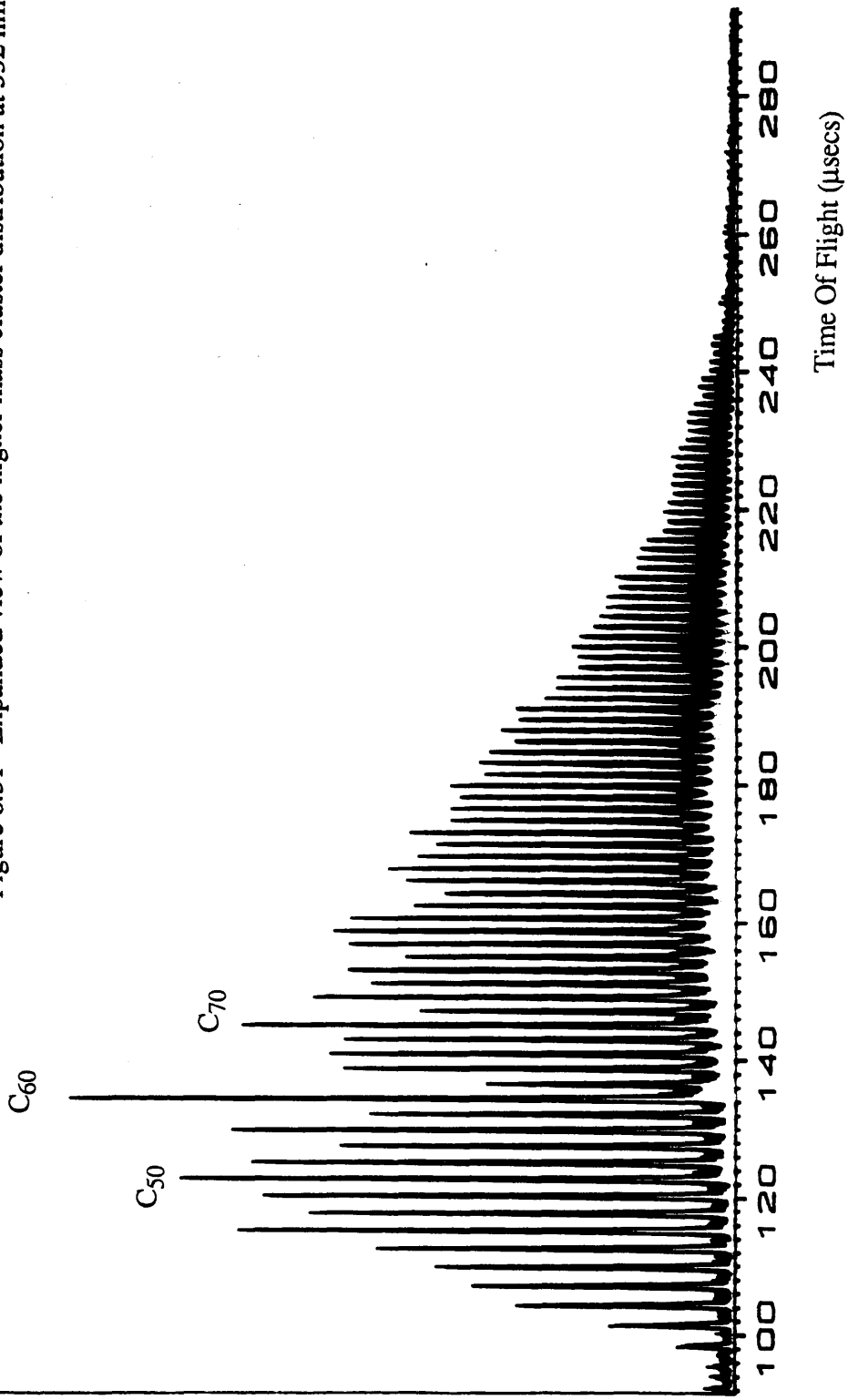
An expanded view of the higher cluster distribution is shown in Figure 6.31. The C_{60} peak, corresponding to the closed shell Buckminsterfullerene cluster, is clearly prominent. Furthermore, the heights of the C_{50} and C_{70} peaks are enhanced, in agreement with other experimental observations (Hahn 1986, Rohlfing 1984 and Kroto 1985). The C_{2n}^+ clusters are thought to form closed structures for maximum stability. The closed sphere structure is favourable as the valence requirements for all carbon atoms can be satisfied, ie. every carbon atom is bonded to three others by two single bonds and one double bond. Minimum strain between bonds is achieved when the bonds are at an angle of 120° to each other. Figure 6.27 showed the proposed truncated icosahedral structure of the C_{60} cluster. This "football" structure is clearly likely to be the most stable cluster since the bond angles are under minimum strain. Figures 6.32 and 6.33 show the structures of the C_{70} and C_{50} clusters, which have less favourably oriented bond angles, but still exhibit a high degree of stability. Only peaks corresponding to even numbered clusters are seen, and a sharp divide in the distribution pattern is observed in the $n = 28$ to $n = 32$ region. The C_{52}^+ , C_{62}^+ and C_{72}^+ peaks are smaller in intensity than expected, the C_{62}^+ peak being the most suppressed. This further supports the

Figure 6.30 Carbon Cluster spectrum at 532 nm (full power focussed)



Relative Ionisation

Figure 6.31 Expanded view of the higher mass cluster distribution at 532 nm



Time Of Flight (µsecs)

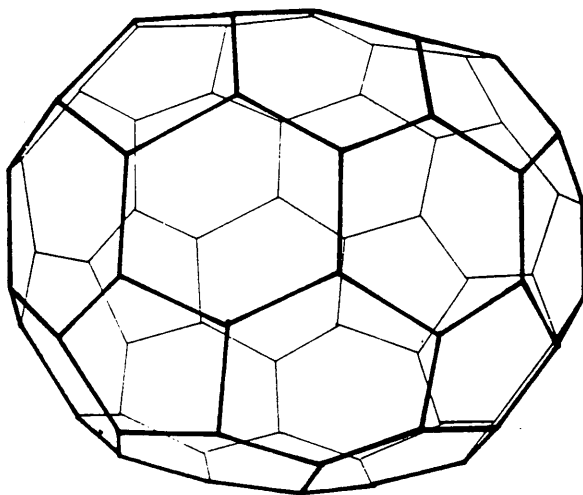


Figure 6.32 Structure of the C_{70} cluster

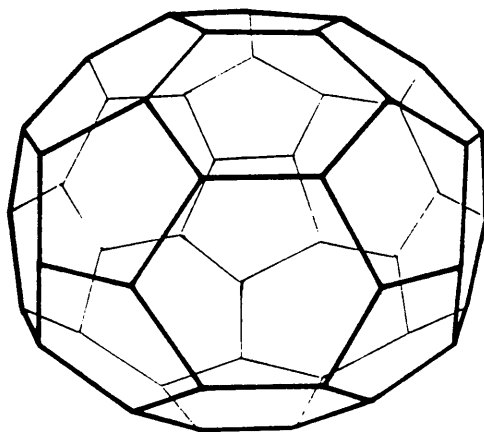
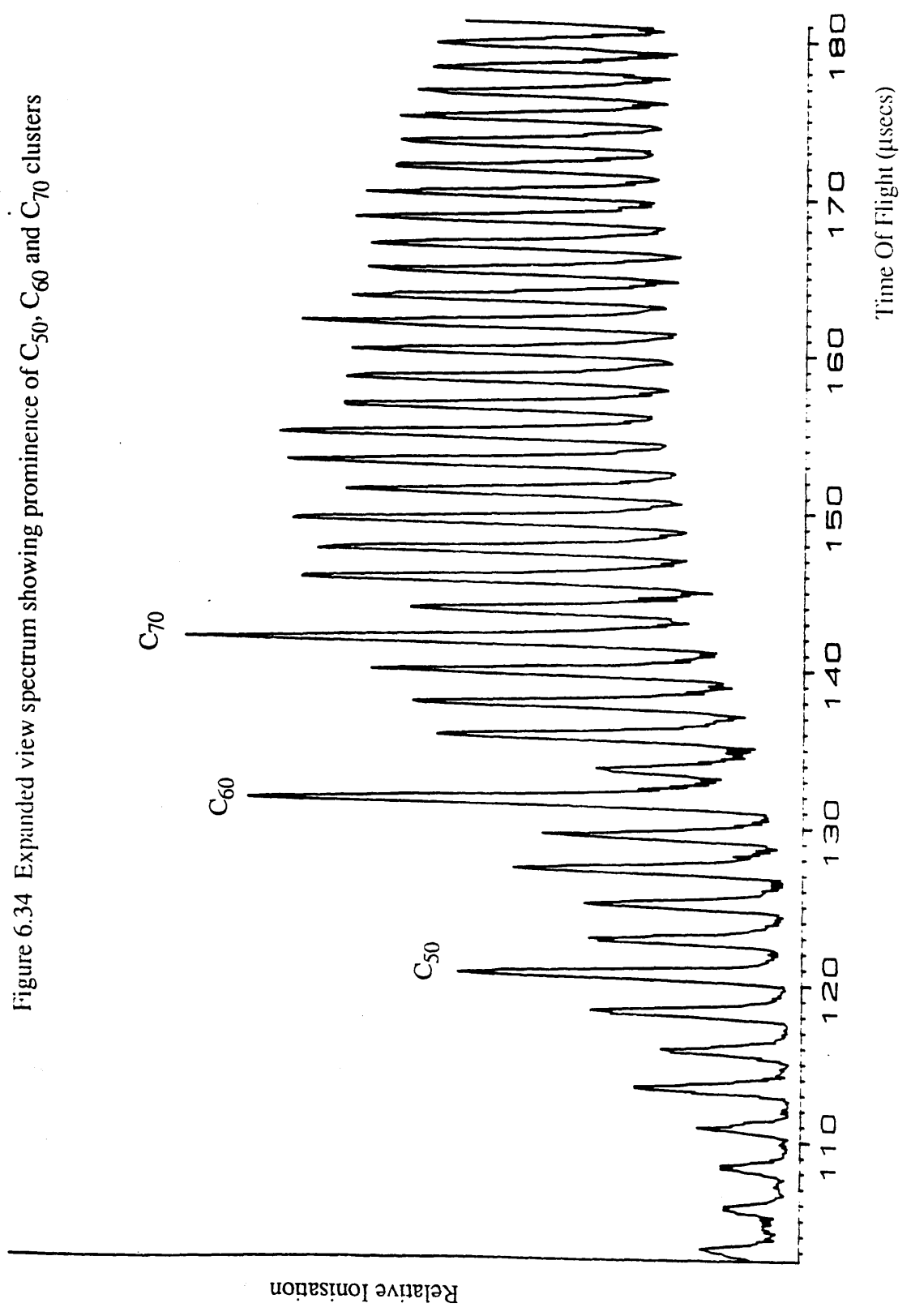


Figure 6.33 Structure of the C_{50} cluster

Figure 6.34 Expanded view spectrum showing prominence of C₅₀, C₆₀ and C₇₀ clusters



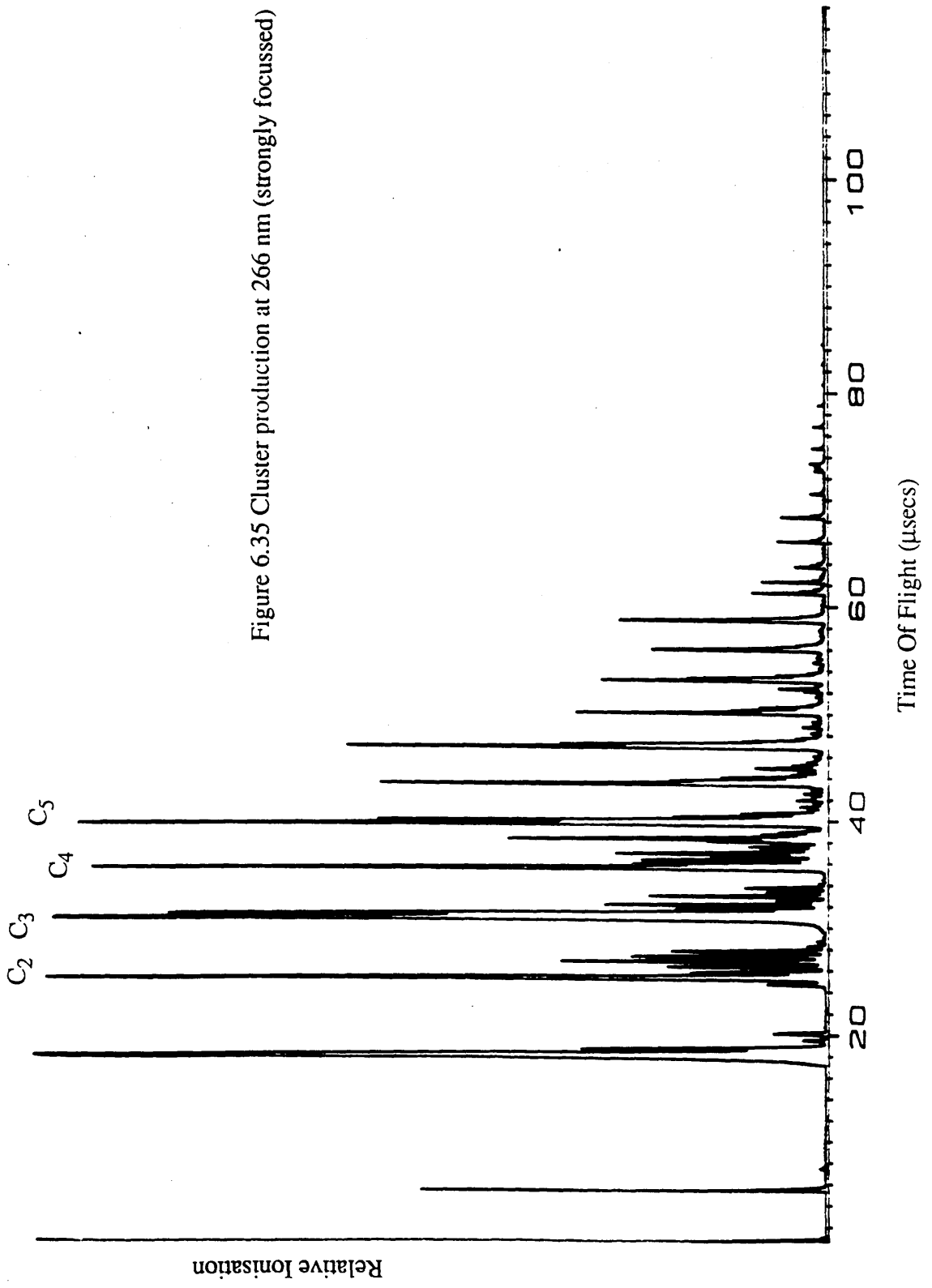


Figure 6.35 Cluster production at 266 nm (strongly focussed)

argument for the special stability of the C_{60}^+ cluster.

Figure 6.34 shows an expanded view of the carbon cluster spectrum taken at wavelength 532nm. Again the three peaks C_{50}^+ , C_{60}^+ , C_{70}^+ dominate the spectrum. The peaks corresponding to C_{52}^+ , C_{62}^+ and C_{72}^+ are again suppressed. These clusters appear to lose a C_2 group, thereby transforming into the more stable closed shell configuration. Production of clusters at wavelength 266nm was also attempted. A reasonable clustering spectrum was obtained when the Nd:YAG laser was strongly focussed onto the sample. The spectrum is shown in Figure 6.35. At this wavelength, the bi - modal structure is no longer apparent, and the fragmentation pattern shows a much higher proportion of smaller clusters centred around C_3^+ . This result is very similar to that obtained by Rohlifing et al (1984) in which fragmentation produced small cluster ions, particularly the stable C_3^+ form.

The above results again confirm the possible interference problems in trace analysis at shorter wavelengths (less than 532 nm) as a result of using a graphite substrate, and supports the use of ion optics or other methods to remove SIMS type ions from the spectra.

CHAPTER 7 CONCLUSIONS AND FUTURE PROGRAMMES

7.1 RIS of Caesium Vapour

The spectroscopic study of caesium and rubidium metals using proportional counters has allowed the selection of efficient methods for ionisation. Caesium has been detected in a proportional counter at a level of less than one part in 10^9 by two photon resonant ionisation via p levels (Houston 1986). In addition, two photon ionisation spectra were observed for the 6s - np Rydberg states, and collisional ionisation from these high lying excited states to the continuum was shown to be an effective means of ionisation requiring a much lower laser fluence than photoionisation. The cross section for photoionisation from Rydberg states is very small compared with the collisional cross section. Collisional ionisation can therefore provide a large increase in the ion yield. The use of lower laser fluence reduces the overall background signal and leads to less fragmentation of molecular signals. Niemax (1983) stated that collisions of the buffer gas atoms with highly excited atoms can result in ionisation with unit efficiency.

Studies of three photon ionisation spectra of caesium showed evidence of molecular hybrid resonance structure as well as atomic ionisation, as observed by Collins et al (1981). These broad resonances result from the photodissociation of caesium dimers to form a ground state atom and an excited atom, which is then resonantly ionised. Experimental wavelengths obtained for these resonances agree well with the calculated wavelength values.

7.2 RIS of Rubidium Vapour

Two and three photon resonant ionisation spectra were obtained for rubidium using firstly a proportional counter and then a quadrupole mass spectrometer. Spectra of

5s - np Rydberg states were recorded. Three photon ionisation spectra of 5s - ns and 5s - nd transitions were studied, and particular transitions, the 5s - ns transitions, were found to have a strong dependence on the pressure of the proportional counter gas. Operation of a proportional counter without gas is possible, but because there is no gas amplification, the detection sensitivity is greatly reduced. Therefore, in order to study the ratio of s / d levels in the absence of collisional effects, the quadrupole mass spectrometer at a pressure of around 10^{-6} torr was used. The experimental results obtained for the s / d ratios at low pressure were similar to theoretical predictions (Pindzola 1984).

Using the quadrupole mass spectrometer at room temperature, it was found that the molecular component of the ionisation was negligible compared to the atomic component. It has been suggested, however, that techniques such as laser ablation or ion sputtering may increase the molecular fraction considerably, with molecules constituting up to 10% of the sputtered particles in ion ablation (Kimock 1984). It is therefore important in RIMS trace detection to employ methods of removing the non resonant ablated ions from the resonant ionisation signal, eg. by ion optics or voltage pulsing as explained in Chapter 6.

7.3 Time of Flight Mass Spectrometer

The first results using RIS in the Glasgow Time of Flight Mass Spectrometer served to demonstrate RIMS as a highly sensitive and selective technique whilst highlighting possible difficulties in trace element detection.

In the laser desorption spectra of the ambient vapour within the mass spectrometer, organic molecules originating from diffusion and rotary vacuum pump oils were identified. These signals were only evident at the shorter UV wavelengths, 266nm

and, to a lesser extent, 355nm. Very few background signals were observed at 532nm or 1064nm even when using a strongly focussed laser beam. At shorter wavelengths, the fragmentation of organic molecules increased with higher laser power and decreasing wavelength. It is clear from these studies that in order to minimise background signals in RIMS, resonant ionisation schemes employing visible light should be used in preference to higher energy UV photons.

The results obtained from the laser desorption and non resonant ionisation of NBS coal samples proved useful in a qualitative sense, but it was evident that this technique alone was quantitatively inaccurate. The non resonant technique, however, could be valuable in determining the constituents of unknown samples.

The study of carbon clustering effects proved to be an interesting topic in itself as well as providing insight into the possible interference effects in spectra caused by using graphite substrates. The spectra showing resonance ionisation of rubidium clearly showed interference from carbon cluster peaks. Use of a longer wavelength for desorption would reduce the intensities of the carbon cluster peaks. As carbon is likely to be a major constituent of most environmental samples, the most practical solution would be to exploit the time difference between the formation of resonant and desorbed/non resonant ions and adapt the extraction optics in order to delay or deviate these "SIMS - like" ions from the resonant ions. Possible methods are described in McLean et al (1988).

7.4 Autoionisation

Research is presently being carried out in the Glasgow Laser Ionisation Group on the autoionisation of calcium, as a method of reducing the required laser fluence, and hence the background signal, for trace detection by RIMS. Use of an autoionising

resonance can reduce the photon fluence requirements by two orders of magnitude (Hurst and Payne 1988).

Autoionisation states are energy levels which lie above the ionisation continuum in an atom (see Figure 7.1) and result from the interaction of discrete states with continuous states. In atoms with two or more valence electrons, there may exist low lying configurations with more than one excited electron. The total energies of these levels can lie above the ionisation limit of a single valence electron. In this case, autoionisation occurs via a coupling to the continuum above the first ionisation limit. Low energy autoionisation levels occur only in elements with two or more valence electrons.

Autoionisation causes resonant structure in the ionisation continuum (Lambropoulos and Zoller 1984). Transitions to autoionisation states are characterised by large cross sections of around 10^{-15} cm^2 compared with direct photoionisation cross sections of $10^{-17} - 10^{-18} \text{ cm}^2$. At present, autoionisation levels have not been thoroughly researched, although some studies have been carried out, eg. Bekov et al have studied autoionisation in gadolinium (1978) and ytterbium (1981), and Buck and Bischel (1988) have produced autoionisation spectra of atomic oxygen. It is thought that once autoionisation levels for suitable elements have been established, they will be used extensively in RIS and in RIMS.

7.5 Further Experiments using the TOF Mass Spectrometer

An extensive comparison between the two ablation techniques of ion gun sputtering and laser ablation/desorption will be carried out using the TOF mass spectrometer at Glasgow. Real environmental samples are likely to be used in the trace element analysis. At present, research is planned into the trace detection of lead in polar

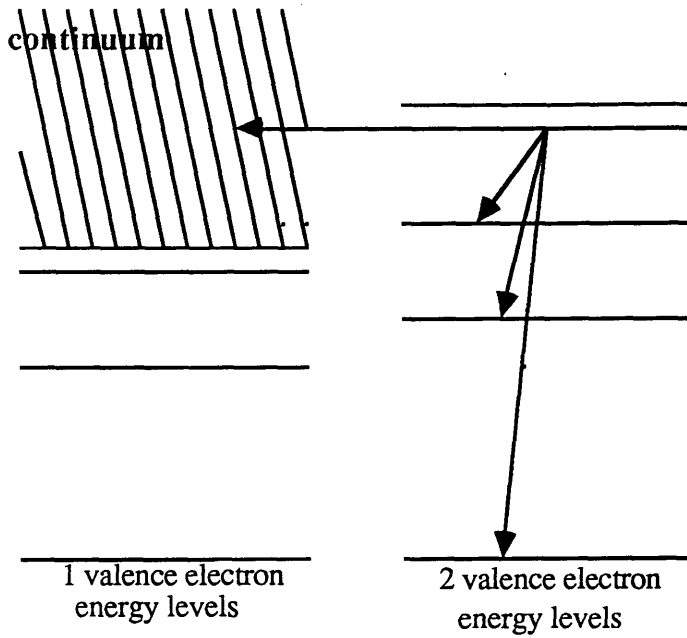


Figure 7.1 Autoionisation

ice samples in collaboration with the British Antarctic Survey. Lead was chosen for detection because of its known toxicity and because it can be used as a gauge for pollution levels. Detection at the level of picogrammes / gramme is likely to be necessary. Lead has an ionisation potential of 7.4eV and a fairly straightforward ionisation scheme achievable using two dye lasers. The water content of the ice samples will be evaporated off a tungsten wire leaving the impurities on the wire for analysis. Absolute concentrations of lead will be determined by comparison with known standards.

A number of improvements could be introduced in order to improve the detection sensitivity of the instrument. Ionisation of excited species by collisions, electric fields or by autoionisation methods would reduce the required laser flux, and would result in a smaller background signal. As the time of flight system is kept under high vacuum (10^{-10} torr) collisional ionisation could only be brought about by introducing a valve or nozzle through which gas such as argon could be introduced into the interaction region in synchronisation with the laser pulse. Also, a reduced laser power requirement allows the laser beam to be used unfocussed, resulting in a larger geometrical overlap with the ionising plume, and consequent smaller signal loss.

The overall efficiency for the conversion of atoms to ions is usually low due to the inherent low temporal duty cycle of the pulsed lasers. An increase in the repetition rate of the laser could be achieved by using copper vapour lasers with repetition rates in the 5 - 10 KHz range, which would increase the duty cycle and thus increase the sensitivity of the instrument. Kroenert et al (1985) have reported a temporal efficiency of near unity using a 6.5 KHz copper vapour pumping system for plutonium detection.

For improved sputtering efficiency, argon ion guns with higher current flux could be used with currents in the mA range to sputter ions of energy up to 30KeV. This would also increase the number of sputtered atoms and improve the sensitivity (Kimock

1983). For example, the use of a 10mA argon ion gun at 25 KeV and pulse length 5µseconds in conjunction with a 5 KHz copper vapour laser would improve the detection limit by five orders of magnitude (Smyth 1988).

A second laser ionisation mass spectrometer has been constructed at Glasgow for the main purpose of depth profiling in semiconductors. This instrument is described in more detail in Appendix 2. Work is presently being carried out on samples of III-V semiconductors, in particular GaAs / AlGaAs layered structures.

7.6 Molecular Spectroscopy

Research work is presently being carried out in the laser ionisation group at Glasgow on a MoD contract to study the RIS of common explosives for the purpose of trace detection of explosives at airports. The experimental work covers two areas; obtaining "fingerprints" of explosives such as TNT, DNT, and EGDN, and secondly studying the wavelength dependence of the laser ablation process for these materials.

Fingerprinting of explosives is being carried out using proportional counters and excimer pumped dye lasers. Preliminary investigations have been carried out using nitrobenzene in a buffer gas of argon / methane, as nitrobenzene is thought to have an ionisation potential close to that of DNT and TNT. The single photon UV absorption spectra of explosives obtained from a Beekman spectrophotometer may also prove valuable for comparison with unknown spectra in a similar manner to the identification of phenol and toluene as impurities in counter gas (Towrie et al 1986, Drysdale et al 1986).

Having obtained the fingerprints, wavelength dependence studies on the laser ablation process will proceed. Once the photon energies at which explosive samples can be readily ionised have been obtained, the resonant ionisation can be initiated using lasers

tuned to the appropriate wavelength.

The introduction of a supersonic jet system (see Section 7.7) would reduce the number of rovibrational energy levels within each electronic state which may lead to blurring or obscuring of important features in the UV fingerprinting. Also, the acquisition of BBO harmonic generation crystals would allow study of molecules with ionisation potentials up to around 11.3eV via two photon processes, and up to 14.1 eV with three photons. This should almost certainly cover the necessary UV range.

7.7 Supersonic Cooling

A major problem in molecular spectroscopy is the complex structure of the many vibrational or rotational levels in most molecules. The use of supersonic beams takes advantage of the internal cooling in a gas as a result of expansion. The molecule to be studied via this technique is expanded through a small orifice, usually in a carrier gas. When a gas expands freely from a high pressure region into a vacuum, adiabatic cooling of the internal energy of the gas occurs. Thus the thermal energy of the molecules, composed of translational, rotational and vibrational energy, is partly transferred into expansion energy. This transfer occurs during the expansion in the orifice where the probability of collisions is high. The degree of cooling depends on the number of collisions during the expansion, and is proportional to the product of the density and the orifice diameter. Free jet expansions have been shown to produce translational temperatures of near 0.006K and rotational temperatures near 0.5K (Levy et al 1980).

The use of internal cooling in molecular spectroscopy has one major advantage. Cooling results in population of only the lowest rotational and vibrational levels in the electronic ground state. Thus, a higher fraction of the molecules can be resonantly ionised from the ground state, thereby increasing the sensitivity of RIMS.

Supersonic jets incorporated into time of flight systems reduce the initial spread of velocities and result in improved resolution.

7.8 Detection of Radioactive Caesium

RIMS offers a method for environmental monitoring of isotopes emitted by nuclear reactors which are difficult to detect by conventional radiometric techniques, eg. the low energy beta emitting nuclides.

Several isotopes of caesium are associated with the nuclear industry, most of which are fission products. ^{137}Cs is the principal reported component of low level liquid waste. In 1982, 2000TBq of the isotope were emitted from the Sellafield reprocessing plant, thereby constituting more than half the total beta activity discharged. ^{134}Cs is also currently assayed separately. However, of more interest from the RIMS viewpoint is ^{135}Cs . It is a low energy beta emitter produced in high yield (6%) from thermal fission of the principal fuel nuclides, but is subject to no discharge restriction apart from the gross beta activity limit. It is also detectable with existing RIMS technology at levels where conventional radiometry becomes unreliable. As discharges of ^{137}Cs and ^{134}Cs are high, it is likely that considerable amounts of ^{135}Cs are also present in low level waste but remain largely undetected. The spectroscopic study of multiphoton transitions of ^{133}Cs have already been carried out in proportional counters, and could easily be used in conjunction with a time of flight mass spectrometer for extremely sensitive radioactive caesium detection.

APPENDIX 1

Applications of Resonant Ionisation Spectroscopy to Accelerator Based High Energy Physics.

A 1.1 Introduction

In recent years, laser induced ionisation has become significant in the field of high energy physics as a useful technique in the calibration of multiwire drift chambers. This appendix describes some preliminary studies of laser induced ionisation in the field of high energy physics. A short synopsis of the significance of laser induced ionisation is given and the experiments leading to the identification of two organic impurities causing ionisation, phenol and toluene, are summarised. Finally, the effect of gas purification on the laser induced ionisation is detailed.

Initial experiments in 1979 by Anderhub and co-workers demonstrated the production of ions by a nitrogen laser in a drift chamber, and subsequently used a tunable dye laser to study doping using various organic molecules (see Anderhub 1980). Zero background laser induced ionisation was reported in a counter gas which was free of doping material. This was confirmed by Freuholz (1980) after conducting experiments on two photon resonance ionisation of naphthalene between 280nm-650nm in a proportional counter filled with P10 gas (90% argon, 10% methane gas). A background ionisation level of 200 ion pairs/cm/ μ J of laser fluence was observed by Bourotte and Sadoulet (1980) in their drift chambers. When a quadrupled Nd:YAG laser is used (wavelength 266nm), the ionisation shows a linear power dependence, whereas with a nitrogen laser of wavelength 337nm, a quadratic dependence is evident. The linear dependence was attributed to the saturation of the excitation step in a two photon process involving a real intermediate stage. Hilke observed a background signal at 337nm of 2×10^3 ion pairs / cm. Here, a linear power dependence is observed at low powers which becomes

exponential as the fluence is increased. A quadratic background dependence was reported by Desalvo and Desalvo (1982) using a nitrogen laser at low power with a background level of 38 ion pairs / cm / μJ of laser light.

The European Organisation for Nuclear Research (CERN) has constructed a Large Electron-Positron storage ring (LEP) which will allow intense beams of electrons and positrons to collide at very high energies to investigate some of the outstanding questions in the understanding of the electroweak forces. At the centre of the detector, built for the ALEPH experiment, is a Time Projection Chamber. A TPC is a type of gas filled multiwire proportional counter and will incorporate a laser calibration system. The simulation of charged particle tracks by pulsed UV lasers is a useful method for the measurement of the relation between drift length and drift time, thus giving a calibration of track distortions due to electric field inhomogeneities. In particular, distortions in the ALEPH Time Projection Chamber can be due to inhomogeneities of the parallel electric and magnetic fields in the chamber.

The source of the ionisation has been the subject of much research. In 1980, Bourotte and Sadoulet observed laser ionisation with and without a low ionisation potential additive (diethylaniline). The mechanism for the ionisation of the gas when no additive was present was attributed to the two photon ionisation of low ionisation potential hydrocarbon impurities. Rockwood et al (1979) had already observed that organic impurities were responsible for background ionisation in some multiphoton studies. The most likely explanation is therefore the presence of some low ionisation potential impurity in the counter gas (Hubricht et al 1985). This may be pump oil vapour or outgassing of the materials from which the counter was constructed.

Outgassing from counter surfaces are caused by adsorption and desorption processes. There exist two basic types of adsorption, namely chemical (chemisorption) and physical

(physisorption). Chemisorption is a result of chemical bonding with the surface. Physisorption is caused by weak van der Waal's forces between the surface and the molecule. For example, random fluctuations in the electron distribution of a molecule can give it a transient dipole moment. The dipole can induce polarisation of a nearby system giving a brief coulombic attraction between the molecule and the system. The net effect is a weak attractive force between molecules in the gas and any surfaces with which the gas is in contact .

With such a wide variation in background ionisation levels being observed, adoption of a more uniform calibration method became essential so that a given amount of laser fluence at a constant wavelength would produce the same ionisation. This can be achieved by seeding small quantities at parts per million of an ionisable molecular species into the counter gas in order to give controllable levels of ionisation without affecting the chamber's performance.

Positive identification of the source of the ionisation would clearly allow a much more reproducible use of this method of calibration. It was felt that an investigation of the wavelength dependence of the two photon 'background' ionisation spectra may produce information leading to the identity of the impurities. This is of importance to the ALEPH programme, but it is also important to identify the background if the ultimate sensitivity of RIS as an analytical technique is to be realised, since the same impurities are likely to exist in a typical RIS system.

A 1.2 Detection of Toluene in Proportional Counter Gas by Resonant Two Photon Ionisation Spectroscopy

The presence of some simple substituted benzenes molecules in P10 gas used at CERN has been recently reported (Boerner 1985). The two groups of organic

compound which commonly absorb in the near UV are those with chromophoric groups and those with conjugated bonds. A chromophoric group contains an atom with a lone pair of electrons and generally will absorb around 310nm (3.8eV). Conjugated molecules contain a chain of carbon molecules with alternate single and double bonds and generally absorb at about 300nm (4.1eV). Some conjugated systems are extremely stable, in particular, aromatic ring systems like benzene and substituted benzenes. These exhibit electronic absorptions in the 260nm - 300nm wavelength range. These molecules often have absorption resonances in the same wavelength range as the background ionisation in the counter gas.

Unfortunately, a comprehensive listing of two photon ionisation spectra is not currently available. There is, however, literature available on single photon absorption spectroscopy. There should be extensive similarities between the single photon absorption spectra and the two photon ionisation spectra as the excitation step of the two photon resonant step involves exactly the transitions which give rise to single photon absorption. The ionisation step has little dependence on wavelength (Brophy and Rettner 1979).

Investigations were made into the single photon absorption spectra of some of these molecules for comparison with the R2PI spectrum. The single photon spectrum for substituted benzene samples were measured using a Beckman UV 5270 spectrophotometer.

By inspection of the wavelength dependence of the two photon ionisation spectrum using a tuned dye laser, phenol has been established as a common impurity in counter gas systems (Towrie et al 1987). Phenol proved difficult to remove by pumping out, baking or flushing with clean gas. For efficient removal, it was necessary to dismantle the counter and clean all parts individually. Having removed the phenol, and

even under extensive baking under vacuum of the proportional counter and gas filling system, the laser induced ionisation remains, although at a greatly reduced level. Resonant peaks due to phenol were not present in the resonant two photon ionisation spectrum of the clean counter, but fine structure was observed near 268nm (see Figure A.1). A high resolution R2PI spectrum between 262 and 269nm is shown (Figure A.2c).

The resonant two photon ionisation spectra of the gas were recorded in the region 260nm-269nm, using a dye laser pumped by a XeCl filled excimer laser (Lumonics). The dye used produced a wavelength range between 520nm - 590nm. This output was then frequency doubled using an Inrad crystal doubler. An LSI-11 computer was used to record wavelength spectra on floppy disc (data acquisition and apparatus are described in detail elsewhere - Ledingham et al 1984).

It was found that the single photon absorption spectrum for toluene measured on the spectrophotometer closely matched the resonance two photon ionisation structure. In order to confirm this observation, a R2PI spectrum of high purity toluene was recorded. A concentration of around 2ppm was introduced into a clean proportional counter by flowing P10 gas over a sample of toluene held at -80°C before entering the counter. The resultant spectrum shown in Figure A.2b proves that toluene is the main source of the residual background ionisation in the clean counter. Comparison of Figures A.1a and A.2 gave an estimation of the background concentration of toluene in a very clean counter at around 1ppb (the observed ionisation at 266nm was 10^4 ion pairs per cm for a laser fluence of $1\mu\text{J} / \text{mm}^2$).

Toluene was also tested as a suitable seeding agent for laser calibration systems and was found to be easily handled and easily removed from counters. Unlike phenol, toluene can be flushed out by flowing clean P10 gas through the counter. It also

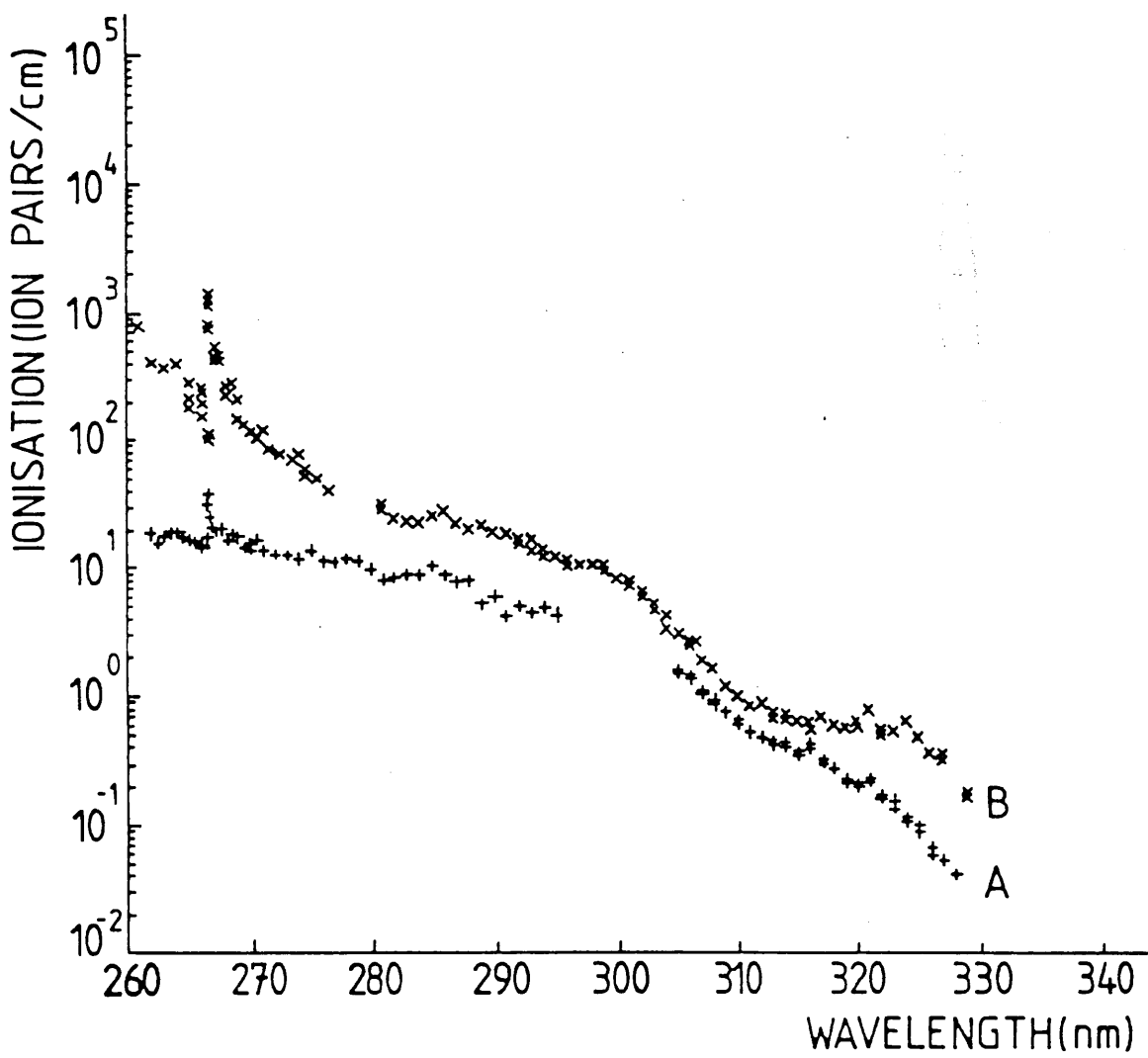


Figure A.1 Background ionisation. Graph B shows the ionisation from a relatively clean counter while graph A indicates the ionisation from a counter baked extensively under vacuum. Some structure at 268nm still remains.

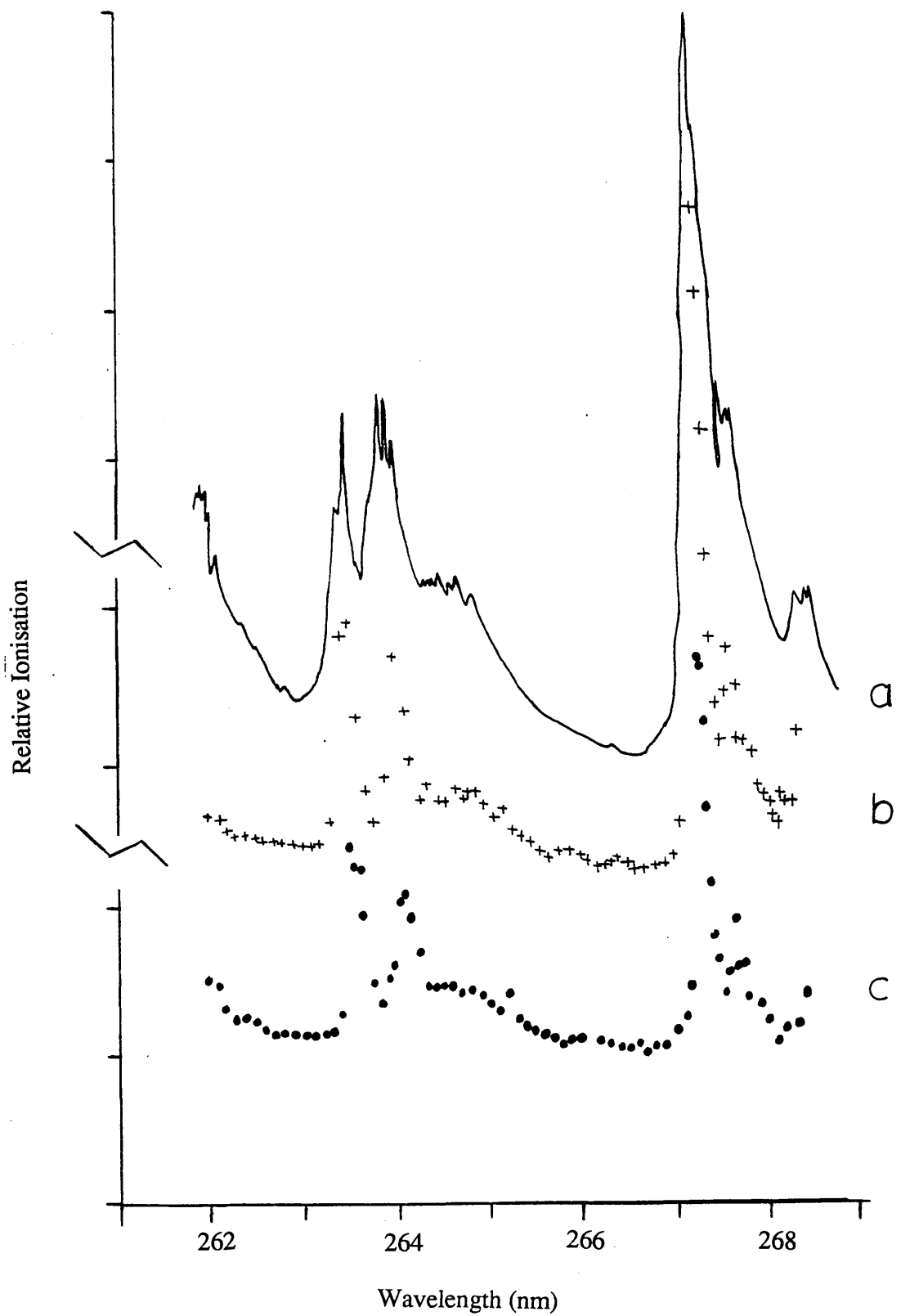


Figure A.2 a) Single photon absorption spectrum of toluene
b) Two photon resonant ionisation spectrum of toluene
c) Background ionisation in relatively clean counter

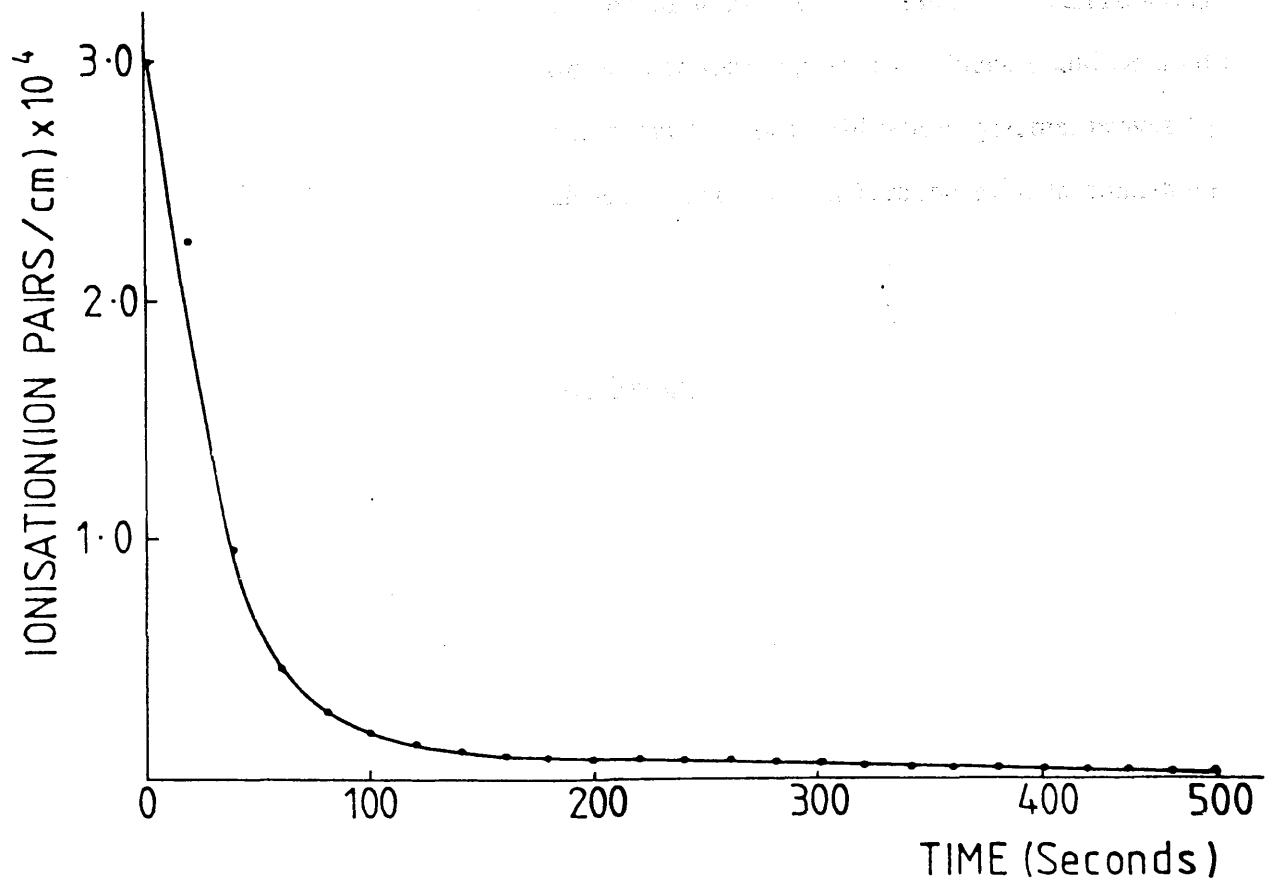


Figure A.3 This graph shows the ease with which toluene is flushed from the counter by argon methane gas.

has the advantages of having a low toxicity and only a slight odour. An experiment in which toluene was seeded at 2ppm into the counter for six hours and then flushed with clean counter gas proved that the background ionisation fell to within a factor of two of the initial background within a few minutes as shown in Figure A.3 and continued to fall off slowly with time. It would therefore appear that toluene could be used as a suitable candidate for a seeding agent for laser calibration systems, providing it is introduced in sufficiently high levels that any background toluene contribution is negligible.

A 1.3 Gas Purification System

In 1985, Hubricht et al studied the effect of laser induced ionisation of purification of counter gases using a titanium getter pump in conjunction with an activated carbon cold trap. It was observed that impurities such as oxygen and organic molecules were removed after a few hours of cleaning, resulting in ionisation produced below the detection limit of around 0.4 ion pairs/cm. When circulation was stopped, the ionisation gradually rose to its initial level after 3-5 days.

Having established the source of the ionisation to be organic impurities in the P10 gas, it became necessary to study the effect on the ionisation of purification of this gas. Cleaning of the gas is a necessary step to remove oxygen and water vapour in order to facilitate seeding in calibration experiments. An investigation was carried out at Glasgow on the effect of gas purification on proportional counter gas. This also served as an introduction for the author to the specialised techniques of clean gas handling systems and laser ionisation techniques.

A gas purification system had previously been constructed prior to experimental work on phenol and toluene using two purification towers containing a

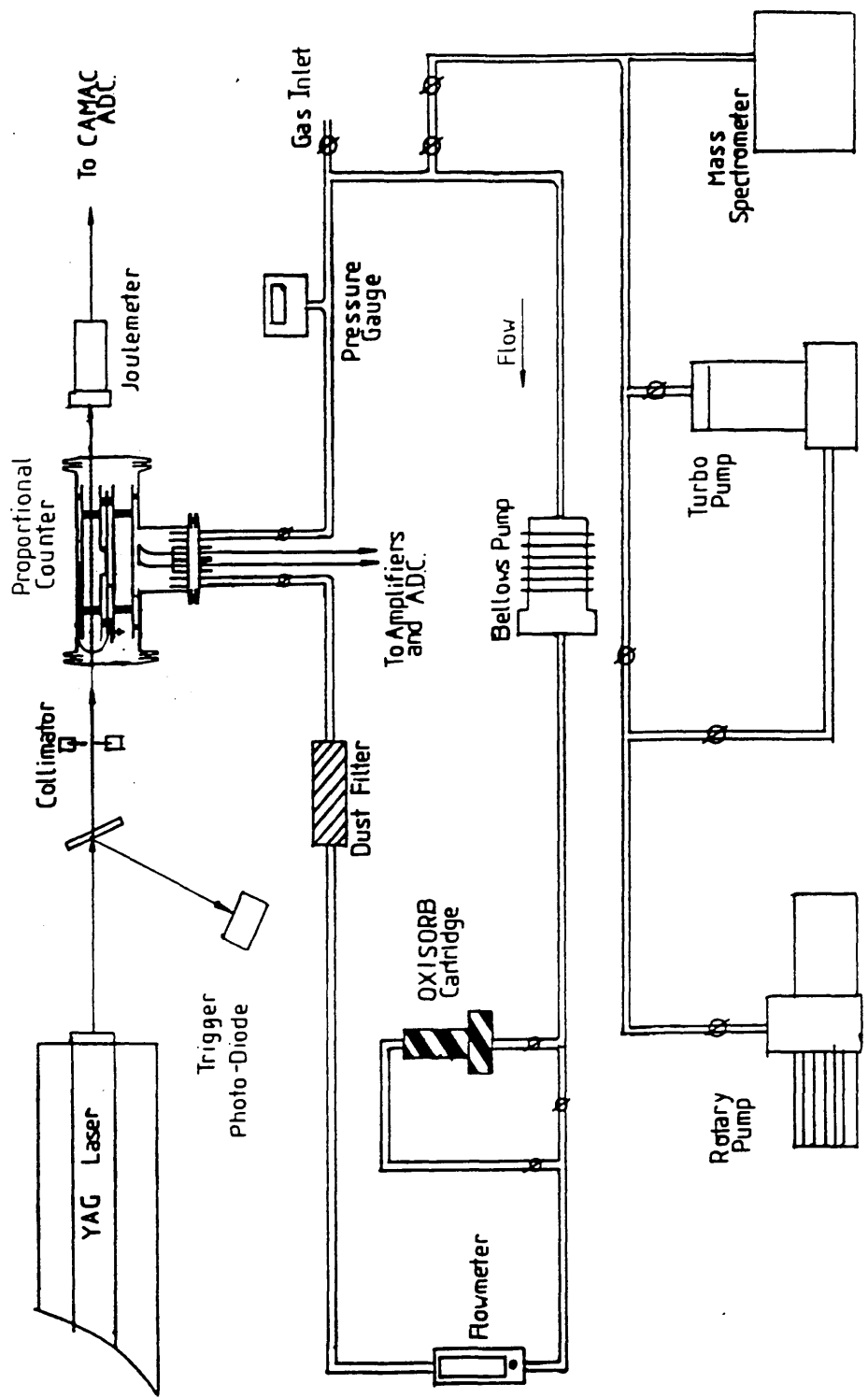
molecular sieve 3A and a freshly reduced copper based catalyst. Ionisation was induced by a nitrogen laser and was monitored as the gas circulated. No reduction in ionisation was observed, and in fact, an increase in ionisation was often recorded due to outgassing from plastic tubing and contamination of dust from the towers into the counter.

A later, more successful system is shown (Figure A.4). The purpose of this system was not principally to reduce background but to remove oxygen and water vapour which can gradually accumulate inside a detector causing a deterioration in performance. The experimental apparatus is described in detail elsewhere (Drysdale et al 1986). It was constructed from stainless steel vacuum components and incorporated into a clean proportional counter circulation system. The purification system consisted of an "Oxisorb" cartridge with a sintered copper gas filter. The cartridge contains reduced chromium oxide plus a molecular sieve size 3A designed to absorb impurities in the gas having a diameter of less than 0.3 nm. The ionisation in the proportional counter was induced by a Nd:YAG pulsed laser with its output quadrupled to give a beam of wavelength 266nm.

The proportional counter was a standard single wire counter containing a ^{55}Fe source to provide an absolute pulse height calibration. The data acquisition system utilised a CAMAC ADC (Le Croy 2259B) and the digitised signals of laser induced ionisation and laser power were stored event by event on floppy disk. Samples of gas could be analysed using a quadrupole mass spectrometer (Edwards Anavac).

The system was initially filled with P10 gas with 50mb of extra air added to a total pressure of 1200mb. The gas mixture was circulated round the system with the Oxisorb cartridge bypassed at a flow rate of 150ml / minute. This corresponds to one complete circuit every 15 minutes. After 12 hours, the ^{55}Fe spectrum was recorded and

Figure A.4 Gas purification system



the resolution was found to be fairly poor at 45% (Figure A.5). A mass spectrum showed the presence of large oxygen and water vapour peaks in the P10 gas (Figure A.6). The gas was then allowed to flow through the Oxisorb cartridge and the ^{55}Fe spectrum was taken after one hour's circulation. Figure A.7 shows that the resolution had substantially improved to 22%. The mass spectrum shows no evidence of oxygen or water vapour peaks, thus demonstrating the efficiency of the cartridge (Figure A.8).

The gas was circulated for a further period of around 80 hours and the ionisation was monitored at regular intervals. Figure A.9 shows a graph of ionisation normalised to $1\text{mJ}/\text{mm}^2$ as a function of circulation time. At each point, a power dependence curve showed the ionisation to be a quadratic function of laser fluence. The ionisation dropped by 50% after about 20 hours and then remained at a constant level. It would therefore appear that either the cartridge has become saturated or that all species which the cartridge can absorb have been removed, and the remaining ionisation is caused by species which are not affected by the Oxisorb.

An investigation was also carried out as to assess the suitability of toluene as a seeding agent for the ALEPH TPC and to monitor its effect on the purification system's ability to absorb oxygen and water vapour. After many investigations on seeding counter gas with organic compounds, toluene established itself as one of the best candidates for the following reasons:

- 1) Toluene is a common impurity in proportional counter gas and seems to be an inherent impurity in argon-methane gas cylinder systems (Drysdale et al 1986).

- 2) It gives a strong ionisation signal (10^4 ion pairs / cm for a laser fluence of $1\text{mJ} / \text{mm}^2$ at 266nm at 2ppm).

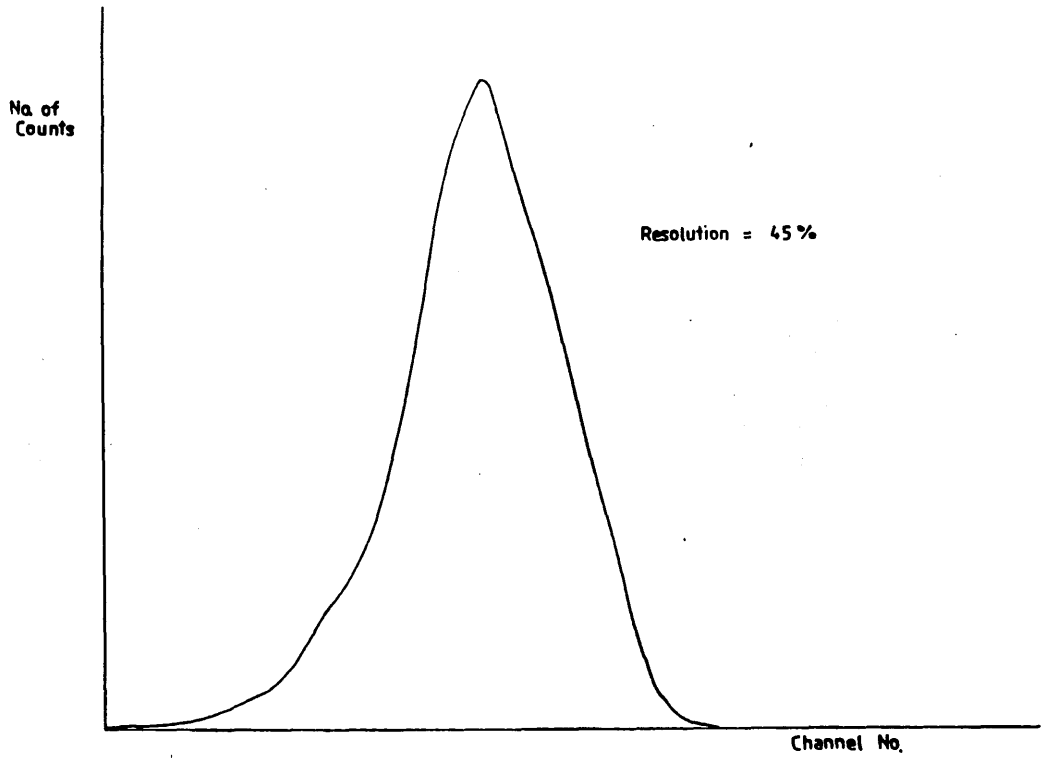


Figure A.5 ^{55}Fe spectrum in a counter filled with 90% argon / 10% methane and air. The resolution is poor at 45%.

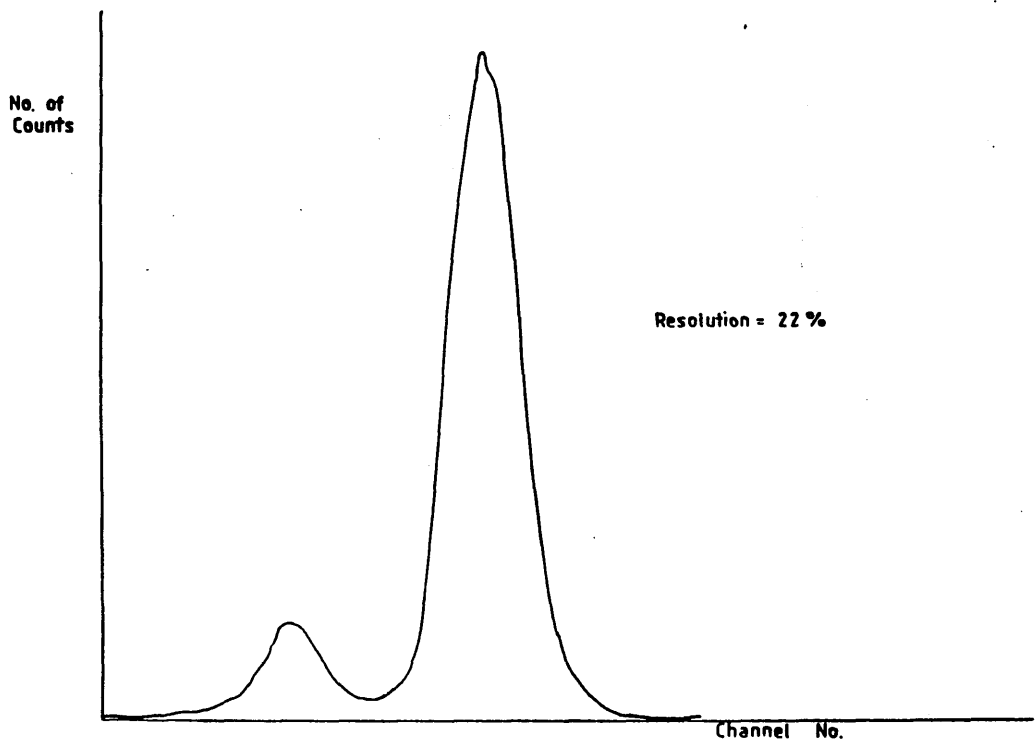


Figure A.7 ^{55}Fe spectrum after purification with resolution improved to 22%

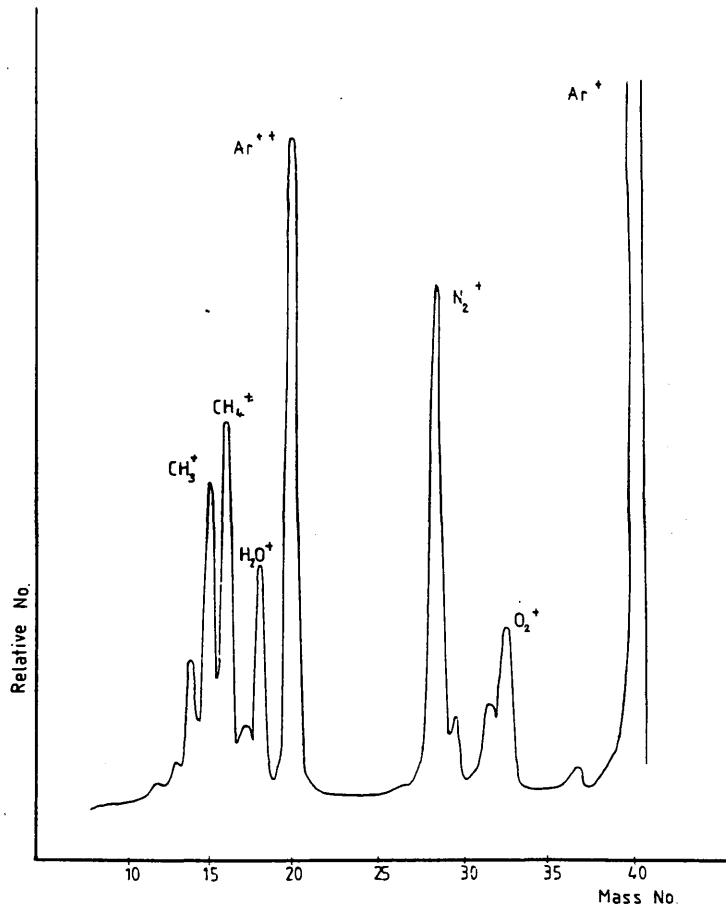


Figure A.6 Mass spectrum of the gas before purification showing strong O_2^+ and H_2O^+ peaks

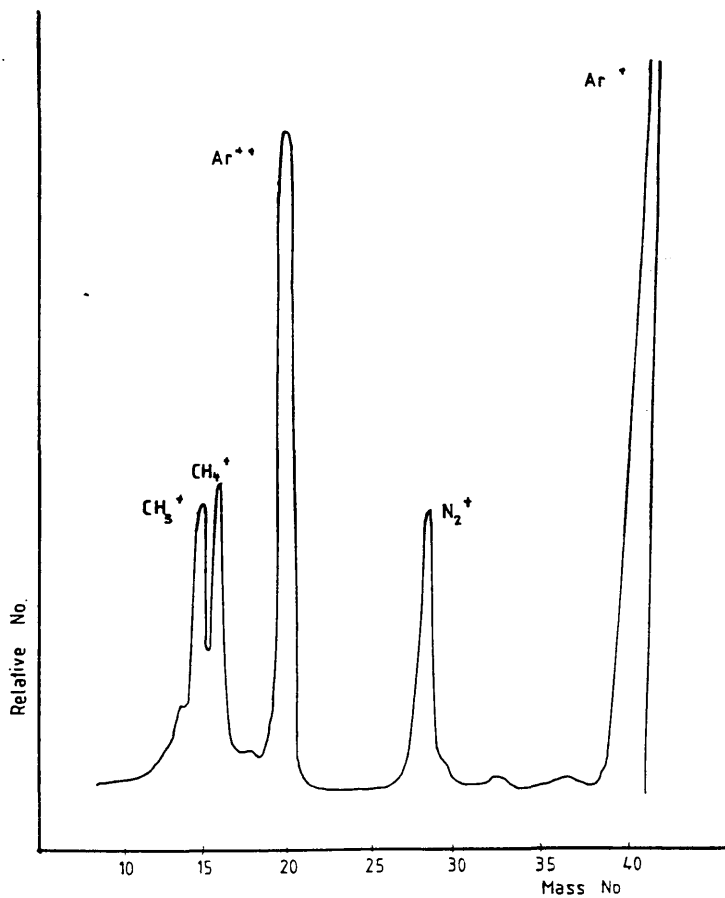
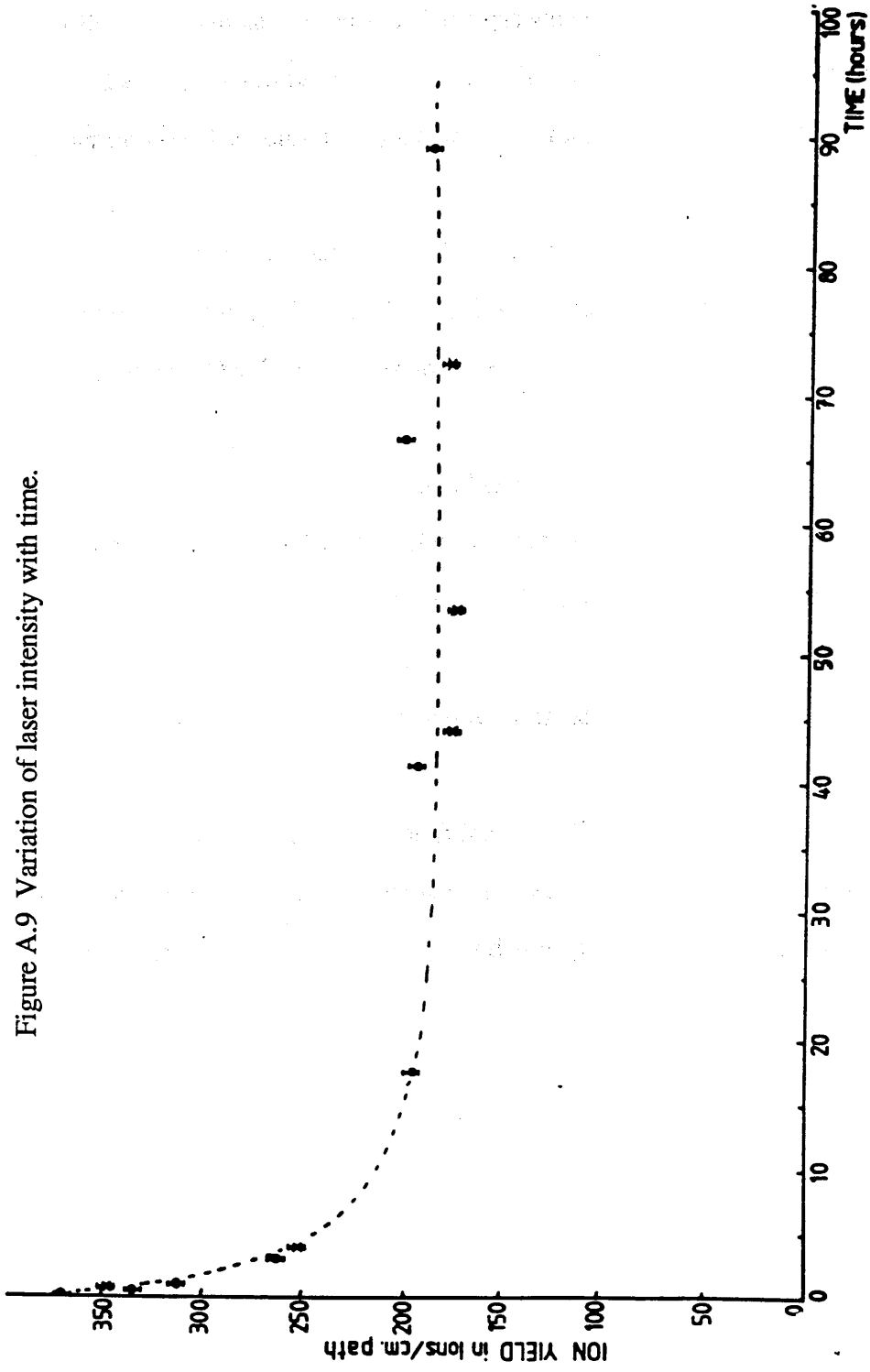


Figure A.8 Mass spectrum after purification showing the absence of the O_2^+ and H_2O^+ peaks

Figure A.9 Variation of laser intensity with time.



3) It does not adhere strongly to proportional counter surfaces and can be removed by flushing with fresh gas.

Using the same experimental apparatus as before, the circulation system was filled with standard argon - methane gas which had been passed over a sample of toluene held at a temperature of -80°C resulting in a toluene concentration of around 2 parts per million. The ionisation yield was 10^4 ions / cm for a laser fluence of $1\text{mJ} / \text{mm}^2$.

After circulation for 12 hours, the ionisation fell to around 500 ions / cm / $1\text{mJ} / \text{mm}^2$, close to the background ionisation yield, indicating that most of the toluene had been trapped by the Oxisorb cartridge.

Heating up the cartridge did not restore the ionisation yield, and it was concluded that the toluene (molecular diameter 6.6Å) had been adsorbed onto the surface of the molecular sieve crystals (pore size 3.1Å). The Oxisorb cartridge was repeatedly seeded with toluene until the ionisation yield was constant at 10^4 ions / cm / $1\text{mJ} / \text{mm}^2$ with circulation time and the cartridge was saturated with toluene.

The gas system was filled with 200mb of air saturated with water vapour to which 1000mb of argon-methane gas was added. No peak could be observed in the pulse height spectrum of ^{55}Fe , and the quadrupole mass spectrum showed strong oxygen and water vapour peaks.

After circulation of gas for 24 hours, the ^{55}Fe spectrum showed an energy resolution of around 25% compared with the usual resolution of 22%. Mass spectrometer scans confirmed the almost complete absence of oxygen and water vapour peaks.

The results demonstrate that although the outer surface of the molecular sieve interacts with the toluene, its ability to absorb oxygen and water is not markedly reduced, while the reduced chromium oxide seems to be unaffected by exposure to toluene.

APPENDIX 2

Laser Mass Spectrometer for Depth Profiling

A second laser mass spectrometer has been designed and constructed at Glasgow. This machine was designed primarily for depth profiling of III-V semiconductors. With very small structures, it is necessary to quantify major elemental concentrations with depth in order to monitor growth efficiency, accuracy and reliability. At present, few existing techniques are capable of the necessary depth resolution or elemental sensitivity. RIMS combines high ionisation efficiency with high ion collection efficiency. Also, the use of sputtered neutrals, which are created in numbers of around two orders of magnitude greater than the secondary ions, should allow a reduction in sputtering rate, and hence a reduction in profile broadening (Broadening effects are dependent on primary ion energy and primary ion to target mass ratio).

It has been suggested that matrix effects are reduced when using neutral ions instead of secondary ions (Parks 1988). A further advantage is that the introduction of oxygen into the sputtering process in order to improve ion yields is unnecessary (Robinson 1984).

A diagram of the laser mass spectrometer is shown in Figure A.10. The spectrometer consists of two vacuum chambers linked by a gate valve. The first chamber is simply an entry lock for rapid sample loading using a vacuum tight transfer

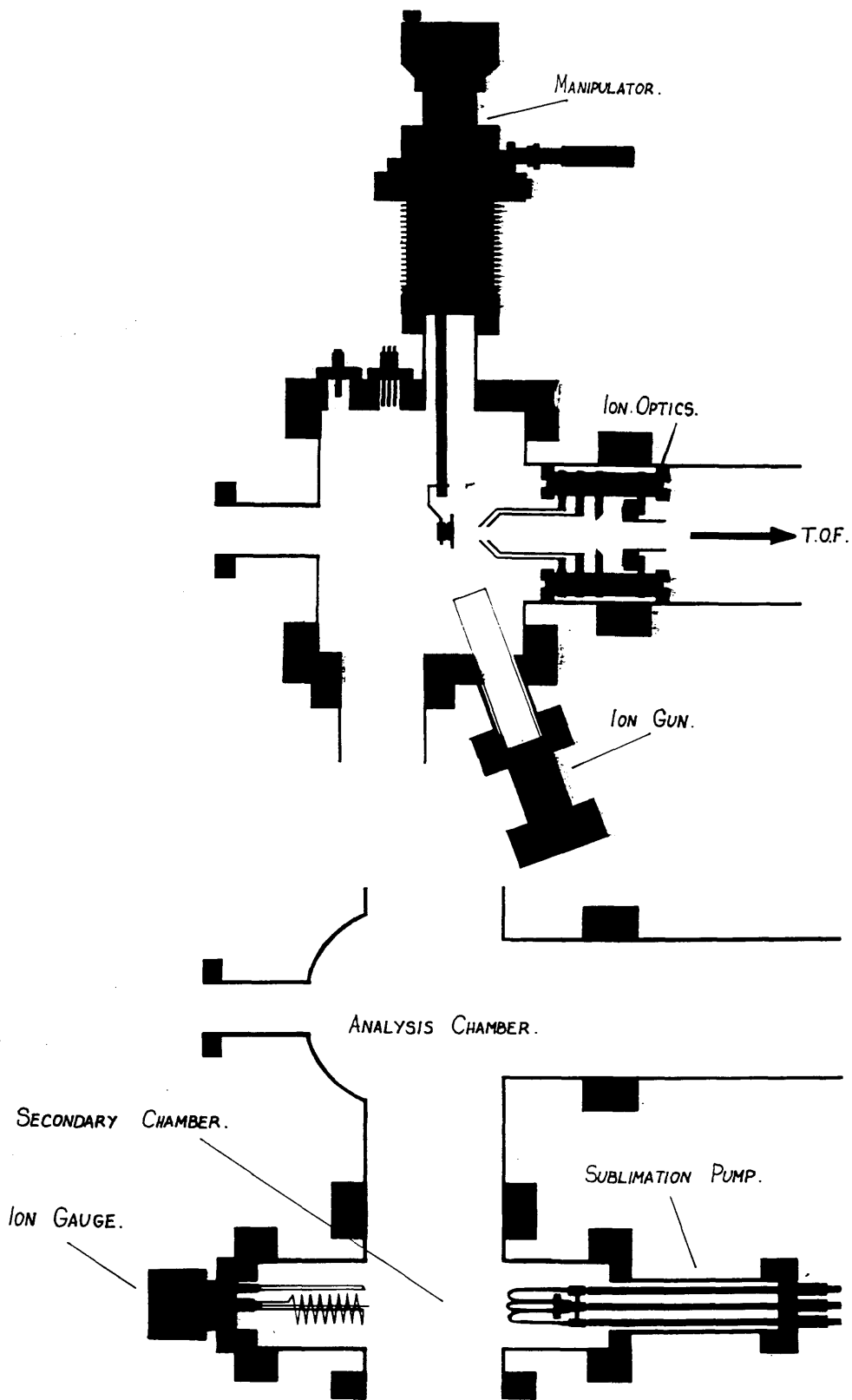


Figure A.10 The laser mass spectrometer for depth profiling

mechanism. The sample analysis takes place in the second chamber. Transfer of the sample to the analysis chamber can take place without a significant deterioration in the quality of the vacuum. The sample is mounted on a manipulator, which is used to position the sample correctly with respect to the ion gun and the extraction system.

The solid samples are vaporised by ion sputtering using a differentially pumped argon ion gun, with a variable energy of between 0-5KeV and beam rastering facility. The gun is also adapted for pulsing for efficient sample utilisation.

A diffusion pump backed by a liquid nitrogen cold trap is used to pump the analysis chamber, whilst the entry chamber is pumped independently by a turbo-molecular pump. Initial tests on this instrument were carried out using a sample of MBE grown GaAs substrate. The system was operated as a TOF SIMS machine, using pulsed ion ablation. Depth profiling requires accurate monitoring of background pressure, as surface adsorption of impurities can seriously affect measurements, especially at the low erosion rates required for accurate profiling of ultra small structures.

This type of mass spectrometer uses electrostatic ion extraction as a means of encouraging the ions produced into the drift tube. Ion optics can be adapted for specific functions, eg, high transmission for trace analysis or high spatial resolution for surface imaging techniques. It is also possible to use ion optics for reducing the number of ablation ions reaching the detector, and this will be the subject of a detailed paper (McLean et al). A possible ion optics design is shown in Figure A.11. A field reversal is created in the laser interaction region which does not permit ablation ions to be liberated from the sample surface, but enables RIMS ions created to the right of the null point to experience the extraction field. Ray tracing programs have been used to obtain the optimum condition for RIMS ion transmission.

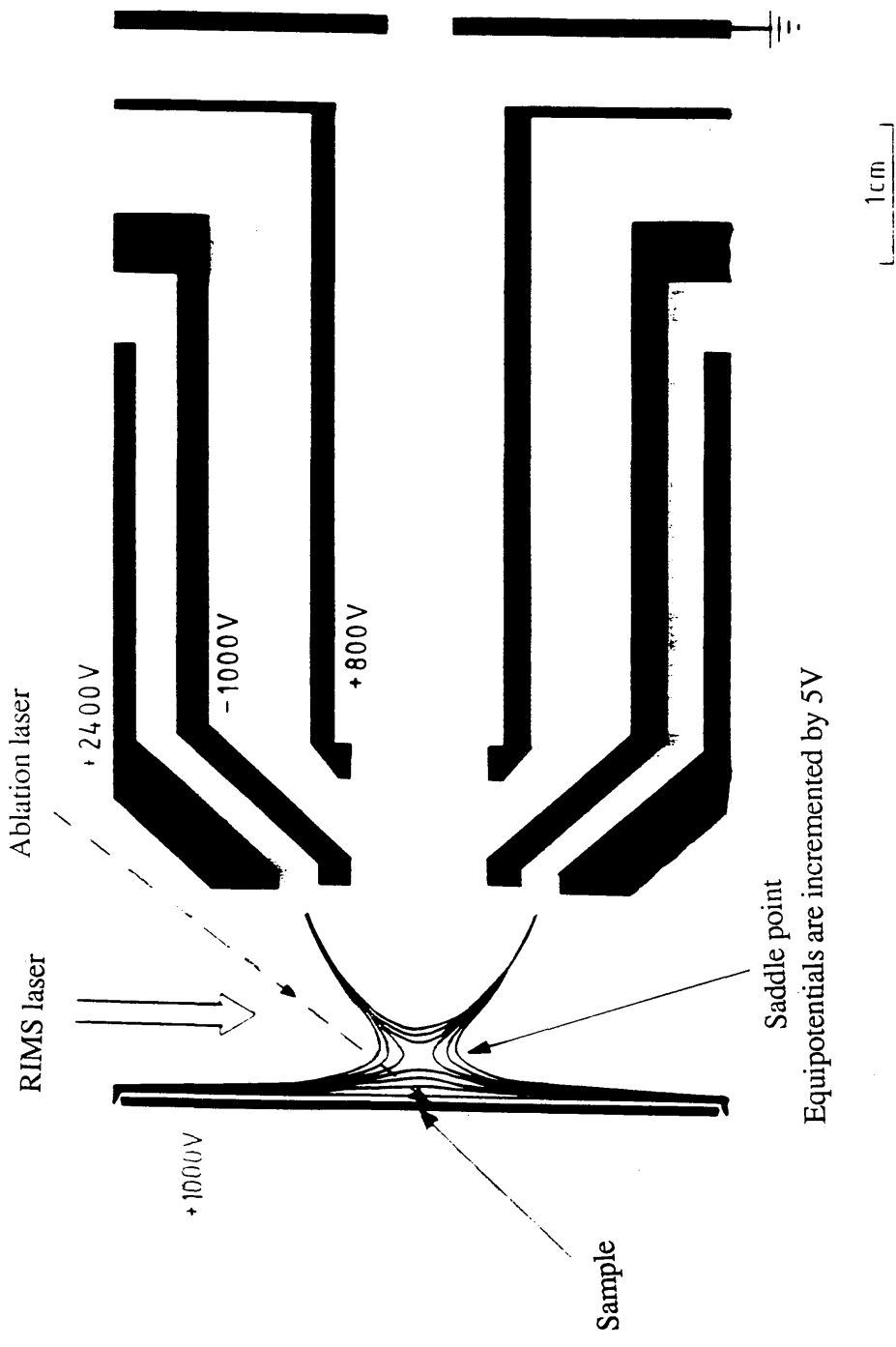


Figure A.11 Ion optics design for reducing ablation ions

In the ion gun, electrons produced from a circular filament are accelerated into the volume of gas by a cylindrical grid, which is positively biased with respect to the filament. The stream of electrons then strip valence electrons from the atoms of the gas, thus forming a cloud of positive argon ions which are consequently extracted and focussed into a tight beam by the optical assembly. Pulsing is achieved by applying a large positive pulse to the grid instead of a d.c. voltage. This has the effect of pulsing the flow of electrons into the gas.

The voltage pulse is normally made as short as possible to avoid unnecessary broadening of the ion pulse, caused by the initial energy spread of the atoms' ionic collisions and charge exchanges in the beam. Work is now in process aimed at depth profiling of GaAs / AlGaAs layered structures, and eventually optimising the operational parameters required to resolve wells down to 10Å in width.

REFERENCES

- Ackerhalt, J.R., Shore, B.W.
Phys. Rev. A 14, 1705 (1976)
- Ackerhalt, J.R., Shore, B.W.
Phys. Rev. A 16, 277 (1977)
- Ambartsumyan, R.V., Kalinin, V.N., Letokhov, V.S.
Soviet Physics JETP Letts. 13, 217 (1971)
- Anderhub, H., Devereux, M., Seiler, P.G.
Nuclear Instruments and Methods 166, 581 (1979)
- Anderhub, H., Devereux, M.J., Seiler, P.G.
Nuclear Instruments and Methods 176, 323 (1980)
- Andersen, C.A., Hinthorne, J.R.
Analytical Chemistry 45, 1421 (1973)
- Antonov, V.S., Knyazev, I.N., Letokhov, V.S., Matuik, V.M., Movshev, V.G.,
Potapov, V.K.
Optics Letts. 3, 37 (1978)
- Apel, E.C., Nogar, N.S., Miller, C.M., Estler, R.C.
"Resonance Ionisation Spectroscopy 1986" Inst. Phys. Conf. Ser. No. 84
- Barth, W.E., Lawton, R.G.
Journal Am. Chem. Soc. 93, 1730 (1971)
- Becker, C.H., Gillen, K.T.
Analytical Chemistry 56, 1671 (1984)
- Beekman, D.W., Callcott, T.A., Kramer, S.D., Arakawa, E.T., Hurst, G.S.,
Nussbaum, E.
Int. J. Mass Spectrom. Ion Phys. 34, 89 (1980)
- Beekman, D.W., Callcott, T.A.
"Resonance Ionisation Spectroscopy 1984" Inst. Phys. Conf. Ser. No. 71
- Bekov, G.I., Letokhov, V.S., Matveev, O.I., Mishin, V.I.
Optics Letters 3, 159 (1978)
- Bekov, G.I., Letokhov, V.S., Matveev, O.I., Mishin, V.I.
Sov. Phys. JEPT 48, 1052 (1978b)
- Bekov, G.I., Letokhov, V.S.
Trends in Analytical Chemistry 2, 252 (1983)
- Bekov, G.I., Letokhov, V.S.
Applied Physics B 30, 161 (1983b)
- Bekov, G.I., Egorov, A.S., Letokhov, V.S., Radayev, V.N.
Nature 301, 410 (1983c)
- Bekov, G.I., Letokhov, V.S., Radayev, V.N.
Journal of the Optical Society of America B 2, 1554 (1985)

- Bekov, G.I., Kudryavtsev, Y.A., Auterinen, I., Likonen, J.
"Resonance Ionisation Spectroscopy 1986" Inst. Phys. Conf. Ser. No. 84
- Boerner, K.
- private communication (1985)
- Boesl, U., Neusser, H.J., Schlag, E.W.
J. Chem Phys. 72, 4327 (1980)
- Boesl, U., Grotemeyer, J., Walter, K., Schlag, E.W.
Analytical Instrum. 16 (1) 151 (1987)
- Bourotte, J., Sadoulet, B.
Nuclear Instruments and Methods 173, 463 (1980)
- Brophy, J.H., Rettner, C.T.
Chem. Phys. Letts. 69, 351 (1979)
- Bushaw, B.A., Whitaker, T.J.
Journal of Chemical Physics 74, 6519 (1981)
- Bushaw, B.A.
Analytical Chemistry 57, 2397 (1985)
- Cannon, B.D., Bushaw, B.A., Whitaker, T.J.
Journal of the Optical Society of America B 2, 1542 (1985)
- Chen, C.H., Hurst, G.S.
Proceedings SPIE - International Society for Optical Engineering 426, 2 (1983)
- Chen, C.H., Kramer, S.D., Allman, S.L., Hurst, G.S.
Applied Physics Letters 44, 640 (1984)
- Chin, S.L., Lambropoulos, P.
Multiphoton Ionisation of Atoms Academic Press (1984)
- Christian, W., Compton, R.N., Stockdale, J.A.D., Miller, J.C., Cooper, C.D.,
Tang, X., Lambropoulos, P.
Physical Review A 30, 1775 (1984)
- Collins, C.B., Johnson, B.W., Popescu, D., Musa, G., Pascu, M.L., Popescu, I.
Physical Review A 8, 2197 (1973)
- Collins, C.B., Johnson, B.W., Mirza, M.Y., Popescu, D., Popescu, I.
Physical Review A 10, 813 (1974)
- Collins, C.B., Curry, S.M., Johnson, B.W., Mirza, M.Y., Chellehmalzadeh,
M.A., Anderson, J.A., Popescu, D., Popescu, I.
Physical Review A 14, 1662 (1976)
- Collins, C.B., Anderson, J.A., Popescu, D., Popescu, I.
Journal of Chemical Physics 74, 1053 (1981)
- Collins, C.B., Lee, F.W., Anderson, J.A., Vicharelli, P.A., Popescu, D.,
Popescu, I.
Journal of Chemical Physics 74, 1067 (1981b)

- Dermtroder, W.
Laser Spectroscopy, Springer Verlag (1982)
- Desalvo, M., Desalvo, R.
Nuclear Instruments and Methods 201, 357 (1982)
- Donohue, D.L., Young, J.P., Smith, D.H.
Int. J. Mass Spectrom. Ion Phys. 43, 293 (1982)
- Donohue, D.L., Smith, D.H., Young, J.P., McKown, H.S., Pritchard, C.A.
Analytical Chemistry 56, 379 (1984)
- Donohue, D.L., Christie, W.H., Goeringer, D.E., McKown, H.S.
Analytical Chemistry 57, 1193 (1985)
- Donohue, D.L., Young, J.P., Smith, D.H.
Applied Spectroscopy 39, 93 (1985)
- Downey, S.W., Nogar, N.S., Miller, C.M.
Analytical Chemistry 56, 827 (1984)
- Drysdale, S.L.T., Ledingham, K.W.D., Raine, C., Smith, K.M., Smyth, M.H.C.,
Stewart, D.T., Towrie, M., Houston, C.M.
Nucl. Inst. and Meth. A252 (1986) 521
- Drysdale, S.L.T., Ledingham, K.W.D., Raine, C., Smith, K.M., Smyth, M.H.C.,
Stewart, D.T., Towrie, M., Houston, C.M.
ALEPH 86-30 (distr. TPCC-AL) (1986b)
- Eastham, D.A.
Atomic Physics of Lasers , Taylor and Francis (1986)
- Eisberg, R.M., Resnick, R.
Quantum Physics of Atoms, Molecules, Solids, Nuclei and Particles, Wiley (1974)
- Fassett, J.D., Travis, J.C., Moore, L.J., Lytle, F.E.
Analytical Chemistry 55, 765 (1983)
- Fassett, J.D., Powell, L.J., Moore, L.J.
Analytical Chemistry 56, 2228 (1984)
- Fassett, J.D., Moore, L.J., Shideler, R.W., Travis, J.C.
Analytical Chemistry 56, 203 (1984b)
- Fassett, J.D., Travis, J.C.
Spectrochim Acta 43B 12, 1409 (1988)
- Fowler, P.W., Steer, J.I.
Journal Chem.Soc. Chem. Commun. 18, 1403 (1987)
- Frueholz, R., Wessel, J., Wheatly, E.
Analytical Chemistry 52, 281 (1980)
- Geusic, M.E., McIlrath, T.J., Jarrold, M.F., Bloomfield, C.A., Freeman, R.R.,
Brown, W.L.
Journal of Chemical Physics 84, 2421 (1986)
- Gladney, E.S.
Analytica Chimica Acta 118 (1980) 385

Granneman, E.H.A., Klewer, M., Nygaard, K.J., Van der Wiel, M.J.
J. Phys. B 9, 865 (1976)

Gupta, R., Happer, W., Wagner, J., Wennmyr, E.
J. Chem. Phys. 68, 799 (1978)

Hahn, M.Y., Honea, E.C., Pagueia, A.J., Schriver, K.E., Camarena, A.M.,
Whetten, R.L.
Chemical Physics Letters 130, 12 (1986)

Harrison, W.W., Savickas, P.J., Hess, K.R., Marcus, R.K.
"Resonance Ionisation Spectroscopy 1984" Inst. Phys. Conf. Ser. No. 71

Heath, J.R. et al
J. Am. Chem. Soc. 109 (1987) 385

Hilke, H.J.
Nuclear Instruments and Methods 174, 145 (1980)

Hoffmann, R.
Tetrahedron 22, 521 (1966)

Houston, C.M.
Ph.D. Thesis Glasgow University (1986)

Houston, C.M., Drysdale, S.L.T., Ledingham, K.W.D., Raine, C., Smith, K.M.,
Smyth, M.H.C., Stewart, D.T., Towrie, M.
"Resonance Ionisation Spectroscopy 1986" Inst. Phys. Conf. Ser. No. 84

Houston, C.M., Drysdale, S.L.T., Jennings, R., Land, A.P., Ledingham, K.W.D.,
Singhal, R.P., Smyth, M.H.C., Stewart, D.T., Towrie, M.
J. Phys. D: Appl. Phys. 21 (1988) S 59

Hubricht, G., Kleinknecht, K., Muller, E., Pollmann, D., Teupe, E.
Nucl. Instrm. Meths. 228, 327 (1985)

Hurst, G.S., Payne, M.G., Nayfeh, M.H., Judish, J.P., Wagner, E.B.
Physical Review Letters 35, 82 (1975)

Hurst, G.S., Nayfeh, M.H., Young, J.P.
Applied Physics Letters 30, 229 (1977)

Hurst, G.S., Nayfeh, M.H., Young, J.P.
Physical Review A 15, 2283 (1977b)

Hurst, G.S., Allman, S.L., Payne, M.G., Whitaker, T.J.
Chemical Physics Letters 60, 150 (1978)

Hurst, G.S., Payne, M.G., Kramer, S.D., Young, J.P.
Reviews of Modern Physics 51, 767 (1979)

Hurst, G.S., Payne, M.G., Kramer, S.D., Chen, C.H.
Physics Today 33, 24 (1980)

Hurst, G.S.
Analytical Chemistry 53, 1448A (1981)

- Hurst, G.S.
Journal of Chemical Education 59, 895 (1982)
- Hurst, G.S., Payne, M.G.
Spectrochim Acta 43B 12, 713 (1988)
- Jones, D.E.H.
New Scientist 245, 3 (Nov 1966)
- Kelly, R., Rothenberg, J.E.
Nucl. Inst. Phys. Res. B 718, 735 (1985)
- Kimock, F.M., Baxter, J.P., Winograd, N
Surface Science 124, L41 (1983)
- Kimock, F.M., Baxter, J.P., Pappus, D.L., Kobrin, P.H., Winograd, N.
Analytical Chemistry 56, 2782 (1984)
- Klein, D.J., Schmalz, T.G., Hite, G.E., Seitz, W.A.
Journal Am. Chem. Soc. 108, 1301 (1986)
- Kronert, U., Bonn, J., Kluge, H.J., Ruster, W., Wallmeroth, K., Peuser, P.,
Trautmann, N.
Applied Physics B38 249 (1985)
- Kroto, H.W., Heath, J.R., O'Brien, S.C., Curl, R.F., Smalley, R.E.
Nature 318, 162 (1985)
- Kroto, H.W.
Nature 329 (1987) 529
- Kroto, H.W., McKay, K.
Nature 331, 328 (1988)
- Lambropoulos, P., Zoller, P.
"Multiphoton Ionisation of Atoms"
Academic Press, Canada (1988)
- Ledingham, K.W.D., Raine, C., Smith, K.M., Campbell, A.M., Towrie, M.,
Trager, C., Houston, C.M.
Nucl. Instrm. Meths. 225, 319 (1984)
- Ledingham, K.W.D., Cahill, J.W., Drysdale, S.L.T., Raine, C., Smith, K.M.,
Smyth, M.H.C., Stewart, D.T., Towrie, M., Houston, C.M.
"Resonance Ionisation Spectroscopy 1986" Inst. Phys. Conf. Ser. No. 84
- Letokhov, V.S.
Non linear Laser Chemistry, Springer Verlag (1983)
- Letokhov, V.S.
Laser Photoionisation Spectroscopy, Academic Press (1987)
- Liu, Y., O'Brien, S.C., Zhang, Q., Heath, J.R., Tittel, F.K., Curl, R.F., Kroto,
H.W., Smalley, R.E.
Chemical Physics Letters 126, 215 (1986)
- Lubman, D.M., Naaman, R., Zare, R.N.
J.Chem. Phys. 72, 3034 (1980)

- Lubman, D.M., Tembreull, R., Sin, C.H.
Analytical Chemistry 57, 1084 (1985)
- Marek, J., Munster, P.
Journal of Physics B 13, 1731 (1980)
- Mark, T.D.
International Journal of Mass Spectrometry and Ion Processes 79, 1 (1987)
- Marks, R.W.
The Dymaxion World of Buckminster Fuller, Reinhold (1960)
- Mayo, S., Lucatorto, T.B., Luther, G.G.
Analytical Chemistry 54, 553 (1982)
- McLean, C.J., Marsh, J.H., Cahill, J.W., Drysdale, S.L.T., Jennings, R., Land, A.P., Ledingham, K.W.D., McCombes, P.T., Singhal, R.P., Smyth, M.H.C., Stewart, D.T., Towrie, M.
"Resonance Ionisation Spectroscopy 1988" Inst. Phys. Conf. Ser. No. 94
- Miller, C.M., Nogar, N.S., Gancarz, A.J., Shields, W.R.
Anal. Chem. 54, 2377 (1982)
- Miller, C.M., Nogar, N.S.
Analytical Chemistry 55, 1607 (1983)
- Moore, C.E.
"Atomic Energy levels"
NBS Publications 467 U.S. Gov. Printing Office, Washington (1952)
- Moore, L.J., Fassett, J.D., Travis, J.C.
Analytical Chemistry 56, 2770 (1984)
- Moore, L.J., Fassett, J.D., Travis, J.C., Lucatorto, T.B., Clark, C.W.
J. Opt. Soc. Am. B2 1561 (1985)
- Nadkarni, R.A.
Analytical Chemistry 56, 2233 (1984)
- Nayfeh, M.H., Hurst, G.S., Payne, M.G., Young, J.P.
Physical Review Letters 41, 302 (1978)
- Nayfeh, M.H.
Optical Engineering 19, 57 (1980)
- Niemax, K.
Appl. Phys. B 32, 59 (1983)
- Nogar, N.S., Downey, S.W., Miller, C.M.
"Resonance Ionisation Spectroscopy 1984" Inst. Phys. Conf. Ser. No. 71
- Nogar, N.S., Downey, S.W., Miller, C.M.
Analytical Chemistry 57, 1144 (1985)
- Nogar, N.S., Estler, R.C., Miller, C.M.
Analytical Chemistry 57, 2441 (1985b)
- Nogar, N.S., Estler, R.C., Rowe, M.W., Fearey, B.L., Miller, C.M.
"Resonance Ionisation Spectroscopy 1988" Inst. Phys. Conf. Ser. No. 94

- Normand, D, Morellec, J.
Journal of Physics B 13, 1551 (1980)
- O'Brien, S.C., Heath, J.R., Kroto, H.W., Curl, R.F., Smalley, R.E.
Chemical Physics Letters 132, 99 (1986)
- O'Brien, S.C., Heath, J.R., Curl, R.F., Smalley, R.E.
Journal of Chemical Physics 88, 220 (1988)
- Oechsner, H., Gerhard, W.
Surf. Sci. 44, 480 (1974)
- O'Keefe, A., Ross, M.M., Baronavski, A.P.
Chemical Physics Letters 130, 17 (1986)
- Parks, J.E., Schmitt, H.W., Hurst, G.S., Fairbank, W.M.
Thin Solid Films 108, 69 (1983)
- Parks, J.E., Schmitt, H.W., Hurst, G.S., Fairbank, W.M.
Proceedings SPIE - International Society for Optical Engineering 426, 32 (1983b)
- Parks, J.E., Schmitt, H.W., Hurst, G.S., Fairbank, W.M.
"Resonance Ionisation Spectroscopy 1984" Inst. Phys. Conf. Ser. No. 71
- Payne, M.G., Hurst, G.S., Nayfeh, M.H., Judish, J.P., Chen, C.H., Wagner, E.B., Young, J.P.
Physical Review Letters 35, 1154 (1975)
- Pellin, M.J., Young, C.E., Calaway, W.F., Gruen, D.M.
Surf. Sci. 144, 619 (1984)
- Pindzola, M.S.
Physical Review A 32, 1883 (1984)
- Pitzer, K.S., Clementi, E.,
Journal Am. Chem. Soc. 21, 4477 (1959)
- Popescu, D, Pascu, M.L., Collins, C.B., Johnson, B.W., Popescu, I.
Physical Review A 8, 1666 (1973)
- Popescu, D, Collins, C.B., Johnson, B.W., Popescu, I.
Physical Review A 9, 1182 (1974)
- Ready, J.F.
Effects of High Power Laser Radiation, Academic Press 109 (1971)
- Robinson, M.T.
"Resonance Ionisation Spectroscopy 1984" Inst. Phys. Conf. Ser. No. 71
- Rockwood, S., Reilly, J.P., Hohla, K., Kompa, K.L.
Opt. Commun. 28, 175 (1979)
- Rohlfing, E.A., Cox, D.M., Kaldor, A.
Journal of Chemical Physics 81, 3322 (1984)
- Savickas, P.J., Hess, K.R., Marcus, R.K., Harrison, W.W.
Anal. Chem. 56, 817 (1984)

- Seifert, G., Becker, S., Dietze, H.J.
International Journal of Mass Spectrometry and Ion Processes 84, 121 (1988)
- Sigmund, P
Rev. Roum. Physics 17, 823 (1972)
- Sin, C.H., Tembreull, R., Lubman, D.M.
Analytical Chemistry 56, 2776 (1984)
- Singhal, R.P., Land, A.P., Ledingham, K.W.D., Towrie, M.
- to be published (1988)
- Siomos, K., Kourouklis, G., Christophorou, L.G.
Chem. Phys. Letts. 80, 504 (1981)
- Smyth, M.H.C., Drysdale, S.L.T., Jennings, R., Ledingham, K.W.D., Raine, C.,
Smith, K.M., Stewart, D.T., Towrie, M., Houston, C.M., Baxter, M.S., Scott, R.D.
"Resonance Ionisation Spectroscopy 1986" Inst. Phys. Conf. Ser. No. 84
- Smyth, M.H.C., Drysdale, S.L.T., Jennings, R., Land, A.P., Ledingham, K.W.D.,
Singhal, R.P., Stewart, D.T., Towrie, M., Houston, C.M.
"Resonance Ionisation Spectroscopy 1988" Inst. Phys. Conf. Ser. No. 94
- Smyth, M.H.C.
Ph.D. Thesis Glasgow University (1988)
- Sobelman, I.I.
Atomic Spectra and Radiative Transitions, Springer Verlag (1979)
- Tembreull, R., Lubman, D.M.
Analytical Chemistry 56, 1962 (1984)
- Tembreull, R., Lubman, D.M.
Analytical Chemistry 58, 1299 (1986)
- Thorne, A.P.
Spectrophysics, Chapman and Hall (1988)
- Towrie, M., Drysdale, S.L.T., Jennings, R., Ledingham, K.W.D., Land, A.P.,
McCombes, P.T., Singhal, R.P., Smyth, M.H.C., Stewart, D.T., Houston, C.M.,
McLean, C.J.
"Resonance Ionisation Spectroscopy 1988" Inst. Phys. Conf. Ser. No. 94
- Towrie, M.
Ph.D. Thesis Glasgow University (1987)
- Travis, J.C., Fassett, J.D., Moore, L.J.
"Resonance Ionisation Spectroscopy 1984" Inst. Phys. Conf. Ser. No. 71
- Tsi - Ze, N., San - Tsiang, T.
Physical Review 52, 91 (1937)
- Weber, K.H., Sansonetti, C.J.
Phys. Rev. A 35, 4650 (1987)
- Whitaker, T.J., Bushaw, B.A.
Chemical Physics Letters 79, 506 (1981)

- Wilcox, L.R., Lamb, W.E.Jr.
Phys. Rev. 119, 1915 (1960)
- Wiley, W.C., McLaren, I.H.
Review of Scientific Instruments 26, 1150 (1955)
- Williams, M.W., Beekman, D.W., Swan, J.B., Arakawa, E.T.
Analytical Chemistry 56, 1348 (1984)
- Winograd, N., Baxter, J.P., Kimock, F.M.
Chemical Physics Letters 88, 581 (1982)
- Winograd, N.
"Resonance Ionisation Spectroscopy 1984" Inst. Phys. Conf. Ser. No. 71
- Wiese, W.L., Martin, G.A.
NBS Pub. NSRDS - NBS 68 Dec 1980
- Yamada, S., Hino, A., Kano, K., Ogawa, T.
Analytical Chemistry 55, 1914 (1983)
- Yang, S.H., Pettiette, C.L., Conceicao, J., Cheshnovsky, O., Smalley, R.E.
Chemical Physics Letters 139, 233 (1987)
- Young, J.P., Hurst, G.S., Kramer, S.D., Payne, M.G.
Analytical Chemistry 51, 1050A (1979)
- Young, J.P., Donohue, D.L.
Analytical Chemistry 55, 88 (1983)
- Young, J.P., Donohue, D.L.
Analytical Chemistry 55, 378 (1983b)
- Young, J.P., Donohue, D.L., Smith, D.H.
"Resonance Ionisation Spectroscopy 1984" Inst. Phys. Conf. Ser. No. 71
- Young, C.E., Pellin, M.J., Calaway, W.F., Jorgensen, B., Schweitzer, E.L., Gruen, D.M.
"Resonance Ionisation Spectroscopy 1986" Inst. Phys. Conf. Ser. No. 84
- Zhang, Q.L., O'Brien, S.C., Heath, J.R., Liu, Y., Curl, R.F., Kroto, H.W., Smalley, R.E.
Journal Phys. Chem. 90, 525 (1986)
- p151 addition - Townsend, D.D., Kelly, J.C., Hartley, N.E.W.

Ion Implantation, Sputtering and their Applications (1976) Academic Press

